SAPIENZA
UNIVERSITÀ DI ROMA

Dottorato in Scienze della Terra
Ciclo XXIV

Magma differentiation in shallow, thermally zoned magma chambers: the example of Sabatini Volcanic District (central Italy)

Matteo Masotta

Dipartimento di Scienze della Terra

Anno Accademico 2010/2011

Facoltà di Scienze Matematiche Fisiche e Naturali

Dottorato in Scienze della Terra

SAPIENZA
UNIVERSITÀ DI ROMA

Magma differentiation in shallow, thermally zoned magma chambers: the example of Sabatini Volcanic District (central Italy)

Matteo Masotta

Docente Guida: Dott. Mario Gaeta

Co-Docente Guida: Dott.ssa Carmela Freda

Anno Accademico 2010-2011

Magma differentiation in shallow, thermally zoned magma chambers: the example of Sabatini Volcanic District (central Italy)

Dottorando: Matteo Masotta

Docente Guida: Dott. Mario Gaeta (Dipartimento di Scienze della Terra, Sapienza – Università di Roma)

Co-Docente Guida: Dott.ssa Carmela Freda (Istituto Nazionale di Geofisica e Vulcanologia, Roma)

Riassunto

Le grandi eruzioni esplosive "*caldera-forming*" sono comunemente associate a camere magmatiche localizzate nella crosta superiore (bassa pressione). In genere i prodotti emessi nel corso di queste eruzioni presentano variazioni delle caratteristiche tessiturali e/o chimiche, ben riconoscibili lungo la successione stratigrafica (es. pomici vetrose e povere in cristalli alla base delle successioni piroclastiche, scorie ricche in cristalli al tetto). Dallo studio delle caratteristiche chimico-tessiturali delle vulcaniti è possibile risalire alle condizioni pre-eruttive del magma (temperatura, pressione e contenuto in volatili), dalla loro variazione lungo una successione stratigrafica è invece possibile ottenere indicazioni sui processi chimico-fisici avvenuti all'interno della camera magmatica. Tali variazioni sono generalmente associate alla presenza di zonature della camera magmatica rispetto a temperatura e composizione chimica del magma genitore.

Altra caratteristica ricorrente nei prodotti emessi nel corso delle grandi eruzioni esplosive è il basso contenuto in cristalli a fronte di un elevato grado di differenziazione. Questo è un ben noto paradosso della vulcanologia. La cristallizzazione frazionata (formazione e rimozione dei cristalli) è infatti il processo più comunemente invocato per spiegare la formazione di magmi differenziati, sebbene i comuni meccanismi di separazione fuso-cristalli (es. affondamento, compattazione) siano scarsamente efficaci in presenza di magmi differenziati, in quanto limitati dalle condizioni fisiche del magma stesso (alta viscosità, basso contrasto di densità fra le fasi solide e il liquido).

Scopo di questo studio è stato individuare a) i processi di differenziazione attivi nelle camere magmatiche termicamente zonate con particolare attenzione all'individuazione di un meccanismo di separazione fuso-cristalli alternativo all'affondamento e b) le condizioni pre-eruttive dei magmi che hanno alimentato le grandi eruzioni esplosive. Come "caso di studio" è stato utilizzato il distretto vulcanico dei Monti Sabatini (Italia centrale) poiché offre numerosi esempi di eruzioni esplosive i cui depositi mostrano variazioni rilevanti della tessitura dei prodotti eruttati.

Per individuare i meccanismi di differenziazione e le condizioni pre-eruttive dei magmi che hanno alimentato le grandi eruzioni esplosive del distretto, è stato quindi affrontato un studio di dettaglio basato su: i) caratteristiche tessiturali e chimiche delle vulcaniti (juvenili e litici) campionate all'interno dei maggiori depositi piroclastici; ii) modellazione mediante bilanci chimici e bilanci di massa sul processo di differenziazione responsabile della formazione dei magmi fonolitici; iii) esperimenti di equilibri di fase e lungo gradienti di temperatura. I modelli di differenziazione magmatica ottenuti sulla base delle evidenze

naturali e dei bilanci di massa sono stati convalidati contemporaneamente dagli esperimenti di equilibri di fase e da quelli di cristallizzazione lungo gradienti di temperatura. Questi ultimi hanno inoltre permesso di valutare i meccanismi fisici di separazione fuso-cristalli all'interno di camere magmatiche termicamente zonate, dimostrando il ruolo chiave dei fronti di solidificazione (regioni di contatto tra magma e incassante) nei processi di differenziazione magmatica e segregazione di fusi differenziati e poveri in cristalli. Infatti, è stato dimostrato come l'instabilità del fronte di solidificazione al tetto di una camera magmatica zonata possa causare l'estrazione di magma differenziato dalla regione cristallina del fronte verso la porzione più superficiale della camera magmatica. La costante presenza di un gradiente di temperatura diretto dall'esterno all'interno del corpo magmatico differenziato estratto dal fronte, produrrebbe una cristallizzazione maggiore nelle porzioni più esterne rispetto a quelle interne. Questa zonatura termica del magma all'interno della camera magmatica giustificherebbe la zonatura tessiturale osservata nei depositi, mediante la messa in posto di prodotti progressivamente più ricchi in cristalli nel corso dei singoli eventi eruttivi. Il raggiungimento della condizione pre-eruttiva di sovra-saturazione in volatili può essere infine spiegato da tale modello mediante la diffusione dei volatili nella direzione del gradiente di temperatura (in risposta al gradiente di cristallinità del magma), compatibilmente con la velocità di diffusione dell'acqua osservata negli esperimenti di gradiente di temperatura.

Abstract

Large explosive eruptions are commonly fed by shallow-level, thermally zoned magma chambers and usually emplace texturally and/or chemically zoned deposits (i.e., crystal-poor *vs.* crystal-rich products). The texture of volcanic rocks represents the best witness of magmatic processes occurring in the magma chamber and of pre-eruptive conditions of feeder magmas (i.e., temperature, pressure and volatile concentration). The challenge is to unlock this information and make it available for the general understanding of volcanic systems.

The eruption of crystal-poor, differentiated products during these explosive eruptions represents a paradox of igneous petrology, being the magmatic differentiation driven by crystallization. Fractional crystallization (formation and removal of crystals) is commonly invoked to explain the origin of zoned magma chambers, although not all the crystal-melt separation mechanisms are feasible in differentiated magmas, because of the high viscosity of the melt and the low solid-melt density contrast. Therefore, alternative models of differentiation and liquid fractionation need to be considered and then constrained by natural evidences (textural features and distribution of volcanic products in the pyroclastic deposits).

The Sabatini Volcanic District (central Italy) offers a lot of examples of explosive eruptions, whose deposits, intriguingly, are at the same time texturally zoned but relatively homogeneous from a chemical point of view. With the purpose to investigate on the differentiation process and the pre-eruptive conditions of magmas feeding these large eruptions, this study focused on: i) the textural and chemical features of volcanic rocks (juvenile and lithic clasts) sampled within the major pyroclastic deposits; ii) the modeling of the differentiation of phonolitic magmas by means of chemical and mass balances; iii) the experimental study of magma differentiation under isothermal conditions (phase equilibria experiments) and along temperature gradients (temperature gradient experiments). Hence, models of magma differentiation obtained on the basis of natural evidences and mass balance calculations have been validated by both phase equilibria and temperature gradient experiments. The latter also shed light into physical mechanisms of crystal-melt separation in thermally zoned magma chambers, emphasizing the role of solidification fronts (i.e., the cooling margins of magma chambers) in driving both melt differentiation and melt extraction, to form batches of differentiated, crystal-poor magma. Indeed, the instability of the solidification front at the crystallizing roof of a thermally zoned magma chamber may eventually produce the extraction of differentiated interstitial melt from the crystalline region where it formed toward the top of the magma chamber. Therefore, the presence of a temperature gradient in the crystal-poor cap formed at the top of the chamber may in turn

cause more crystallization in the outer, cooler region than in the inner, hotter one. The temperature gradient in the magma chamber explains the textural zoning observed in pyroclastic deposits by means of the eruption of progressively more crystalline magma in the course of each eruptive event. In such model, the pre-eruptive volatile over-saturation is finally achieved by means of volatiles diffusion in the same direction of the temperature gradient, induced by the crystallization of the cooler region. This is also consistent with the fast diffusivity of water observed in temperature gradient experiments, showing homogeneous profile of water in spite of the variable amount of crystal in each point along the temperature gradient.

1. Introduction

The complexity of volcanism in central Italy animated the scientific debate during the last decades. The peculiar potassium-rich magmatism of the Roman Province (Washington, 1906; Peccerillo, 2005; Conticelli et al., 2010) aimed numerous scientific contributions focused on the petrology of the numerous volcanic districts. Among these, the Sabatini Volcanic District (hereafter SVD) is one of the largest, being characterized by a number of explosive eruptions emplaced during the last 800 Kyr that produced pyroclastic deposits cropping out in a widespread area north of Rome (~1800 km^2, Sottili et al., 2010). During these explosive eruptions (mostly known as yellow tuffs and red tuffs), large volumes of phonolitic magmas were emplaced (an average of 10 km^3 dense rock equivalent of magma for yellow tuff and red tuff eruptions). The interest for these pyroclastic deposits (quarried since the ancient Roman age) promoted detailed studies on stratigraphy (Lombardi and Meucci, 2006 and references therein) and geochronology (Karner et al., 2001; Sottili et al., 2010), whereas petrological studies on the major eruptions are scarce. In particular, these petrological studies are limited to lava flows and scoria cones with primitive chemical composition (i.e., Cundari, 1979; Conticelli and Peccerillo, 1992; Conticelli et al., 1997) that represent only a small fraction (less than 10%) of the total volume of the emplaced products.

One of the major features of SVD pyroclastic deposits is the textural variability of juvenile clasts. Indeed, these are commonly characterized by the transition from crystal-poor juvenile clasts at the bottom of the deposits, toward crystal-rich ones at their top. Phonolitic volcanism in general offers numerous examples of pyroclastic successions showing analogue textural variations of the juvenile component, often accompanied by variation of the chemical composition of juvenile clasts. This is the case of El Abrigo ignimbrite in Tenerife (Ablay, 1995), Laacher See in the Eifel Province (Wörner and Schminke, 1984; Schmitt et al., 2010), and many of the Quaternary volcanic districts in Italy (e.g., Campi Flegrei, Piochi et al., 2005; Vesuvius, Cioni et al., 1995; Vulsini, Palladino and Agosta, 1997), where these variations are commonly interpreted in the light of compositional variation of the erupted magma, resulting from the compositional layering of the magma chamber. The compositional zoning models invoked for these magmatic systems, do not apply in the case of SVD eruptions, given that no significant chemical variation is observed between the crystal-poor and the crystal-rich juvenile fraction, which actually share similar bulk composition.

In addition to the problem of textural variations of the juvenile component not accompanied by chemical variation, it comes up the paradox on the genesis of crystal-poor, differentiated magmas. Numerous experimental studies were carried out to constrain both

differentiation and pre-eruptive conditions of these phonolitic magmas, but all of them left unaddressed the problem of crystal-melt separation and the origin of crystal-poor textures (Berndt et al., 2001; Harms et al., 2004; Andujar et al., 2008; Fabbrizio et al., 2008).

In this study, the products from large explosive eruptions of SVD have been collected and investigated in detail. Phase equilibria experiments, coupled with MELTS simulations (Ghiorso and Sack, 1995), were used to constrain both differentiation and pre-eruptive conditions of the phonolitic system. Moreover, thermal gradient experiments have been performed with the aim to mimic conditions occurring in a thermally zoned magma chamber. Through the coupling of natural and experimental data, magmatic processes occurring in the shallow, thermally zoned magma system of SVD have been modelled, addressing the problems of melt differentiation, crystal-melt separation and achievement of pre-eruptive conditions of phonolitic magmas feeding large explosive eruptions.

2. Geological setting

The variety of volcanic rocks erupted along the Tyrrhenian margin reflects the complexity of the geodynamic setting of the Italian peninsula (e.g., Doglioni et al., 1999; Cavazza and Wezel, 2003). The geochemical signature of magmas erupted from the volcanic districts along the peri-Thyrrenian margin and the Aeolian arc has been interpreted as reflecting subduction-modified mantle sources (Figure 2.1). Conversely, in Sicily and in several seamounts in the Tyrrhenian Sea, volcanic rocks with intraplate-like geochemical signatures have been reported (Peccerillo, 2003; Lustrino et al., 2007). Intraplate and orogenic volcanics coexist in the Thyrrenian Sea and Sardinia.

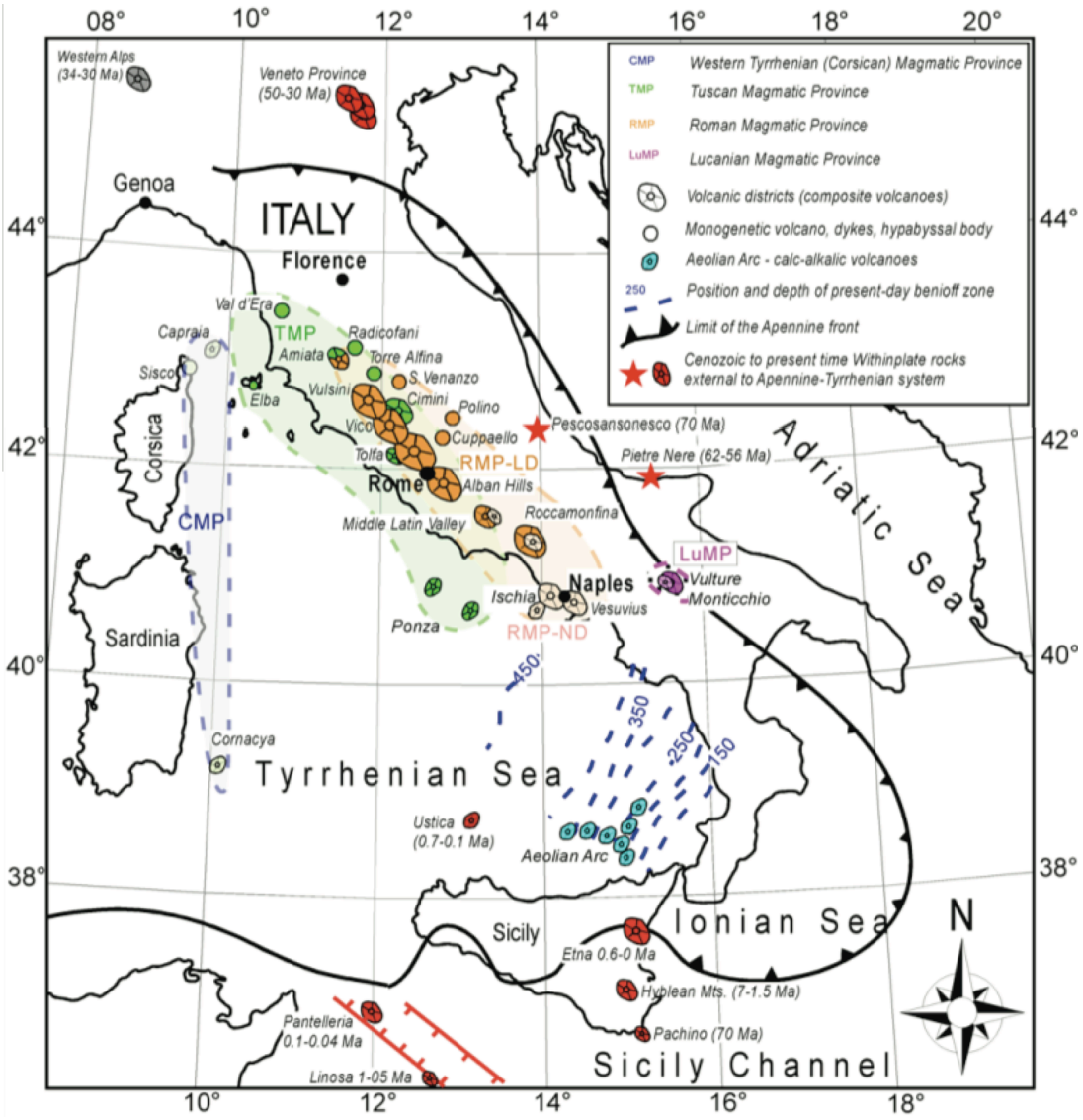

Figure 2.1 - Distribution of recent magmatism in Italy (from Conticelli et al., 2010).

2.1 Geodynamic setting

The present-day structure of the central Mediterranean region derives from the convergence of Africa and Eurasia plates, which initiated at least 70 Myr ago. During the Mesozoic, widespread carbonate platforms were formed at passive continental margins of such plates as a consequence of the opening of the Tethys oceanic basin. The extensional regime was followed in the late Mesozoic by the convergence of the two plates, with the consumption of the European oceanic lithosphere. During this period, the Mediterranean area was dominated (from east to west) by the Cimmerian, Dinarides, and Alps-Betics subduction zones. After the collision of the Europe and Africa continental margins (i.e., formation of Alps), a new subduction initiated at least 35 Myr ago with the onset of the Dinarides-Hellenides and Apennines-Maghrebides subduction zones and occurred over the Tertiary at a rate of about 1-2 cm/yr on average (Dewey et al., 1989). A major change happened during the Eocene, when convergence rates reduced to <1 cm/yr and the convergence direction changed to N-NW (e.g., Rosenbaum et al., 2002). During such time, the Ionian-Adriatic lithosphere continuously subducted toward W-NW beneath the Eurasia plate, leading to the progressive closure of the intervening Mesozoic oceanic basins (i.e., Tethyan domain; Figure 2.2), with the consequent formation of the Apennine-Maghrebide orogenic belt and of the Ligure-Provençal and Tyrrhenian extensional back-arc basins (Dewey et al., 1989; Horvath & Berckheimer, 1982). The eastward migration of the subduction front was caused by the rollback of the subducting slab (Gueguen et al., 1999; Doglioni et al., 1999), proceeding faster in the southern Ionian sector (i.e., oceanic lithosphere) than in the northern Adriatic segment (i.e., continental lithosphere; Figure 2.3).

Recent space geodesy data confirm this main frame, where Africa has about 4-5 mm/yr of N-S component of convergence relative to Europe (e.g., Devoti et al., 2008). The subducting slab is still recognizable beneath the Calabrian arc, where deep seismicity is detected along a narrow (~200 km) and steep (70°) Benioff plane dipping north-westward down to about 500 km. Continental collision is probably still active in the central-northern Apennines, where intermediate earthquakes occur down to 90 km (Selvaggi and Amato, 1992; Carminati et al., 2005). The two distinct signatures of Mediterranean orogens (i.e., Alps and Apennines) result from the different direction over which the convergence between Africa and Eurasia plates occurred. On one hand, high morphological and structural elevations, double vergence, thick crust, involvement of deep crustal rocks, and shallow foredeeps characterize the East-directed subduction zones (Alps-Betics and Dinarides-Hellenides). On the other hand, low morphological and structural elevations, single vergence, thin crust, involvement of shallow rocks, deep foredeeps, and a widely developed back-arc basins characterize the West-directed

subduction zones (Apennines and Carpathians). This asymmetry can be ascribed to the 'westward' drift of the lithosphere relative to the mantle, at rates of about 49 mm/year as computed from the hotspots reference frame (Figure 2.2; Carminati and Doglioni, 2005).

Structural setting of central Italy

The Italian peninsula is a tectonically active region, as testified by earthquakes distribution. Focal mechanisms are prevalently compressional at the fronts of Alps and Apennines and extensional along the Apennines backbone, the latter being the product of the eastward migration of the Apennines subduction (Carminati et al., 2010 and references therein). From a lithological point of view, the Apennines are mainly made up of Jurassic-Tertiary limestones (deposited both in shallow and deep-sea environment) and dolostones of African (Adriatic) origin, Late Tertiary foredeep silicoclastic deposits, Early Miocene carbonate successions and subordinate ophiolitic melange (Carminati et al., 2010 and references therein).

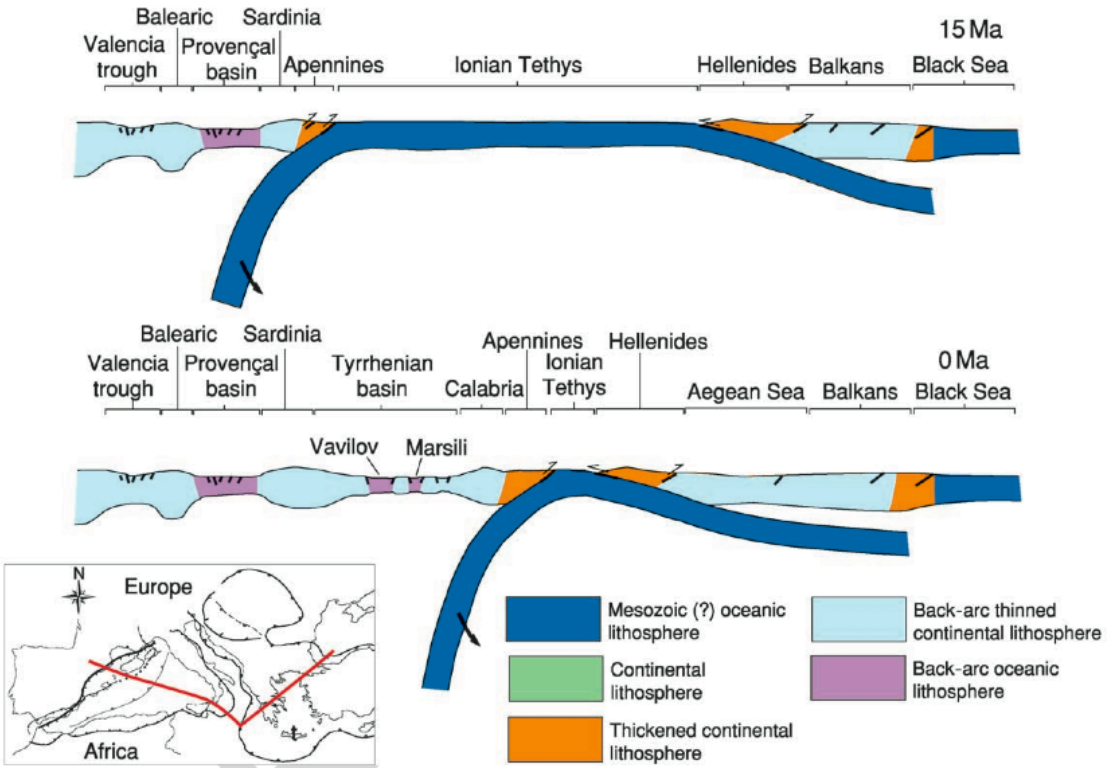

Figure 2.2 - Evolution of the Mediterraneran area along the trace shown on the map (inset), showing the Dinarides-Hellenides subduction at 15 Myr and at present day. The last two slabs retreated at the expense of the inherited Tethyan Mesozoic oceanic or thinned continental lithosphere. In their hanging walls, a few rifts formed as back-arc basins, which are progressively younger towards the subduction hinges. The slab is steeper underneath the Apennines, possibly owing to the westwards drift of the lithosphere relative to the mantle (from Carminati and Doglioni, 2005).

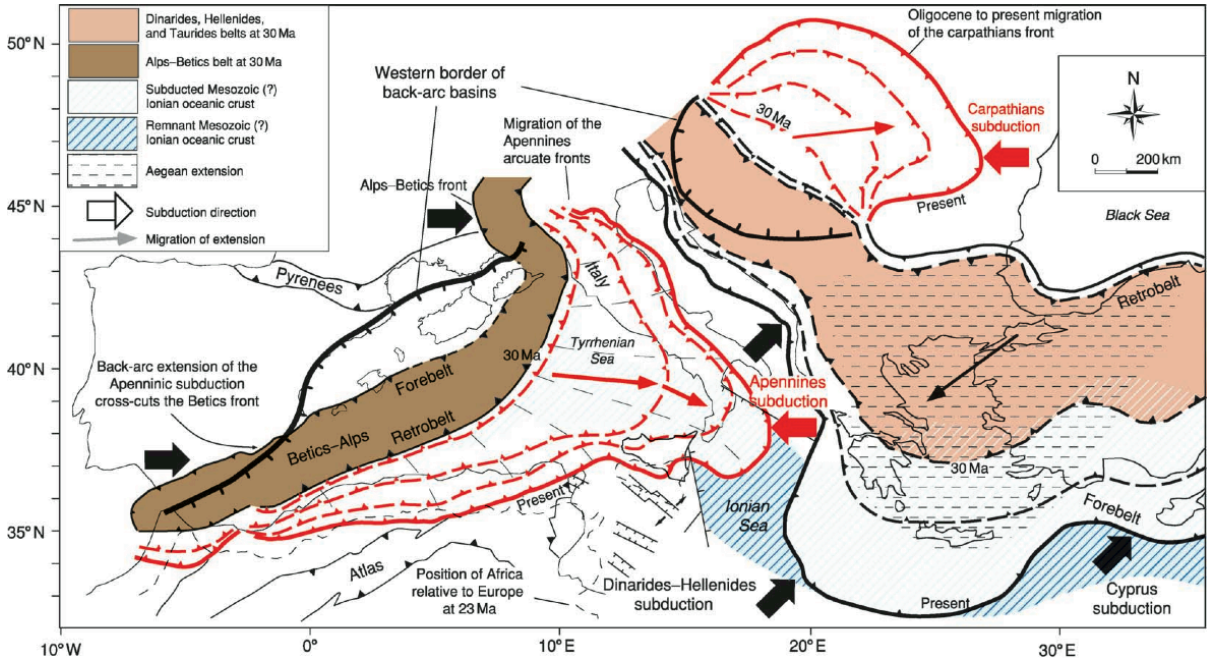

Figure 2.3 - Main tectonic features of the Mediterranean realm, which has been shaped during the last 45 Myr by a number of subduction zones and related belts: the double-vergent Alps-Betics; the single eastwards-vergent Apennines-Maghrebides and the related western Mediterranean back-arc basin; the double-vergent Dinarides-Hellenides-Taurides and related Aegean extension; the single eastwards-vergent Carpathians and the related Pannonian back-arc basin; and the double-vergent Pyrenees (from Carminati and Doglioni, 2005).

Faulting systems in the Apennines chain share a main orientation NW-SE. Several basins formed by the intersection between NW-SE and NE-SW normal fault systems (Bartolini et al., 1982). Among the principal faults, the Ancona-Anzio line is an important NE-SW-trending tectonic line that crosses the Italian peninsula and divides the Umbria-Marche from Abruzzi-Latium sequences (Castellarin et al., 1982; Locardi, 1988). The northern part, above the Ancona-Anzio line, is composed by Tuscany, Liguride and Umbria-Marche allochthonous sequences, and of neo-autochthonous Miocene to Quaternary shallow marine to continental clays, sands, and conglomerates filling post-orogenic extensional basins (Buonasorte et al., 1987; Barberi et al., 1994). In the southern part, the Abruzzi-Latium sequence consists of a thick sequence (several kilometers) of Mesozoic carbonates formed in a shallow marine environment. These lithologies, constitute the rock substrate over which the volcanism of the Roman Province developed.

2.2 Volcanism of the Roman Province

Washington (1906) defined the Roman Province as the large region of potassium-rich volcanism, expending from southern Tuscany to the Campanian region. More recently, on the

basis of geochemical features of volcanic rocks, Peccerillo (2005) redefined this province as the belt of potassium-rich volcanoes running parallel to the border of the Tyrrhenian Sea, from southern Tuscany to the city of Rome, including the volcanic complexes of Monti Vulsini, Vico, Monti Sabatini and Colli Albani (Figure 2.4). Generally, the last eruptive age of these volcanic districts progressively decrease going southward. This trend continues along the peri-Thyrrenian margin, being the last eruptions of volcanoes in southern Italy more recent than those of volcanoes in central Italy.

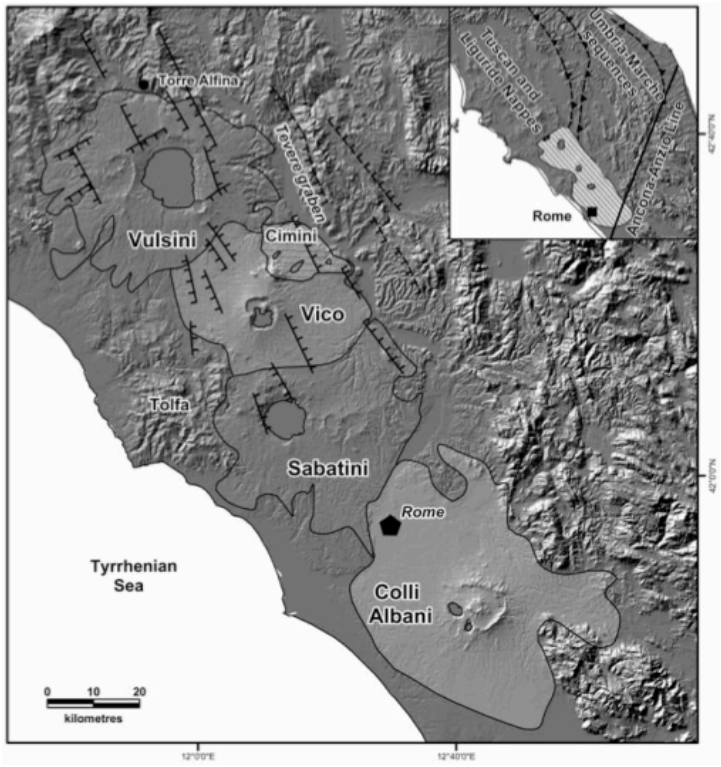

Figure 2.4 - Location map of volcanoes of the Roman Province. Inset: schematic structural map of northern Apennines (from Peccerillo, 2005).

The Roman Province was characterized by prevalently explosive activity. Over a time span from ~800 to ~36 kyr, about 900 km^3 volcanic products were erupted (Peccerillo, 2005). Plinian deposits and caldera collapses have been often associated to large explosive eruptions. These eruptions also produced large ignimbrite flows, whose geologic interest is strongly increased by the role of these thick deposits for ancient civilization. Many historical towns in the Latium area are in fact built on thick pyroclastic plateaux surrounded by steep cliffs and many important buildings of the historical city of Rome have been built up using pyroclastics quarried from these thick ignimbrites (Figure 2.5).

Figure 2.5 - Towns in the Roman Province that have been built on large tuff deposits: (a) Civita di Bagnoregio (Vulsini, several pyroclastic eruptions), (b) Orte (Sabatini, Tufo Rosso a Scorie Nere), (c) Calcata (Sabatini, Tufo Giallo della Via Tiberina) and (d) Ceri (Sabatini, Tufo Rosso a Scorie Nere).

Volcanic rocks from the Roman Province range in composition from potassic to ultrapotassic and from SiO_2-undesaturated to SiO_2-saturated (Peccerillo, 2005; Conticelli et al., 2010). Differentiated trachytic and phonolitic compositions are dominant in all the explosive activity of volcanic district in the Roman Province, with the exception of Colli Albani Volcanic District (hereafter CAVD), where differentiated products range in composition from foidite to phono-tephrite. Comparable trace elements patterns and $^{143}Nd/^{144}Nd$ and $^{87}Sr/^{86}Sr$ isotopic ratios characterize the primitive volcanic rocks (MgO >4wt.%) of the Roman Province, indicating a common geochemical signature of their mantle sources (Figure 2.6). These geochemical data have been interpreted as the result of the input of crustal material in the mantle (Peccerillo, 1999 and 2003; Peccerillo and Lustrino, 2005; Conticelli et al., 2010). The potassium-rich nature of the volcanic rocks, in particular, is explained with the presence in the upper mantle of large volumes of metasomatic components (i.e., K-rich minerals such as phlogopite), accommodated within a network of veins in the sub-continental lithosphere. Their partial melting would have generated ultrapotassic magmas of either lamproitic or kamafugitic nature (Avanzinelli et al., 2009). The interaction between the K-rich fluids produced in the metasomatic veins and the surrounding mantle would have

increased over time, diluting the alkaline component in favour of production of shoshonitic and high-K calcalcaline magmas.

Several studies on the geochemistry of primitive volcanic rocks in the Roman Province, indeed, suggest that the most feasible explanation for the enrichment in K, LIL elements and radiogenic Sr of the primary magmas is the metasomatism of the mantle wedge above a subduction zone (Cox et al., 1976; Thompson, 1977; Civetta et al., 1981; Peccerillo, 1999). Then, the differentiation of these primary magmas during their ascent toward the surface through a relatively thin continental crust (~25 km; Bianchi et al., 2008) may have been controlled by magma-crust interaction processes. In particular, such interaction has been abundantly described and demonstrated by several experimental and petrologic studies for the CAVD (Mollo et al., 2010 and references therein).

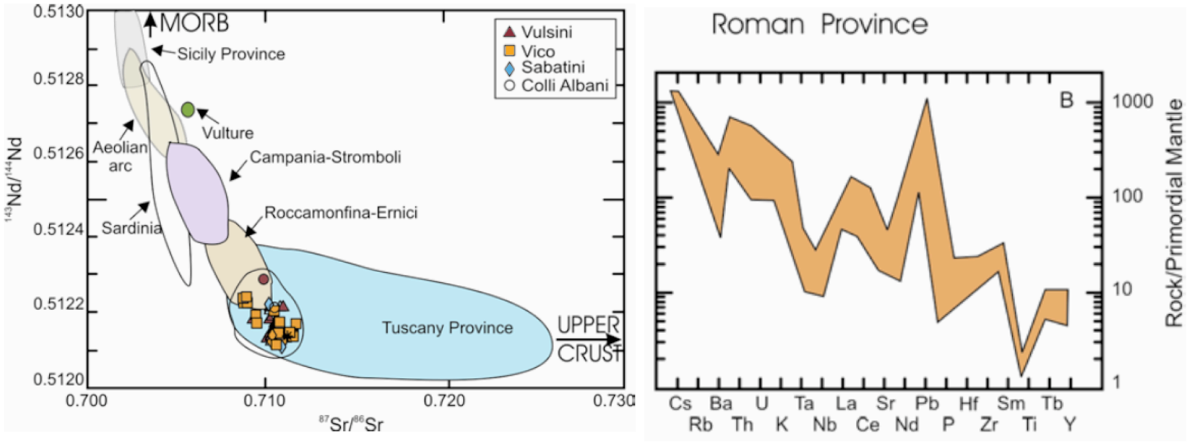

Figure 2.6 - Initial $^{143}Nd/^{144}Nd$ vs. $^{87}Sr/^{86}Sr$ diagram for Plio-Quaternary mafic (MgO >4 wt.%) volcanic rocks from the Roman Province and from other Italian volcanic districts (left) and incompatible element patterns of mafic volcanic rocks from the Roman Province normalized to primitive mantle estimate (right). Note the narrow range of geochemical variation of the primitive rocks of volcanoes of the Roman Province (modified after Peccerillo et al., 2003).

2.3 Sabatini Volcanic District

Sabatini Volcanic District extends over an area of ~1800 km^2 in the central part of the Roman Province and is bordered by the Tolfetano-Cerite-Manziate silicic volcanic district (6.4-1.8 Myr, Lombardi et al., 1974; de Rita et al., 1993, 1997) on the west side and by the Tiber Valley to the east side (Figure 2.7). Volcanic products interfinger to the south with the 0.56-0.35 Myr-old pyroclastic deposits of the Tuscolano-Artemisio phase (de Rita et al., 1988) of the CAVD, and they are buried to the north by the 0.15 Myr-old Vico C Ignimbrite (Cioni et al., 1987) from the Vico Volcanic District.

The areal activity of the SVD was characterised by highly explosive, caldera-forming eruptions that produced widespread sub-plinian and plinian fall deposits. These eruptions were generally associated to weakly explosive post-caldera activity that produced lavas and scoria cones. Hydromagmatic activity dominated the most recent activity, occurring prevalently in the *horst* areas of the carbonate substrate (i.e., presence of shallow aquifers).

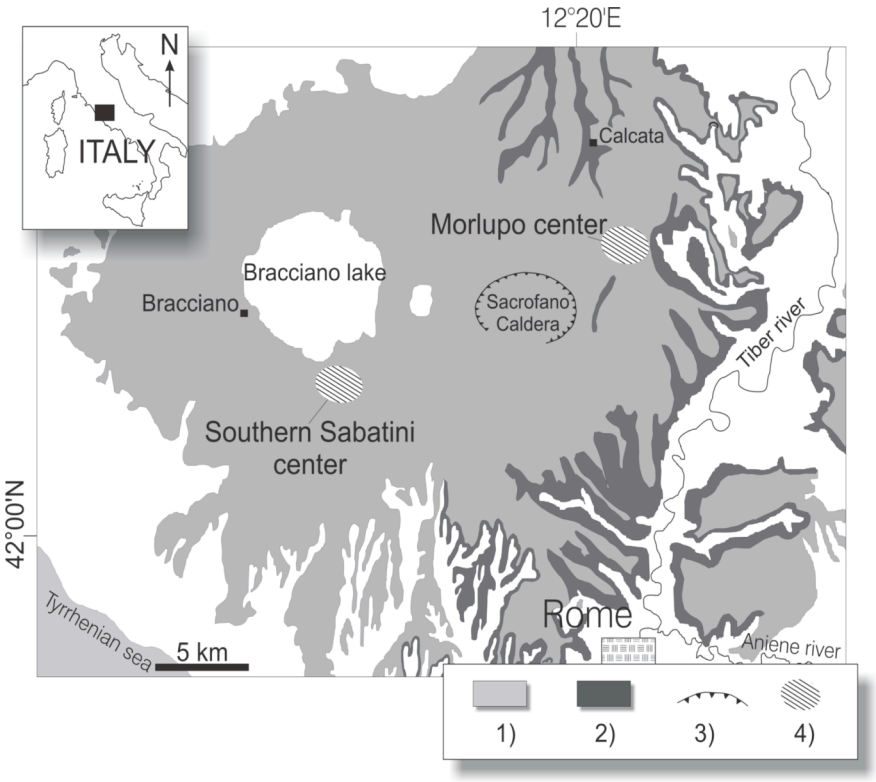

Figure 2.7 - Sketch map of SVD. Legend: 1) SVD volcanics; 2) outcrop area of TGVT eruption products; 3) caldera rim; 4) inferred source areas during the Morlupo (ca. 800-500 kyr) and Southern Sabatini (ca. 500-400 kyr) activity periods. The volcano-tectonic depression hosting Bracciano Lake and the Sacrofano Caldera are also shown.

Eruptive history of SVD

The eruptive history of SVD can be summarized in three main periods: 1) early activity (eastern sector), 2) Southern Sabatini and Sacrofano activity (Sottili et al., 2004), and 3) final hydromagmatic activity. The oldest volcanic product of SVD is a ~600 kyr-old trachytic lava flow (Cioni et al., 1993), however older (~800 kyr) plinian deposits of uncertain attribution are reported in Karner et al. (2001). Numerous explosive eruptions characterized the early activity of the volcanic district in the time span from ~600 to 400 kyr (Sottili et al., 2010), producing voluminous pyroclastic flow and plinian to sub-plinian deposits. According to chrono-stratigraphic data of Karner et al. (2001), the early activity of SVD includes the large explosive eruptions of Tufo Giallo della Via Tiberina (561±1 to 548±4 kyr), Tufo Giallo di

Prima Porta (514±3 kyr), the Grottarossa Pyroclastic Sequence (514±5 kyr), Tufo Rosso a Scorie Nere (449±1 kyr) and Tufi Varicolori di La Storta (~410 kyr). Intense explosive activity occurred between 300 and 200 kyr, with the eruption of Tufo Giallo di Sacrofano (286±6 kyr; Sottili et al., 2010) and Tufo di Bracciano (316±5 to 307±5; Sottili et al., 2010). The last eruptive phase (<150 kyr) was prevalently hydromagmatic (de Rita et al., 1993; Sottili et al., 2010, 2011), with subordinate strombolian eruptions. The most recent products were erupted during the 85 kyr-old activity of the Baccano eruptive centre (Fornaseri, 1985; Di Filippo, 1993).

Interestingly, the eruptive history of SVD partially overlaps that of the neighbour CAVD. These SVD and CAVD were contemporaneously active and quiescent during most part of their history (Figure 2.8). In particular, a correspondence between the volumes of erupted magmas during each phase of activity is observed. The largest eruptions of CAVD occurred during the early activity (Marra et al., 2003 and references therein), whereas strombolian and hydromagmatic activity characterized respectively the intermediate and late phases of eruptive activity of both SVD and CAVD.

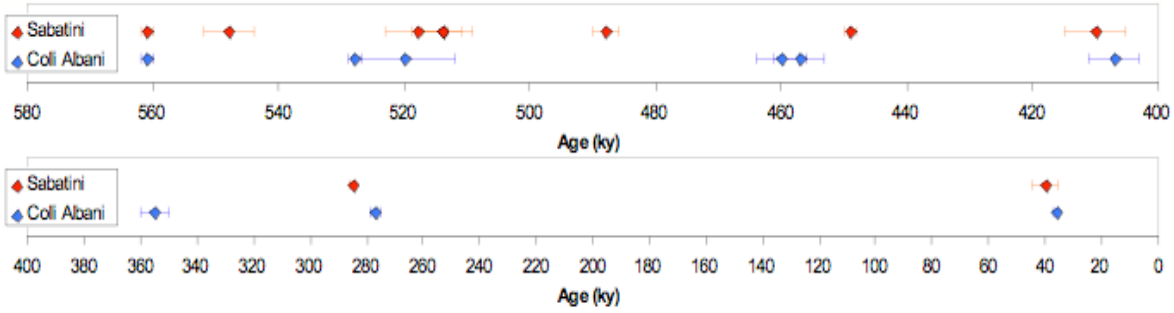

Figure 2.8 - Diagram showing the chronology of major eruptions of SVD and CAVD. Note the partial juxtaposition of most of the major eruptions (data from Karner et al., 2001 and references therein).

Petrology of SVD volcanics

The SVD products cover the entire spectrum from tephrite to phonolite, with minor latitic and trachytic types (Figure 2.9). On the basis of the Ba content, Conticelli et al. (1997) distinguished two series of magmatic evolution representative of a two-stage magma differentiation system: a high-Ba series and a low-Ba series, the latter evolving at higher pressure and lower temperature than the former. The delineation between these two magmas may have been caused by RTFA (Refilling Tapping Fractionation Assimilation) processes and/or the different volume of magma rising from the source. The Ba-rich rocks commonly have leucite phenocrysts, whereas the Ba-poor group contains plagioclase as phenocryst and leucite confined to the groundmass. These two groups of rocks, however, do not show

relevant differences for major elements and incompatible element ratios. Conversely, Sr-isotope ratios exhibit more radiogenic compositions in the highly Ba-enriched rock group, although $^{87}Sr/^{86}Sr$ ratios of both kinds of rocks resemble closely other mafic potassic volcanics from the Roman Province (Peccerillo, 2005).

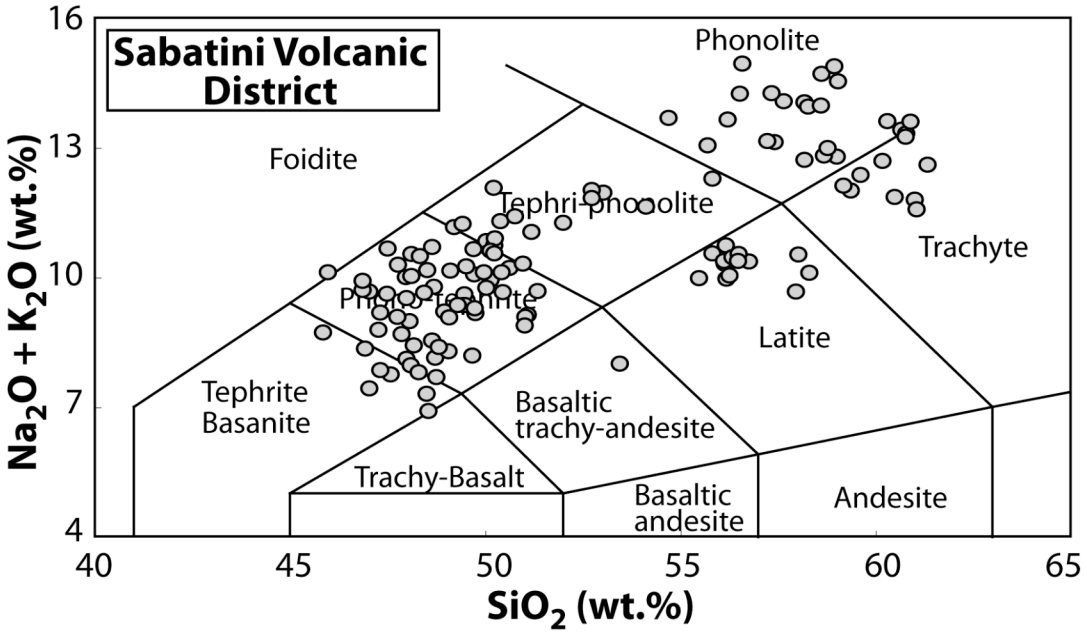

Figure 2.9 - TAS diagram showing composition of SVD volcanics (data from Lustrino et al., 2011 and references therein).

3. Analytical methods and experimental techniques

Natural samples were prepared in double polished thin sections and their textures were analyzed using both optic and electronic microscopy. Products obtained by experiments at high pressure-high temperature were mounted in epoxy mounts, polished and analyzed under scanning electron microscope (SEM). Chemical composition of phases (glasses and crystal) in both natural and experimental samples was obtained by electron microprobe analyses (WDS-EMP).

3.1 Microscopy and image analysis

Microscope images were collected at Dipartimento di Scienze della Terra, Sapienza - Università di Roma, using an optic microscope, equipped with a digital camera and acquisition software. Back-scattered images of natural and experimental products were obtained at Istituto Nazionale di Geofisica e Vulcanologia (INGV - Roma, Italy) using a Jeol FE-SEM 6500F equipped with an energy dispersive microanalysis system. The free WEB software package ImageJ (Image Processing and Analysis in Java; http://rsb.info.nih.gov/ij/) has been used for image analysis (modal analysis of natural and experimental samples).

3.2 Quantitative analyses

Bulk composition of natural samples were determined by XRF analysis on glassy beads by using the Philips PW1480/10 spectrometer at Dipartimento di Scienze della Terra, Sapienza Università (Roma, Italy). The following standards have been adopted for various chemical elements: dolerite (Si, Ti, Fe, Na), quartz-latite (Al, K), basalt Hawaiian volcano (Mg, Ca). Matrix effects for major elements were corrected by using the method of Franzini et al. (1972).

EMP analyses were performed both at CNR-Istituto di Geologia Ambientale e Geoingegneria (IGAG - Rome, Italy) and INGV. Compositional analyses were performed at CNR-IGAG using a CAMECA SX-50 WDS microprobe and at INGV using a Jeol-JXA8200 EDS-WDS combined electron microprobe, both equipped with five wavelength-dispersive spectrometers. Analytical conditions were 15 kV accelerating voltage and 10 nA beam current. Glasses were analyzed with a defocused electron beam of 5 to 15 μm and a counting time of 5 s on background and 15 s on peak, whereas for crystals, a beam size of 2 to 10 μm and counting time of 20 and 10 s on peaks and background were used respectively. The following standards have been adopted for the various chemical elements, during EMP

analyses performed with the CAMECA SX-50 at CNR-IGAG: wollastonite (Si, Ca), orthoclase (K), jadeite (Na), periclase (Mg), rutile (Ti), barite (Ba), magnetite (Fe), corundum (Al) and spessartine (Mn). The following standards have been adopted for the various chemical elements, during EMP analyses performed with the Jeol- JXA8200 at INGV: jadeite (Si and Na), labradorite (Al and Ca), forsterite (Mg), andradite (Fe), rutile (Ti), orthoclase (K), barite (Ba), apatite (P) and spessartine (Mn). Sodium and potassium were analyzed before other elements to reduce possible volatilization effects.

Mössbauer spectroscopy was performed at Dipartimento di Scienze della Terra, Sapienza Università di Roma. Sample was prepared by pressing together the powdered run product glass and an acrylic resin to obtain self-supporting absorbers with Fe thickness in the range 1–2 mg/cm^2. Spectra were collected at room temperature using a conventional spectrometer system operating in constant acceleration mode with a ^{57}Co source of nominal 50 mCi in Rh matrix. Spectral data in the velocity range from −4 to +4 mm/s were recorded by a 512 multichannel analyser. After velocity calibration against a spectrum of high-purity α-iron foil (25 μm thick), the raw data were folded to 256 channels. The spectra were fitted, assuming Lorentzian peak shapes, using the fitting program Recoil 1.04. The reduced χ^2 was used as a parameter to evaluate statistical best fit, and uncertainties were calculated using the covariance matrix. Errors are estimated at about ±0.02 mm/s for isomer shift, quadrupole splitting, and no more than ±3% for doublet areas.

Trace elements in glasses and crystals were measured at the CNR-Istituto di Geoscienze e Georisorse (Pavia, Italy) using a pulsed Nd:YAG laser working at 213 nm coupled to an inductively coupled plasma sector field mass spectrometer (Thermo Finnigan Element I). Instrumental and analytical details have been reported by Tiepolo et al. (2003). For this study the laser was operated at a repetition rate of 10 Hz, and the spot diameter was set at 40 μm with a pulse energy of about 0.1 mJ. Ablation signal integration intervals were selected by carefully inspecting the time-resolved analysis to ensure that no inclusions were present in the analysed volume. Data reduction was performed using the software package 'Glitter' (van Achterbergh et al., 2001). NIST SRM 612 was used as an external standard and 44Ca was used as an internal standard. Reproducibility and accuracy of trace element concentrations were evaluated for a control sample BCR2-glass [inductively coupled plasma mass spectrometry (ICP-MS) unpublished data]. For this sample the error on reproducibility and accuracy is <7% and 510%, respectively.

3.3 Piston cylinder experiments

Phase equilibria and thermal gradient experiments were performed at the HP-HT Laboratory of Experimental Volcanology and Geophysics of INGV (Rome, Italy), using a Quickpress type non end-load piston cylinder produced by Depths of the Earth Co. (Figure 3.1). Further H_2O-CO_2-bearing phase equilibria experiments were performed at the HP Laboratory of the Department of Chemistry and Biochemistry of Arizona State University (Tempe, Arizona, US) using the same piston cylinder device. Experiments were carried out in 19mm, 19-25mm and 25mm assemblies (see Appendix for details on assemblies and calibration techniques) in the pressure range 200 to 300 MPa, in the temperature range 1050-800 °C. Assembly were pressurized before heating. Temperature fluctuations were constantly monitored and maintained at the set point temperature ±5 °C, using NaCl-Pyrex-graphite-crushable MgO assemblies with capsule surrounded by pyrophillite powder to prevent water loss from sample (Freda et al., 2001). Both Pt and Au-Pd capsule were used, the former for phase equilibria and thermal gradient experiments, the latter for H_2O-CO_2-bearing phase equilibria experiments; iron diffusion toward capsule metal occurred only in Pt-capsule (see above in text). Run duration varied from 3 to 50 hours (the standard duration for phase equilibria experiments was fixed at 24 hours, see results and discussion). Oxygen fugacity was assessed at NNO+2 by Mössbauer spectroscopy on experimental glasses obtained at 1300 °C and P = 0.5 GPa (Masotta et al., 2011).

Figure 3.1 - Quickpress piston cylinder at HP-HT Laboratory of INGV (Rome, Italy)

Natural samples selected to be used as starting material (see above in the text) were fine-crushed (particle size <1μm) in an agate mortar mill and melted in a Pt crucible at 1600 °C (1400 °C for the phonolite) and 1 atm (air fO_2); the resulting glass was crushed, re-melted in the same crucible at same conditions and then, fine-crushed in the agate mortar mill (particle size <1μm). In order to prevent alkali loss a Pt cap was placed on the crucible and melting duration did not exceed 1 hour. Deionised H_2O was added in charges by using a micro-syringe after dehydration of sample powder at 110 °C, whereas silver carbonate (Ag_2CO_3) was used together with H_2O in mixed H_2O-CO_2 experiments. Dissociation of silver carbonate produces gaseous CO_2 in a weight fraction of 0.16 (1g of Ag_2CO_3 = 0.16g of CO_2); Ag_2CO_3 was used in order to have CO_2 <1 wt% in each experiment. Capsule weight was checked after welding and after 30 minutes in 110 °C dryer, in order to ensure that water did not escape during sample preparation.

Experimental design

The experimental design of piston cylinder experiments implies the existence of a temperature gradient along the furnace assembly, due to the physical properties of the materials used and their geometry (Watson et al., 2002 and references therein). However, the graphite furnace is characterized by a relatively isothermal region in the centre of the assembly, defined hot-spot (temperature variations within ±10 °C), which usual length is 5-8 mm and that is used for standard phase equilibria experiments. In the piston cylinder used for this study, the length of the hot-spot has been measured and phase equilibria experiments were performed using <6 mm long capsules, in order to maintain the sample in the hot-spot.

Thermal gradient experiments were designed taking advantage of the innate temperature gradient of the furnace. Experiments were carried out by using the same assembly used in phase equilibria experiments, but longer capsules (up to 11 mm), in order to have the top of the charge a few millimeters above the furnace hot-spot zone. Temperature gradient along the furnace was determined by running several calibration experiments in which the thermocouple was placed each time at a different position along the axis of the assembly (10, 14, 19, and 25 mm, Figure 3.2). Current, voltage and temperature were recorded constantly at different output conditions and then regressed into four equations (each one for each different position of the thermocouple). Temperature distribution along the furnace was calibrated for different conditions of current, tension, and percentage of output and used to reconstruct the temperature zoning in T-gradient experiments. The experiments were designed in order to have the vertical temperature distribution constant with time. The achievement of this

condition has been demonstrated by experiment reproducibility. In order to constrain temperatures along the furnace, textural and chemical zoning along charges were then compared with textural and chemical features of phase equilibria experiments performed at different temperatures within the thermal range 1050-850°C. The largest variation in temperature is about 150°C. Thermal gradient measured in the assembly is in agreement with values reported in Watson et al. (2002), for similar 19 mm experimental assemblies. Several experiments at 24 hours time duration, plus one 50 hours-long, were performed in order to demonstrate reproducibility (see results section).

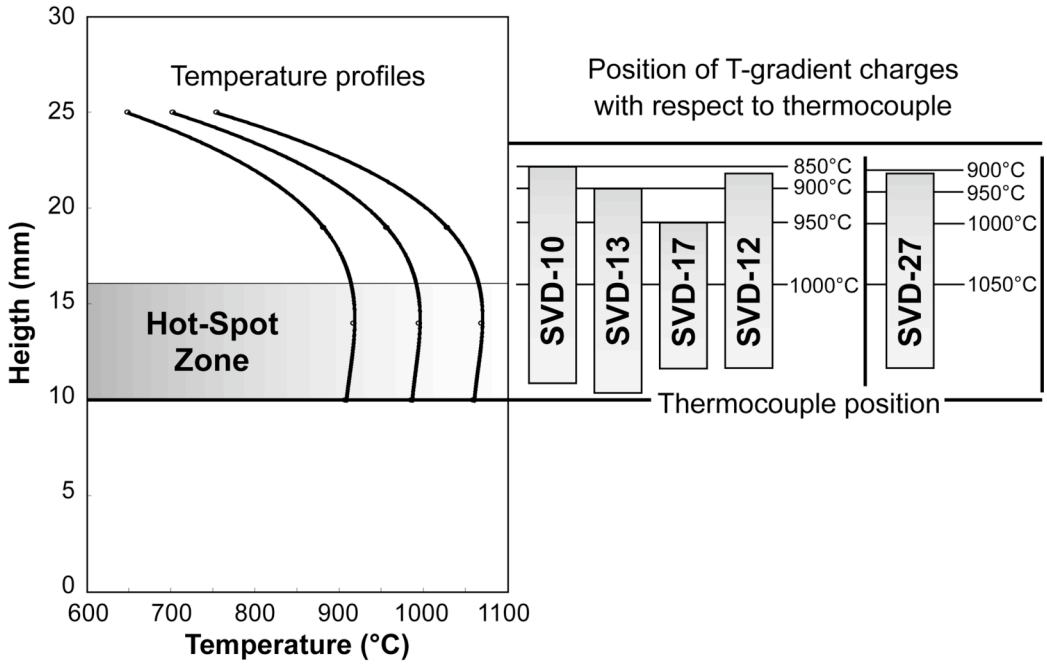

Figure 3.2 - Temperature profile along furnace and position of experimental charges with respect to thermocouple.

4. Results

4.1 Natural products

Textural and chemical features of natural products of the SVD are presented in this section. More than 70 samples of natural products (juvenile clasts and lithic enclaves) representative of the explosive activity of the SVD (Figure 4.1) were collected and analyzed. Several studies have been carried out on explosive volcanism of this district (Scherillo, 1941; de Rita et al., 1993; Sottili et al., 2004) but the petrology of large explosive eruptions has been poorly investigated and the knowledge of these eruptions is often limited to the bulk chemical composition of the products. Detailed petrologic studies have been carried out prevalently on primitive rocks (essentially lava flows and scoria cone; Cundari, 1979; Conticelli and Peccerillo, 1992; Conticelli et al., 1997), however representing only a small fraction of the total volume of the erupted products. These studies gave insights into the source region of the SVD magmas (Peccerillo, 2005) although they left unexplored pre-eruptive processes occurring in the shallow magma system.

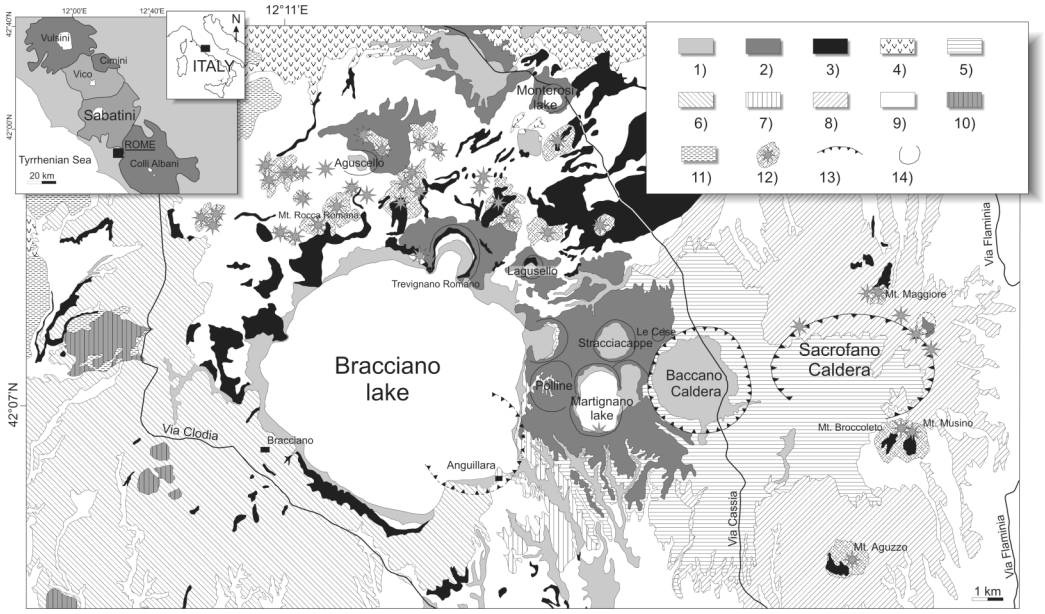

Figure 4.1 - Geological sketch map of SVD (from Sottili et al., 2010). Top left inset: the SVD within the Quaternary Potassic Roman Province of central Italy. Map legend: 1) recent alluvium; 2) products of hydromagmatic activity; 3) lava flows; 4) pyroclastic products of the Vico Volcanic District; 5) pyroclastic products of the Baccano eruptive centre; 6) Tufo di Bracciano unit; 7) Tufo di Pizzo di Prato unit; 8) Tufo Giallo di Sacrofano unit; 9) other pyroclastic products of the SVD; 10) M.ti Ceriti-Tolfetano-Manziate silicic volcanics (mainly from lava dome activity); 11) carbonate and silicoclastic sedimentary substrate (Mesozoic to Pliocene); 12) scoria cone; 13) caldera rim; 14) maar crater rim.

4.1.1 Textural and chemical features of explosive products

Sampling encompasses the whole eruptive activity of the SVD. A representative number of samples were collected from pyroclastic deposits emplaced during the main explosive eruptions of the SVD. Details on chronological data of eruptions are summarized in Table 4.1. These eruptions emplaced large volumes of highly differentiated magmas, ranging in composition from phonolitic to latitic and trachytic (Figure 4.2).

Table 4.1 - Stratigraphic relations of the main SVD eruptions.

Eruption	Label	Age (kyr)	Composition
Hydromagmatic Activity		<132*	variable
Tufo Vigna di Valle		193±7*	
Tufo Pizzo di Prato	TPP	249±16*	Pho, Tr
Tufo Giallo di Sacrofano	TGS	286±6	Pho
Tufo di Bracciano	TBR	307±5, 316±6*	Te-Pho, Pho
Tufi Stratificati Varicolori di La Storta		ca. 410**	
Tufo Rosso a Scorie Nere	TRSN	449±1**	Te-Pho
Tufo Terroso con Pomici Bianche	TTPB	488±2**	Lt, Pho
Grottarossa Pyroclastic Seq.	GRPS	518±5, 514±5**	Te-Pho, Fo
Tufo Giallo di Prima Porta	TGPP	514±3**	Pho
Tufo Giallo della Via Tiberina	TGVT	561±1 to 548±4**	Pho, Tr
Undefined pyroclastic succ. 2 Pumice Fall + Pyr. Flow			Lt, Tr
Ancient activity		800-580**	Pho, Tr

Pho: phonolite, Tr: trachyte; Te-Pho: tephritic phonolite, Lt: latite, Fo: foidite

** Chronological data from Sottili et al. (2010) and references therein*
*** Chronological data from Karner et al. (2001)*

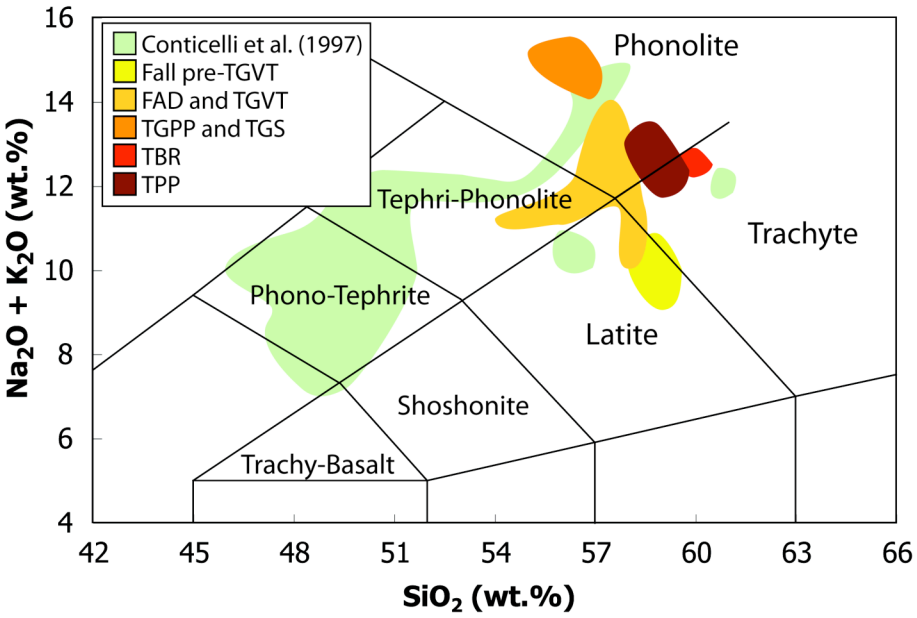

Figure 4.2 - TAS diagram showing compositional range of the explosive products of SVD (shaded fields include bulk XRF analyses and EMP analyses of glasses; labels as in Table 4.1). Compositional data from Conticelli et al. (1997) are reported for comparison. Legend: FAD, First Ash fall Deposits; TGVT, Tufo Giallo della Via Tiberina; TGPP, Tufo Giallo di Prima Porta; TGS, Tufo Giallo di Sacrofano; TPP, Tufo di Pizzo Prato.

Ancient activity (~800-580 kyr)

The ancient activity of the SVD took place in the Morlupo eruptive centre, in the eastern sector of the district, controlled by major NE-SW-trending tectonic lineaments (Baldi et al., 1974; Biasini et al., 1993; de Rita et al., 1993). The ancient activity was characterized by both explosive (pyroclastic flows) and effusive activity. Sanidine dominates the mineralogical assemblage of the rocks, mostly with trachytic or phonolitic composition.

The First Ash fall Deposits (FAD) eruptive unit (Karner et al., 2001) is the oldest fall deposit recognized in the SVD area and consists of a basal ash layer (~20 cm thick) with abundant white lapilli-sized pumice, overlaid by a thicker (~100 cm) layer of alternating white and grey lapilli and by a stratified layer of grey scoria and yellow pumice in a pale yellow ash matrix (~160 cm thick). White pumice clasts (sample FAD-13; Figure 4.3) are glassy and highly vesiculated, with a Porphyricity Index <10 % (PI = area covered by phenocrysts over a given area). The scarce phenocrysts are represented only by round-shaped, partially resorbed sanidine. Rare leucite and clinopyroxene are observed in the glassy groundmass only. Conversely, grey pumices (sample FAD-13B; Figure 4.3) are more crystalline (PI = 20-40 vol.%) and poorly vesiculated. The mineral assemblage is made up of prevailing leucite and clinopyroxene both in phenocrysts and in the groundmass. Plagioclase is also abundant in the groundmass. Notably, the textural zoning observed in these deposits is

not accompanied by a remarkable chemical variation of the juvenile component, as white pumice and grey scoria share a comparable bulk phonolitic composition (Table 4.4; Figure 4.2). The different phase assemblage may explain small differences of interstitial glass composition.

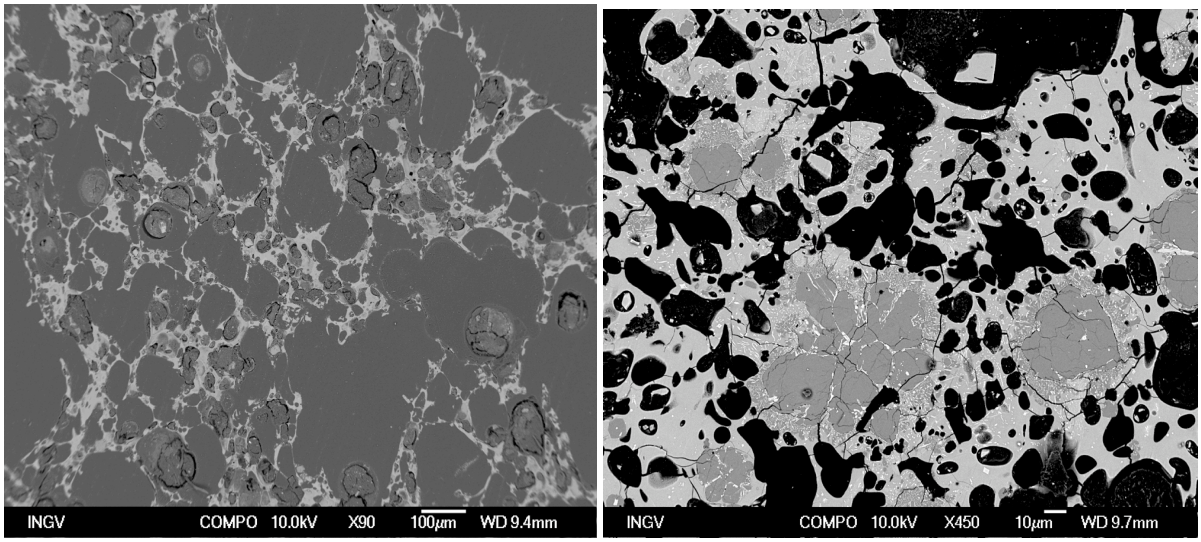

Figure 4.3 - SEM images of FAD juvenile clasts: glassy texture of white pumice clasts (left) and Leucite-bearing, crystalline texture of grey pumices (right).

The Morlupo lava flow is moderately porphyric (PI = 15 vol.%) and highly vesiculated. The mineral assemblage is made up of euhedral to subhedral sanidine phenocrysts with minor subhedral weakly pleochroic clinopyroxene phenocrysts. Groundmass phases are represented by euhedral to subhedral plagioclase, scarce clinopyroxene, opaques and glass (<10 vol.%). Both bulk chemistry and interstitial glass are trachytic in composition.

Two unidentified pumice fall deposits have been sampled in Capena locality, in between a pyroclastic sequence underlying the lower eruptive unit of Tufo Giallo della Via Tiberina. The fall deposits are ~50 cm and ~100 cm thick, well sorted (centimeter-sized clasts) and do not show grading or compositional variation of the juvenile component. Pumice clasts are whitish and crystal-poor, showing a mineral assemblage made up of sanidine and clinopyroxene. Bulk compositions are latitic to trachytic (Figure 4.2; Table 4.8).

Tufo Giallo della Via Tiberina (561±1 to 548±4 kyr)

The Tufo Giallo della Via Tiberina (TGVT) is composed by several units emplaced during two distinct time intervals, separated by about 10 kyr (Karner and Renne, 1998). In between these two intervals, the CAVD Tufo Pisolitico di Trigoria was deposited. The TGVT has been divided in two main eruptive units, respectively the lower TGVT, composed of a single

pyroclastic flow aged 561±1 kyr and the upper TGVT, composed by several pyroclastic sub-units aged 548±4 kyr (Karner et al., 2001; Figure 4.4).

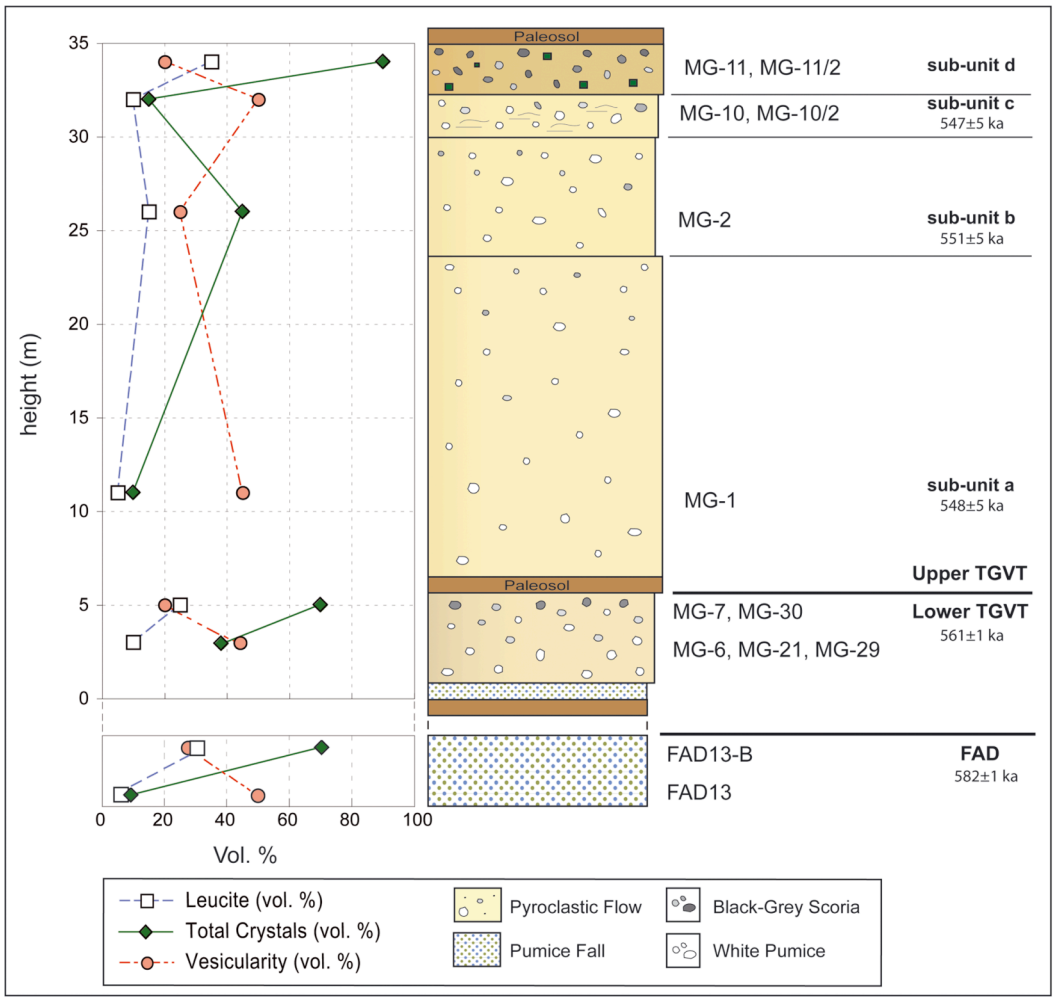

Figure 4.4 - Stratigraphy of the studied pyroclastic succession in the Morlupo area, including FAD and TGVT, showing upsection location of analysed samples. Leucite and total crystal (phenocrysts+microcrysts, on a vesicle-free basis) contents, and degree of vesicularity of juvenile clasts, from modal analyses in thin section, are also reported.

The lower TGVT unit consists of a massive, light grey to pale yellow, pyroclastic flow deposit, containing abundant whitish pumice and dark grey scoria lapilli and diffuse accretionary lapilli, reaching a maximum thickness of 8 m in paleovalleys. A 3 cm-thick ash layer, associated with a 4 cm-thick pumice lapilli layer, is often recognized at the base of the deposits. The upper TGVT unit has been divided into four sub-units (a-d; Figure 4.4). The lowermost sub-unit (a) is a massive, accretionary lapilli-bearing, yellow ash deposit containing diffuse white pumice and scarce grey scoria, lava and non-metamorphosed sedimentary lithic fragments, reaching a maximum thickness of ~20 m at the Calcata locality. Sub-unit (b) is texturally and petrographically similar to sub-unit (a), from which is separated

by a poorly defined discontinuity; the thickness of the deposit at the Calcata outcrop is 8-10 m. Sub-unit (c), the thinnest one (max 5 m-thick), displays alternating planar and cross-laminated lapilli and ash layers, containing white pumice lapilli and subordinate dark grey scoria. Finally, the uppermost sub-unit (d) consists of a lithic-rich breccia deposit, containing centimeter-sized granular inclusions, lava lithic clasts and dispersed feldspar, leucite and clinopyroxene crystals in a greyish ash matrix. The juvenile component is characterized by the prevalence of black-grey scoria lapilli over whitish pumice lapilli. Notably, two kinds of juvenile clasts coexist throughout the whole TGVT pyroclastic succession, i.e. white pumice and black-grey scoria (Figure 4.5). Similarly to what observed in the underlying FAD pyroclastic deposit, the abundance of dark grey-black scoria versus whitish pumice increases upward in individual eruptive unit of TGVT (i.e., lacking intervening temporal breaks). Many samples of these juvenile clasts where collected throughout the succession, as well as lithic enclaves from the upper unit (see below in this section).

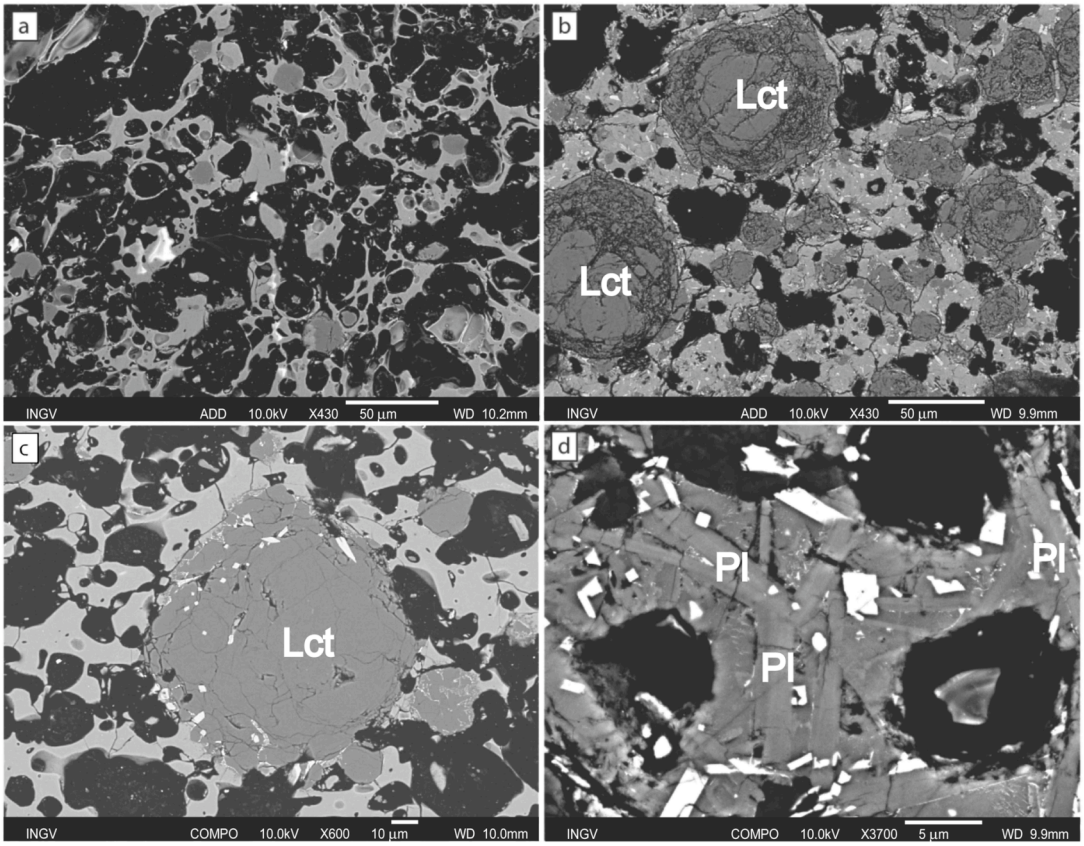

Figure 4.5 - SEM images of TGVT juvenile clasts (sample location in Figure 4.4): a) different crystal and vesicle contents in coexisting white pumice (sample MG-29) and b) black-grey scoria (sample MG-7); c) crown-like poikilitic texture of leucite in black-grey scoria (sample MG-11/2); d) high-magnification of plagioclase microcrysts in the highly crystalline groundmass of black-grey scoria (sample MG-11).

Based on colour and degree of porphyricity, the two juvenile clast types were distinguished as follows: white pumice (glass ≥50 vol.%, up to 80-90 vol.%) and black-grey scoria (glass ≤30 vol.%). Centimeter-sized white pumice clasts occur throughout the deposits, reaching the maximum concentration in the lower portions of the lower and the upper TGVT eruptive units. Conversely, centimeter-sized black-grey scoria clasts mostly occur in the middle-upper portions of the two units, reaching the maximum concentration at the top of both. Sub-unit (d) of the upper TGVT is also characterized by the occurrence of mafic granular inclusions made up of clinopyroxene, leucite and dark mica, and occasional sanidine-rich, clinopyroxene-bearing, granular inclusions, phonolitic in composition.

White pumices are characterized by subaphyric texture (PI <10 %), vitrophyric groundmass (glass ≥50 vol.%) and moderate vesicularity (up to 50 vol.% in thin section). They contain scarce clinopyroxene, sanidine, plagioclase and oxide phenocrysts (>100 μm; Cashman, 1992). In particular, sub-millimeter-sized, euhedral to subhedral, clinopyroxene occurs as either single phenocrysts or glomerocrysts associated with plagioclase and oxides. Sanidine is millimeter- to submillimeter-sized, round-shaped, and often glass-embayed. Very small-sized (<30 μm) leucite typically occurs in glassy vesicle septa.

Black-grey scoria shows low vesicularity (<25 vol.% in thin section), highly crystalline groundmass (glass ≤30 vol.%), and abundant phenocrysts (PI up to 35%). Leucite, the most abundant phenocryst, is often characterized by crown-like poikilitic texture (Figure 4.5c) made up of clinopyroxene microcrysts (<30 μm; Cashman, 1992). Clinopyroxene (the second mineral in order of abundance) is present as a submillimeter-sized, euhedral to subhedral, green- to deep-green-coloured phenocryst, similar to that occurring in white pumice, and as a millimeter-sized, anhedral and colourless, phenocryst. The latter has been interpreted as a xenocrystic population of clinopyroxene, on the basis of textural and chemical disequilibrium with the surrounding melt (see above in the text). The scarce sanidine is similar in shape as in white pumice. Plagioclase occurs either in glomerocrysts with clinopyroxene, or as microcrysts in the groundmass. Rare phenocrysts of biotite and apatite are also present.

White pumice and black-grey scoria show similar major element bulk compositions, which essentially plot in a relatively narrow area in the phonolite field of the TAS diagram (Figure 4.6; Table 4.4). Nevertheless, the compositions of interstitial glasses slightly differ in the two kinds of juvenile components (Table 4.5). In particular, the residual glass in black-grey scoria is more variable in composition than in white pumice and shows lower SiO_2 and K_2O, possibly as consequence of leucite and sanidine crystallization (20-35 vol.%). Mineral compositions are also comparable. Clinopyroxenes show high Ca contents, wide ranges of SiO_2 and mg-*number* (0.30-0.45, calculated as $MgO/[MgO+FeO_{tot}]$), and plot along the Di-

Hd joint of the pyroxene quadrilateral (Table 4.6); the xenocrysts population in black-grey scoria is Mg-richer (mg-*number* = 0.64-0.86; Figure 4.7). Plagioclase (An_{88-95}) and sanidine (Or_{88-95}) plot near the vertexes of the feldspars ternary diagram (Table 4.7); in some cases sanidine shows higher BaO contents (up to 2.50 wt.%).

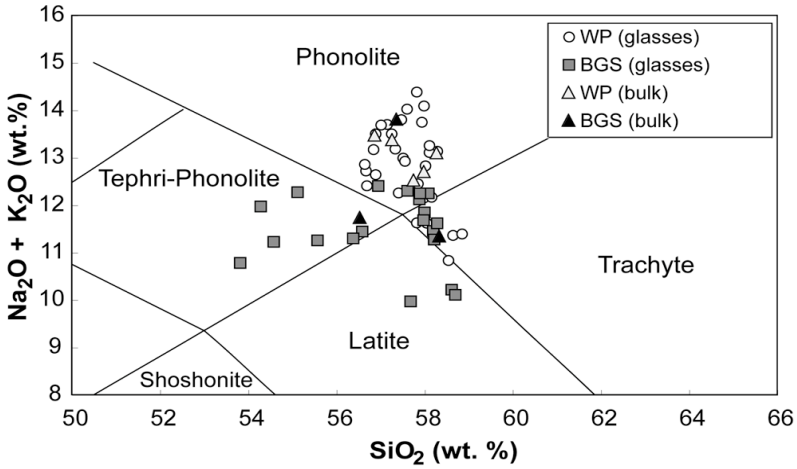

Figure 4.6 - Bulk (XRF) and glass (EMP) compositions of FAD and TGVT juvenile clasts in the TAS diagram. WP=white pumice; BGS=black-grey scoria.

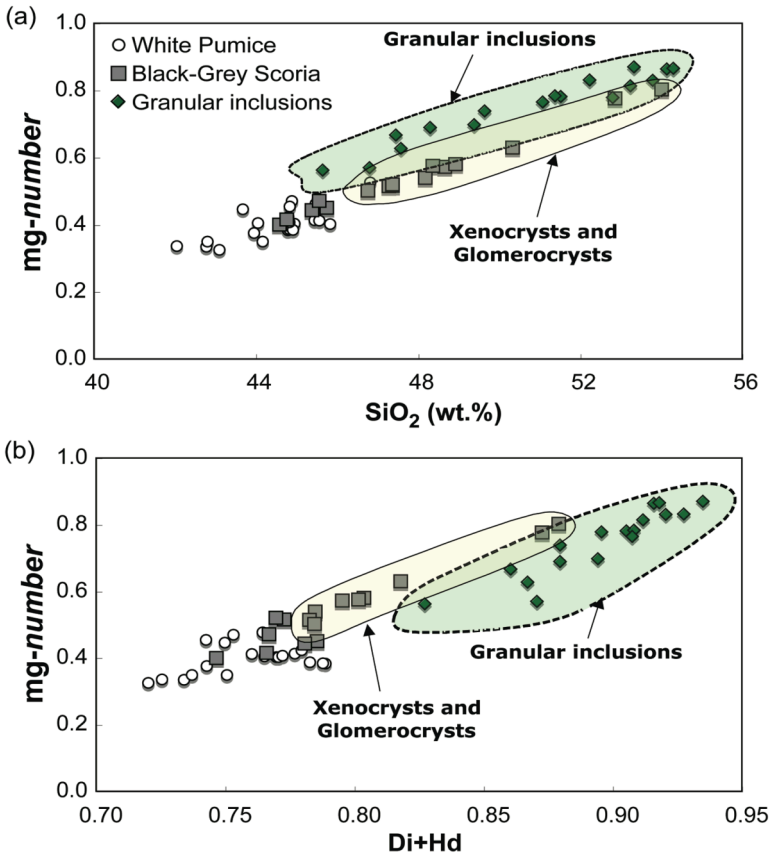

Figure 4.7 - (a) Plots of the mg-*number vs.* SiO_2 and (b) Di+Hd (calculated after Putirka et al., 2008) for clinopyroxenes from TGVT white pumice and black-grey scoria. Clinopyroxene crystals from lithic enclaves (see above in the text) are also reported in comparison with the field of clinopyroxene xenocrysts in black-grey scoria.

Tufo Giallo di Prima Porta (514±3 kyr)

The volcanic activity that followed TGVT phonolitic eruptions was mostly strombolian. Several small pyroclastic flows, tephri-phonolitic in composition, were also emplaced. However, after a short interval of less than 50 kyr, another large phonolitic "yellow tuff" deposit was emplaced, named Tufo Giallo di Prima Porta.

The Tufo Giallo di Prima Porta has two distinct facies: a non-lithified lower distal facies and a lithified upper one (Karner et al., 2001; Figure 4.8a). The non-lithified facies is a massive ash deposit with abundant pale grey scoria, altered leucite crystals and characteristic large grey-to-green pumice blocks containing altered leucite crystals. Large lithic fragments are common, consisting of holocrystalline lava, and unmetamorphosed limestone and travertine clasts. The lithified facies is a typically yellow pyroclastic flow deposit with yellow pumice and rare grey scoria. Large black scoriae locally occur, together with sedimentary lithic clasts and italite clasts (i.e., leucite and clinopyroxene in holocrystalline texture).

As already described for previous eruptions, whitish pumice clasts are glassy (phenocrysts <5 vol.%) and highly vesiculated (Figure 4.8b). Scarce sanidine and clinopyroxene phenocrysts are present, showing euhedral to sub-euhedral habits. Vesicles are often ellipsoidal showing a preferential elongation that may testify the occurrence of shear stresses in the conduit during the eruption. Bulk and glass composition are phonolitic (Table 4.8; Figure 4.2).

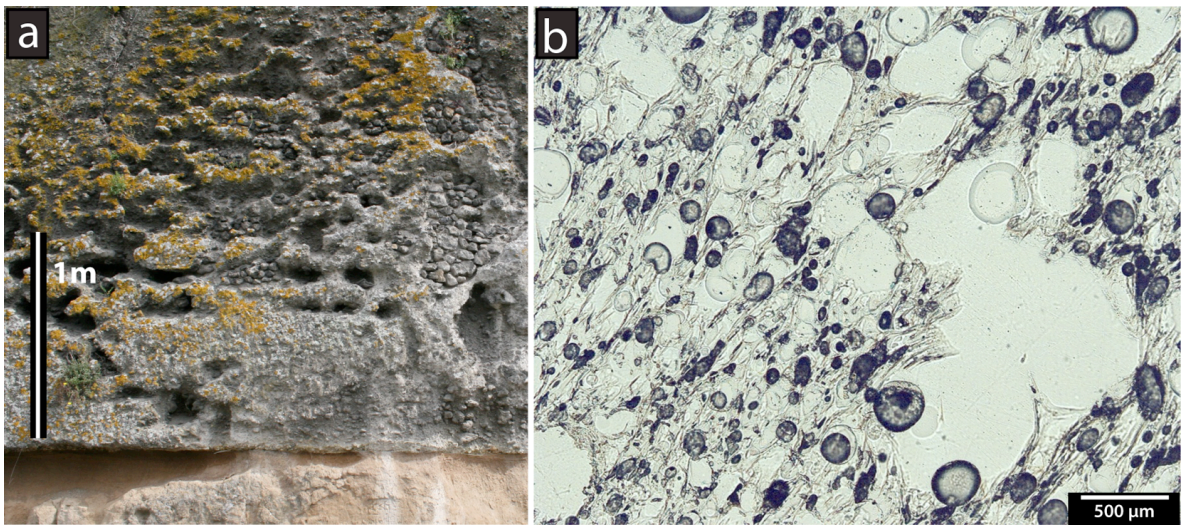

Figure 4.8 - (a) Tufo Giallo di Prima Porta outcrop at Isola Farnese, the yellow ash deposit (non-lithified facies) is at the base of the upper lithified facies, and (b) microscope image of a glassy white pumice.

Grottarossa pyroclastic sequence (518±5 kyr, 514±5 kyr)

The Grottarossa pyroclastic sequence has been divided into four sub-units (a-d; Karner et

al., 2001). Sub-unit a consists of an ash flow deposit preceded by a plinian ash fall. Sub-unit b is a semi-lithified pyroclastic flow deposit, showing textural and petrographic features similar to those of the Tufo del Palatino of CAVD, overlaying a plinian ash fall deposit made of lapilli-sized grey scoria and yellow-whitish pumice. Sub-unit c is a pyroclastic flow showing similar features to sub-unit a. The last sub-unit d was emplaced as an ash fall, normally graded containing light brown ash and small grey lapilli-sized clasts. Juvenile clasts, collected from the uppermost sub-unit d, are highly crystallized (glass <10 vol.%), moderately vesiculated (<20 vol.%) and tephri-phonolitic to foiditic in composition. Mineral assemblage is made up of abundant leucite, followed by scarce clinopyroxene, feldspars, mica and oxides.

Tufo Terroso con Pomici Bianche (488±2 kyr)

The pyroclastic deposit of Tufo Terroso con Pomici Bianche is almost entirely composed of weathered brown ashes and represents an important stratigraphic marker of SVD, due to its widespread occurrence in volcanic deposits emplaced from other volcanoes of the Roman Province. Two horizons of white to yellow pumice occur in the middle of this deposit (Figure 4.9). The lowermost one is continuous throughout the area with a relatively uniform thickness and it is also known with name of "Granturco" layer (Fornaseri et al., 1963). Sanidine dominates the mineral assemblage of these pumice clasts, whose composition ranges from latitic to phono-tephritic (Sottili et al., 2004).

Figure 4.9 - Tufo Terroso con Pomici Bianche outcrop near Isola Farnese locality.

Tufo Rosso a Scorie Nere (449±1 kyr)

Tufo Rosso a Scorie Nere is a lithified ignimbrite with large black scoria in a reddish ash matrix. This ignimbrite filled paleo-valleys throughout the volcanic deposits of the Roman Province, forming tuff plateau that, after the inversion of the topography due to the differential erosion, represented the ground over which many medieval towns arose (Civita Castellana, Ceri, Mazzano, Orte; see also Figure 2.4 and 4.10a). The base of the Tufo Rosso a Scorie Nere lays over at least 4 fall units (A-D; Sottili et al., 2004). The uppermost of them is coeval with the main pyroclastic unit of Tufo Rosso a Scorie Nere and hence has been interpreted as the plinian fall associated to the pyroclastic flow (Figure 4.10b). Walker (1985) described one of the proximal outcrops of the ignimbrite and interpreted this deposit as a lag-breccia, characterized by chaotic aspect, high lithic content and fines-poor matrix. Aside from the proximal area, the deposits appear massive (several tens of meters thick) and consist of two flow units, a lower unit characterized by black vitreous fiamme and thermo-metamorphosed sedimentary lithics and an upper unit rich in highly vesiculated, black scoria clasts in a reddish ash matrix (Figure 4.10c).

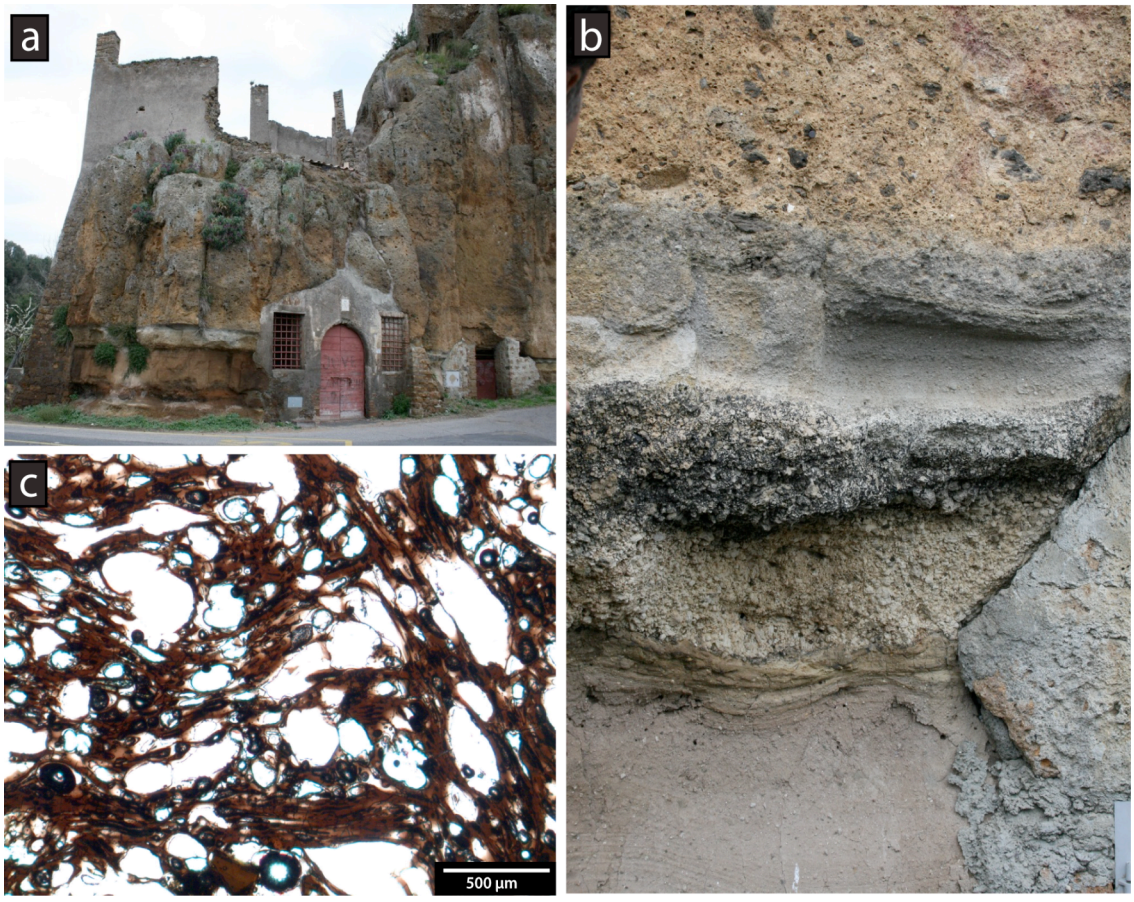

Figure 4.10 - Tufo Rosso a Scorie Nere outcrop at the Ceri locality (a), particular of the basal fall deposit (b) and reddish aphyric juvenile clast (c).

Tufi Stratificati Varicolori di La Storta (ca 410 kyr)

The Tufi Stratificati di La Storta represent a series of pyroclastic fall deposits emplaced north of Rome. Due to the limited extent of this deposit and the poor correlation among outcrops, no samples were collected from this eruptive sequence (more detailed studies are reported in Mattias and Ventriglia, 1970; Alvarez, 1972; Corda et al., 1978).

Tufo di Bracciano (307±5 kyr, 316±6 kyr)

The Tufo di Bracciano deposits usually occur at the top of many distal deposits of SVD. The maximum thickness of the main pyroclastic unit is of a few tens of meters in the western part of Bracciano Lake (Figure 4.11a). Field and sub-surface data likely indicate a source area and related caldera collapse broadly located in the NW sector of present-day Bracciano depression (Sottili et al., 2010). Juvenile scoria clasts collected in this eruptive unit are low to moderately porphyric (PI = 5-10 vol.%) and made up of clinopyroxene, sanidine and mica phenocrysts whereas the groundmass is moderately crystallized (glass <15 vol.%). Interstitial glass is phonolitic to trachytic in composition (Table 4.8; Figure 4.2). Lithic enclaves (also clinopyroxenites) and thermo-metamorphosed sedimentary clasts (flysh and carbonate rocks) were also sampled from the Anguillara cliff outcrop (Figure 4.11b).

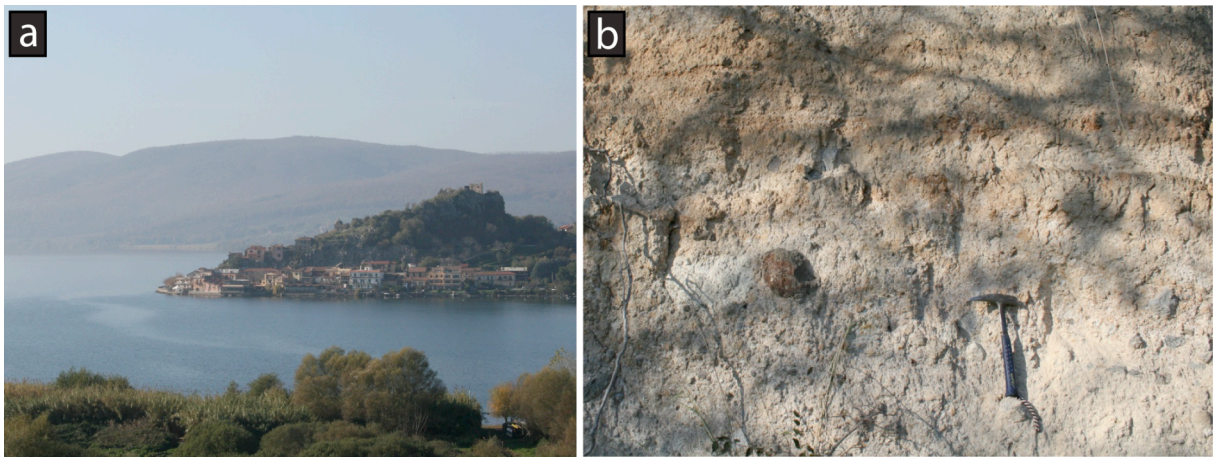

Figure 4.11 - Bracciano village (a) and Tufo di Bracciano at the Anguillara cliff outcrop (b).

Tufo Giallo di Sacrofano (286±6 kyr)

The Tufo Giallo di Sacrofano was erupted from the Sacrofano eruptive centre in the eastern sector of SVD and is considered one of the major caldera-forming eruption of SVD, covering an area of some hundreds km^2. The main lithofacies consists of a few tens of meters thick, massive and zeolitised yellow tuff, containing centimeter-sized white pumice clasts (Figure 4.12). At the bottom of the pyroclastic flow deposits larger pumice (decimetric in size) and thermo-metamorphosed sedimentary clasts (skarn) were collected. White pumice

clasts are crystal-poor (glass >90 vol.%) and highly vesiculated. Mineral assemblage is made up of prevailing feldspars and biotite. Chemical composition of glass is phonolitic, as well as the bulk composition (Table 4.8; Figure 4.2).

Strombolian activity persisted during the formation of Sacrofano caldera, and along its rims several scoria cone and hydromagmatic deposits were emplaced. M.te Aguzzo scoria cone represents one of the small centres associated to Sacrofano caldera and consists of tephri-phonolitic leucite-bearing scoria. These tephri-phonolitic scoria clasts were used as starting material for HP-HT experiments (see below in the result section).

Figure 4.12 - Tufo Giallo di Sacrofano outcrop at Magliano Romano locality (after Sottili et al., 2010)

Tufo Pizzo di Prato (249±16 kyr)

The Pizzo di Prato eruption consists of a basal plinian fall deposit and a main pyroclastic flow unit. In near vent area along south-eastern coast of present-day Bracciano Lake, the main flow unit is composed by the association of a coarse spatter and lithic-rich deposits (Figure 4.13). Walker (1985) recognized in this eruption a caldera-forming event, although the low volume of erupted magma (less than 1 km^3). Juvenile clasts from the spatter are lowly porphyric (PI<10 vol.%), poorly vesiculated and phenocrysts assemblage is made of sanidine, clinopyroxene and less mica and plagioclase. Interstitial glass (<20 vol.%) is phonolitic in composition. Scoria clasts from the pyroclastic flow deposits are similar to juvenile clasts of the spatter deposits, but slightly more glassy (<40 vol.%) and trachy-phonolitic in composition (Table 4.8; Figure 4.2).

Figure 4.13 - Spatter deposit of Tufo Pizzo di Prato near Anguillara locality.

Tufo Vigna di Valle (193±7 kyr)

The Tufo Vigna di Valle consists of a few meter thick pyroclastic flow unit, cropping out in the southern rim of the Bracciano Lake. The deposit commonly shows planar- to cross-lamination and locally overlies decimeter-thick pumice fall horizon.

Hydromagmatic activity (less than 132 kyr)

Hydromagmatic activity of the last eruptive phase of SVD was characterized by numerous maar-forming eruptions (Table 4.2, Figure 4.14). Previous structural and gravimetric studies (de Rita and Sposato, 1986; Di Filippo and Toro, 1993), coherently with data from erupted lithic inclusions (de Rita and Zanetti, 1986) and geothermal exploration drillings (Funiciello et al., 1979), have indicated that maar-feeder magmas mostly interacted explosively with water reservoirs located in Meso-Cenozoic carbonate and silicoclastic horst areas, although in some cases explosive interaction may have occurred with shallow surface waters. Among samples collected from maar-forming eruptions, four kinds of juvenile clasts have been recognized, on the basis of their texture, composition and mineral assemblage (Tables 4.2 and 4.9; Figure 4.15). A detailed discussion on SVD maar-forming eruptions is reported in Sottili et al. (2011).

Table 4.2 - Age, crater diameter, classfication and composition of juvenile clasts sampled in maar-forming eruptions (as reported in Sottili et al., 2011).

Eruptive centre	Label	Age (kyr)	Crater diameter (m)	Type	Composition
Martignano Upper	UMT	n.d.	1250	I	K-Basalt Phonolite
Martignano Middle	MMT	n.d.	1490	II	K-Basalt Phonolite
S. Bernardino	SBR	≤172	1720	III	Pho-Te Te-Pho
Lagusiello	LAG	158±4	790	III	Pho-Te Te-Pho
Monterosi	MTR	150±4	890	III	Pho-Te Te-Pho
Stracciacappa Lower	LSK	97±4	1490	III	Pho-Te Te-Pho
Stracciacappa Upper	USK	n.d.	1480	III	Pho-Te Te-Pho
Acquarella	ACQ	n.d.	650	III	Pho-Te Te-Pho
Le Cese	LCS	95±5; 89±29	560	III	Pho-Te Te-Pho
Polline	POL	<89±12	1470	III	Pho-Te Te-Pho
Martignano Lower	LMT	<86	1570	IV	Phonolite
Piana dei Falliti	PDF	89±12	1620	IV	Phonolite
Valle dei Preti	VDP	134±33	1010	IV	Phonolite Te-Pho

n.d.: not determined; Pho-Te: phononolitic tephrite, Te-Pho: tephritic phonolite

Figure 4.14 - Stracciacappa maar. The well-preserved flat-floored crater is ca. 1500 m wide and hosted a lake that was drained in AD 1834.

The four types of juvenile clasts have been divided as follows:

i) *Clinopyroxenite-type.* This clast type only occurs in the upper Martignano unit and is characterized by relatively high porphyricity (PI = 20 vol.%) due to the occurrence of abundant, millimeter-sized, clinopyroxene, dark mica and olivine phenocrysts, associated with scarce spinel, in clinopyroxene-bearing, nearly vitrophiric, poorly vesicular groundmass;

ii) *Leucite-bearing tephrite-type.* This clast type, only found in the middle of Martignano unit, displays low porphyricity (PI <10 vol.%) due to the occurrence of phenocrysts and glomerocrysts of millimeter-sized clinopyroxene, plagioclase and spinel. The poorly vesicular groundmass is made up of plagioclase, clinopyroxene and leucite, associated with scarce sanidine, spinel and glass.

iii) *Leucitite-type.* This is the most common juvenile clast type in the SVD maar deposits and is characterized by prevailing leucite and clinopyroxene, occurring both as sub-millimeter- to millimeter-sized phenocrysts and in the groundmass assemblage. The degree of porphyricity is usually <10-15 vol.%. The fine- to coarse-grained groundmass is scarcely vesicular and highly crystalline (leucite + clinopyroxene + plagioclase + spinel ± sanidine) and contains scarce glass almost totally transformed into zeolites.

iv) *Phonolite-type.* This juvenile clast type occurs in the Valle dei Preti, Piana dei Falliti and Martignano deposits. With respect to the above-reported rock types, it is

characterized by higher vesicularity, a glassy to holocrystalline groundmass, and by the occurrence of abundant sanidine phenocrysts, associated with leucite and scarce clinopyroxene, plagioclase, dark mica and spinel (PI ~10 vol.%).

Bulk composition of clasts erupted during maar-forming eruptions show a variable composition, ranging from trachy-basalt to phonolite (Table 4.9; Figure 4.16a). Clinopyroxene composition is also highly variable (Table 4.10), with mg-*number* ranging from 0.80-0.85 in clinopyroxenite-type to 0.22-0.56 in the other groups. Worth noting few high mg-*number* clinopyroxene (0.80-0.86) have been recognized in the leucite-bearing tephrite-type. Importantly, only clinopyroxene occurring in clinopyroxenite-type and leucitite-bearing tephrite-type (those with high mg-*number*) are Cr-bearing (<1 wt.%). These clinopyroxenes provide a rare snapshot of the most primitive magmas involved in the SVD activity. Feldspars vary in composition according to their group (plagioclase and sanidine range from An_{33}-Or_{69} in leucite-bearing tephrite-type to An_{95}-Or_{86} in phonolite-type).

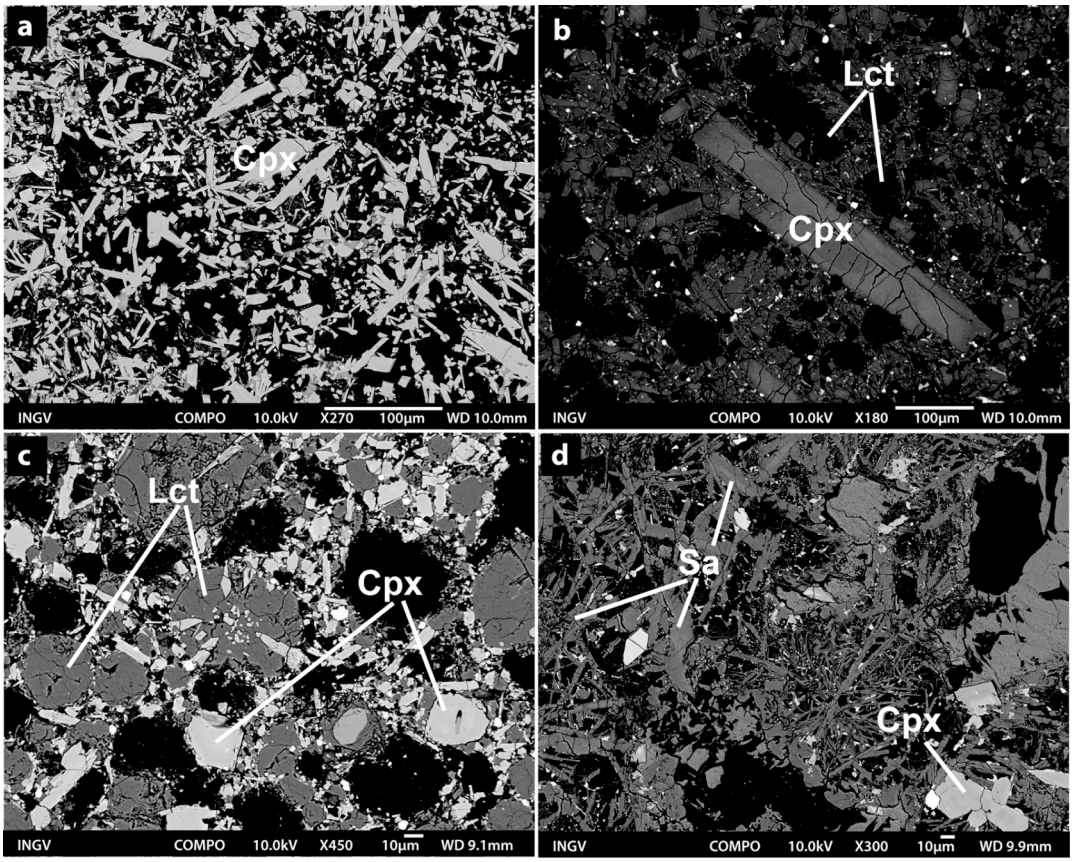

Figure 4.15 - Representative SEM images showing microtextures of juvenile lapilli from selected hydromagmatic centers: (a) clinopyroxenite-type rock type from the upper Martignano unit; (b) leucite-bearing tephrite-type from the middle Martignano unit; (c) leucitite-type from Lagusiello; (d) sanidine-rich phonolite-type from Piana dei Falliti.

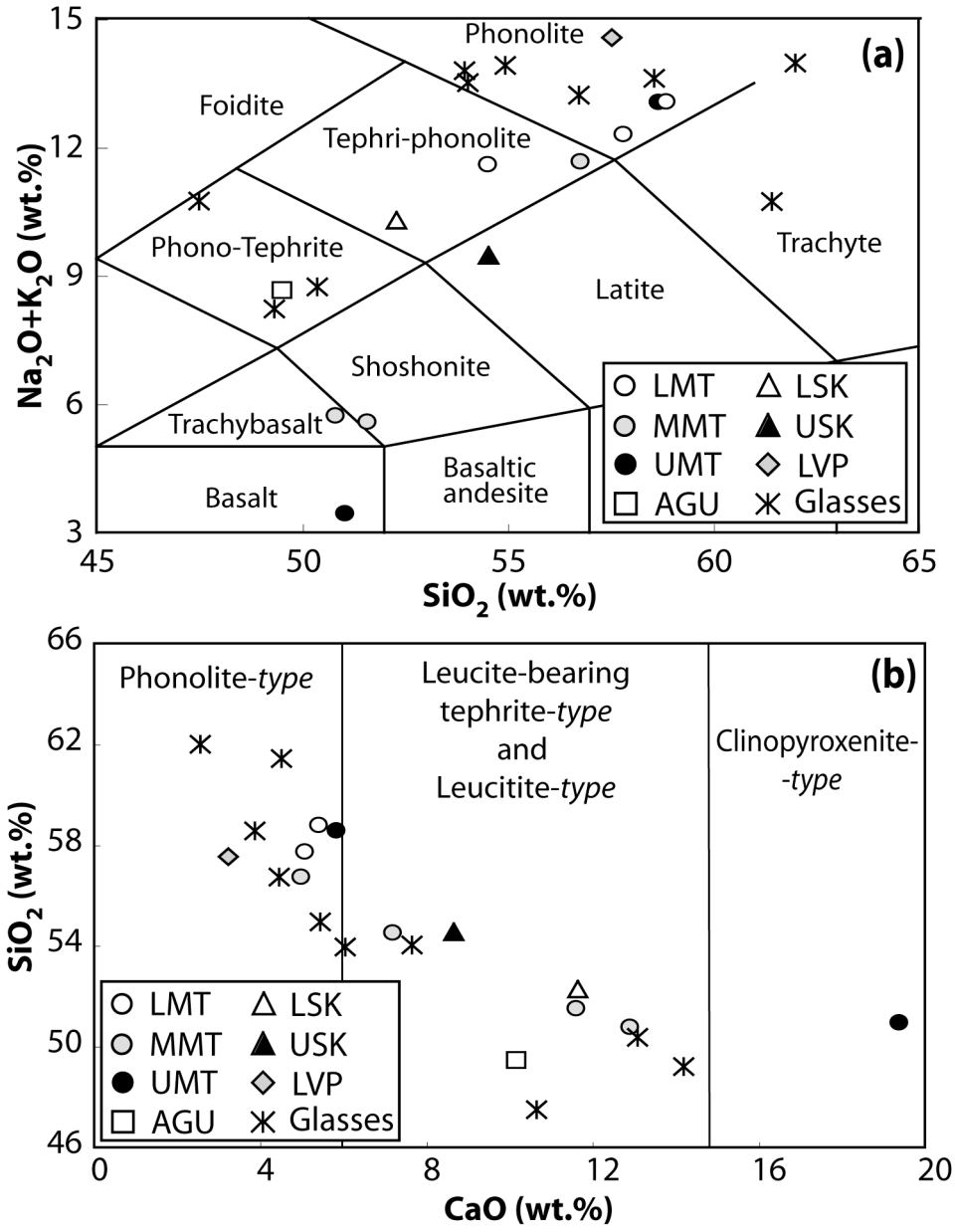

Figure 4.16 - (a) TAS classification diagram of bulk compositions and interstitial glasses spanning a wide compositional range from basalts to phonolites; (b) CaO–SiO_2 plot of the maar juvenile eruption products (see Table 4.2 for sample labels) defining the typical Roman Province magma differentiation trend towards phonolite rock types (from Sottili et al., 2011).

4.1.2 Lithic enclaves

Lithic enclaves represent crystalline rocks formed at the cooling margin of the magma chambers and thus they witness crystallization and magma differentiation processes in the system. Samples analysed in this study range in size from few centimetres to decimeter in size. These were collected mostly in the uppermost deposit of TGVT eruptive sequence (sub-unit d of Masotta et al., 2010) and Tufo di Bracciano deposit at the Anguillara outcrop (Sottili et al., 2010). Further samples were collected in several SVD hydromagmatic centres (Sottili et al., 2011). All these deposits were emplaced during highly energetic eruptions induced by

magma-water interaction. Figure 4.17 reports the modal analyses of selected samples obtained at the optical microscope using a point counter (2000 pts). The lithic enclaves were petrographically classified in four main types (A, B, C, and M).

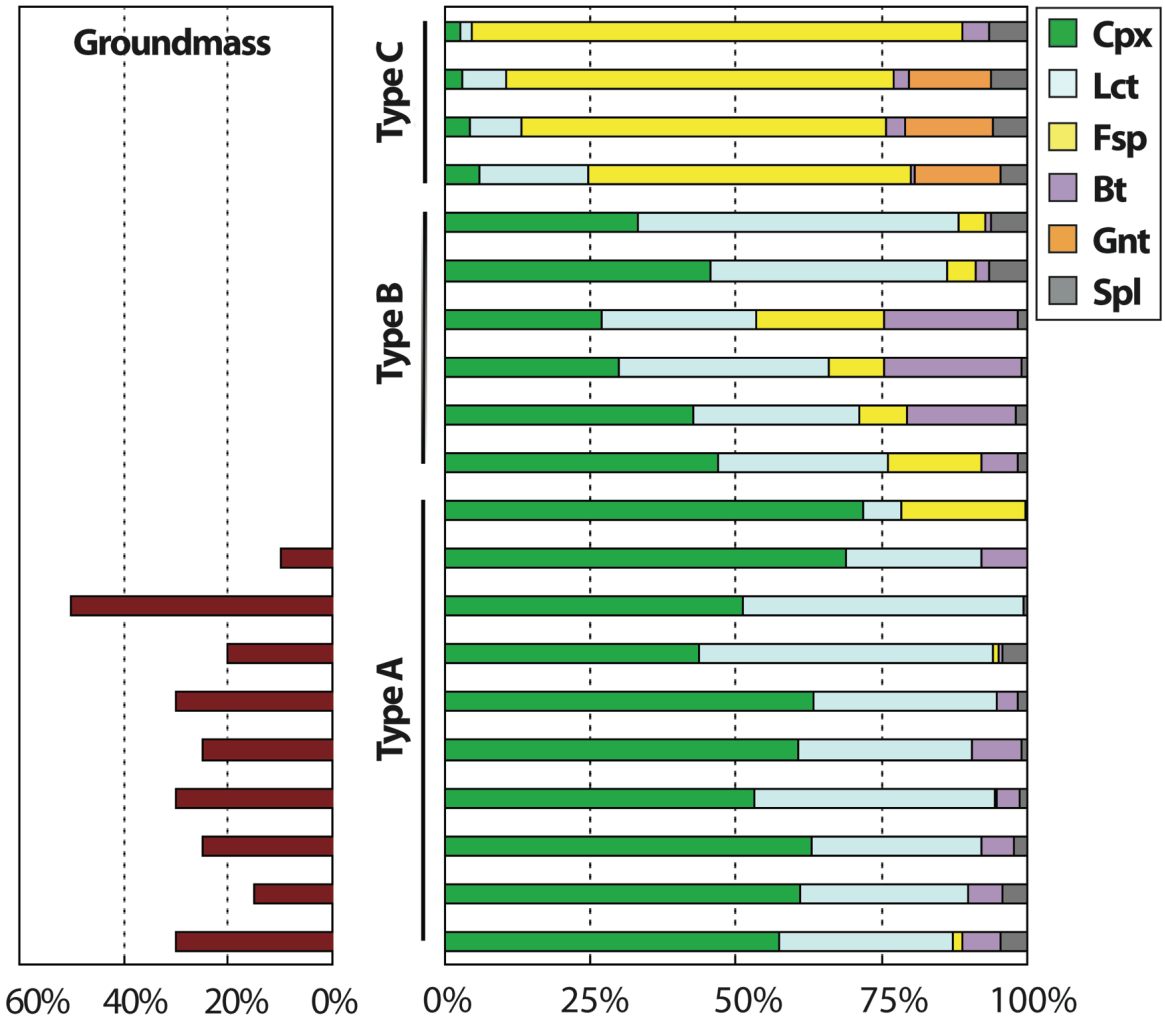

Figure 4.17 - Groundmass (left) and mineral assemblage (right) of lithic enclaves representative of the three main classes A, B and C, expressed in vol.%.

Type A enclaves

The enclaves of this type are the most common in all the deposits and are characterized by porphyric texture (PI = 40-60%) and holocrystalline groundmass (Figure 4.18). Clinopyroxene is the most abundant mineral occurring both as phenocryst (ranging in size from ~0.1 to 2-3 mm) and as groundmass phase (<100 µm). Clinopyroxene phenocrysts are euhedral to sub-euhedral, light to deep green coloured and weakly pleochroic, showing slightly zoned greenish rims. Leucite is scarce as phenocryst but is the most abundant mineral of groundmass, occurring in both cases in round-shaped sub-euhedral crystals. Plagioclase is scarce, occurring as partially altered phenocrysts (>100 µm), whereas sanidine is usually

absent or scarcely represented by anhedral microcrysts (<100 µm) in the groundmass. Mica and oxide are scarce (<3 vol.%). The enclaves of this group have been defined “mafic”.

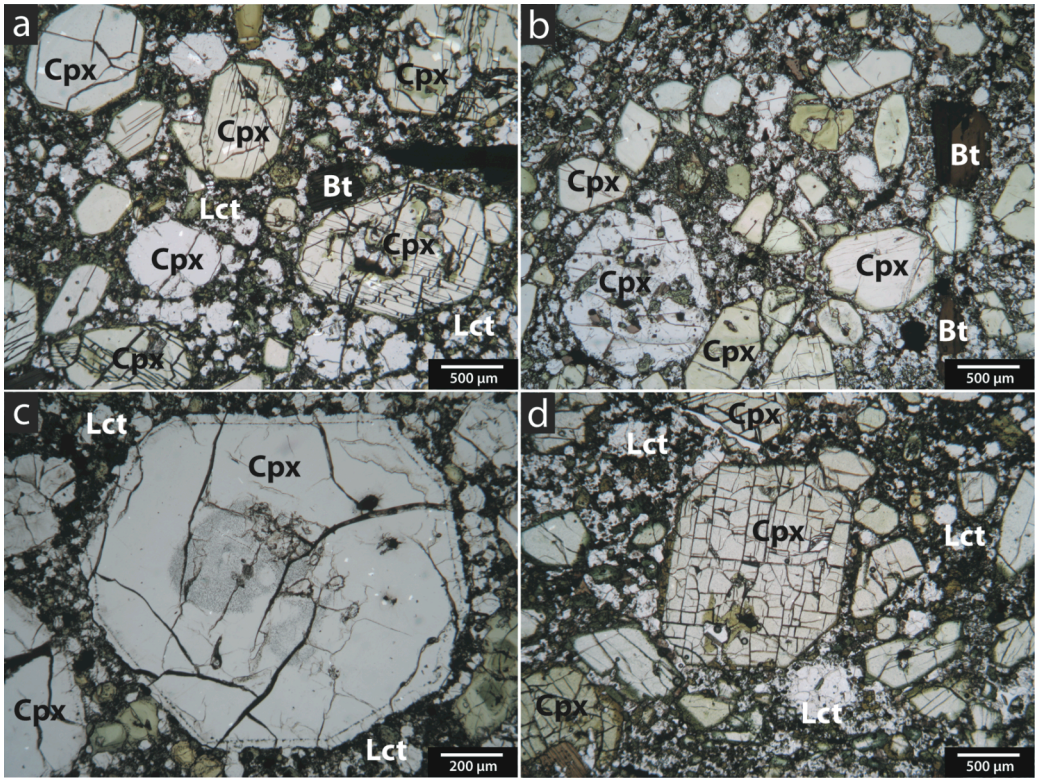

Figure 4.18 - Microphotographs of type A enclaves showing euhedral to sub-euhedral clinopyroxene phenocrysts and sub-euhedral microcrysts of leucite in the groundmass (a-b), detail of euhedral to sub-euhedral clinopyroxene crystals (c-d).

Type B enclaves

Type B enclaves are common in all the deposits and are characterized by highly porphyritic (PI >80%) to holocrystalline inequigranular texture (Figure 4.19). Clinopyroxene is the most abundant phase, occurring prevalently as anhedral phenocryst (<500 µm). Large (>500 µm) euhedral leucite phenocrysts occur frequently, showing typical cross-geminated structures. Sanidine is anhedral and occurs prevalently in large poikilitic phenocrysts enclosing clinopyroxene crystals. Mica is relatively abundant (>10 vol.%), varying in size from 500 µm to 4 mm; oxides are scarce (<3 vol.%). Leucite and scarce clinopyroxene constitute the scarce groundmass, when present. Due to the increasing presence of feldspars with respect to clinopyroxene, enclaves of this group have been defined “intermediate”.

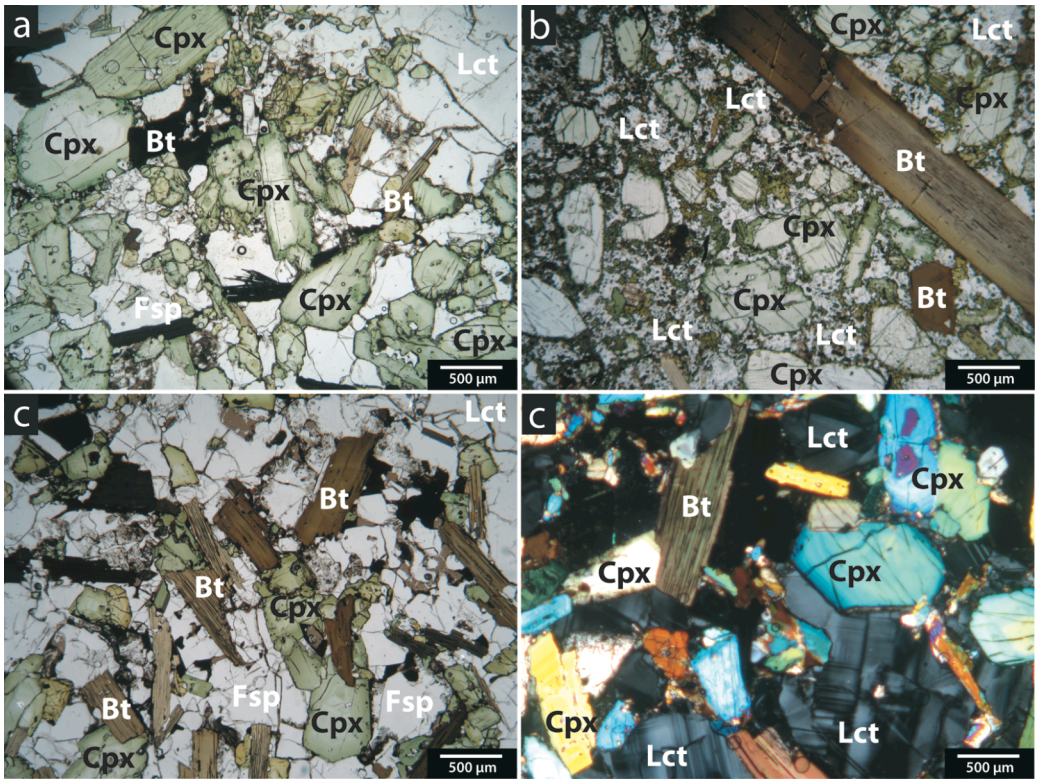

Figure 4.19 - Microphotographs of type B enclaves showing sub-euhedral to anhedral clinopyroxene, leucite and biotite phenocrysts (a-b). Note the intense chemical zoning of clinopyroxene (a-b), the variable amount of biotite (b-c) and the poikilitic texture of feldspar (c) and leucite (d) in holocrystalline samples.

Type C enclaves

These enclaves occur rarely compared with the other types. They are more frequent in the Tufo di Bracciano outcrop and are characterized by equigranular holocrystalline texture (Figure 4.20). Sanidine is prevalent (70-95 vol.%), occurring in euhedral to sub-euhedral phenocrysts with a size ranging from ~0.5 mm to ~3 mm. The modal abundance of mica and garnet varies significantly in each sample (0-20 vol.%) whereas clinopyroxene and leucite are absent or scarce (<10 vol.%). Oxides are abundant (4-5 vol.%). The enclaves of this group constitute the felsic type and have been defined "sanidinites". The presence of garnet could indicate the occurrence of post-magmatic (pneumatolitic) crystallization enhanced by fluid circulation (Naimo et al., 2003). Otherwise, garnet-bearing sanidinites of SVD have been interpreted as the product of plutonic crystallization of phonolitic magma bodies, under condition of high H_2O fugacity (Facchinelli and Gaeta, 1992; Capitanio and Mottana, 1998).

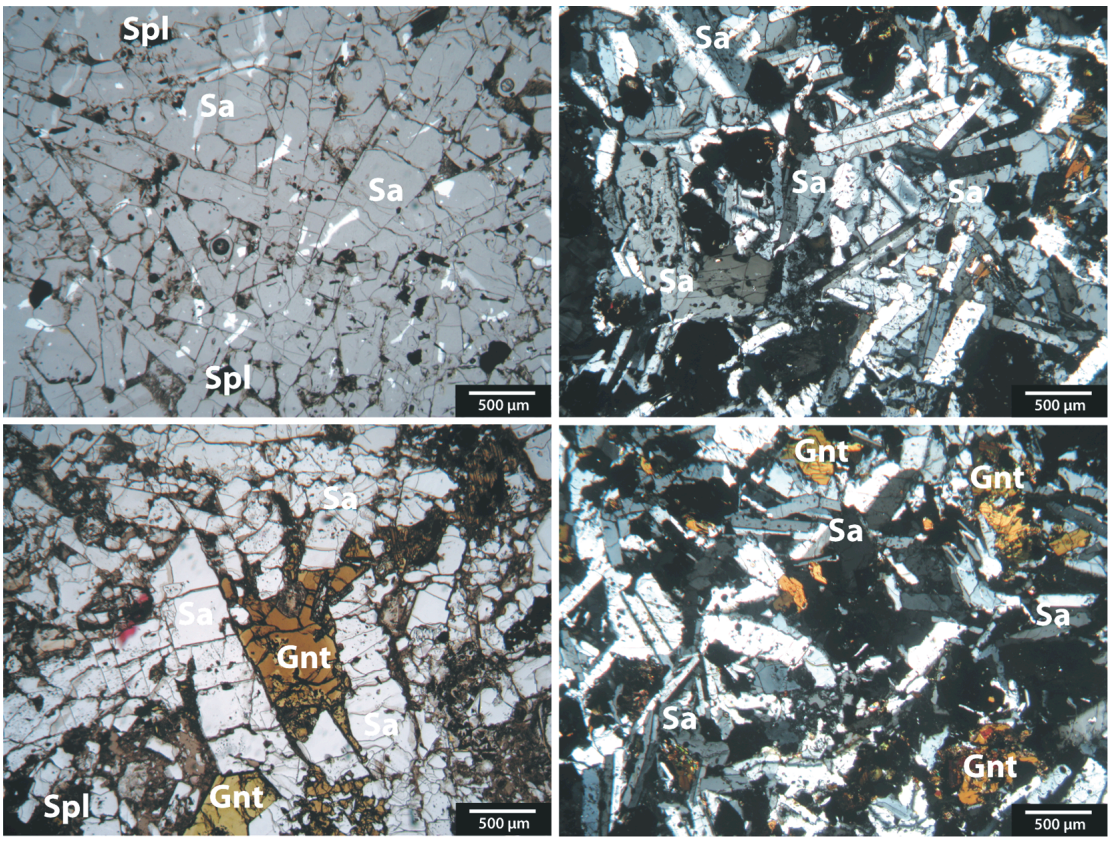

Figure 4.20 - Microphotographs of type C enclaves showing variability in the abundance of garnet.

Type M enclaves

This kind of enclave occurs exclusively in the uppermost deposit of upper TGVT eruptive unit (sub-unit d; Masotta et al., 2010). They show completely different features with respect to other groups, in terms of texture and mineral assemblage (Figure 4.21). Clinopyroxene and phlogopite are the most abundant mineral phases, followed by leucite and scarce olivine and feldspars. Phenocrysts are mostly anhedral or sub-euhedral whereas groundmass contains scarce glass (<5 vol.%) and abundant phlogopite microcrysts. Notably, sieve textured olivine phenocrysts are sited along micro-fractures of the samples, surrounded by phlogopite microcrysts and characterized by numerous micro-inclusions (<2 µm). Oxides are frequent, whereas scarce quantities of garnet have been recognized. Due to their peculiar mineral assemblage, enclaves of this group were defined "metasomatic" (hence the name type M). Their original composition may have been altered by intense (post magmatic) fluid circulation, as deduced by the presence of phlogopite-rich veins.

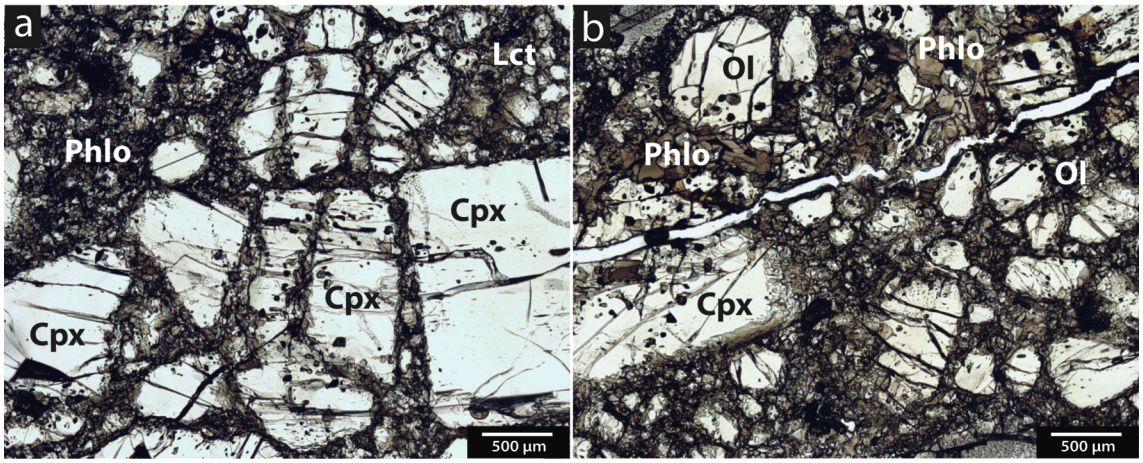

Figure 4.21 - Microphotographs of type M enclaves showing sub-euhedral to anhedral, partially resorbed, clinopyroxene (a) and abundant phlogopite, and sieve-textured olivine and clinopyroxene near small micro fractures.

Thermo-metamorphosed sedimentary lithics

Several thermo-metamorphosed sedimentary clasts (ranging in size from 2 to 4 centimeters) were collected from both the deposits of sub-unit d of the upper TGVT (Masotta et al., 2010) and of Tufo di Bracciano. Mineral assemblage of thermo-metamorphosed sedimentary lithics has been qualitatively inferred via XRD and SEM-EDS analyses. Mica is abundant in TGVT lithic enclaves and occurs in association with zeolites. Lithic enclaves collected from Tufo di Bracciano show mineral assemblages characterized by zeolites ± mica ± quartz ± garnet. Carbonatic clasts are also occurring in the same deposit. The mineral assemblage of different clasts inferred by XRD is consistent with that produced by thermo-metamorphism of a pelitic protolith, whereas zeolites (cabasite and phillipsite) may have formed by means of fluids-induced alteration of the clasts.

Chemical features

The bulk composition of type A and type B enclaves ranges from shoshonitic to phono-tephritic and foiditic (Figure 4.22; Table 4.11), whereas the composition of the type C enclaves varies from tephri-phonolite to phonolite. Compositional variations among different groups of enclaves are mostly related to variable abundances mineral phases. In particular, the variability of clinopyroxene and leucite reflect the vertical distribution (alkalies vary more than SiO_2) of enclaves of types A and B in the TAS diagram, whereas the variable abundance of mica and garnet produce in enclaves of group C larger variations in the content of SiO_2 (Figure 4.22).

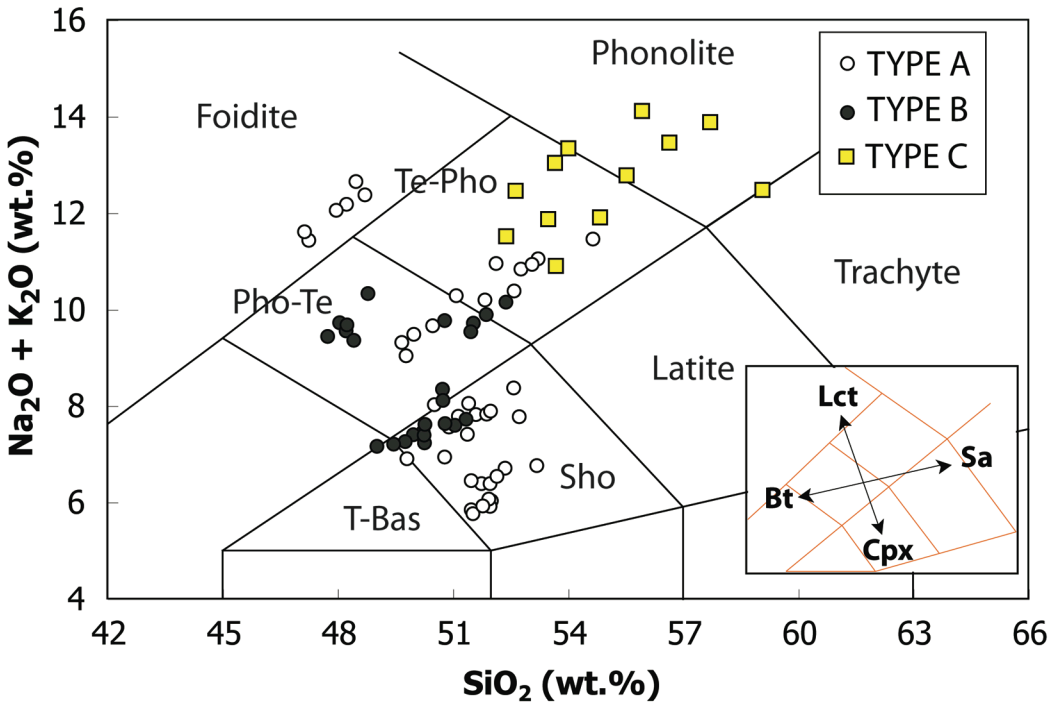

Figure 4.22 - Bulk chemical composition of lithic enclaves reported in TAS diagram. The inset panel illustrates how the variability of the bulk composition of the enclaves (relatively to the averaged bulk composition) can be explained in terms of the abundance of mineral phases.

Clinopyroxenes analyzed in each type of lithic plot along the Di-Hd line of the pyroxene tetrahedron, mg-*number* varying between 0.50 and 0.85 (Figure 4.23; Table 4.12). Although no large chemical variations have been observed between clinopyroxene populations of type A and B enclaves, the clinopyroxenes of the latter type are characterized by a more intense chemical zoning (rims are depleted in MgO with respect to cores).

Feldspars and leucite show rather constant chemical composition among different types of enclaves (Table 4.13). Plagioclase is anhortitic (An >95%) whereas sanidine (Or = 85-95%) is SrO- and BaO-rich (up to 3 wt.% and 5 wt.%, respectively) in type B enclaves. Leucite composition is similar to that of the products of the nearby CAVD (SiO_2 = 55-56 wt.%, Na_2O < 0.70 wt.%). Dark mica is classified as biotite, for its low Mg/Fe ratio. The oxides are mostly Ti-magnetite and show similar composition in all the types of lithic enclaves. Garnet is andraditic in composition.

Rare earth elements (REE) analyzed in clinopyroxene of different enclave types show a parallel, convex-upward, chondrite-normalized pattern (Figure 4.24). Notably, clinopyroxene of type C enclaves are slightly enriched in REE with respect to clinopyroxene of types A and B (Table 4.14).

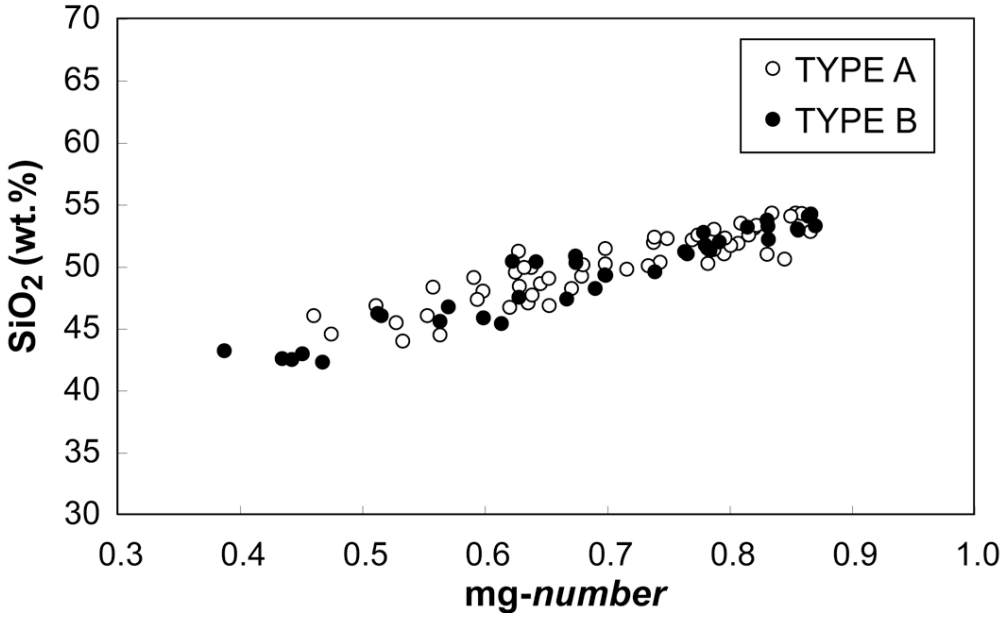

Figure 4.23 - mg-*number vs.* SiO_2 diagram showing the variability of clinopyroxene composition of types A and B enclaves. Note the juxtaposition among clinopyroxenes of the two types of enclaves.

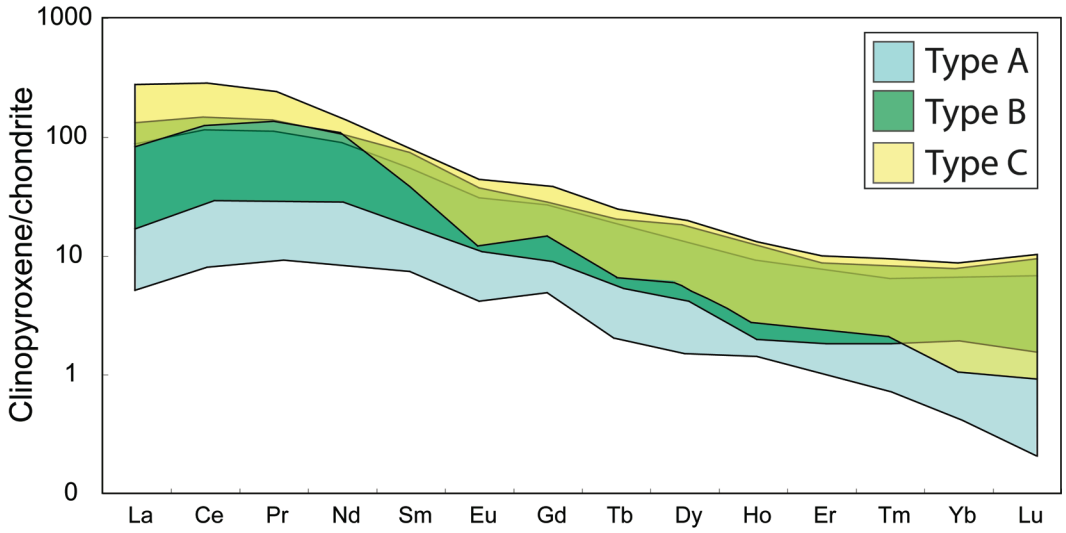

Figure 4.24 - REE abundances (normalized to chondrite; Sun and McDonough, 1989) in clinopyroxene crystals of types A, B and C lithic enclaves.

Table 4.4 - Bulk major element composition of FAD and TGVT juvenile clasts, determined by X-Ray Fluorescence.

E.U.	FAD		LTGVT			UTGVT		
Sample	FAD13	FAD13-B	MG-29	MG-21	MG-30	MG-2	MG-10/2	MG-11/2
Type	WP	BGS	WP	WP	BGS	WP	WP	BGS
SiO_2	56.01	55.24	53.79	54.69	52.82	55.78	54.28	54.80
TiO_2	0.48	0.54	0.41	0.46	0.52	0.49	0.47	0.45
Al_2O_3	19.26	19.13	18.30	19.34	18.49	19.55	19.32	19.54
Fe_2O_3	3.61	4.16	2.92	3.43	4.33	3.77	3.44	3.24
MnO	0.25	0.25	0.24	0.25	0.25	0.26	0.25	0.25
MgO	0.60	0.61	0.55	0.60	1.13	0.67	0.63	0.47
CaO	3.20	3.86	4.68	3.81	4.74	3.83	4.09	3.48
Na_2O	3.09	5.70	3.90	4.87	4.79	5.83	4.33	4.29
K_2O	9.50	5.05	7.89	7.91	6.18	6.27	8.55	8.91
P_2O_5	0.12	0.16	0.11	0.12	0.19	0.14	0.12	0.11
LOI	3.78	5.00	6.41	4.04	5.62	2.89	4.30	3.56
Total	99.90	99.70	99.20	99.52	99.06	99.48	99.78	99.10

E.U.: eruptive unit; BGS: black-grey scoria; WP: white pumice.
LOI: Loss On Ignition, determined by weight loss after 24 hours at 900 °C.

Table 4.5 - Average composition of glasses in FAD and TGVT juvenile clasts, determined by EMP analyses, normalized to 100 on a H_2O-free basis.

E. U.	FAD				LTGVT				UTGVT									
Sample	FAD13		FAD13-B		MG-29		MG-7		MG-1		MG-2		MG-10		MG-10/2		MG-11		MG-11/2	
Type	WP		BGS		WP		BGS		WP		WP		WP		WP		BGS		BGS	
		σ(4)*		σ(4)*		σ(5)*		σ(6)*		σ(3)*		σ(5)*		σ(5)*		σ(6)*		σ(6)*		σ(5)*
SiO_2	58.01	0.32	58.02	0.17	57.74	0.22	57.76	0.87	57.02	0.13	57.86	0.63	56.73	0.11	58.08	0.48	54.96	0.93	57.98	0.27
TiO_2	0.48	0.04	0.59	0.01	0.40	0.05	0.59	0.06	0.52	0.03	0.58	0.03	0.56	0.04	0.50	0.04	0.68	0.03	0.50	0.04
Al_2O_3	19.75	0.20	19.23	0.09	20.23	0.08	19.22	0.35	19.96	0.14	20.18	0.17	19.56	0.14	20.78	0.19	19.02	0.42	20.87	0.21
FeO	3.20	0.11	4.19	0.06	2.62	0.06	4.43	0.87	3.36	0.14	3.49	0.15	3.86	0.12	3.32	0.15	5.33	0.37	3.33	0.21
MnO	0.15	0.05	0.12	0.02	0.20	0.02	0.17	0.03	0.17	0.04	0.21	0.04	0.17	0.06	0.21	0.05	0.23	0.03	0.18	0.02
MgO	0.55	0.02	0.79	0.03	0.29	0.02	0.68	0.07	0.48	0.03	0.53	0.03	0.73	0.02	0.52	0.03	1.08	0.38	0.49	0.03
CaO	4.22	0.65	4.70	0.15	3.55	0.21	5.25	0.95	4.12	0.12	4.11	0.35	4.83	0.26	4.05	0.18	5.93	0.92	4.08	0.19
Na_2O	3.28	0.08	3.43	0.20	4.27	0.19	4.02	0.62	4.37	0.28	4.64	0.37	3.88	0.09	3.04	0.32	4.49	0.19	3.07	0.23
K_2O	9.83	0.10	8.32	0.67	9.76	0.41	7.05	0.98	9.27	0.39	7.85	0.49	8.89	0.36	8.76	0.56	6.99	0.40	8.81	0.38
SO_2	0.16	0.03	0.17	0.04	0.35	0.16	0.23	0.08	0.21	0.05	0.20	0.03	0.24	0.04	0.18	0.02	0.42	0.07	0.18	0.05
F	0.22	0.07	0.26	0.10	0.45	0.03	0.39	0.23	0.37	0.02	0.15	0.09	0.32	0.06	0.42	0.12	0.55	0.08	0.36	0.12
Cl	0.06	0.02	0.07	0.01	0.11	0.01	0.07	0.04	0.08	0.02	0.09	0.02	0.09	0.02	0.09	0.02	0.09	0.01	0.08	0.01
P_2O_5	0.09	0.02	0.11	0.02	0.03	0.02	0.14	0.03	0.07	0.04	0.11	0.04	0.14	0.02	0.05	0.04	0.23	0.04	0.07	0.03
Total	100.00		100.00		100.00		100.00		100.00		100.00		100.00		100.00		100.00		100.00	
Total**	94.26		94.56		93.86		96.54		95.50		95.17		94.06		95.11		94.36		96.01	

*1σ standard deviation; number of analyses in parentheses;

** WDS-EMP total; E.U.: eruptive unit; BGS: black-grey scoria; WP: white pumice.

Table 4.6 - Selected EMP analyses of clinopyroxenes in TGVT juvenile clasts.

E.U.	**Lower TGVT**				**Upper TGVT**									
Sample	**MG-6**	**MG-6**	**MG-7**	**MG-7**	**MG-1**	**MG-1**	**MG-2**	**MG-2**	**MG-10**	**MG-10**	**MG-11**	**MG-11**	**MG-11***	**MG-11***
Type	**WP**	**WP**	**BGS**	**BGS**	**WP**	**WP**	**WP**	**WP**	**WP**	**WP**	**BGS**	**BGS**	**BGS**	**BGS**
	core	rim	core	rim	core	rim	core	rim	core	rim	core	rim	core	rim
SiO_2	46.80	45.46	47.35	47.36	42.76	44.77	42.03	43.93	44.82	45.51	44.57	44.75	52.85	54.00
TiO_2	1.04	1.42	1.17	1.23	2.80	1.83	2.31	1.97	1.43	1.33	1.49	1.34	0.56	0.53
Al_2O_3	8.32	8.38	7.53	7.52	9.95	8.20	10.53	9.44	9.05	8.34	9.58	9.14	3.41	2.68
FeO	9.01	10.76	9.92	9.68	13.70	12.76	13.80	12.87	10.88	10.50	12.40	11.72	4.35	3.90
MnO	0.24	0.33	0.25	0.29	0.49	0.70	0.38	0.65	0.29	0.24	0.25	0.34	0.10	0.05
MgO	10.07	9.33	10.63	10.56	6.94	8.00	7.04	7.80	9.12	9.65	8.32	8.38	15.25	16.03
CaO	22.69	22.51	23.04	22.88	22.55	23.04	22.68	22.68	22.64	22.87	23.13	23.24	24.12	24.13
Na_2O	0.37	0.33	0.27	0.31	0.60	0.56	0.44	0.50	0.34	0.30	0.35	0.34	0.18	0.16
K_2O	0.02	0.04	0.03	0.05	0.02	0.06	0.00	0.00	0.09	0.02	0.03	0.00	0.02	0.02
Cr_2O_3	0.02	0.00	0.03	0.03	0.02	0.00	0.00	0.00	0.07	0.04	0.02	0.00	0.00	0.00
Total	98.58	98.56	100.22	99.91	99.83	99.92	99.21	99.84	98.73	98.80	100.14	99.25	100.84	101.50
	Cpx components calculated following Putirka et al. (1996)													
DiHd	0.75	0.75	0.77	0.77	0.73	0.79	0.73	0.74	0.74	0.76	0.75	0.77	0.87	0.88
EnFs	0.05	0.07	0.07	0.07	0.06	0.04	0.07	0.06	0.07	0.06	0.06	0.05	0.04	0.05
Jd	0.03	0.02	0.02	0.02	0.05	0.04	0.03	0.04	0.03	0.02	0.03	0.03	0.01	0.01
CaTs	0.13	0.11	0.10	0.10	0.07	0.06	0.10	0.09	0.12	0.11	0.12	0.12	0.05	0.05
CaTi	0.04	0.07	0.06	0.05	0.13	0.10	0.13	0.11	0.08	0.07	0.09	0.08	0.01	0.01
CrCaTs	0.00	0.00	0.00	0.00	0.00	0.00	0.00	0.00	0.00	0.00	0.00	0.00	0.00	0.00
Wo	51.88	51.29	50.55	50.70	52.56	52.21	52.44	52.04	51.66	51.40	52.11	52.76	49.49	48.77
En	32.04	29.58	32.46	32.56	22.51	25.23	22.65	24.91	28.96	30.18	26.08	26.47	43.54	45.08
Fs	16.08	19.13	16.99	16.74	24.93	22.57	24.91	23.05	19.38	18.42	21.80	20.77	6.97	6.15
mg-*number*	0.53	0.46	0.52	0.52	0.34	0.39	0.34	0.38	0.46	0.48	0.40	0.42	0.78	0.80

E.U.: eruptive unit; BGS: black-grey scoria; WP: white pumice; *Xenocrysts.

Table 4.7 - Selected EMP analyses of feldspars and leucite in TGVT juvenile clasts.

	Plagioclase							Sanidine							Leucite	
E.U.	**Lower TGVT**			**Upper TGVT**				**Lower TGVT**		**Upper TGVT**					**Lower TGVT**	**Upper TGVT**
Sample	**MG-7**	**MG-7**	**MG-7**	**MG-1**	**MG-2**	**MG-10**	**MG-10**	**MG-6**	**MG-6**	**MG-7**	**MG-7**	**MG-10**	**MG-10**	**MG-11**	**MG-7**	**MG-11**
Type	**BGS**	**BGS**	**BGS**	**WP**	**WP**	**WP**	**WP**	**WP**	**WP**	**BGS**	**BGS**	**WP**	**WP**	**BGS**	**BGS**	**BGS**
	core	rim						core	rim	core	rim	core	rim			
SiO_2	48.10	47.48	47.33	47.57	48.63	47.46	47.20	66.75	66.46	64.91	65.01	63.92	63.78	65.90	58.40	56.55
TiO_2	0.02	0.00	0.02	0.05	0.05	0.01	0.03	0.00	0.00	0.05	0.06	0.11	0.11	0.08	0.06	0.04
Al_2O_3	33.05	33.03	32.85	32.51	32.44	33.54	33.99	18.09	18.55	19.33	19.52	19.11	19.14	18.78	23.66	23.78
FeO	0.63	0.61	0.60	0.58	0.58	0.49	0.53	0.06	0.08	0.17	0.23	0.17	0.20	0.19	0.37	0.43
MnO	0.00	0.03	0.02	0.00	0.00	0.03	0.00	0.00	0.00	0.04	0.03	0.01	0.00	0.01	0.00	0.08
MgO	0.02	0.01	0.02	0.02	0.02	0.02	0.00	0.01	0.00	0.02	0.01	0.00	0.01	0.00	0.00	0.01
CaO	17.29	17.60	18.02	17.54	16.76	17.23	18.35	0.34	0.34	0.41	0.45	0.45	0.44	0.36	0.01	0.05
BaO	0.00	0.05	0.01	0.00	0.00	0.01	0.01	0.00	0.00	1.81	1.87	1.60	1.61	0.23	0.09	0.13
Na_2O	1.34	1.25	1.01	1.34	1.60	1.23	0.73	0.84	0.86	0.86	0.85	0.94	0.96	0.95	0.55	0.66
K_2O	0.36	0.26	0.23	0.19	0.30	0.20	0.14	14.76	14.84	13.39	13.49	13.58	13.45	14.50	16.90	19.17
Total	100.82	100.35	100.113	99.83	100.43	100.23	100.98	100.86	101.16	100.99	101.52	99.93	99.7	101.03	100.10	100.90
T-site	3.99	3.99	3.98	3.98	3.99	4.00	3.99	4.00	4.01	4.02	4.02	4.01	4.02	4.01		
A-site	0.98	0.99	0.99	1.00	0.98	0.97	0.97	0.95	0.95	0.91	0.92	0.94	0.93	0.95		
An	0.86	0.87	0.90	0.87	0.84	0.87	0.93	0.02	0.02	0.02	0.02	0.02	0.02	0.02		
Ab	0.12	0.11	0.09	0.12	0.14	0.11	0.07	0.08	0.08	0.09	0.09	0.09	0.10	0.09		
Or	0.02	0.02	0.01	0.01	0.02	0.01	0.01	0.90	0.90	0.89	0.89	0.88	0.88	0.89		

E.U.: eruptive unit; BGS: black-grey scoria; WP: white pumice.

Table 4.8 - Representative EMP analyses of juvenile clasts from major explosive eruptions of SVD, normalized to 100 on a H_2O-free basis.

Sample	MG-26		MG-27		TGPP		TGS		TBR		TPP	
Type	pumice fall		pumice fall		pumice fall		scoria		scoria		scoria	
		σ(8)		σ(8)		σ(8)		σ(8)		σ(8)		σ(8)
SiO_2	59.96	0.97	59.53	0.26	57.15	0.15	57.23	0.48	61.00	0.63	60.23	0.19
TiO_2	0.60	0.15	0.54	0.04	0.41	0.05	0.40	0.04	0.26	0.05	0.48	0.04
Al_2O_3	19.98	0.89	20.33	0.21	20.47	0.13	20.19	0.23	18.10	0.17	18.74	0.26
FeO_{tot}	3.81	1.03	3.70	0.17	2.79	0.09	2.93	0.12	2.48	0.24	3.25	0.12
MnO	0.18	0.08	0.18	0.01	0.20	0.05	0.21	0.08	0.05	0.03	0.16	0.03
MgO	0.59	0.22	0.64	0.04	0.25	0.02	0.35	0.03	1.00	0.26	0.55	0.05
CaO	5.30	0.42	4.98	0.21	3.67	0.12	3.96	0.13	4.09	0.40	3.52	0.15
Na_2O	2.59	0.33	2.49	0.12	4.05	0.15	4.09	0.27	2.62	0.12	3.64	0.44
K_2O	6.44	1.00	6.99	0.25	10.50	0.31	10.07	0.35	10.00	0.35	8.88	0.30
P_2O_5	0.10	0.05	0.11	0.06	0.03	0.02	0.05	0.03	0.30	0.09	0.06	0.02
F	0.38	0.18	0.43	0.18	0.41	0.08	0.40	0.10	0.10	0.02	0.39	0.06
Cl	0.06	0.02	0.06	0.03	0.09	0.02	0.12	0.02	0.00	0.00	0.09	0.02
Total	100.00		100.00		100.00		100.00		100.00		100.00	
Total*	95.19		95.14		93.81		93.20		95.94		93.64	

MG-26 and MG-27: pumice fall before TGVT; TGPP: Tufo Giallo di Prima Porta; TGS: Tufo Giallo di Sacrofano; TBR: Tufo di Bracciano; TPP: Tufo Pizzo Prato;

*EMP total

Table 4.9 - Bulk major element composition of juvenile clasts erupted during maar-forming eruptions, determined by XRF and EMP (sample labels as reported in table 4.2).

type	Clinopyroxenite-type	Leucite-bearing tephrite-type		Leucitite-type			Phonolite-type				
sample	UMT-1[a]	MMT-1[a]	MMT-2[b]	LCS[b]	AGU[b]	USK[a]	LMT[b]	LMT-1[b]	LMT-2[b]	MMT-3[b]	UMT-2[b]
SiO_2	50.66	50.83	49.84	52.29	48.76	54.34	56.49	56.11	53.32	55.43	55.17
TiO_2	0.65	0.90	0.75	0.93	0.87	0.63	0.32	0.46	0.55	0.57	0.31
Al_2O_3	18.16	19.30	17.34	18.67	15.97	19.69	18.47	18.73	18.76	19.26	18.10
FeO	2.23	5.22	-	2.15	2.13	4.48	-	-	-	-	-
Fe_2O_3	-	-	7.11	-	6.69	-	2.22	3.63	4.67	4.72	2.11
MnO	0.10	0.13	0.11	0.18	0.17	0.16	0.08	0.10	0.12	0.14	0.08
MgO	4.77	4.67	4.35	3.73	4.94	2.03	0.55	0.97	1.76	1.09	0.40
CaO	19.22	12.89	11.23	11.63	10.00	8.59	5.17	4.90	6.96	4.81	5.46
Na_2O	1.86	4.02	3.54	1.66	0.64	4.87	2.20	4.43	3.71	5.13	2.40
K_2O	1.59	1.74	1.88	8.63	7.91	4.57	10.37	7.54	7.67	6.30	9.92
P_2O_5	0.08	0.40	0.51	0.13	0.42	0.28	0.16	0.23	0.35	0.24	0.16
LOI	-	-	3.34	-	1.50	-	3.97	2.90	2.13	2.31	5.89
Total	99.32	100.10	100.00	100.00	100.00	99.64	100.00	100.00	100.00	100.00	100.00

[a] Bulk composition obtained by EMP analyses on glassy beads obtained by melting at 1400 °C;
[b] Bulk composition obtained by XRF analyses.

Table 4.10 - Selected EMP analyses of clinopyroxenes in juvenile clasts from maar-forming eruptions.

Type	**Clinopyroxenite type**		**Leucite-bearing tephrite type**		**Leucitite type**		**Phonolite type**	
Sample	**UMT-1**		**MMT-1**	**MMT-2**	**LCS**	**LCS**	**LMT**	**VDP-1**
SiO_2	52.23	53.88	43.04	45.11	52.46	42.92	47.69	40.54
TiO_2	0.32	0.30	2.05	1.59	0.39	1.76	0.83	1.88
Al_2O_3	1.97	1.80	8.50	6.42	2.47	10.21	5.65	9.16
FeO	3.44	3.40	11.86	11.78	3.74	11.90	9.01	17.54
MnO	0.01	0.11	0.27	0.47	0.09	0.24	0.22	1.04
MgO	16.68	17.40	9.98	9.38	16.37	9.27	11.71	4.96
CaO	23.75	23.53	23.14	23.61	24.84	23.49	23.69	22.82
Na_2O	0.18	0.18	0.45	0.56	0.14	0.43	0.25	0.69
K_2O	0.00	0.00	0.10	0.03	0.00	0.23	0.11	0.02
Cr_2O_3	0.86	0.36	0.02	0.00	0.28	0.00	0.00	0.00
Total	99.44	100.96	99.41	98.95	100.78	100.45	99.16	98.65
	Cpx components calculated following Putirka et al. (1996)							
DiHd	0.91	0.88	0.79	0.86	0.92	0.75	0.85	0.80
EnFs	0.06	0.08	0.09	0.03	0.04	0.08	0.05	0.05
Jd	0.01	0.01	0.03	0.04	0.01	0.03	0.02	0.05
CaTs	0.01	0.02	0.03	0.01	0.01	0.08	0.05	0.02
CaTi	0.03	0.02	0.15	0.12	0.04	0.14	0.07	0.17
CrCaTs	0.00	0.00	0.00	0.00	0.00	0.00	0.00	0.00
Wo	47.84	46.69	49.99	51.49	49.15	51.43	50.39	52.57
En	46.75	48.04	30.01	28.46	45.07	28.24	34.66	15.90
Fs	5.41	5.27	20.00	20.05	5.78	20.33	14.96	31.54
mg-*number*	0.83	0.84	0.46	0.44	0.81	0.44	0.57	0.22

Table 4.11 - Selected major element composition of lithic enclaves clasts obtained from EMP analyses on glassy beads obtained by melting at 1400 °C.

Type	**Type A**								**Type B**				**Type C**	
Sample	**CFL-A3**		**CFL-C3**		**CFL-C6**		**CFL-C8**		**CFL-C7**		**CFL-F6**		**TR-23**	
		σ(5)		σ(5)		σ(5)		σ(5)		σ(5)		σ(5)		σ(5)
SiO_2	52.26	0.70	50.52	0.88	48.11	0.82	51.81	0.36	50.47	0.56	48.39	0.38	53.57	3.76
TiO_2	0.83	0.14	0.85	0.06	0.77	0.14	0.93	0.04	0.99	0.12	1.40	0.04	0.89	1.04
Al_2O_3	11.98	0.17	15.84	0.72	17.72	0.33	12.70	0.15	13.37	0.11	16.83	0.15	23.30	1.43
FeO_{tot}	1.06	0.33	4.70	1.11	8.30	1.11	2.96	0.08	4.28	0.31	3.02	0.49	4.02	3.74
MgO	10.27	0.34	5.98	0.46	3.63	0.11	9.84	0.11	9.37	0.12	7.60	0.29	0.75	0.28
MnO	0.15	0.03	0.13	0.03	0.17	0.06	0.14	0.03	0.11	0.04	0.19	0.03	0.13	0.11
CaO	16.58	0.34	11.71	0.66	8.51	0.30	15.31	0.32	13.67	0.29	11.74	0.47	3.09	0.85
BaO	0.19	0.06	0.09	0.06	0.33	0.11	0.21	0.03	0.25	0.09	0.45	0.16	0.32	0.18
SrO	0.14	0.08	0.15	0.08	0.26	0.05	0.12	0.05	0.14	0.05	0.30	0.08	0.47	0.10
Na_2O	0.56	0.03	0.77	0.07	1.52	0.07	0.51	0.02	0.62	0.03	1.87	0.09	2.09	0.09
K_2O	6.01	0.18	8.92	0.49	10.58	0.49	5.43	0.12	6.81	0.12	7.86	0.29	10.94	1.09
P_2O_5	0.05	0.04	0.35	0.16	0.37	0.18	0.03	0.03	0.15	0.04	0.28	0.12	0.11	0.06
F	0.16	0.08	0.12	0.09	0.05	0.06	0.10	0.07	0.22	0.08	0.42	0.13	0.15	0.11
Cl	0.00	0.00	0.01	0.01	0.01	0.01	0.00	0.00	0.01	0.01	0.00	0.01	0.01	0.01
Total	100.26		100.14		100.34		100.09		100.47		100.35		99.85	

Table 4.12 - Selected EMP analyses of clinopyroxenes in cognate enclaves.

Type	**Type A**				**Type B**				**Type C**		**Type M**	
Sample	**CFL-A1**		**CFL-C6**		**CFL-F6**		**CFL-D1**		**CFL-F8**		**CN-7**	
	core	rim	core	rim	core	rim	core	rim	core	rim	core	rim
SiO_2	48.28	49.34	49.99	49.10	50.37	46.28	50.11	47.03	49.80	47.25	51.49	50.91
TiO_2	0.76	0.58	0.84	0.97	0.62	1.13	0.71	0.85	0.69	1.16	0.19	0.19
Al_2O_3	5.26	4.50	4.37	5.42	3.74	6.90	4.24	5.13	4.66	6.85	2.13	2.73
FeO	6.92	6.32	7.51	7.03	6.64	10.00	6.42	12.61	0.00	0.04	5.50	6.67
MnO	0.16	0.11	0.14	0.18	0.11	0.25	0.11	0.24	13.99	12.27	0.12	0.22
MgO	14.08	14.63	12.87	13.16	13.72	10.49	14.30	9.59	24.73	24.56	15.51	14.18
CaO	24.03	24.36	24.07	24.36	24.60	24.11	24.52	23.93	0.10	0.21	23.98	24.35
Na_2O	0.15	0.12	0.21	0.13	0.18	0.28	0.17	0.69	6.68	8.38	0.36	0.35
K_2O	0.01	0.01	0.02	0.01	0.00	0.00	0.00	0.01	0.13	0.24	0.00	0.02
Cr_2O_3	0.00	0.03	0.00	0.05	0.00	0.04	0.00	0.01	0.00	0.01	0.00	0.00
Total	99.64	100.00	100.01	100.41	99.98	99.48	100.57	100.10	100.80	100.95	99.29	99.63
	Cpx components calculated following Putirka et al. (1996)											
DiHd	0.86	0.88	0.88	0.86	0.91	0.84	0.89	0.89	0.88	0.84	0.92	0.93
EnFs	0.07	0.07	0.04	0.05	0.03	0.04	0.05	0.03	0.05	0.05	0.06	0.04
Jd	0.01	0.01	0.02	0.01	0.01	0.02	0.01	0.05	0.01	0.02	0.03	0.03
CaTs	0.03	0.03	0.05	0.06	0.03	0.06	0.03	0.00	0.04	0.05	0.00	0.00
CaTi	0.08	0.07	0.04	0.06	0.05	0.08	0.06	0.09	0.06	0.09	0.04	0.05
CrCaTs	0.00	0.00	0.00	0.00	0.00	0.00	0.00	0.00	0.00	0.00	0.00	0.00
Wo	49.02	49.06	50.31	50.58	50.33	51.84	49.61	50.79	50.05	50.98	48.10	49.40
En	39.97	41.00	37.44	38.03	39.06	31.38	40.26	28.32	39.40	35.44	43.29	40.03
Fs	11.02	9.93	12.25	11.39	10.60	16.78	10.14	20.89	10.55	13.58	8.61	10.56
mg-*number*	0.67	0.70	0.63	0.65	0.67	0.51	0.69	0.43	0.68	0.59	0.74	0.68

Table 4.13 - Selected EMP analyses of feldspars and leucite in cognate enclaves.

	Plagioclase				Sanidine					
Sample	**TYPE B**		**TYPE C**		**TYPE B**		**TYPE C**			
Type	**CFL-C2A**		**CFL-F6**		**CFL-F6**		**CFL-F8**		**MG-25**	
	core	rim	core	rim	core	rim	core	rim	core	rim
SiO_2	44.60	43.68	44.60	44.21	59.52	59.32	63.84	64.11	65.02	65.29
TiO_2	0.04	0.03	0.04	0.00	0.01	0.02	0.02	0.00	0.00	0.00
Al_2O_3	34.49	35.15	34.49	34.13	19.94	19.62	18.11	18.53	18.63	18.25
FeO	0.25	0.18	0.25	0.33	0.31	0.20	0.10	0.18	0.15	0.07
MnO	0.00	0.00	0.00	0.00	0.00	0.00	0.06	0.03	0.02	0.00
MgO	0.00	0.01	0.00	0.00	0.01	0.01	0.00	0.00	0.01	0.00
CaO	19.10	19.82	19.10	19.26	0.45	0.47	0.26	0.48	0.19	0.10
Na_2O	0.44	0.17	0.44	0.32	1.50	1.38	1.09	1.30	1.11	1.09
K_2O	0.05	0.03	0.05	0.00	10.69	11.31	14.02	13.58	14.72	14.90
SrO	-	-	-	-	2.65	2.28	0.65	0.97	-	-
BaO	-	-	-	-	4.83	4.95	0.92	0.35	-	-
Total	98.97	99.07	98.97	98.25	99.91	99.55	99.08	99.52	99.84	99.71
T-site	3.99	3.98	3.99	3.98	3.99	3.98	3.99	4.00	4.01	4.00
A-site	1.00	1.01	1.00	1.00	0.98	1.01	0.98	0.98	0.97	0.98
An	0.96	0.98	0.96	0.97	0.03	0.03	0.01	0.03	0.01	0.01
Ab	0.04	0.02	0.04	0.03	0.17	0.15	0.10	0.12	0.10	0.10
Or	0.00	0.00	0.00	0.00	0.80	0.82	0.88	0.85	0.89	0.90

Table 4.13 - *continued*.

Sample	Leucite									
	TYPE A				TYPE B		TYPE C		TYPE M	
Type	CFL-A3		CFL-C3		CFL-F6		CFL-F8		CN-7	
	core	rim	core	rim	core	rim	core	rim	core	rim
SiO_2	55.54	55.77	56.37	55.88	56.24	56.27	56.12	56.28	55.89	55.77
TiO_2	0.01	0.04	0.10	0.02	0.08	0.01	0.04	0.01	0.08	0.08
Al_2O_3	22.74	22.74	21.95	21.65	21.79	22.07	21.62	21.96	21.81	22.23
FeO	0.32	0.34	0.35	0.39	0.13	0.18	0.21	0.12	0.47	0.61
MnO	0.00	0.00	0.01	0.00	0.00	0.00	0.00	0.00	0.01	0.04
MgO	0.00	0.01	0.00	0.00	0.00	0.02	0.00	0.00	0.00	0.00
CaO	0.00	0.00	0.00	0.00	0.00	0.01	0.00	0.00	0.00	0.00
Na_2O	0.07	0.08	0.04	0.04	0.11	0.15	0.10	0.07	0.02	0.03
K_2O	20.78	20.44	20.57	20.78	20.71	20.63	20.95	20.73	21.23	21.18
BaO	0.06	0.06	0.05	0.02	0.10	0.00	0.08	0.00	0.00	0.04
Total	99.53	99.48	99.44	98.79	99.14	99.35	99.11	99.18	99.5	99.97

Table 4.14 - REE composition of clinopyroxenes in cognate enclaves, obtained by LAM-ICPMS.

Type	TYPE A		TYPE B						TYPE C		
Sample	CFL-A3		CFL-D1		CFL-F6		CFL-F9		CFL-F8		MG-25
		σ(3)		σ(3)		σ(4)		σ(3)		σ(3)	
La	14.87	3.55	39.66	7.13	66.07	21.46	173.00	55.59	193.50	32.4	498.07
Ce	21.58	4.34	61.77	7.11	98.18	28.95	231.06	55.51	243.60	45.23	522.33
Pr	25.09	6.58	68.36	8.51	110.12	29.01	240.95	45.32	270.89	36.31	449.09
Nd	23.75	5.35	59.44	4.13	92.99	25.55	195.43	30.65	227.03	28.15	263.57
Sm	19.68	4.17	42.52	6.73	69.41	18.17	127.51	23.36	150.78	19.75	74.03
Eu	9.66	0.35	26.87	6.73	40.18	9.42	74.03	5.03	84.70	7.18	25.59
Gd	11.25	0.61	22.14	3.71	34.31	5.17	60.67	11.76	70.45	7.26	29.97
Tb	6.53	2.45	12.86	1.82	20.47	1.36	36.75	5.16	50.95	3.18	13.34
Dy	4.43	1.32	10.48	2.29	15.27	2.98	30.83	5.73	36.72	1.69	5.89
Ho	3.60	0.45	6.69	3.24	9.34	2.37	20.66	5.15	24.28	2.2	5.78
Er	2.75	0.63	4.49	0.93	7.59	2.34	16.62	0.34	20.10	1.73	3.09
Tm	2.09	0.64	3.94	0.02	6.49	2.87	16.47	1.95	18.90	2.33	4.65
Yb	1.35	0.49	4.64	0.42	6.39	1.22	14.45	2.49	17.11	1.98	2.24
Lu	0.93	0.55	4.17	0.49	4.87	1.89	13.50	7.04	16.79	5.32	2.13

4.2 Piston cylinder experiments

High pressure and high temperature experiments have been performed to constrain differentiation and pre-eruptive conditions of SVD magmas. At this purpose, three sets of experiments were carried out. Phase equilibria experiments and thermal gradient experiments were performed to constrain differentiation, whereas H_2O-CO_2-bearing phase equilibria experiments were performed to constrain the pre-eruptive conditions of the phonolitic system. Experimental conditions and phase relationships are summarized in Tables 4.15, 4.16, 4.17.

Table 4.15 - Phase equilibria experiments performed using the SVD-0 tephri-phonolite starting material (M.te Aguzzo scoria) and ~2 wt.% H_2O.

Run	P (MPa)	T (°C)	t (h)	Phases
SVD-26	300	1100	24	G(100)
SVD-32	300	1050	24	G(100)
SVD-29	300	1000	24	G(94)+Cpx(6)
SVD-19	300	950	24	G(85)+Cpx(14)+Spl(1)
SVD-31	300	950	8	G(85)+Cpx(14)+Spl(1)
SVD-30	300	950	3	G(87)+Cpx(12)+Spl(1)
SVD-21	300	900	24	G(73)+Cpx(18)+Spl(1)+Bt(3)+Pl(5)
SVD-23	300	850	24	G(52)+Cpx(20)+Spl(1)+Bt(3)+Pl(16)+Sa(8)
SVD-18	300	800	24	G(13)+Cpx(25)+Spl(1)+Bt(3)+Pl(31)+Sa(17) +Lct(5)+Am(5)

G: Glass, Cpx: Clinopyroxene, Spl: Spinel, Bt: Biotite, Pl: Plagioclase, Sa: Sanidine, Lct: Leucite, Am: Amphibole

Table 4.16 - Thermal gradient experiments performed using the SVD-0 tephri-phonolite starting material (M.te Aguzzo scoria) and ~2 wt.% H_2O.

Run	P (MPa)	T (°C)	t (h)	length*	Phases
SVD-27	300	1050-900	24	9.5	G+Cpx+Spl+Fsp**
SVD-17	300	1000-950	24	7.2	G+Cpx+Spl
SVD-13	300	1000-900	24	10.5	G+Cpx+Spl+Pl+Sa
SVD-10	300	1000-850	24	11.0	G+Cpx+Spl+Pl+Sa
SVD-12	300	1000-850	50	9.5	G+Cpx+Spl+Pl+Sa

G: Glass, Cpx: Clinopyroxene, Spl: Spinel, Fsp: Feldspar, Pl: Plagioclase, Sa: Sanidine
* length of the capsule
** Plagioclase megacrysts with sanidine rims

Table 4.17 - Phase equilibria experiments using the TGVT-0 phonolite starting material (pumice clast from upper Tufo Giallo della Via Tiberina).

Run	P (MPa)	T (°C)	t (h)	H_2O (wt.%)*	CO_2 (wt.%)*	Phases
TGVT-1	200	850	24	3.00	-	G+Cpx+Pl+Sa
TGVT-2	200	850	24	1.50	-	G+Cpx+Pl+Sa
TGVT-3	200	900	24	2.89	-	G+Cpx+Pl+Sa
TGVT-4	200	900	24	2.12	-	G+Cpx+Pl+Sa
TGVT-5	200	900	24	3.89	0.17	G+Cpx+Pl
TGVT-6	200	900	24	3.93	0.40	G+Cpx+Pl
TGVT-7	200	900	24	3.92	-	G+Cpx+Pl
TGVT-8	200	900	24	2.63	0.11	G+Cpx+Pl+Sa
TGVT-9	200	900	24	2.92	0.35	G+Cpx+Pl+Sa
TGVT-10	200	925	24	2.47	-	G+Cpx+Pl
TGVT-11	200	925	24	5.36	-	G
TGVT-12	200	925	24	3.31	0.27	G+Cpx+Pl+Sa
TGVT-13	200	950	24	3.40	0.21	G+Cpx+Pl
TGVT-14	200	950	24	2.11	0.19	G+Cpx+Sa
TGVT-15	200	950	24	4.00	-	G

* amount of H_2O and CO_2 added in the capsule
G: Glass, Cpx: Clinopyroxene, Spl: Spinel, Bt: Biotite, Pl: Plagioclase, Sa: Sanidine

4.2.1 Starting materials

As starting material for the first two sets of experiments (phase equilibria and T-gradient experiments), a tephri-phonolitic scoria (Table 4.18) from Mt. Aguzzo scoria cone, emplaced during the activity of Sacrofano eruptive center (Sottili et al., 2010), was used. The SVD liquid line of descent is characterized by two main clusters of compositions, roughly corresponding to the effusive/strombolian activity (phono-tephrites to teprhi-phonolites) and to the explosive activity (phonolites), respectively (Figure 4.25). Magma compositions in between these two end-members are poorly represented. Notably, also lithic enclaves can be associated to two opposite magma compositions (Figure 4.22), on the basis of their mineral assemblage, respectively phono-tephritic (clinopyroxene- and leucite-rich enclaves of types A and B) and phonolitic (sanidine-rich enclaves of type C). In this frame, the Mt. Aguzzo

tephri-phonolitic composition, being an intermediate between the Roman Province parental K-basaltic magma (Conte et al., 2009) and the phonolitic magma feeding the SVD explosive eruptions, represents a suitable parental composition for phonolitic products. About 2 wt.% of deionised H_2O was added in tephri-phonolitic charges (phase equilibria and T-gradient experiments) by using a micro-syringe. This water amount is compatible with an average water content of 4-5 wt.% in the SVD phonolitic melts by assuming about 50 wt.% crystallization of initial mass (Masotta et al., 2010). The H_2O-CO_2-bearing phase equilibria experiments were carried out using as starting material a phonolitic (crystal-poor) pumice from the upper TGVT eruptive unit (Table 4.18; Figure 4.25), in order to investigate the role of volatile on phase relations and better explore the pre-eruptive condition of the crystal-poor phonolitic magma.

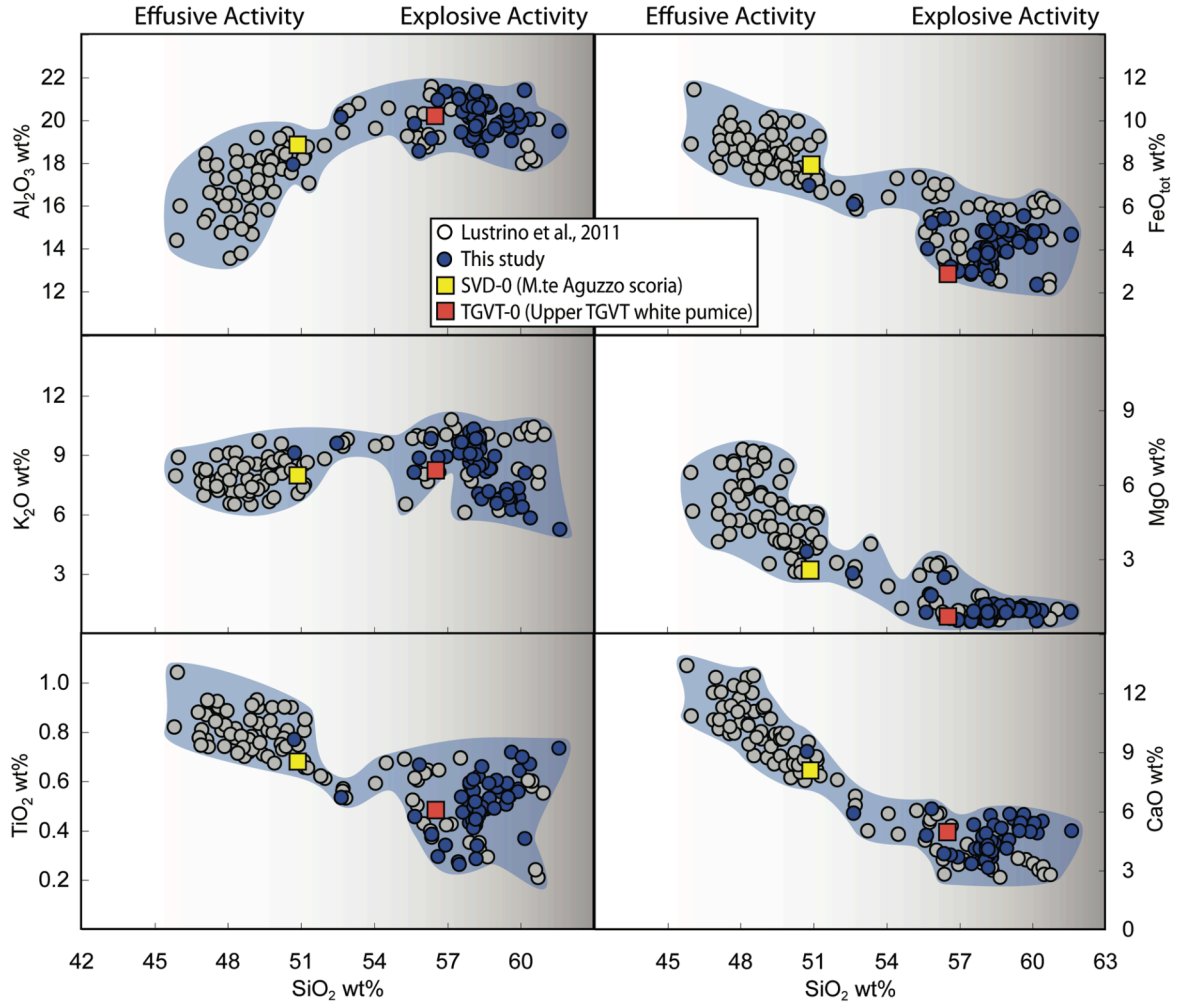

Figure 4.25 - Variation diagrams showing the Sabatini Volcanic District liquid line of descent described by natural products (grey circles: data from Lustrino et al., 2011 and references therein; blue circles: data from this study). The yellow square is M.te Aguzzo tephri-phonolitic scoria used as starting material for phase equilibria and T-gradient experiments, the red square is a phonolitic pumice from upper TGVT eruptive unit used in H_2O-CO_2-bearing phase equilibria experiments.

Table 4.18 - Chemical analyses of natural samples used as starting material in experiments normalized to 100 wt.% (XRF on bulk composition and EPMA on sintered glass).

	XRF		WDS-EPM			
	SVD-0	TGVT-0	SVD-0		TGVT-0	
			Glass*	sd(8)**	Glass*	sd(8)**
SiO_2	50.59	56.85	50.84	0.30	56.39	0.44
TiO_2	0.63	0.49	0.68	0.07	0.54	0.07
Al_2O_3	18.79	20.23	18.97	0.14	20.45	0.20
Fe_2O_3	8.13	3.60	7.91	0.17	2.86	0.54
MnO	0.14	0.26	0.17	0.03	0.16	0.06
MgO	2.34	0.66	2.31	0.05	0.78	0.09
CaO	7.34	4.28	8.11	0.09	5.64	0.50
Na_2O	2.74	4.53	2.62	0.04	4.64	0.11
K_2O	8.84	8.95	7.93	0.07	8.39	0.16
P_2O_5	0.46	0.13	0.46	0.04	0.16	0.03
LOI	0.91	4.30				
Sum	99.09	99.78	99.59		99.59	

* Glass used as starting material in experiments, obtained by melting the natural clast.
** Standard deviation, number in parenthesis refers to number of analyses

4.2.2 Phase equilibria experiments with tephri-phonolite

Textural features

Phase relationships of runs are reported in Table 4.15. The runs performed at 1100 and 1050 °C produced only glass (super-liquidus condition). In the sub-liquidus runs, crystals are idiomorphic and homogeneously distributed. Experimental products obtained at different experimental times (3, 8, and 24 hours) demonstrate that a constant crystal size of 10-12 μm is reached for time duration between 8 and 24 hours (Figure 4.26).

Crystal assemblage at sub-liquidus conditions is made up of clinopyroxene, spinel, plagioclase, mica, sanidine, leucite, and amphibole (Figures 4.27 and 4.28). Clinopyroxene is the liquidus phase (1000 °C), is ubiquitous at any investigated temperature and forms diffuse clusters in runs carried out at 1000 and 950 °C. Spinel occurs in scarce amount (≈1 vol.%) starting from 950 °C. Plagioclase appears, simultaneously with mica, at 900 °C and becomes abundant at 850 °C forming large poikilitic crystal (>100 μm) characterized by An-rich cores and Or-rich rims. At 800 °C the crystal fraction steeply increases as a consequence of multi-phase saturation of the liquid and leucite and amphibole appear on liquidus. At this temperature, the interstitial glass is scarce (as low as 13 vol.%) and feldspars prevail over clinopyroxenes.

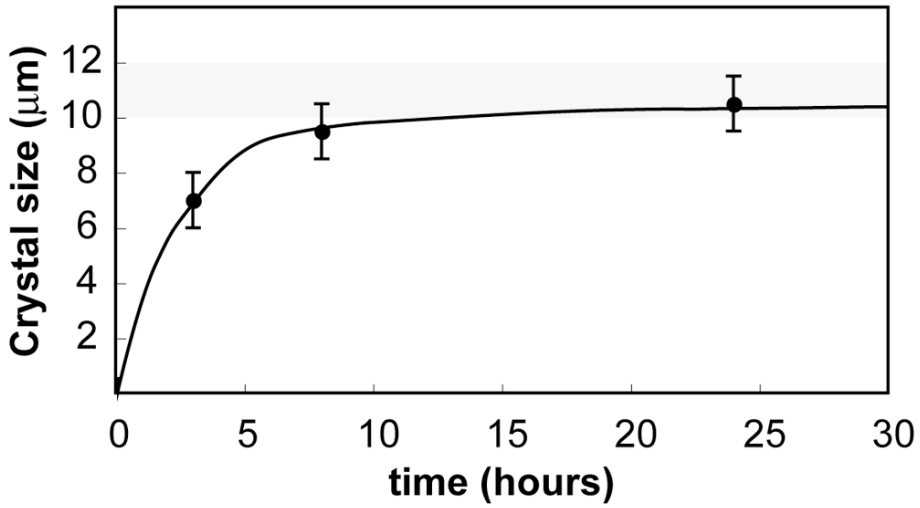

Figure 4.26 - Crystal size *vs.* time duration diagram for phase equilibria experiments performed at 950 °C using the tephri-phonolitic starting material (SVD-0). Notably, crystals obtained in the 8 hours-long run show sizes comparable with those crystallizing in the 24 hours-long experiment.

Phase compositions

In general, clinopyroxene is chemically homogeneous, showing a linear decrease of mg-*number* (0.50-0.20) with decreasing experimental temperature (Table 4.19; Figure 4.29). Plagioclase crystallizes along the cotectic with clinopyroxene below 950 °C and occurs in large, chemically zoned, poikilitic crystals (>100 μm) in low temperature runs (<900 °C). Notably, the anorthite fraction increase with temperature, ranging from An_{65} at 800 °C to An_{75} at 900 °C (Table 4.20). Sanidine (Or_{75-90}) crystallizes cotectically with the chemically zoned rim of large poikilitic plagioclase. Spinel, classified as magnetite, is characterized by a relatively low TiO_2 content (<3 wt.%). Mica shows a Mg/Fe ratio below 2, and has been classified as biotite (Table 4.20).

Glass obtained in the 1050 °C run was used as reference to estimate iron diffusion into Pt-capsule. At this temperature a maximum iron loss of about 2 wt.% (Table 4.21) was estimated by comparison with the starting glass; this implies that in runs performed under sub-liquidus condition, because of lower iron diffusivity and crystallization of FeO-bearing minerals, the loss of iron was lower than 2 wt.%. The chemical composition of the interstitial glass varies as a function of temperature and degree of crystallization, spanning from tephri-phonolite (i.e., starting material) to phonolite (Table 4.21; Figure 4.30). In particular, interstitial melt becomes phonolitic in composition (comparable to SVD major eruptions products) at 900 °C and after ~30% crystallization. In the 850 °C run, the amount of glass decreases significantly (crystallinity ~50%). The composition of this glass appears slightly silica-depleted overlapping that obtained in 900 °C run (Figure 4.30). This is most probably due to

clinopyroxene and/or plagioclase contamination during the EMP analyses. Notably, the extensive crystallization observed in low temperature runs lead to an increase of water content in glass, from the original ~2 wt.% added to the charge to about 3.5 wt% (estimated by using the "by difference" method of Devine et al., 1995; Table 4.21).

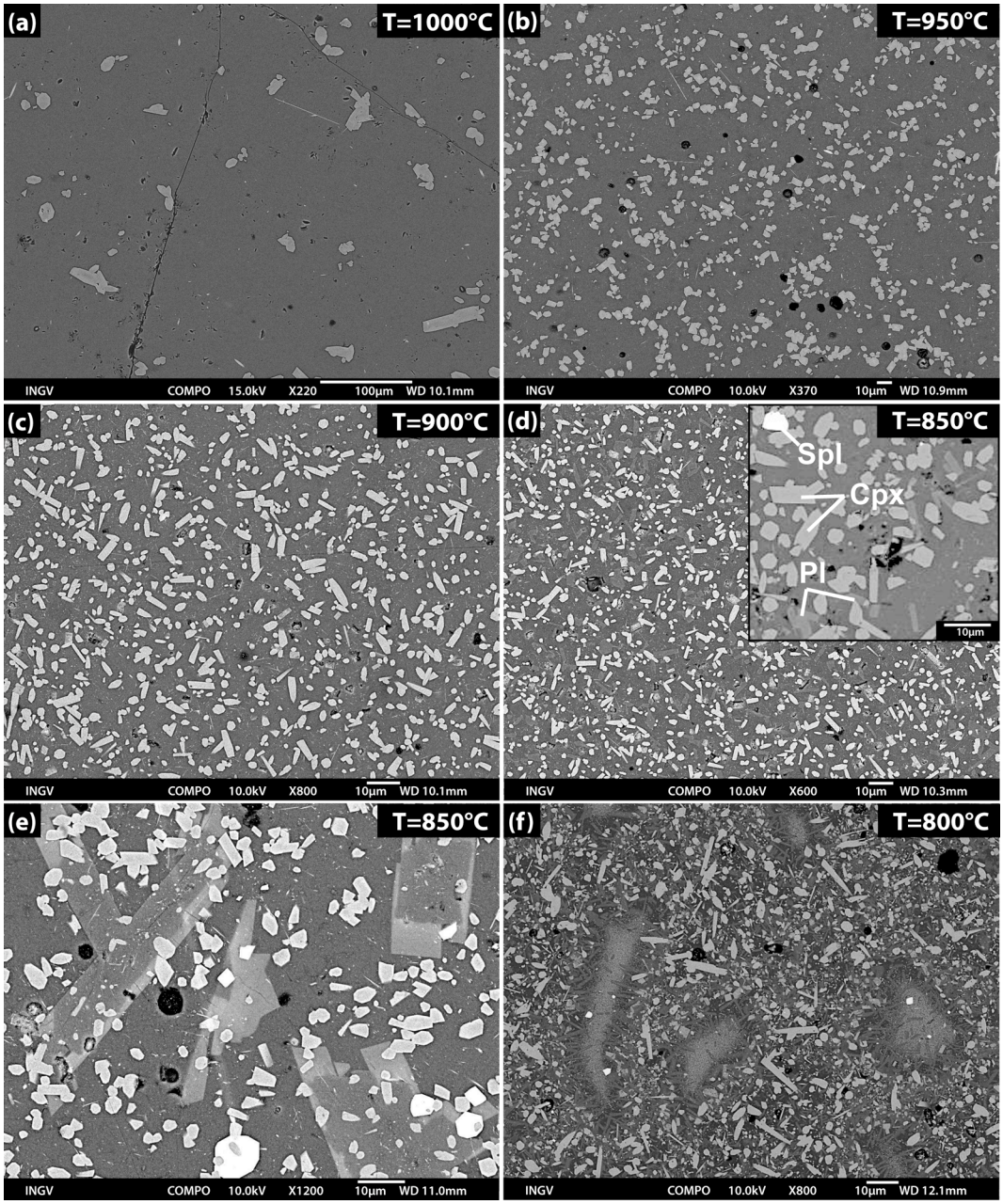

Figure 4.27 - Backscattered images of phase equilibria experiments at different temperatures. Panels show: (a) clinopyroxene crystallizing in run performed at near-liquidus temperature; (b) increase of crystallization and formation of clinopyroxene clusters; (c) and (d) further increase of crystallization at lower temperature, the inset panel in (d) illustrates in better details clinopyroxene (Cpx), spinel (Spl) and plagioclase (Pl) crystals; (e) detail of 850 °C run showing large poikilitic, chemically zoned feldspars; (f) at 800°C the interstitial glass is scarce (<15 vol.%).

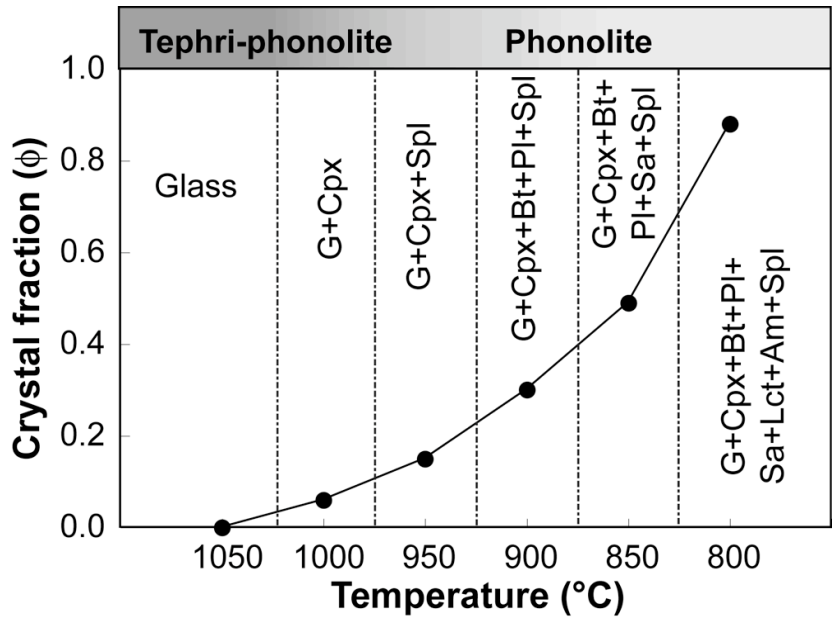

Figure 4.28 - Diagram showing phase relations in phase equilibria experiments. Note the steep increase of crystallization below 900 °C. At this temperature, the interstitial glass is phonolitic in composition.

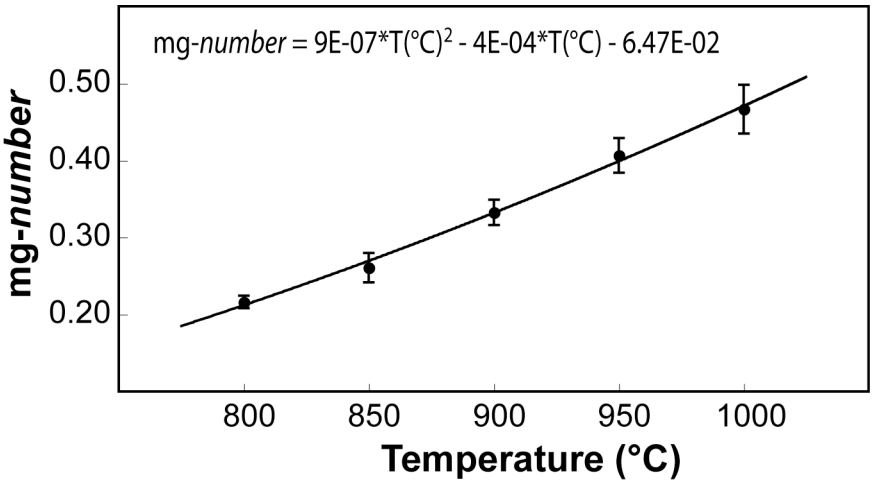

Figure 4.29 - mg-*number vs*. temperature diagram showing the chemical composition of clinopyroxenes in phase equilibria experiments.

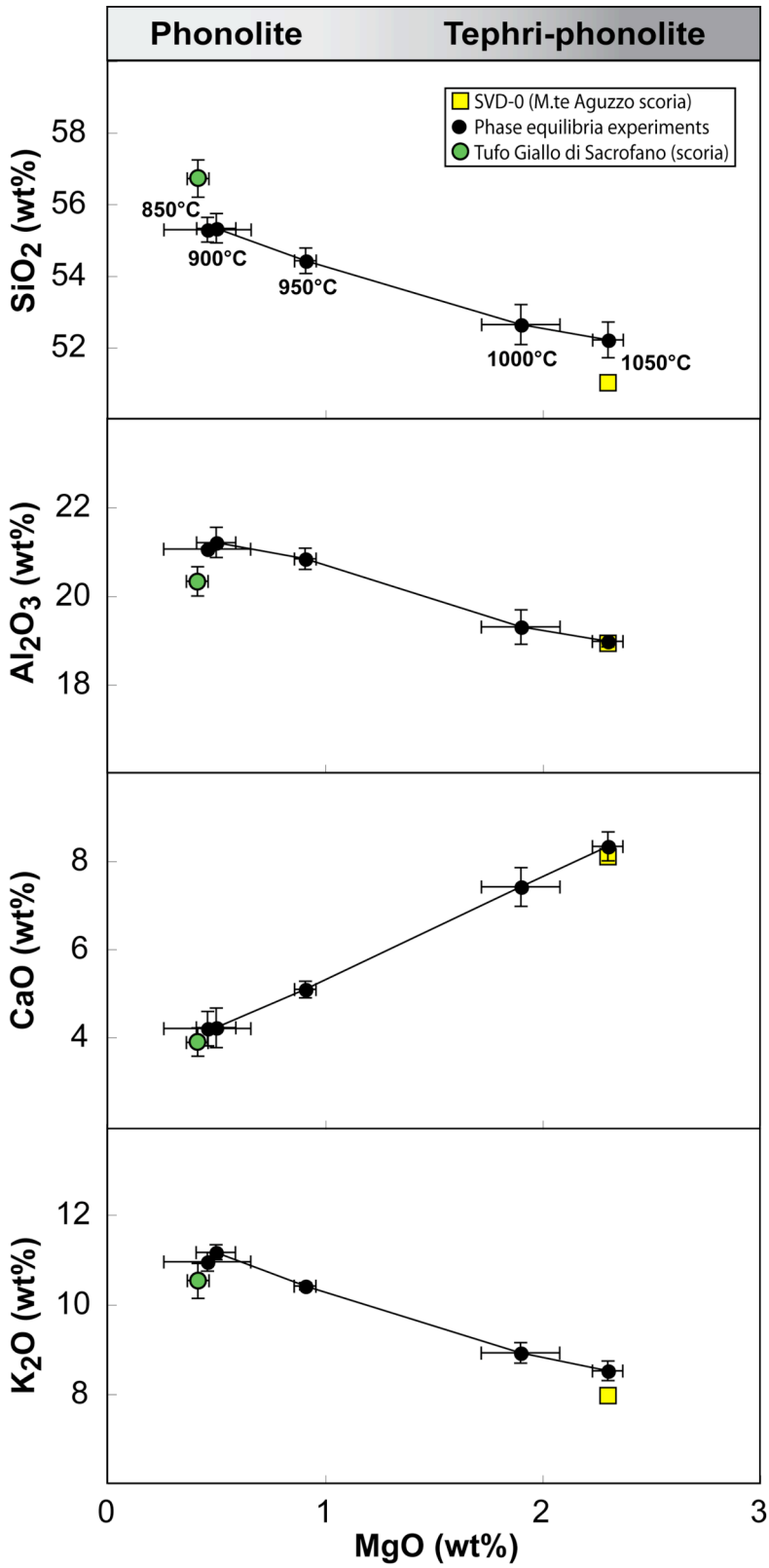

Figure 4.30 - Selected major element variation *vs*. MgO diagrams in the experimental products. Melt composition in phase equilibria (filled circles) varies as a function of temperature and degree of crystallization, spanning from tephri-phonolite to phonolite. The starting material Monte Aguzzo scoria (yellow square) and the phonolitic scoria from Tufo Giallo di Sacrofano (green circle) are reported for comparison.

4.2.3 Thermal gradient experiments

Textural features

Phase relations and crystal fraction vary within T-gradient charges, according to the temperature gradient along the furnace (Figure 4.31). Crystalline phases are idiomorphic and, as in phase equilibria experiments, show a constant size of 10-12 μm, with the exception of larger clinopyroxene and plagioclase (12-15 μm) in the near-liquidus region, and poikilitic feldspar (>100 μm) and elongated sanidine (>50 μm) in the low-temperature region. Experimental reproducibility has been constrained performing several runs in the same range of temperature and same experimental time duration and also by doubling the time duration (e.g. SVD-10 and SVD-12, and SVD-13; Table 4.16). All experimental products show comparable textures and phase relations. In particular, five zones characterized by distinct textures have been recognised (e.g., SVD-10; Figure 4.31):

Zone 1: glassy zone. The extent of this zone is controlled by the furnace hot spot (T = 1000 ± 5 °C). This is a glassy zone although phase relationships in phase equilibria experiments would have predicted clinopyroxene crystallization (see Table 4.15 and Figure 4.28). Vesicles are scarce in this zone (<1 vol.%).

Zone 2: slightly crystalline zone (PI <10 vol.%). A quasi-linear thermal gradient characterizes this zone whose extent is limited to about one millimeter. On the basis of the capsule position in the furnace and by complementary comparison with phase equilibria experiments (Figure 4.28), it is possible to infer for this zone a temperature slightly below 1000 °C. Mineral assemblage is made up exclusively of idiomorphic clinopyroxenes forming drop-shaped clusters (downward convexity). Scarce vesicles are also present (<2 vol.%). Notably, crystal clustering is known in literature as synneusis (Vogt, 1921; Vance and Gilreath, 1967) and may indicate the movement and aggregation of crystals in the melt.

Zone 3: moderately crystalline zone (PI = 10-20 vol.%). The increasing distance from the hot spot produces a significant temperature drop (~50 °C) in this 2 mm-thick zone characterized by a non-linear thermal gradient. Capsule position in the furnace and comparison with phase equilibria experiments (Figure 4.28), account for a temperature range between 975 and 950 °C. Clinopyroxene crystals are idiomorphic, moderately zoned, and grouped in clusters. Noteworthy, the clinopyroxene clustering is highly enhanced in the 50 hours-long run (Figure 4.32). Spinel, plagioclase and biotite crystallize in idiomorphic crystals, in spite of the temperature variation. Vesicularity is scarce (<2 vol.%).

Zone 4: highly crystalline zone (PI = 20-30 vol.%). This zone is about 1 mm-thick. Capsule position and phase equilibria experiments (Figure 4.28) allow us to deduce a

temperature range in this zone from 950 to 900 °C. Mineral phases (clinopyroxene + plagioclase + spinel) are prevalently idiomorphic. The interstitial glass is moderately vesiculated (2-3 vol.%).

Zone 5: heterogeneously crystallized zone (Figure 4.33). This zone spans from zone 4 up to the top of the charge. It is characterized by sharp contacts among a mushy region (PI up to 50 vol.%), a rigid crystal framework (PI = 50-80 vol.%), and glassy pockets and belts (100 μm thickness). The structure of this zone represents the experimental analogue of the theoretical "solidification front" proposed by Marsh (1996). Large poikilitic crystals of plagioclase, characterized by sharp chemical zoning (sanidine rim), occur in the mushy region whereas elongated, deformed sanidine crystals (30-50 μm) occur at the boundary between the glassy belts and the rigid crystal framework.

Phase compositions

SEM images show significant chemical zoning in feldspar and clinopyroxene crystals. Chemical analyses of large poikilitic feldspars occurring in zone 5 reveal An_{72-78} cores and Or_{73-85} rims whereas elongated sanidines are characterized by Or_{80-85} (Table 4.22) Chemical analyses of clinopyroxenes crystallizing in each zone are reported in table 4.23. Figure 4.34 shows a comparison between these clinopyroxenes and those crystallized during phase equilibria experiments.

Melt chemical composition varies from the glassy zone 1 at the bottom of the charge (hot spot zone) toward the heterogeneously crystallized zone 5 at the top (Table 4.24; Figure 4.35). In particular, glass composition ranges from tephri-phonolite in zone 1 (i.e., the starting material) to phonolite in the zone 4 (where crystal fraction approaches 30 vol.% and temperature is ~900 °C) and in the large glassy pockets and belts of zone 5. Intriguingly, the most differentiated composition (highest silica content) shown by glassy pockets and belts may provide a more accurate composition of the end of the liquid line of descent, not correctly quantifiable in phase equilibria experiments due to the very high crystallinity that prevents uncontaminated glass analyses. Although different zones show variable crystallinity, the water concentration in glasses is nearly constant around 4 wt.% (Table 4.24). This content is almost double than the initial amount of water added in the charge (2.3 wt.%) and allows to estimate a total crystal content around 40 vol.%.

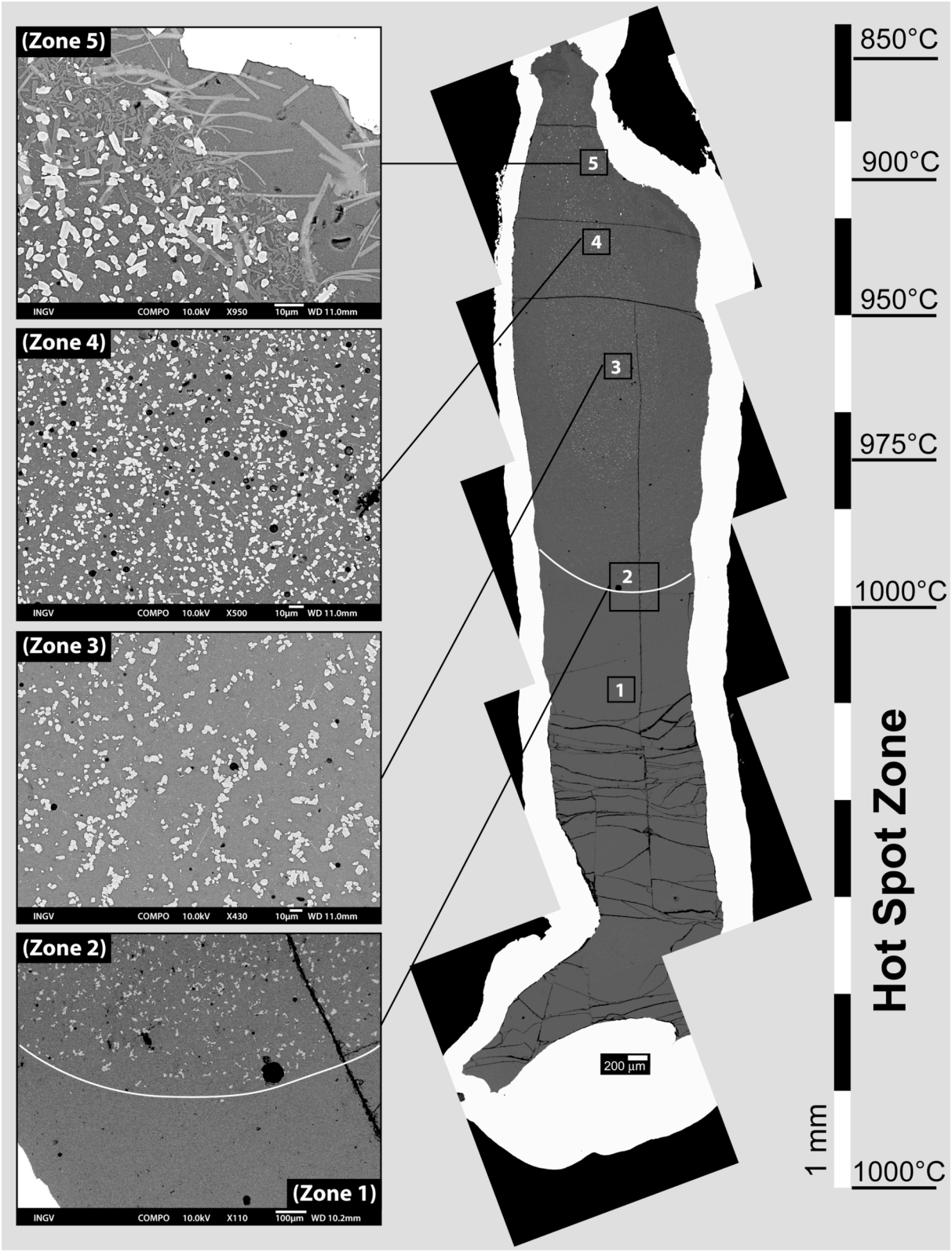

Figure 4.31 - Back-scattered images of the SVD-10 T-gradient experiment showing different zones as described in the text. Note the U-shaped boundary dividing the glassy zone 1 and the low-crystalline zone 2 (evidenced by a white line), clusters of clinopyroxenes in the low and moderately crystalline zones 2 and 3, and deformed, elongated sanidines in zone 5.

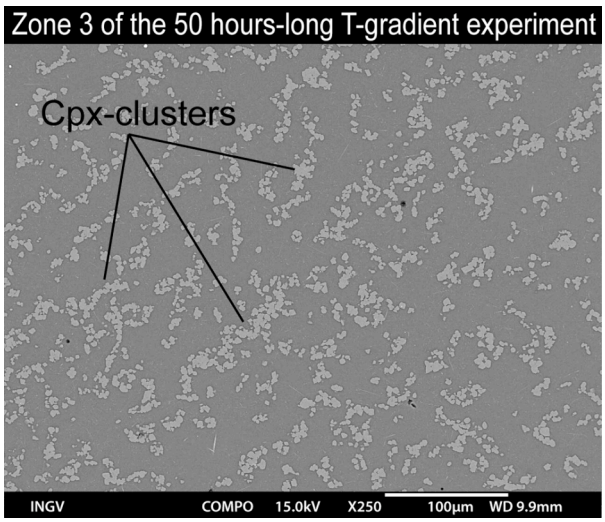

Figure 4.32 - Backscattered image of zone 3 of the 50 hours-long T-gradient experiment detailing clinopyroxene size and the formation of clusters (synneusis). Notably, clinopyroxenes from this run are comparable in size to those occurring in the 24 hours-long run.

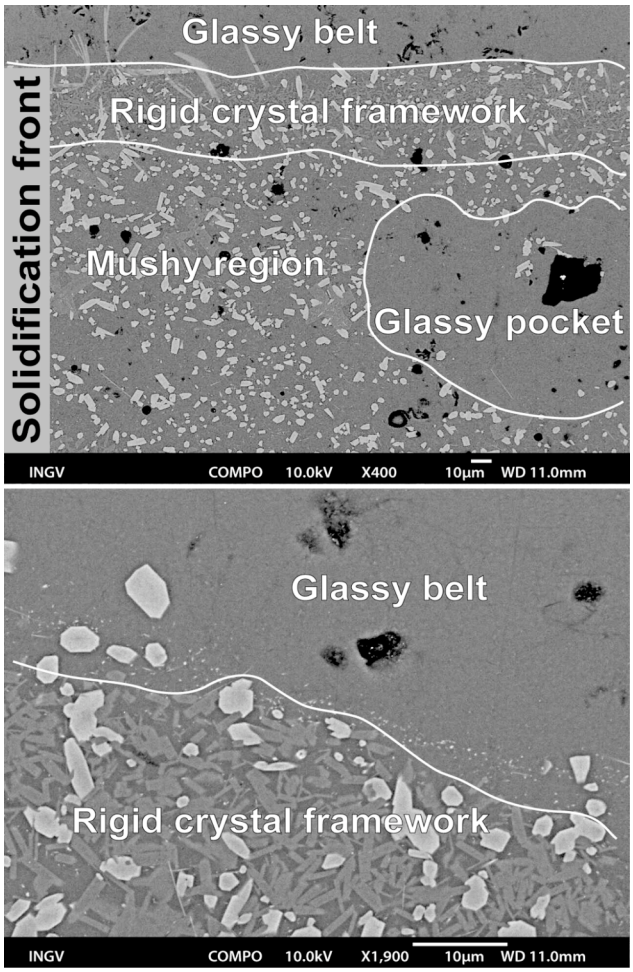

Figure 4.33 - Details (backscattered images) of the zone 5 in SVD-10 run showing the glassy belts and pockets, the clinopyroxene + feldspar touching framework (rigid crystal framework), and the underlying crystal-rich portion (mushy region). This heterogeneously crystallized zone is the experimental analogue of the theoretical "solidification front" proposed by Marsh (1996).

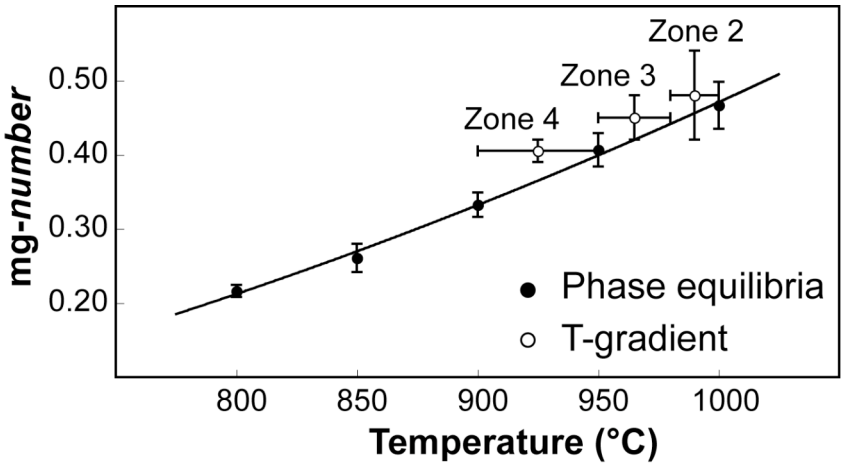

Figure 4.34 - mg-*number vs.* temperature diagram showing the chemical composition of the clinopyroxenes produced in T-gradient experiments (empty circles). Phase equilibria experimental clinopyroxenes are also reported for comparison (filled circles).

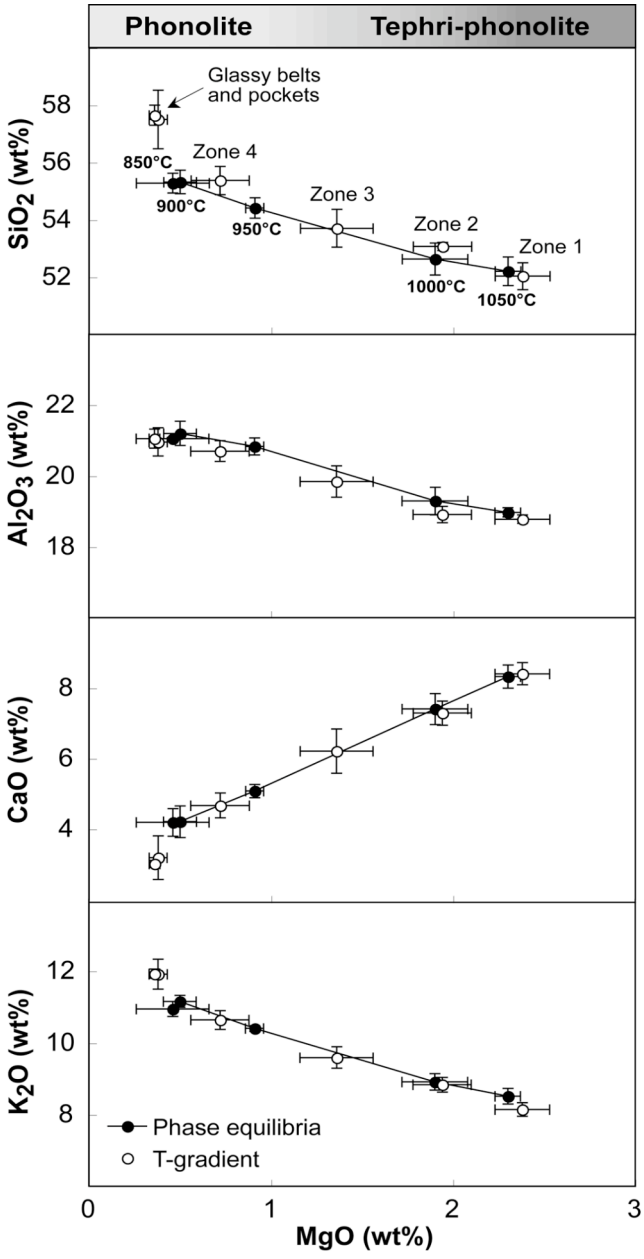

Figure 4.35 - Selected major element variation diagrams in experimental glass using MgO concentration as differentiation index. Melt composition T-gradient experiments (empty circles) varies as a function of the temperature and the degree of crystallization, spanning from tephri-phonolite (i.e., starting material) to phonolite. Chemical composition phase equilibria experiments (filled circles) are also reported for comparison; note the highest SiO_2 concentration in glassy belts and pockets, see text for further explanation.

Crystallization kinetics in T-gradient experiments

The use of glassy starting material guaranteed the absence of crystal seeds that could have grown into crystal nuclei during experimental timeframe. Both phase equilibria and T-gradient experiments show euhedral crystals of constant size (10-12 μm), indicating that kinetic equilibrium was approached in both cases (see Figures 4.27 and 4.31). The constant crystal size suggests a progressive decrease of growth rate during crystal coarsening (Figure 4.26). On this basis, a minimum growth rate of 1.16×10^{-7} mm/s has been calculated for clinopyroxene in both kinds of experiments.

Clinopyroxene crystals forming near liquidus temperature (1000-950 °C) are the largest in size (12-14 μm), indicating that a growth-dominant behaviour occurs at low degree of super-saturation (Kirkpatrick, 1981), in agreement with nucleation and growth theory, and experimental evidences (Hammer and Rutherford, 2002; Shea et al., 2009). The exceptionally large, chemically zoned, poikilitic feldspars occurring in zone 4 of T-gradient experiments could have formed in response to under-cooled conditions of the melt in this segment (Baker and Freda, 1999, 2001). Chemical zoning of feldspars forms consequently to the differentiation of melt.

Phase equilibria experimental products and zones at analogous crystallinity and temperature in T-gradient experiments show comparable textures (i.e., crystal size and shapes) thus recording similar histories of crystal nucleation and growth. In particular, crystal number density increases in T-gradient products proportionally with the increase of crystallinity, in agreement with phase equilibria products (Figure 4.28). On the basis of these evidences, it is thus possible to assess that the temperature gradient plays a minor role on the crystallization kinetics.

4.2.4 Phase relations in a H_2O+CO_2-bearing phonolitic system

Phase equilibria experiments using phonolite were carried out at 200 MPa and in the temperature range of 850-950 °C, accordingly with the pre-eruptive conditions determined for TGVT phonolitic system (Table 4.17; Masotta et al., 2010). In agreement with natural observations, clinopyroxene and feldspars dominate the mineral assemblage, being ubiquitous in all the sub-liquidus runs and varying in proportions accordingly with temperature and volatiles concentration (Figures 4.36 and 4.37).

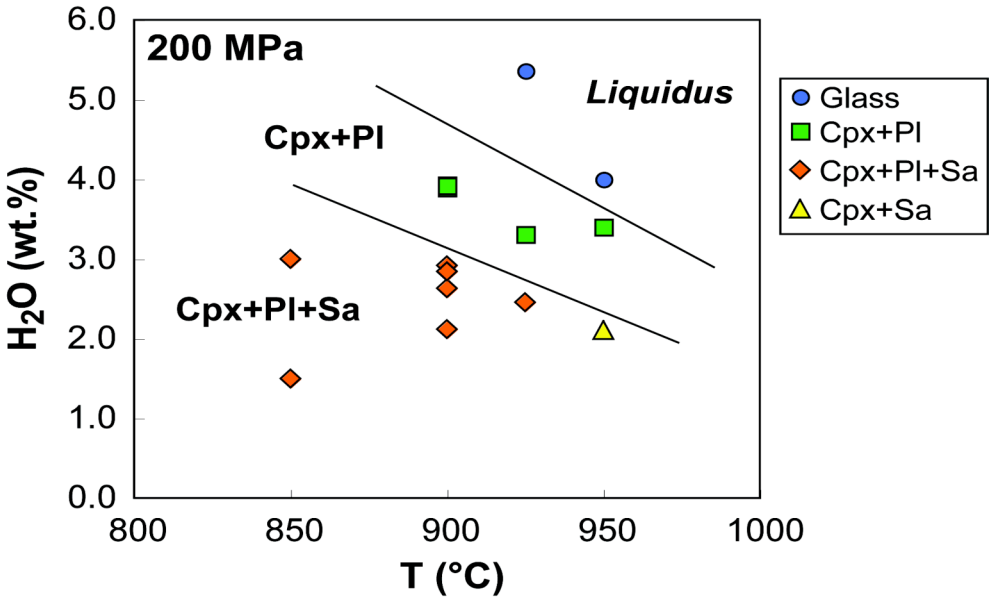

Figure 4.36 - Temperature *vs*. H_2O diagram showing phase relations at 200 MPa.

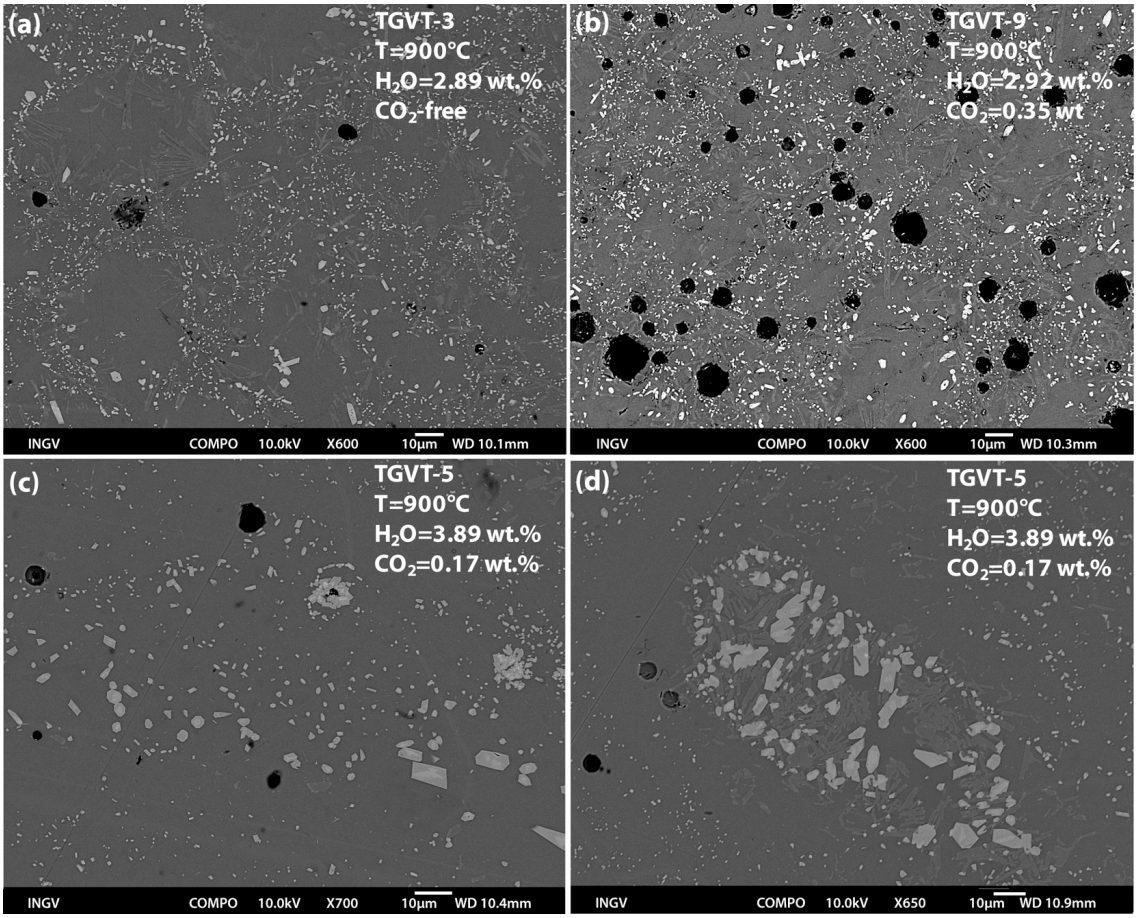

Figure 4.37 - Back-scattered images of phonolite phase equilibria experiments showing: (a) CO_2-free run at 900 °C, (b) CO_2-bearing run at same temperature and similar H_2O concentration (note the increase of crystallization of feldspars and the presence of bubbles), (c-d) CO_2-bearing run at same temperature but higher H_2O/CO_2 ratio showing clinopyroxene and clinopyroxene + plagioclase aggregates.

Textural features

Clinopyroxene and feldspars dominate the mineral assemblage of phase equilibria experiments. Apparently, the presence of CO_2 does not affect significantly the stability of the mineral phases, although small variations in phase proportions are observed in experiments with similar conditions of T and X_{H2O}, but different CO_2 concentration (Figure 4.37 a-b). Crystals are idiomorphic and range in size between 4 to 8 μm, being hence smaller and less homogeneous in size than those described in tephri-phonolite experiments. Clinopyroxene is roughly prismatic, whereas sanidine and plagioclase tend to form elongated crystals.

Experiments performed with CO_2 show textures that are slightly different than experiments with H_2O only. In some cases, mostly at higher concentrations of CO_2, experimental products are characterized by crystal aggregates of clinopyroxene and plagioclase (Figure 4.37 c-d). These structures are randomly observed throughout the charges and usually enclose melt pockets of the same composition of the surrounding glass.

Phase compositions

Clinopyroxene varies in composition accordingly with temperature and volatiles concentration. Generally the mg-*number* increases with increasing temperature and H_2O content, varying from 0.22 to 0.30 at 850 °C and from 0.47 to 0.51 at 925-950 °C (Table 4.25; Figure 4.38a). CO_2 seems not to affect significantly clinopyroxene composition, whereas mg-*number* increases with increasing H_2O (Figure 4.38b). Plagioclase ranges from An_{32} to An_{67}, whereas sanidine ranges from Or_{67} to Or_{80}, however some feldspars plot in the immiscibility field of the feldspars ternary diagram suggesting that intergrowth of plagioclase and sanidine may have occurred (Table 4.26; Figure 4.39). The composition of both feldspars shows a marked dependence on the H_2O concentration in the melt, whereas the effect of the CO_2 cannot be quantified. The variation of plagioclase and sanidine composition due to the H_2O in the melt is greater than that produced by the small temperature variations (Figure 4.40).

Experiments carried out with H_2O and CO_2 show composition of the interstitial melt varying from phonolitic to trachytic, whereas in those performed adding only H_2O, melt is always phonolitic in composition and slightly enriched in alkalies (Table 4.27).

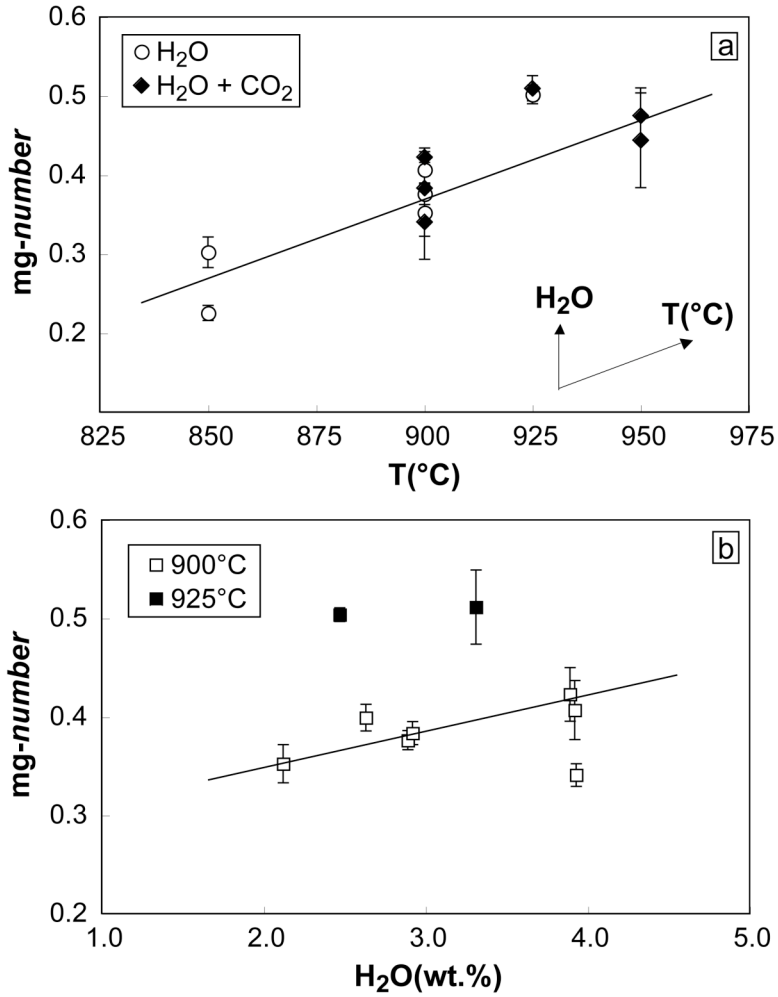

Figure 4.38 - Mg-*number* of experimental clinopyroxene plotted against temperature (°C) and H_2O (initial concentration, wt.%), showing the increasing concentration of MgO in clinopyroxene at increasing temperature (a) and/or water in the melt (b).

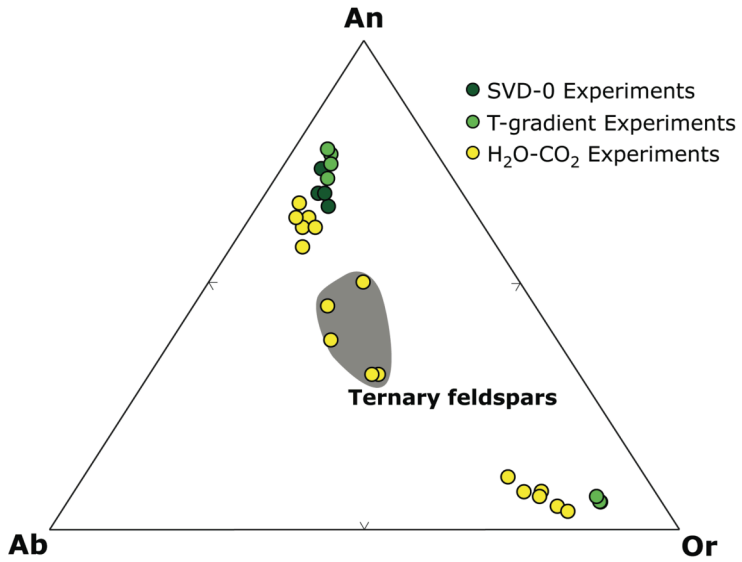

Figure 4.39 - Ternary diagram showing chemical composition of feldspars crystallized in phase equilibria and thermal gradient experiments.

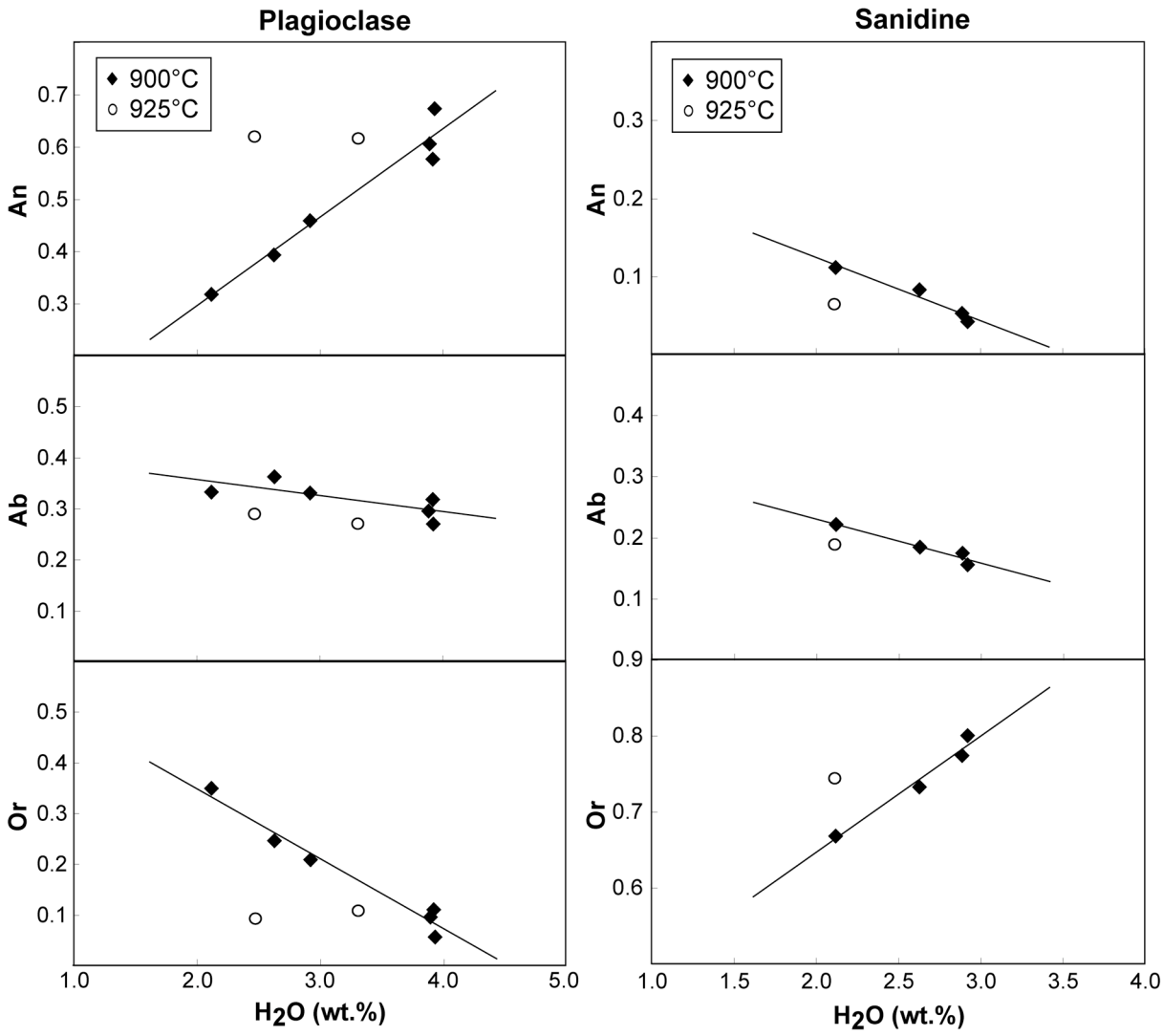

Figure 4.40 - Feldspars composition (An-Ab-Or) *vs*. H_2O diagram showing the relation between the composition of experimental feldspars and water concentration, at 900 °C and 925 °C. The actual concentration of water in the melt could not be determined by direct measurements, so the water refers to the initial concentration inserted in the capsule; this value should not be far from the real dissolved water, considering that crystallization is in general less than 30 vol.%.

Table 4.19 - Averaged EMP analyses (wt. %) of clinopyroxene in tephri-phonolite phase equilibria experiments.

Type	**SVD-29**		**SVD-19**		**SVD-21**		**SVD-23**		**SVD-18**	
Sample	**1000**		**950**		**900**		**850**		**800**	
		sd(8)*		sd(8)		sd(8)		sd(6)		sd(8)
SiO_2	43.48	1.30	43.36	0.86	42.84	0.69	40.62	0.66	39.57	0.64
TiO_2	1.32	0.23	1.44	0.15	1.50	0.07	1.53	0.09	1.70	0.15
Al_2O_3	9.18	1.05	9.41	0.98	10.75	0.37	10.28	0.49	11.54	0.29
FeO	11.36	1.03	12.65	0.37	13.25	0.68	16.76	0.42	17.17	0.24
MnO	0.20	0.04	0.25	0.03	0.26	0.02	0.38	0.05	0.39	0.05
MgO	9.90	0.46	8.30	0.63	6.89	0.25	5.49	0.18	4.74	0.19
CaO	23.44	0.20	22.87	0.07	22.24	0.34	22.55	0.23	22.33	0.25
Na_2O	0.30	0.05	0.32	0.05	0.49	0.05	0.52	0.08	0.85	0.03
K_2O	0.15	0.04	0.19	0.03	0.51	0.19	0.21	0.05	0.40	0.12
Cr_2O_3	0.01	0.01	0.01	0.02	0.01	0.01	0.01	0.01	0.00	0.00
Total	99.34		98.80		98.74		98.35		98.69	
	Cpx components calculated following Putirka et al. (1996)									
DiHd	0.77		0.75		0.70		0.75		0.72	
EnFs	0.08		0.07		0.07		0.07		0.07	
Jd	0.02		0.02		0.04		0.04		0.07	
CaTs	0.08		0.10		0.14		0.08		0.08	
CaTi	0.12		0.10		0.09		0.14		0.16	
CrCaTs	0.00		0.00		0.00		0.00		0.00	
Wo	**50.86**		**51.63**		**52.74**		**52.11**		**52.76**	
En	**29.89**		**26.08**		**22.74**		**17.66**		**15.58**	
Fs	**19.24**		**22.29**		**24.52**		**30.23**		**31.66**	
mg-*number*	**0.47**		**0.4**		**0.34**		**0.25**		**0.22**	

* standard deviation, number in parenthesis refers to number of analyses
** calculated as $MgO/(MgO+FeO_{tot})$

Table 4.20 - Averaged EMP analyses (wt. %) of feldspars and biotite in tephri-phonolite phase equilibria experiments.

Sample	SVD-21		SVD-23		SVD-18		SVD-23			SVD-21	
T(°C)	900		850		800		850			900	
	Pl	sd(5)	Pl	sd(5)	Pl	sd(5)	Pl core	Pl rim		Bt	sd(4)
SiO_2	48.94	0.84	49.99	0.91	49.30	1.65	50.21	60.82		34.44	0.24
TiO_2	0.30	0.02	0.05	0.05	0.06	0.05	0.09	0.14		3.73	0.13
Al_2O_3	31.83	0.60	31.30	0.50	30.37	1.06	31.18	21.10		16.52	0.42
FeO	0.57	0.13	0.38	0.17	0.71	0.16	0.03	0.21		15.44	1.01
MnO	0.01	0.01	0.02	0.03	0.03	0.03	0.00	0.00		0.25	0.04
MgO	0.06	0.09	0.10	0.10	0.10	0.11	0.06	0.02		13.18	1.50
CaO	14.40	0.87	13.58	0.71	13.00	1.57	13.52	1.03		0.48	0.29
Na_2O	2.20	0.13	2.44	0.21	2.43	0.42	2.38	1.00		0.28	0.02
K_2O	0.96	0.22	1.31	0.31	1.74	0.65	1.56	13.09		9.27	0.08
Cr_2O_3	0.00	0.00	0.01	0.01	0.01	0.01	0.00	0.02		0.01	0.02
Total	99.28		99.19		97.73		99.02	97.41		93.60	
T-site	**4.02**	**3.12**	**4.02**	**3.10**	**4.01**	**3.01**	**4.01**	**4.05**	Mg/Fe	**1.54**	
A-site	**0.97**	**2.78**	**0.97**	**2.97**	**0.98**	**3.31**	**0.97**	**0.93**			
An	**0.74**		**0.69**		**0.67**		**0.69**	**0.06**			
Ab	**0.20**		**0.23**		**0.23**		**0.22**	**0.10**			
Or	**0.06**		**0.08**		**0.11**		**0.09**	**0.85**			

Table 4.21 - Averaged EMP analyses (wt. %) of glasses occurring in tephri-phonolite phase equilibria experiments.

Run	**SVD-32**		**SVD-29**		**SVD-19**		**SVD-21**		**SVD-23**	
T(°C)	**1050**		**1000**		**950**		**900**		**850**	
		sd(8)*		sd(10)		sd(10)		sd(12)		sd(4)
SiO_2	52.19	0.50	52.63	0.56	54.40	0.36	55.32	0.41	55.28	0.34
TiO_2	0.75	0.07	0.73	0.10	0.50	0.06	0.41	0.07	0.30	0.06
Al_2O_3	18.97	0.13	19.29	0.39	20.83	0.24	21.20	0.34	21.05	0.04
FeO	2.98	0.18	3.12	0.21	2.16	0.06	1.51	0.13	1.51	0.13
Fe_2O_3	2.61	0.16	2.72	0.18	1.89	0.05	1.32	0.12	1.31	0.11
MnO	0.17	0.03	0.15	0.03	0.13	0.05	0.12	0.04	0.10	0.00
MgO	2.30	0.07	1.90	0.18	0.91	0.05	0.50	0.09	0.46	0.20
CaO	8.33	0.33	7.41	0.44	5.08	0.19	4.21	0.45	4.19	0.39
Na_2O	2.64	0.08	2.71	0.06	3.28	0.08	3.69	0.11	4.22	0.11
K_2O	8.51	0.22	8.91	0.23	10.40	0.08	11.16	0.17	10.95	0.21
P_2O_5	0.54	0.03	0.43	0.05	0.41	0.17	0.56	0.20	0.63	0.14
Total	100.00		100.00		100.00		100.00		100.00	
Total**	97.87		98.00		97.78		97.11		96.52	
H_2O***	2.13		2.00		2.22		2.89		3.48	

* standard deviation, number in parenthesis refers to number of analyses
** EMP total
*** H_2O estimates “by difference” 100-EPM total (Devine et al., 1995)

Table 4.22 - Representative EMP analyses of feldspars in T-gradient experiment SVD-10.

Zone	3		4		4	
	Pl	Pl	Pl	Sa	Pl core	Sa rim
SiO_2	47.57	47.11	47.01	59.94	49.84	59.60
TiO_2	0.13	0.00	0.10	0.15	0.09	0.07
Al_2O_3	32.48	31.87	30.68	22.18	31.90	21.52
FeO	0.77	0.87	0.65	0.58	0.00	0.59
MnO	0.07	0.00	0.01	0.00	0.04	0.00
MgO	0.02	0.11	0.41	0.03	0.06	0.04
CaO	14.79	15.60	14.34	0.99	13.90	1.35
Na_2O	1.84	1.86	1.90	1.00	2.12	1.02
K_2O	0.91	0.86	1.12	12.69	1.33	12.85
Cr_2O_3	0.00	0.00	0.04	0.00	0.03	0.00
Total	98.57	98.27	96.24	97.54	99.30	97.03
T-site	**4.03**	**4.00**	**3.99**	**4.07**	**4.02**	**4.05**
A-site	**0.96**	**1.00**	**0.98**	**0.90**	**0.95**	**0.94**
An	**0.77**	**0.78**	**0.75**	**0.06**	**0.72**	**0.07**
Ab	**0.17**	**0.17**	**0.18**	**0.10**	**0.20**	**0.10**
Or	**0.06**	**0.05**	**0.07**	**0.84**	**0.08**	**0.83**

Table 4.23 - Representative EMP analyses of clinopyroxene in T-gradient experiment SVD-10.

Zone	**2**		**3**		**4**	
SiO_2	48.17	43.47	46.04	42.57	41.89	39.58
TiO_2	0.84	1.42	1.49	1.69	1.36	1.50
Al_2O_3	5.74	9.43	9.04	11.36	10.19	11.24
FeO	9.75	12.42	10.06	11.79	12.39	13.10
MnO	0.21	0.21	0.23	0.26	0.23	0.20
MgO	11.29	8.97	9.46	8.40	9.15	8.42
CaO	23.41	22.82	22.69	22.09	23.28	23.06
Na_2O	0.22	0.30	0.30	0.33	0.25	0.38
K_2O	0.14	0.20	0.53	0.76	0.26	0.16
Cr_2O_3	0.00	0.00	0.03	0.03	0.00	0.01
Total	99.77	99.24	99.87	99.28	99.00	97.65
	Cpx components calculated following Putirka et al. (1996)					
DiHd	0.83	0.74	0.73	0.67	0.75	0.74
EnFs	0.06	0.09	0.06	0.10	0.09	0.10
Jd	0.02	0.02	0.02	0.02	0.02	0.03
CaTs	0.07	0.10	0.13	0.14	0.09	0.08
CaTi	0.05	0.11	0.06	0.10	0.14	0.17
CrCaTs	0.00	0.00	0.00	0.00	0.00	0.00
Wo	**50.10**	**50.72**	**51.91**	**51.39**	**50.96**	**51.24**
En	**33.62**	**27.74**	**30.12**	**27.20**	**27.87**	**26.04**
Fs	**16.28**	**21.54**	**17.97**	**21.41**	**21.17**	**22.72**
mg-*number*	**0.54**	**0.42**	**0.48**	**0.42**	**0.42**	**0.39**

Table 4.24 - EMP analyses (wt. %) of glasses occurring in T-gradient experiment SVD-10.

Zone	1		2		3		4		Pockets		Belts	
		sd(6)*		sd(9)		sd(6)		sd(6)		sd(4)		sd(5)
SiO_2	52.03	0.47	53.07	0.14	53.70	0.66	55.37	0.49	57.50	1.02	57.65	0.35
TiO_2	0.67	0.07	0.73	0.09	0.63	0.08	0.47	0.11	0.38	0.08	0.40	0.06
Al_2O_3	18.78	0.12	18.91	0.23	19.84	0.44	20.70	0.29	20.96	0.40	21.05	0.27
FeO	3.30	0.12	3.05	0.05	2.67	0.22	2.02	0.25	1.01	0.54	1.14	0.07
Fe_2O_3	2.88	0.10	2.67	0.05	2.33	0.19	1.76	0.22	0.89	0.47	0.99	0.06
MnO	0.17	0.04	0.14	0.02	0.16	0.05	0.10	0.05	0.12	0.01	0.12	0.02
MgO	2.38	0.15	1.94	0.16	1.36	0.20	0.72	0.16	0.38	0.05	0.36	0.03
CaO	8.41	0.31	7.29	0.34	6.21	0.63	4.67	0.35	3.19	0.62	3.01	0.10
Na_2O	2.76	0.05	2.85	0.04	3.01	0.10	3.19	0.04	3.30	0.02	3.28	0.08
K_2O	8.14	0.19	8.83	0.20	9.59	0.30	10.64	0.26	11.92	0.42	11.93	0.13
P_2O_5	0.48	0.04	0.52	0.04	0.50	0.27	0.36	0.18	0.35	0.44	0.07	0.02
Total	100.00		100.00		100.00		100.00		100.00		100.00	
Total**	95.68		96.01		95.52		95.65		95.07		95.32	
H_2O***	4.32		3.99		4.48		4.35		4.93		4.68	
ϕ	0		0-10		10-20		30-40		0		0	

* standard deviation, number in parenthesis refers to number of analyses
** EMP total
*** H_2O estimates “by difference” 100-EPM total (Devine et al., 1995)
ϕ Crystal content (vol. %).

Table 4.25 - Averaged EMP analyses (wt. %) of clinopyroxene in H_2O-CO_2-bearing phonolite phase equilibria experiments.

Sample	**TGVT-1**		**TGVT-2**		**TGVT-3**		**TGVT-4**		**TGVT-5**		**TGVT-6**		**TGVT-7**	
T(°C)	**850**		**850**		**900**		**900**		**900**		**900**		**900**	
H_2O	**3**		**1.5**		**2.89**		**2.12**		**3.89**		**3.93**		**3.92**	
CO_2	**-**		**-**		**-**		**-**		**0.17**		**0.4**		**-**	
		sd(8)*		sd(8)		sd(8)		sd(8)		sd(8)		sd(8)		sd(8)
SiO_2	41.70	0.15	41.96	1.06	43.74	0.99	43.86	0.95	44.18	0.84	42.08	0.66	44.31	0.43
TiO_2	1.64	0.42	2.29	0.35	2.16	0.50	1.54	0.31	1.54	0.31	1.62	0.06	1.56	0.01
Al_2O_3	9.73	1.54	8.72	1.21	8.36	0.93	9.27	1.13	7.74	0.49	10.43	0.64	8.97	0.91
FeO	14.28	0.55	16.63	0.43	12.44	0.15	13.15	0.64	12.00	0.21	13.46	1.04	11.19	0.16
MnO	0.52	0.04	0.73	0.06	0.45	0.01	0.51	0.07	0.41	0.03	0.43	0.10	0.40	0.12
MgO	6.19	0.48	4.84	0.28	7.50	0.44	7.16	0.69	8.79	0.10	6.96	0.97	7.68	0.76
CaO	22.08	0.24	21.68	0.28	22.57	0.39	22.60	0.49	22.47	0.55	23.64	0.12	21.91	0.20
Na_2O	0.45	0.14	0.82	0.09	0.49	0.02	0.59	0.03	0.47	0.02	0.49	0.03	0.57	0.04
K_2O	0.23	0.11	0.30	0.09	0.22	0.02	0.33	0.16	0.17	0.06	0.14	0.03	0.47	0.30
Cr_2O_3	0.11	0.06	0.03	0.03	0.01	0.02	0.00	0.00	0.02	0.02	0.00	0.00	0.12	0.10
Total	96.93		98.00		97.94		99.00		97.80		99.27		97.17	
	Cpx components calculated following Putirka et al. (1996)													
DiHd	0.74		0.76		0.78		0.76		0.79		0.77		0.74	
EnFs	0.06		0.05		0.04		0.05		0.06		0.04		0.04	
Jd	0.04		0.06		0.04		0.04		0.04		0.04		0.04	
CaTs	0.11		0.04		0.07		0.10		0.06		0.10		0.12	
CaTi	0.11		0.13		0.10		0.09		0.10		0.13		0.07	
CrCaTs	0.00		0.00		0.00		0.00		0.00		0.00		0.00	
Wo	**52.77**		**52.37**		**52.84**		**52.77**		**50.99**		**53.93**		**53.01**	
En	**20.59**		**16.27**		**24.43**		**23.26**		**27.76**		**22.10**		**25.86**	
Fs	**26.64**		**31.36**		**22.73**		**23.97**		**21.25**		**23.97**		**21.13**	
mg-*number*	**0.30**		**0.23**		**0.38**		**0.35**		**0.42**		**0.34**		**0.41**	

* standard deviation, number in parenthesis refers to number of analyses

Table 4.25 - *continued*.

Sample	**TGVT-8**		**TGVT-9**		**TGVT-10**		**TGVT-12**		**TGVT-13**		**TGVT-14**	
T(°C)	**900**		**900**		**925**		**925**		**950**		**950**	
H_2O	**2.63**		**2.92**		**2.47**		**3.31**		**3.4**		**2.11**	
CO_2	**0.11**		**0.35**		**-**		**0.27**		**0.21**		**0.19**	
		sd(8)*		sd(8)		sd(8)		sd(8)		sd(8)		sd(8)
SiO_2	44.82	0.57	43.57	0.48	46.25	0.55	46.24	0.96	43.53	0.51	46.90	0.79
TiO_2	1.73	0.31	1.78	0.34	1.39	0.18	1.24	0.28	1.06	0.31	1.19	0.09
Al_2O_3	8.55	0.89	8.11	0.26	7.16	0.70	6.32	0.84	9.76	0.29	5.83	0.88
FeO	12.54	0.39	12.55	0.40	9.72	0.30	9.53	0.21	11.60	0.46	10.72	0.72
MnO	0.46	0.04	0.51	0.11	0.40	0.04	0.36	0.04	0.28	0.13	0.49	0.06
MgO	8.33	0.43	7.83	1.01	9.87	0.25	9.99	0.43	9.26	0.56	9.71	0.75
CaO	23.04	0.34	22.53	0.40	22.89	0.33	23.26	0.25	23.49	0.46	22.34	0.30
Na_2O	0.56	0.08	0.54	0.05	0.50	0.04	0.38	0.08	0.51	0.05	0.47	0.06
K_2O	0.23	0.09	0.18	0.04	0.32	0.14	0.19	0.01	0.19	0.02	0.18	0.03
Cr_2O_3	0.00	0.00	0.03	0.05	0.03	0.03	0.03	0.05	0.00	0.01	0.01	0.02
Total	100.27		97.65		98.54		97.54		99.67		97.85	
	Cpx components calculated following Putirka et al. (1996)											
DiHd	0.78		0.79		0.80		0.84		0.77		0.82	
EnFs	0.05		0.05		0.04		0.03		0.07		0.05	
Jd	0.04		0.04		0.04		0.03		0.04		0.04	
CaTs	0.07		0.06		0.07		0.06		0.09		0.06	
CaTi	0.10		0.11		0.07		0.07		0.12		0.06	
CrCaTs	0.00		0.00		0.00		0.00		0.00		0.00	
Wo	**51.87**		**52.13**		**51.77**		**52.15**		**51.71**		**50.52**	
En	**26.10**		**25.21**		**31.07**		**31.17**		**28.36**		**30.56**	
Fs	**22.03**		**22.66**		**17.16**		**16.68**		**19.93**		**18.92**	
mg-*number*	**0.40**		**0.38**		**0.50**		**0.51**		**0.44**		**0.48**	

* standard deviation, number in parenthesis refers to number of analyses

Table 4.26 - Averaged EMP analyses (wt. %) of feldspars in H_2O-CO_2-bearing phonolite phase equilibria experiments.

Sample	**TGVT-1**		**TGVT-2**		**TGVT-3**				**TGVT-4**				**TGVT-5**	
T(°C)	**850**		**850**		**900**				**900**				**900**	
H_2O	**3.00**		**1.50**		**2.89**				**2.12**				**3.89**	
CO_2	**-**		**-**		**-**				**-**				**0.17**	
	sanidine		**plagioclase**		**plagioclase**		**sanidine**		**plagioclase**		**sanidine**		**plagioclase**	
		sd(8)*		sd(8)		sd(8)		sd(8)		sd(8)		sd(8)		sd(8)
SiO_2	60.77	0.72	49.87	1.21	62.22	0.04	58.24	0.34	58.31	0.81	60.78	1.30	50.76	0.50
TiO_2	0.13	0.09	0.08	0.12	0.10	0.07	0.21	0.09	0.14	0.04	0.19	0.10	0.09	0.07
Al_2O_3	20.29	0.25	30.53	0.78	20.07	0.27	24.04	0.09	24.72	0.90	20.72	0.83	29.17	0.42
FeO	0.54	0.12	0.81	0.34	0.31	0.04	0.96	0.37	0.65	0.23	0.73	0.52	0.72	0.16
MnO	0.02	0.04	0.02	0.03	0.01	0.01	0.01	0.01	0.01	0.01	0.01	0.02	0.04	0.04
MgO	0.02	0.02	0.03	0.02	0.00	0.00	0.04	0.05	0.04	0.02	0.05	0.04	0.05	0.05
CaO	1.49	0.19	12.78	1.49	0.99	0.32	6.16	0.14	6.41	1.26	2.18	1.12	11.95	0.85
SrO	-	-	-	-	-	-	-	-	0.68	0.14	0.57	0.09	-	-
Na_2O	2.26	0.19	2.98	0.44	1.82	0.03	3.47	0.16	3.72	0.39	2.40	0.29	3.23	0.23
K_2O	11.50	0.66	1.56	0.72	12.30	0.16	5.79	0.07	5.90	1.45	11.02	1.32	1.61	0.43
P_2O_5	0.04	0.02	0.01	0.01	0.06	0.04	0.06	0.00	0.00	0.00	0.00	0.00	0.03	0.03
Total	97.05		98.67		97.87		98.98		100.59		98.66		97.65	
T.site	4.02		4.02		4.03		4.02		4.01		4.02		4.01	
A-site	0.98		1.00		0.95		0.95		0.99		0.99		0.99	
An	**0.08**		**0.64**		**0.05**		**0.32**		**0.32**		**0.11**		**0.61**	
Ab	**0.21**		**0.27**		**0.17**		**0.32**		**0.33**		**0.22**		**0.30**	
Or	**0.71**		**0.09**		**0.77**		**0.36**		**0.35**		**0.67**		**0.29**	

* standard deviation, number in parenthesis refers to number of analyses

Table 4.26 - *continued*.

Sample	**TGVT-6**		**TGVT-7**		**TGVT-8**				**TGVT-9**				**TGVT-10**	
T(°C)	**900**		**900**		**900**				**900**				**925**	
H_2O	**3.93**		**3.92**		**2.63**				**2.92**				**2.47**	
CO_2	**0.40**		**-**		**0.11**				**0.35**				**-**	
	plagioclase		**plagioclase**		**plagioclase**		**sanidine**		**plagioclase**		**sanidine**		**plagioclase**	
		sd(8)*		sd(8)		sd(8)		sd(8)		sd(8)		sd(8)		sd(8)
SiO_2	50.03	0.57	52.29	0.65	56.15	0.44	62.31	0.77	53.80	1.54	61.70	0.90	51.93	0.73
TiO_2	0.03	0.02	0.07	0.08	0.20	0.10	0.14	0.02	0.12	0.12	0.15	0.04	0.07	0.05
Al_2O_3	31.79	0.42	29.03	1.17	25.88	1.12	20.44	0.73	26.71	1.04	19.93	0.32	29.94	0.98
FeO	0.81	0.12	0.83	0.16	1.05	0.51	0.66	0.06	0.89	0.10	0.30	0.04	0.71	0.12
MnO	0.02	0.02	0.04	0.03	0.04	0.03	0.03	0.01	0.08	0.00	0.01	0.01	0.02	0.03
MgO	0.03	0.02	0.09	0.02	0.12	0.06	0.07	0.06	0.14	0.02	0.03	0.03	0.05	0.04
CaO	13.43	0.37	11.90	0.50	7.76	0.93	1.61	0.61	9.07	1.14	0.83	0.22	12.20	0.50
SrO	0.78	0.07	-	-	0.68	0.26	0.61	0.25	-	-	-	-	-	-
Na_2O	2.99	0.15	3.60	0.13	3.94	0.23	1.97	0.19	3.60	0.00	1.65	0.09	3.19	0.10
K_2O	0.94	0.16	1.91	0.57	4.05	0.88	11.85	0.71	3.47	0.79	12.83	0.40	1.54	0.51
P_2O_5	0.00	0.00	0.03	0.02	0.00	0.00	0.00	0.00	0.06	0.00	0.05	0.08	0.00	0.00
Total	100.84		99.77		99.86		99.69		97.95		97.47		99.63	
T.site	4.03		4.00		4.02		4.02		4.01		4.03		4.02	
A-site	0.98		1.02		0.97		0.96		0.99		0.96		0.97	
An	**0.67**		**0.58**		**0.39**		**0.08**		**0.46**		**0.04**		**0.62**	
Ab	**0.27**		**0.31**		**0.36**		**0.18**		**0.33**		**0.16**		**0.29**	
Or	**0.06**		**0.11**		**0.25**		**0.73**		**0.21**		**0.80**		**0.09**	

* standard deviation, number in parenthesis refers to number of analyses

Table 4.26 - *continued*.

Sample	**TGVT-10**		**TGVT-12**		**TGVT-13**		**TGVT-14**	
T(°C)	**925**		**925**		**950**		**950**	
H_2O	**2.47**		**3.31**		**3.40**		**2.11**	
CO_2	**-**		**0.27**		**0.21**		**0.19**	
	plagioclase		**plagioclase**		**plagioclase**		**sanidine**	
		sd(8)*		sd(8)		sd(8)		sd(8)
SiO_2	51.93	0.73	50.29	0.59	51.77	1.02	60.44	0.55
TiO_2	0.07	0.05	0.08	0.00	0.05	0.02	0.12	0.03
Al_2O_3	29.94	0.98	29.79	1.04	30.22	0.47	19.52	0.16
FeO	0.71	0.12	0.75	0.09	1.10	0.19	0.46	0.11
MnO	0.02	0.03	0.01	0.01	0.03	0.03	0.02	0.03
MgO	0.05	0.04	0.09	0.08	0.04	0.03	0.03	0.00
CaO	12.20	0.50	12.37	0.59	12.98	0.64	1.24	0.26
SrO	-	-	-	-	0.76	0.05	-	-
Na_2O	3.19	0.10	3.01	0.04	3.19	0.19	2.00	0.03
K_2O	1.54	0.51	1.85	0.40	1.20	0.36	11.86	0.20
P_2O_5	0.00	0.00	0.01	0.01	0.00	0.00	0.01	0.01
Total	99.63		98.24		101.34		95.68	
T-site	4.02		4.01		4.01		4.02	
A-site	0.97		1.00		1.00		0.98	
An	**0.62**		**0.62**		**0.64**		**0.07**	
Ab	**0.29**		**0.27**		**0.29**		**0.19**	
Or	**0.09**		**0.11**		**0.07**		**0.74**	

* standard deviation, number in parenthesis refers to number of analyses

Table 4.27 - Averaged EMP analyses (wt. %) of glasses in H_2O-CO_2-bearing phonolite phase equilibria experiments, normalized to 100 on a H_2O-free the basis.

Sample	**TGVT-1**		**TGVT-2**		**TGVT-3**		**TGVT-4**		**TGVT-5**		**TGVT-6**		**TGVT-7**		**TGVT-8**	
T(°C)	**850**		**850**		**900**		**900**		**900**		**900**		**900**		**900**	
H_2O	**3.00**		**1.50**		**2.89**		**2.12**		**3.89**		**3.93**		**3.92**		**2.63**	
CO_2	**-**		**-**		**-**		**-**		**0.17**		**0.40**		**-**		**0.11**	
		sd(8)*		sd(8)		sd(8)		sd(8)		sd(8)		sd(8)		sd(8)		sd(8)
SiO_2	59.63	0.41	58.82	0.28	59.72	0.34	58.58	0.09	59.30	0.70	58.25	0.35	59.30	0.34	57.67	0.19
TiO_2	0.42	0.05	0.26	0.04	0.41	0.07	0.54	0.06	0.51	0.08	0.46	0.06	0.52	0.07	0.52	0.06
Al_2O_3	21.23	0.29	22.54	0.75	20.92	0.26	20.14	0.10	20.94	0.43	20.85	0.18	20.09	0.33	20.50	0.23
FeO	2.33	0.23	2.11	0.09	2.50	0.20	2.88	0.04	2.63	0.12	2.45	0.07	2.47	0.24	2.71	0.10
MnO	0.14	0.05	0.17	0.03	0.13	0.03	0.16	0.06	0.16	0.04	0.10	0.04	0.13	0.04	0.15	0.06
MgO	0.20	0.03	0.04	0.03	0.18	0.05	0.21	0.03	0.35	0.05	0.36	0.03	0.42	0.05	0.30	0.03
SrO	2.57	0.08	2.28	0.16	2.93	0.25	3.11	0.13	3.73	0.31	3.90	0.11	4.18	0.18	3.29	0.23
CaO	0.00	0.00	0.10	0.10	0.10	0.06	0.12	0.07	0.00	0.00	0.18	0.05	0.00	0.00	0.19	0.06
Na_2O	4.35	0.11	4.19	0.09	4.17	0.12	5.03	0.10	3.86	0.13	4.42	0.08	4.19	0.10	4.96	0.08
K_2O	9.11	0.19	9.50	1.04	8.90	0.18	9.17	0.12	8.45	0.19	8.97	0.09	8.63	0.17	9.63	0.14
P_2O_5	0.03	0.02	0.01	0.02	0.04	0.03	0.06	0.05	0.08	0.03	0.05	0.02	0.07	0.03	0.07	0.04
Total	100.00		100.00		100.00		100.00		100.00		100.00		100.00		100.00	
Total**	94.86		94.95		96.48		98.34		94.61		96.46		95.95		95.71	
H2O***	5.15		5.05		3.52		1.66		5.39		3.54		4.05		4.29	

* standard deviation, number in parenthesis refers to number of analyses
** EMP total
*** H_2O estimates “by difference” 100-EPM total (Devine et al., 1995)

Table 4.27 - *continued*.

Sample	**TGVT-9**		**TGVT-10**		**TGVT-11**		**TGVT-12**		**TGVT-13**		**TGVT-14**		**TGVT-15**	
T(°C)	**900**		**925**		**925**		**925**		**950**		**950**		**950**	
H_2O	**2.92**		**2.47**		**5.36**		**3.31**		**3.40**		**2.11**		**4.00**	
CO_2	**0.35**		**-**		**-**		**0.27**		**0.21**		**0.19**		**-**	
		sd(8)*		sd(8)		sd(8)		sd(8)		sd(8)		sd(8)		sd(8)
SiO_2	59.39	0.33	58.57	0.21	57.51	0.46	57.94	0.40	57.77	0.17	58.62	0.43	57.81	0.41
TiO_2	0.53	0.09	0.52	0.08	0.49	0.04	0.52	0.09	0.48	0.05	0.53	0.06	0.50	0.03
Al_2O_3	20.58	0.11	20.14	0.23	20.74	0.17	20.43	0.23	19.81	0.13	20.46	0.31	20.59	0.19
FeO	2.44	0.22	2.80	0.10	2.55	0.37	2.85	0.14	3.24	0.10	3.17	0.16	2.62	0.37
MnO	0.12	0.05	0.15	0.04	0.17	0.05	0.15	0.04	0.13	0.03	0.16	0.04	0.18	0.04
MgO	0.32	0.04	0.54	0.07	0.61	0.04	0.51	0.06	0.46	0.05	0.41	0.04	0.64	0.05
SrO	3.39	0.26	4.38	0.12	5.07	0.14	4.44	0.24	4.76	0.17	3.84	0.40	4.97	0.12
CaO	0.16	0.08	0.15	0.07	0.15	0.11	0.21	0.09	0.25	0.07	0.00	0.00	0.13	0.09
Na_2O	4.46	0.11	4.16	0.09	4.13	0.17	4.18	0.06	4.46	0.07	4.07	0.09	4.10	0.12
K_2O	8.56	0.23	8.52	0.19	8.51	0.16	8.69	0.14	8.53	0.09	8.66	0.17	8.38	0.18
P_2O_5	0.05	0.03	0.07	0.03	0.09	0.02	0.07	0.01	0.11	0.03	0.08	0.02	0.08	0.02
Total	100.00		100.00		100.00		100.00		100.00		100.00		100.00	
Total**	96.38		97.20		94.57		96.69		97.71		3.44		95.77	
H2O***	3.62		2.80		5.43		3.31		2.29		96.56		4.23	

* standard deviation, number in parenthesis refers to number of analyses
** EMP total
*** H_2O estimates “by difference” 100-EPM total (Devine et al., 1995)

5. Discussion

Explosive phonolitic eruptions characterized the volcanism of SVD over the past 800 Kyr, producing large volumes of texturally zoned pyroclastic deposits. The merging of field and analytical work allowed recognizing several features that are recurrent in the explosive volcanism of the SVD. These features are: 1) crystal-poor texture of clasts erupted in the early stage of each eruption, 2) crystal-rich texture of clasts erupted in the late eruptive stage (notably, crystal-poor and crystal-rich clasts show similar bulk composition), and 3) occurrence of lithic enclaves (representative of cooling margins of the magma chamber, i.e., the solidification front) in association with crystal-rich clasts.

All these points need to be taken into account when addressing the problem of magma differentiation in a shallow feeding system, given that a mere process of fractional crystallization may explain neither the crystal-poor nature of differentiated magmas nor the stratigraphic relations among eruptive products. Hence, considering the role played by temperature and volatiles in shallow, thermally zoned magma chambers, alternative mechanisms of differentiation and crystal-melt separation are proposed in this study. Temperature gradients are in fact intrinsic of these systems, being central in the formation of crystallinity gradients (i.e., solidification fronts) and, thus, compositional gradients. At this purpose, evidences obtained from both natural and experimental products were used to constrain differentiation processes and pre-eruptive conditions of SVD magmas.

5.1 Differentiation of SVD magmas

Determining the liquid line of descent is the first step in understanding the physical processes that lead to the formation of the phonolitic magmas feeding explosive eruptions of the SVD. At this purpose, the composition of natural products provides snapshots of the differentiation process from more primitive to highly differentiated magmas. Notably, intermediate magmas (SiO_2 ranging from ~51 to 56 wt.%) are poorly represented among the composition of natural products of the SVD, which are indeed clustered into two main groups representative of primitive (SiO_2<51 wt.%) and differentiated (SiO_2>56 wt.%) magmas, respectively (Figure 4.25). A similar bimodal distribution is also observed among different types of lithic enclaves (Figure 4.22), which phase assemblages are either clinopyroxene-dominated (types A and B) or sanidine-dominated (type C). This sharp division between differentiated and primitive compositions may indicate the existence of a two stage magmatic system, characterized by deep reservoirs feeding effusive (i.e., lava flows) or weakly explosive (i.e., strombolian) eruptions and shallow magma chambers feeding large explosive

eruptions. The differentiation of the SVD magmas is here discussed in light of this evidence. At this purpose, MELTS simulations (Ghiorso and Sack, 1995), phase equilibria and thermal gradient experiments allowed constraining the differentiation of primitive and intermediate magmas toward the phonolite magma.

5.1.1 Deep *vs.* shallow magma system

Geophysical (e.g., low velocity zones, earthquakes foci in volcanic areas) and petrologic data (e.g., phase equilibria experiments, fluid inclusion barometry) provide important evidence for the shallow level (i.e., low pressure) residence of differentiated magmas feeding large explosive eruptions. In the case of phonolitic volcanism, magma chambers are generally located at about 3-6 km, corresponding to a pressure of about 150±50 MPa. Examples of important phonolitic eruptions, for which shallow level conditions have been demonstrated, are reported in table 5.1.

In the case of the SVD, different volumes and eruptive stiles characterizing differentiated and primitive magmas may actually relate with the depth of the feeding magma system. From what stated above it comes out that the differentiated magmas may provide information on the shallow magma system whereas the undifferentiated magmas, which usually represent only a minor fraction of the total erupted volume, may provide information on the source region (cfr. Conticelli et al., 1997; Peccerillo and Lustrino, 2005). Because primitive magmas represent only a minor aliquot of the erupted products, further information on the deeper magma system and the relation between primitive and differentiated magmas may be extrapolated from the petro-chemical features of differentiated juvenile clasts and/or from the stratigraphic relations of the erupted products. For example, the occurrence of high-mg-*number* clinopyroxene xenocrysts in black-grey scoria clasts from TGVT phonolitic eruptions records a more primitive magma, although this magma was never erupted. Conversely, less differentiated magmas of the SVD were commonly erupted during the post-caldera activity (i.e., lava flows and strombolian activity) that followed the emplacement of large volumes of phonolitic magmas. In both cases, differentiated and primitive magmas are not associated within the same eruption, constraining a different depth for their origin.

Table 5.1 - Examples of phonolitic eruptions and their pre-eruptive P-T conditions.

Volcano/Eruption	Pressure/Depth	Temperature	Reference
Vesuvio, 79 AD	100 MPa (4 km)	EU1 830-840 °C EU2 850-925 °C	Shea et al., 2009
Campi Flegrei, Campanian Ignimbrite	140-200 MPa (5-7 km)	780 °C	Fabbrizio and Carrol, 2008
Laacher See Tephra	115-145 MPa (5-6 km)	Lower 750-760 °C Upper 840-860 °C	Berndt et al., 2001 Harms et al., 2004
Teide, El Abrigo	130±50 MPa (3-6 km)	825±25 °C	Andujar et al., 2008
Teide, Lavas Negras	150±50 MPa (3-7 km)	900±20 °C	Andujar et al., 2010

Clinopyroxene is considered as the main mineral driving the chemical differentiation of the K-Basalt parental magmas of the Roman Province volcanoes. With the exception of rare highly differentiated products, clinopyroxene is ubiquitous in the SVD rocks. At intermediate compositions leucite and/or feldspars become abundant. Assuming a poorly differentiated SVD rock-type as possible parental composition (e.g., San Celso phono-tephritic lava, Conticelli et al., 1997), MELTS simulations indicates that at least 70 vol.% crystallization of the initial mass is required to obtain a phonolitic composition matching those of the yellow tuffs. Such large amount of crystals is incompatible with textures of natural products (either differentiated or undifferentiated), as the massive crystallization of a primitive magma would have produced phonolitic melt locked into a non-eruptible crystal mush. Therefore at least two stage of crystallization-differentiation (i.e., two different depths) are required to produce the volumes of erupted phonolitic magma. This is in agreement with the whole compositions of natural products (Figure 4.25) and, hence, with the inferred two-stage plumbing system (deep and primitive *vs.* shallow and differentiated).

In such a system, differentiated magmas may form at shallow crustal levels from the differentiation of intermediate magmas (e.g., tephri-phonolite) that are indeed erupted prevalently during the syn- and post-caldera activity associated to phonolitic caldera-forming eruptions. Differently, more primitive magmas (e.g., phono-tephrite) evolve at deeper levels in the crust and feed effusive/weakly explosive eruptions. The compositional gap between these two groups may actually mean that deep (undifferentiated) magma crystallization occurs until a less dense intermediate magma (i.e., tephri-phonolite) is separated and migrates toward a shallow magma chamber, where it definitely differentiates and forms phonolites (Figure 5.1). The composition of the bulk solid removed from a primitive magma (e.g., K-basalt) to

generate an intermediate one (e.g., tephri-phonolite), as well as the bulk solid removed from the intermediate to generate a differentiated (e.g., phonolite), are given by MELTS simulations. Accordingly, Cpx+Ol and Cpx+Lct+Fsp are the bulk solids obtained during the early (deep) and late (shallow) stage of magma differentiation, respectively (Figure 5.1). The first mineral assemblage is typical in primitive products (e.g., San Celso lava flow, M.te Maggiore scoria cone; Conticelli et al., 1997) whereas the latter is common in differentiated explosive products and, more importantly, it constitutes the mineral assemblage of lithic enclaves emplaced during large explosive eruptions (see above in the text).

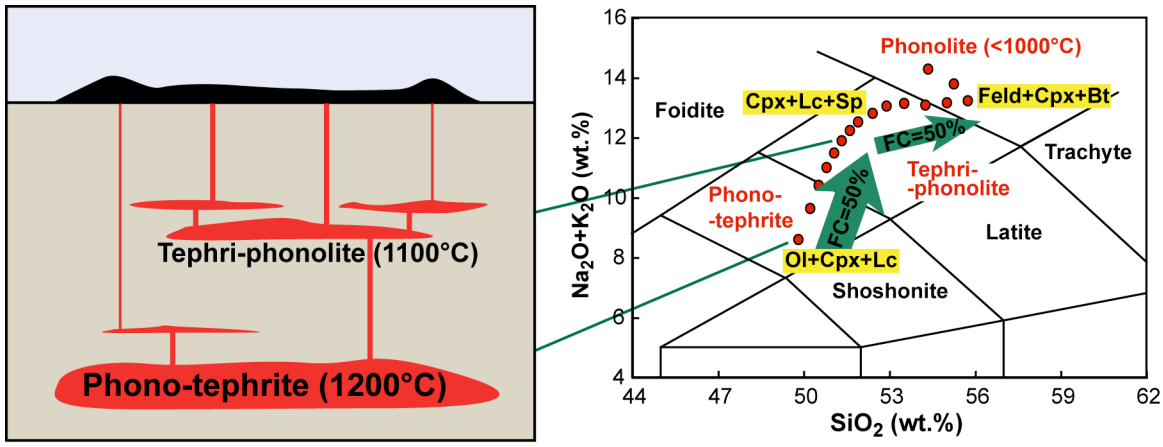

Figure 5.1 - Sketch model of the SVD plumbing system as inferred from the overall composition of juvenile products (Figure 4.25) and mass balance calculations obtained using MELTS code. Note that assuming a phono-tephritic primitive magma evolving toward phonolite, about 75% crystallization of initial mass would be required; this would freeze the system into a non-eruptible condition. Contrarily, a two-stage plumbing system would allow the differentiation of initial magma to produce and segregate an intermediate magma that in turn differentiates at shallow crustal level producing phonolites.

The assumption of a tephri-phonolitic intermediate magma as parental magma of the phonolite is at the base of the experimental strategy followed for both phase equilibria and thermal gradient experiments. The starting material used, is indeed a tephri-phonolitic scoria (Table 4.17) that was emplaced during the calderic activity of the Tufo Giallo di Sacrofano. Both phase equilibria and thermal gradient experiments performed using this starting composition confirmed the role of clinopyroxene in driving melt differentiation and also revealed that phonolitic interstitial glass is formed at temperature below 950 °C. However, the best matching between composition of glasses in experimental and natural products (Tufo Giallo di Sacrofano, representing the caldera forming eruption after which M.te Aguzzo scoria cone was formed) is at 900 °C with about 4 wt.% of H_2O in the melt. At these

conditions, the chemical composition of the clinopyroxene matches the average composition of clinopyroxene in TGVT juvenile clasts. Notably, although the good matching of phases compositions between natural and experimental products, the crystal-poor textures of juvenile clasts set against the ~30 vol.% of crystals coexisting with the phonolitic melt at 900 °C, observed in both phase equilibria and thermal gradient experiments.

Therefore, given the experimental evidences on crystallization and melt differentiation, three main questions arise from the mismatch between natural and experimental textures: 1) Does crystallization-differentiation occur everywhere in the magma chamber? 2) How does crystal-melt separation occur? 3) What are the pre-eruptive conditions and how are they achieved? These problems are addressed in the following paragraphs, in the light of the textural variability of the juvenile clasts (crystal-poor *vs.* crystal-rich) and the lithic enclaves, and of the experimental evidences provided by phase equilibria and thermal gradient experiments.

5.1.2 Differentiation in shallow thermally zoned magma chambers

The most reasonable answer to the question "when does crystallization occur" would definitely be "when the system cools down". Thus, the rule "the cooler the system, the more crystalline the magma" should apply in differentiating magmas, and it effectively does. Thus, being temperature gradients intrinsic of shallow magma chambers, the differentiation should occur prevalently in cooler regions. These regions generally correspond to the margins of the magma chambers, where magmas are in contact with the country rocks. Crystallization in these boundary regions proceeds faster than in the centre of the magma chamber, leading to the formation of the so-called solidification front (Marsh, 1996). Cooling and degassing of the magmatic body continuously sustain the *in situ* growth of granular rocks (McBirney and Noyes, 1979; Campbell, 1987). Conversely, crystal sinking and accumulation may lead to the formation of cumulate textures (Vernon, 2004 and references therein). Generally, solidification fronts are associated to the roof and the sidewalls of the chamber (Humpreys and Holness, 2010) where temperature is lower than at the floor. Thus, rocks formed in solidification front would be texturally different from cumulate rocks formed by gravitative accumulation of denser crystals.

Lithic enclaves investigated in this study are texturally heterogeneous and do not show mineral assemblage typical of cumulate rocks (with the exception of rare clinopyroxenite rocks occurring in Tufo di Bracciano). Moreover, they are commonly erupted in association with the crystal-rich phonolitic magma, during late stage of explosive eruptions (Masotta et al., 2010). On these grounds, their crystallization can be associated to the formation of a

solidification front at the margin of the magma chamber (e.g., Hermes and Cornell, 1981; Tait, 1988; Tait et al., 1989; Turbeville, 1993; Holness and Bunbury, 2006). Therefore, their modal and textural variability can be use to recover both the magma composition and the crystallization conditions in the solidification front.

Crystallization conditions in the solidification front

Lithic enclaves erupted from the solidification front of the magma chamber, have been divided into four main types (see above in the results section). Types A and B show mineral assemblages typical of magmatic crystallization, whereas the abundance of andraditic garnet and F-rich phlogopite respectively in enclaves of types C and M makes their interpretation more complex. A general increase of LREE is observed from enclaves of type A and B to enclaves of type C (Figure 4.24), consistently with the more differentiated composition of the magma from which they originated.

The paucity or lack of interstitial glass prevented the use of crystal-melt equilibria model to determine crystallization temperature and pressure of lithic enclaves. However, because a good correlation is observed between composition of clinopyroxene in lithic enclaves and in phase equilibria experiments with tephri-phonolite starting material (Figure 5.2), it is reasonable to use this correlation to infer the crystallization temperature of clinopyroxene in enclaves. The overlapping of mg-*number* in natural and experimental clinopyroxenes records a minimum crystallization temperature of 950 °C, whereas the range of mg-*number* of natural clinopyroxene (up to 0.85) suggests a maximum crystallization temperature of about 1100 °C. Such range of temperature may be interpreted in light of the variable cooling rates at the margins of the magma chamber. Clinopyroxene cores are indeed consistently Mg-enriched with respect to rims. Clinopyroxene composition of type C and M was not used at this purpose, due to the uncertain origin of these rocks and their interaction with country rocks.

Lithic enclaves do not provide information on crystallization pressure. Nevertheless, thermo-metamorphosed lithic enclaves (erupted together with lithic enclaves) may be helpful in determining the depth of magma-crust interaction. The mineralogy inferred by XRD analyses (mica+zeolites+garnet±quartz) is typical of clay thermo-metamorphism (Battaglia et al., 2007). Being the SVD volcanics placed over a thick sequence of clays, marly limestone and “flysch” rocks (Fazzini et al., 1972), thermo-metamorphosed clasts allows constraining the depth of the magma-rock interaction to a depth of about 4-5 km, close to the transition to the carbonate bedrock (de Rita and Sposato, 1986). Notably, type M enclaves and thermo-metamorphosed lithics share a mica-prevailing mineral assemblage (XRD spectra are comparable), thus providing another evidence of the interaction between magma and crustal

rocks at the boundary of the magma chamber. Indeed, textural features of type M lithics, as the iso-orientation of phlogopite crystals along fractures, witness the role of metasomatic fluids in the region where the magma-crust interaction occurred. In a few samples phlogopite is associated with Fo >95 olivine "spongy" phenocrysts, in clear disequilibrium with the surrounding crystals.

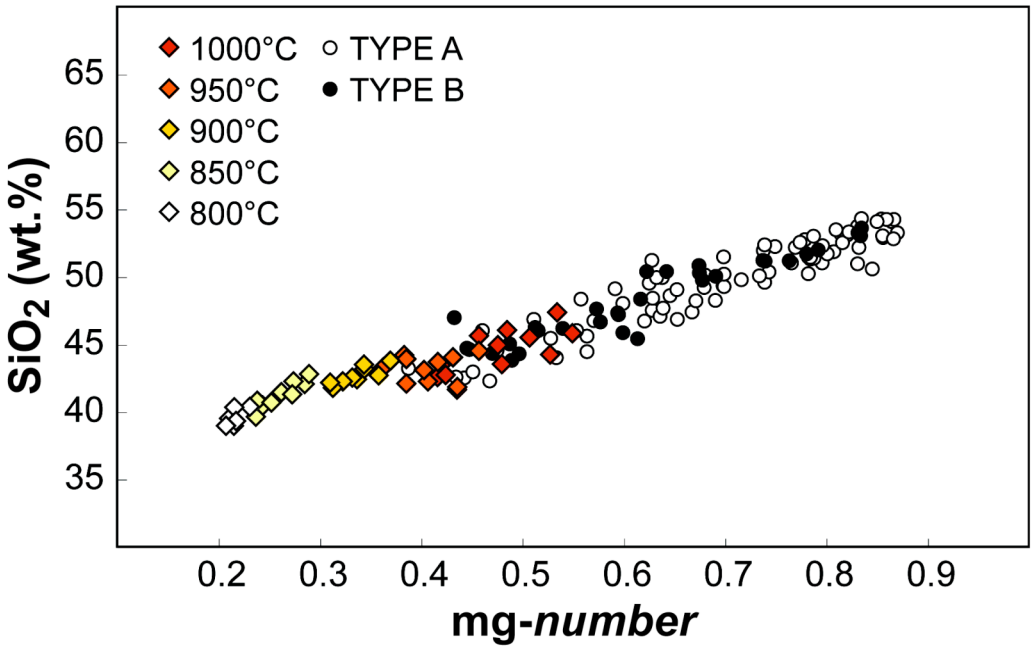

Figure 5.2 - Comparison between mg-*number* in clinopyroxene from lithic enclaves of types A and B and clinopyroxene in phase equilibria experiments.

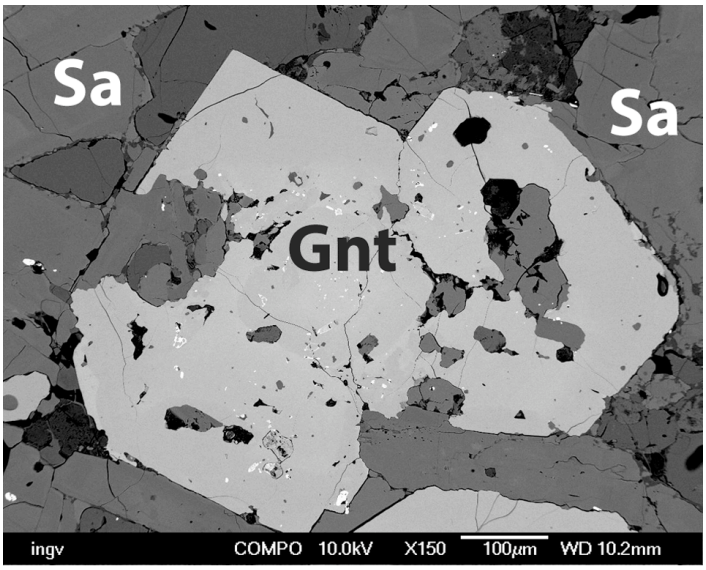

Figure 5.3 - Euhedral garnet in type C enclave (sanidinites). The euhedral shape of garnet is consistent with magmatic crystallization rather than post-magmatic origin. Notably, some enclaves of type C show anhedral garnet, crystallized interstitially between euhedral sanidine crystals.

Sanidine-rich, garnet-bearing enclaves (type C lithics; Figure 5.3) have been frequently recognized in the SVD deposits (Facchinelli and Gaeta, 1992; Capitanio and Mottana, 1998) and interpreted as the results of the hypoabissal solidification of trachytic bodies (Capitanio and Mottana, 1998). Garnet-bearing sanidinites have been also recognized in deposits associated to large phonolitic eruptions of Italian volcanoes, such as Neapolitan Yellow Tuff (Naimo et al., 2003 and reference therein), being interpreted as product of post-magmatic (pneumatolitic) crystallization. Facchinelli and Gaeta (1992) interpreted the presence of andraditic garnet in several SVD breccia deposits as consequence of magmatic crystallization at high CO_2 fugacity.

The wide range of variability of HREE in clinopyroxene of type C enclaves (Figure 4.24) may indicate either the cotectic crystallization of garnet and clinopyroxene (i.e., depletion of HREE in clinopyroxene due their preferential partition in the garnet lattice), or the late crystallization of garnet with respect to clinopyroxene (i.e., not-depleted HREE clinopyroxene crystallizing earlier). In both cases, sanidinites are representative of magmatic crystallization at relatively low temperatures (T <850 °C) of highly differentiated magma (i.e., enriched in REE), whereas the origin of garnet account for high concentration of volatiles either as dissolved H_2O-CO_2 or as metasomatic fluid (post-magmatic origin).

Cooling history of the magma chamber

The cooling of the magma chamber was numerically simulated in order to investigate the relation between the solidification front volume and the time required to cool the magma body down to 900 °C (phonolite temperature inferred from phase equilibria experiments). To simulate the conductive cooling of the magma body, a numerical model consisting in a finite element analysis 2D scheme was solved using heat diffusion equation (e.g., Mollo et al., 2011). Different shapes of the magma body were considered, with the purpose to define their effect on cooling time and thickness of the solidification front, assuming a 700 °C solidus temperature. The aspect ratio (AR, defined as width/height) of the ellipsoidal magma body was thus varied from AR = 0.15 (vertically oblate ellipsoid) to AR = 10 (horizontally oblate ellipsoid), being AR = 1 the aspect ratio of a sphere. The length of the axes of the magma body was calculated in order to have a final volume for the magma chamber of about 25 km^3, assuming the averaged volume of 10 km^3 DRE of magmas erupted during large explosive eruptions being produced by 50-60% fractionation of initial mass (i.e., intermediate magma differentiating in a shallow crustal level). The following conditions were assumed in the calculations: (1) an initial temperature of 1150 °C for the magma body (as inferred from maximum clinopyroxene crystallization temperature of lithic enclaves) and a geothermal

gradient for the upper crust of Sabatini area of 1 °C/10 m (see Baldi et al., 1976); (2) a specific heat of 1200 J/kgK and thermal conductivity of 1.8 W/mK for the magma body, and specific heat of 1150 J/kgK and thermal conductivity of 3 W/mK for the country rock; (3) a density of 2400 kg/m^3 for both the magma and the substrate rocks (no buoyancy). Both latent heat of crystallization and convective heat transfer were assumed negligible. Snapshots of numerical simulations for a cylinder and an irregular ellipsoid (Figure 5.4) are captured at the time required to have cooling of ~50% of initial magma volume below 850 °C (according to crystal content measured in phase equilibria experiments with tephri-phonolite), thus having a 850-950 °C suspended (eruptible) magma.

The time required to cool down the magma body to the temperature around 900 °C was then compared to typical time intervals between large eruptions of 10^3-10^4 years. Hence, the different geometries were interpreted as follows:

1) Cylindrical magma chamber. The vertical geometry is more similar to a volcanic conduit rather than a storage system. The distribution of the temperature after 5000 years allow calculating the position of the solidification front about 1000 m below the roof of the chamber. In this case the thickness of the front is extremely reduced (less than 100 m) at the sidewalls, due to the steep temperature gradient. The higher temperature of the floor of the chamber (~800 °C) would probably limit the formation of a solidification front, likely favouring the formation of cumulate rocks by sinking of denser minerals (clinopyroxenites). Notably, the portion of suspended magma is located in the lower half of such a system, where the formation of a rigid neck may reduce the possibility of this magma of being erupted.
2) Spherical magma chamber. Numerical simulations indicate that cooling times in a spherical magma chamber are too high if compared to the average eruptive intervals of SVD (10^3-10^4 years). After 10^4 years since magma intrusion, the solidification front constitute a thin shield (~100 m) on the top of the sphere, whereas the inner temperature is still too high if compared to the eruptive temperature of differentiated magmas.
3) Sill-shaped magma chamber. The sub-horizontal sill intrusion represents a common geometry for shallow magma chambers (see Bachmann and Bergantz, 2004). In this frame, the horizontally extended low velocity zone below Vesuvius and Campi Flegrei (Auger et al., 2001; De Natale et al., 2001) may be interpreted as a magma body horizontal in shape. Unfortunately, no geophysical data are available in the SVD area. Simulations conducted with this geometry (7000 m wide and 700 m thick magma body, AR = 10) matches with temperature distribution inferred for magmas feeding TGVT

phonolitic eruptions (Masotta et al., 2010) and, more importantly, with the large volume of magma at nearly constant temperature of 900 °C. Indeed, assuming crystallization temperatures analogue to those determined by phase equilibria experiments, the ratio between the volume of the magma in a mush-state (crystallinity >50 vol.%) and the crystal-bearing plus crystal-poor magmas (crystallinity = 15-50 and 0-15 vol.%, respectively) is approximately 1:1 after 5000 years (i.e., crystallization of ~50% initial mass). Notably, the thermal gradient produces maximum crystallization at the roof of the chamber (i.e., a thicker solidification front) rather than at the floor, where on the contrary, the formation of cumulate (i.e., due to crystal settling) rocks is likely to occur. The different rock forming process may also control the rock mineralogy, leading to the preferential formation of denser rocks (clinopyroxenite) at the chamber floor and lighter rocks (feldspars- and leucite-bearing rocks) at the roof. Accordingly, the Tufo di Bracciano outcrops is characterized by clinopyroxenites associated with thermo-metamorphosed flysch and carbonate rocks, whereas Tufo Giallo della Via Tiberina outcrops, feldspars- and leucite-bearing lithics are associated with thermo-metamorphosed clay sedimentary rocks, indicating different depth of magmas feeding these eruptions.

The numerical models on magma bodies cooling provide useful information on time-propagation of the solidification front and geometrical relations among rock-forming processes. Nevertheless, neither chemical (i.e., differentiation, diffusion) nor physical (i.e., settling, compaction) mechanism is considered, thus the application of thermal models is limited only to the determination of cooling times and solidification front thickness (even without the assumption of negligible latent heat of crystallization the time scale of cooling and the geometry of solidification fronts would not vary). On these grounds, the cooling model of the sill-shaped magma body offers the best matching between both the cooling times and volumes of crystallized portions (50 vol.% crystallization in a time-span of 10^3-10^4 years), indicating a maximum thickness of the solidification front at the sidewalls (200-500 m; Figure 5.4) and the temperature distribution in the magma chamber (the roof is cooler than the floor). Notably, this is the same temperature distribution reproduced by the thermal gradient experiments (as discussed in the results section), confirming the key role of solidification front in driving the magma differentiation.

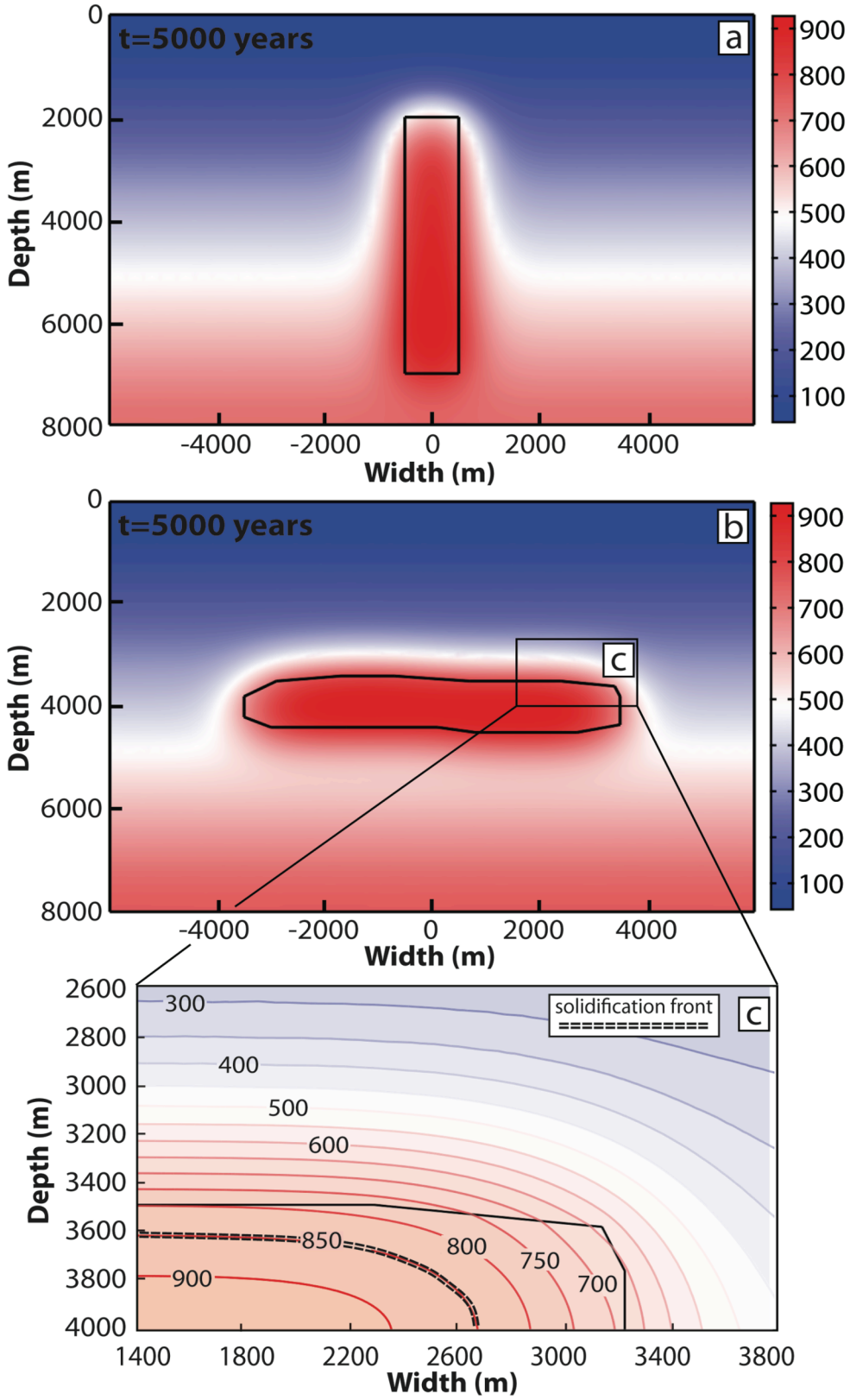

Figure 5.4 - Cooling models of a cylinder (a) and an irregular ellipsoid (b). Magnification of the boundary region of the irregular ellipsoid (c) shows the position of the solidification front (T <850 °C) at t = 5000 years; note that this time indicates the time elapsed since the intrusion, in order to have a final temperature of ~900 °C in the centre of the magma body and ~50 vol.% crystallization of initial mass.

Geometry of the solidification front

On the basis of both textural classification of lithic enclaves and results from numerical modelling of a cooling sill-shaped magma body, the solidification front was divided into three main regions (Figure 5.5):

1) Inner region: higher crystallization temperatures and low cooling rates characterize the inner portion of the mush zone (phenocrysts content ~30-60 vol.%), enhancing the equilibrium crystallization of clinopyroxene and leucite (euhedral phenocrysts). Textures of type A lithic enclaves may have formed in these conditions. The lack of late-forming interstitial mineral phases (poikilitic sanidine and mica) in type A, indeed indicates higher crystallization temperature with respect to type B. The abundance of leucite in the groundmass witnesses the differentiated composition of the interstitial melt (tephri-phonolitic or phonolitic) that eventually crystallized during the eruption of the crystal-poor magma (hotter region of the chamber), in response to sin-eruptive decompression induced by volatile loss (Mastrolorenzo and Pappalardo, 2006; Humphreys et al., 2008; Brophy, 2009). Decompression and volatile exsolution in the lately erupted cooler portions of the magma chamber may have occurred consequently to the eruption of the hotter, crystal-poor phonolitic magma (Masotta et al., 2010). The abundance of type A enclaves and the wide range of crystallinity indicate a wide region of the solidification front where this type of enclaves formed.

2) Intermediate region: a range of crystallization temperatures (at least 200 °C) and higher cooling rates characterize the intermediate region, leading to higher degree of crystallization (>60 vol.%) and pre-eruptive crystallization of interstitial melt. This region has been associated to type B lithic enclaves. As deduced from the extrapolation of the experimentally determined relation temperature-mg-$number_{Cpx}$ to natural products (Figures 4.29 and 5.2), clinopyroxene crystallized at a higher temperature (T >950 °C) than feldspars and biotite. The latter two minerals, indeed, crystallized lately and at lower temperature (T< 950°C) from the H_2O-rich and differentiated interstitial melt, producing poikilitic textures (Figure 4.19). Anhedral shapes of clinopyroxene likely indicate conditions of disequilibrium crystallization, due to the faster cooling of this region relatively to the inner one. The direct compositional zoning of clinopyroxene (Fe-richer rims compared with cores) remarks the progressive differentiation of the interstitial melt. Isolated batches of differentiated (phonolitic) melts may have lead to the formation of sanidine-rich enclaves of type C. However, compared to porphyric texture of type A enclaves,

the holocrystalline texture of types B and C lithic enclaves indicates that these enclaves were already formed at the moment of their eruption, thus constraining their lower formation temperature (T <950°C) with respect to enclaves of type A.

3) Boundary region: phlogopite-bearing mineral assemblages of type M enclaves suggest their crystallization at the magma-rocks interface (with consequent thermo-metamorphism of pelitic rocks surrounding the shallow magma chamber; Figure 5.5). Type C enclaves also record crystallization at temperature lower than those of the enclaves A and B, whereas the occurrence of garnet may in some cases indicate the effect of post-magmatic fluid circulation, constraining the proximity of the magma-crust interface. The different mineral assemblage of types C and M enclaves records two different composition of the crystallizing magma. In particular, type C enclaves crystallized from pockets of differentiated (phonolitic) melt, possibly segregated within the highly crystallized region of the solidification front, whereas mineral assemblage of type M is consistent with crystallization from a less differentiated magma (phono-teprhite), broadly similar to that producing types A and B enclaves.

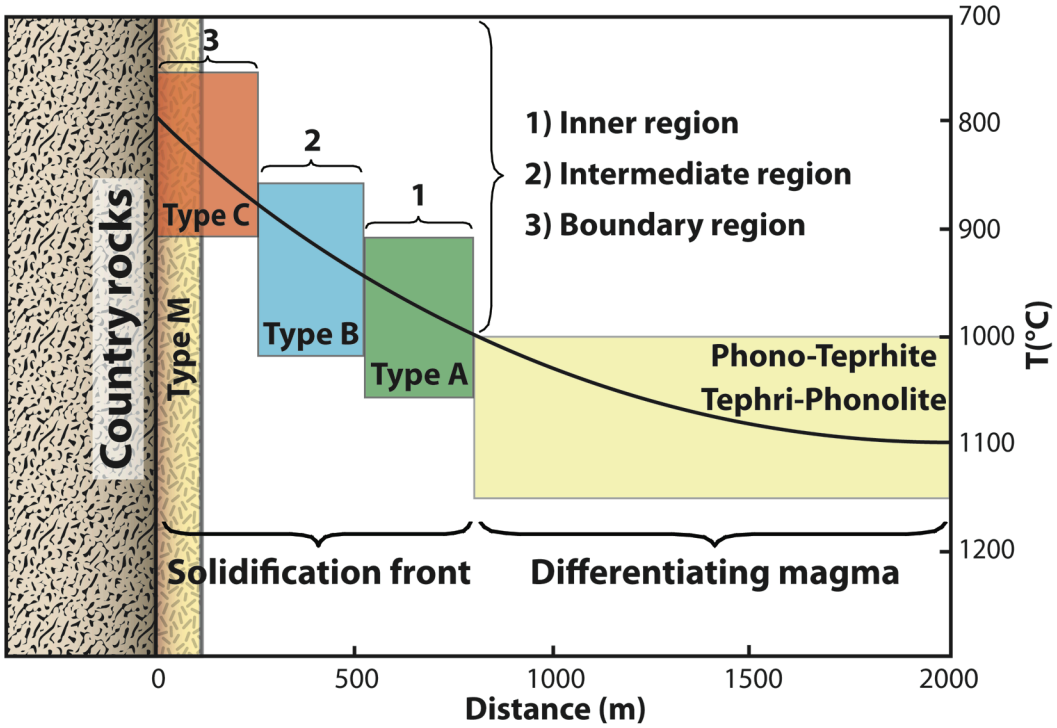

Figure 5.5 - Sketch diagram showing the geometry of the solidification front as inferred from textural features of lithic enclaves and numerical simulations.

5.1.3 Extraction of differentiated melt from solidification fronts: insights from thermal gradient experiments

The formation of a solidification front implicitly assumes magma differentiation, given that melt differentiates more and more as crystallization increases. In a solidification front, however, the most differentiated (and viscous) melts are produced and, at least partially, locked into the crystal-rich zone (crystal-mush). The questions of how these interstitial melts are extracted to produce the differentiated crystal-poor magma remain unanswered. In particular, the differentiated magmas feeding large explosive eruptions (e.g., Tufo Giallo della Via Tiberina) are commonly erupted from crystal-poor and compositionally homogeneous reservoirs. What is between the melt differentiation in a solidification front and its further accumulation in crystal-poor reservoirs is a debated question. Seeking for this missing step, a number of mechanisms has been proposed involving either chemical (i.e., diffusion) or physical (i.e., gravitative forces, convection) processes, but none of them has been constrained by experimental observations.

Thermal gradient experiments performed in this study, by reproducing both solidification front and glassy belts of differentiated melt lying on its top may be the key for unravelling the paradox of the origin of crystal-poor differentiated magmas in natural systems.

Crystallization and melt differentiation along temperature gradient

As already pointed out, the composition of the interstitial glass along T-gradient charges, in agreement with what observed in phase equilibria experiments, varies with the amount of crystallization from tephri-phonolite (zone 1) to phonolite (zone 4). Importantly, both phase equilibria and T-gradient experiments produced phonolitic glass at T ≤900°C and a minimum of crystallization of ~30 vol.%. Therefore, different zones in T-gradient experiments may be interpreted as snapshots comparable to isothermal phase equilibria runs. The different crystallinity observed between the phase equilibria experiment at 1000 °C (clinopyroxene = 6 vol.%) and the corresponding zone 1 of T-gradient experiments (glassy), is most likely due to different water concentrations in melts. Although the initial water content in both systems was similar (~2 wt.% of water added to charges), the final concentration is higher in the glassy zone 1 due to water diffusion from the H_2O-enriched highly crystallized zones. Conversely, the chemical heterogeneity of the melt along the charge (Figure 5.6) suggests that chemical diffusion of major elements is not efficient enough to ensure melt homogenisation (neither in the 24 nor in the 50 hours runs), although melt-interconnection exists among the different zones. This is in agreement with the experimental determinations of Lesher and Walker (1988) that demonstrated the limited efficacy of chemical diffusion in a temperature gradient

(i.e., Soret effect; Soret, 1879). However, for very long run duration (months scale), thermal migration may actually cause melt differentiation in the hottest zone (Huang et al., 2009).

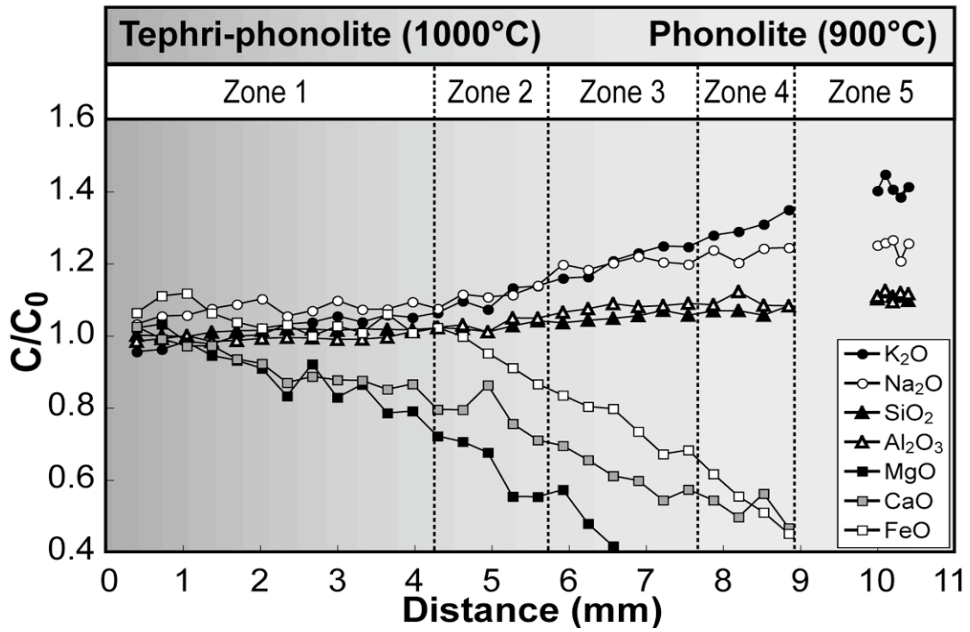

Figure 5.6 - Major oxide concentration (C) in glass along the SVD-10 run normalised to the composition of the glass obtained at super-liquidus temperature (1050 °C) in phase equilibria experiments (C_0). Note the chemical variation of glass along the charge as function of temperature. The lack of data between highly crystalline zone 4 and zone 5 is due to the tiny size of interstitial glass in the rigid crystal framework dividing these two zones.

Extraction of differentiated melt

Phonolitic glass occurs only interstitially in low-temperatures phase equilibria experiments (T ≤950 °C). Differently, phonolitic glass occurs both interstitially in the highly crystalline zone 4 and as belts and pockets in the heterogeneously crystallized zone 5 of the T-gradient charges (Figure 4.33). The phonolitic glassy pockets represent pools of residual melt that accumulated and remained locked up in the mushy region. The phonolitic glassy belts, on the other hand, overlie the mushy region and are separated from it by the presence of a rigid crystal framework. The key question is how such a differentiated melt was extracted from the underlying regions where it formed.

Variable gravitative mechanisms may be responsible for the crystal-melt separation observed at the top of experimental charges, however, the most suitable for the formation of glassy belts in the investigated phonolitic (i.e., differentiated) system are the following: 1) crystal settling, 2) compaction-induced segregation, and 3) collapse of the rigid crystal framework.

1) Crystal settling. The occurrence of crystal settling is witnessed by the clinopyroxene drop-shaped clusters in zones 2 and 3, and by the U-shaped settling front separating the glassy zone 1 from zone 2 (Figures 4.31 and 4.32). The latter feature, in turn, is due to shear effects at the capsule margins, leading to a maximum settling along the main axis of the capsule of 100 μm and >200 μm in the 24 hours and 50 hours runs, respectively.
In zones 2 and 3, particle displacement can be quantified by using the Stokes law of sinking velocity (U_{Stokes}):

$$U_{Stokes} = \frac{2gr^2\Delta\rho}{9\mu}$$

where g is the gravitational acceleration, r is the particle radius, Δρ is the density difference between crystal and liquid and μ is the liquid viscosity. Assuming a constant growth rate of 1.16×10^{-7} mm/s for a single crystal (as inferred above) and values of melt viscosity ($\eta = 10^4$ Pa s) and phase densities (ρ_{melt}=2450 kg/m^3, ρ_{Cpx}=3320 kg/m^3) as inferred by composition of experimental phases (Masotta et al., 2010), it results for the 24 hours experiment a displacement of less than 20 μm, which fails to explain the U-shaped settling front observed at the boundary between zones 1 and 2. Conversely, assuming the clinopyroxene cluster as sinking particle (i.e., 2-3 times higher growth rate), the calculated sinking velocities are in agreement with the vertical displacements of 100 and >200 μm measured in the 24 hours and 50 hours experiments settling front, respectively.
In highly crystalline and heterogeneously crystallized zones the Stokes law fails to explain the observed displacement (viscosity is too high). Indeed, in the case of a crystal-rich suspension (i.e., the mushy zone), the hindered settling velocity (Davis and Acrivos, 1985) is related to the crystal fraction (c), thus we need to correct the Stokes relation by the *f*(c) factor (Barnea and Mizrahi, 1973):

$$U_{hs} = U_{Stokes} \cdot f(c)$$

By assuming a constant increase of the crystal fraction, it results a displacement for the mushy region and rigid crystal framework of a few microns only.
Thus, although the occurrence of crystal settling has been demonstrated for the low crystalline zone 2 of T-gradient experiments, calculations indicate that such a process fails to explain the size of glassy belts in zone 5.

2) Compaction-induced segregation of melt and its upward migration. Compaction of a crystal mush leads to the extrusion of interstitial melt upwards as a result of deformation and settling of a denser crystal matrix (McKenzie, 1984; Bachmann and Bergantz, 2004). In this frame, the glassy belts form because of the upward extraction of differentiated interstitial melt from the mushy region; this, in turn, causes the formation of the rigid

crystal framework. The crystallizing mush behaves like a compacting porous media, in which the interstitial pressure is constantly increased by the ongoing crystallization and crystal compaction along a thermal gradient.

Due to the large variability of empirical parameters involved in the numerical relations of compaction (detailed discussion and formalism are given in Bachmann and Bergantz, 2004; Tegner et al., 2009), it is difficult to quantify compaction at the scale of the experiment. However, an estimate of the thickness of the mushy region feeding the glassy belts (δ_s) can be obtained by using the empirical relation of Marsh (2002):

$$\delta_s(t) = S(t) \cdot (\overline{1-\phi})^{-1}$$

where S(t) represents the thickness of the segregation after 24 hours and (1-ϕ) the mean porosity of the solidification front. By applying the above relation it results a thickness of 300-500 μm for the supply region, i.e., three-four times larger than the thickness of the segregation zone. Such a thickness is in agreement with the size of the heterogeneously crystallized zone 5.

3) Collapse of the rigid crystal framework. Alternatively to settling and compaction processes, the mechanism leading to melt segregation could be the failure/sloping of the upper part of the solidification front, induced by the downward directed tensional forces of the rigid crystal framework (Figure 5.7). The tensile strength (σ) acting on the rigid crystal framework is proportional to the density contrast (Δρ) between the framework (solid continuum) and the underlying mushy region (liquid continuum) according to the relation (Marsh, 2002):

$$\sigma = \Delta\rho \cdot g \cdot h$$

where g is the gravitational acceleration and h is the thickness of the feeding zone. Considering a 500 μm maximum thickness for the feeding zone (as calculated above), we obtain a tensile strength of about 5 bars acting on the rigid crystal framework of the T-gradient experiments. The calculated tensile strength is comparable with values reported by Marsh (2002) in order to cause the instability and tearing of a solidification front (Figure 5.8).

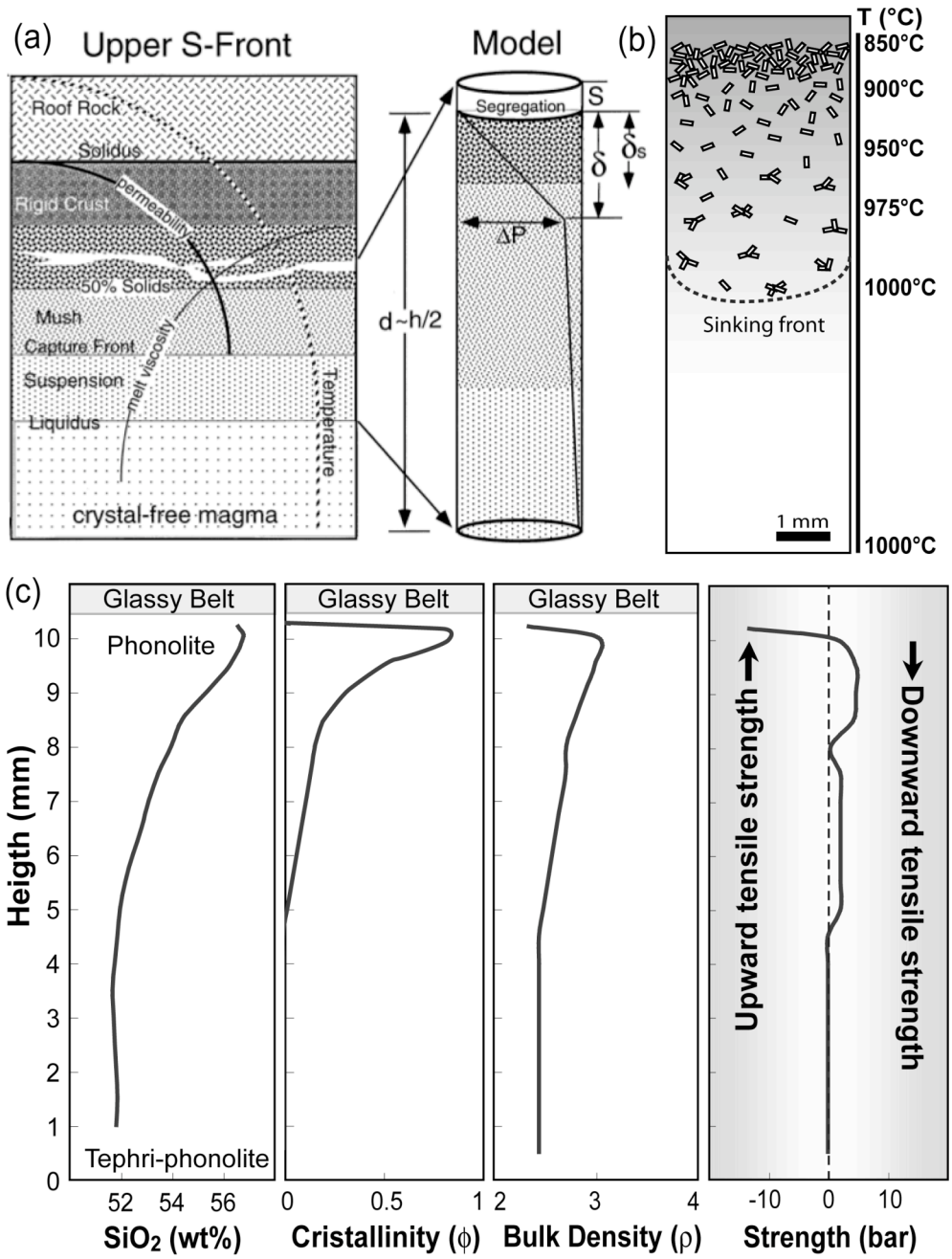

Figure 5.7 - (a) Schematic representation of a solidification front used by Marsh (2002) to model melt segregation; note the analogy of the model geometry with the experimental design. (b) Sketch drawn of a T-gradient charge and (c) related profiles of composition (SiO_2 wt.%), crystallinity, and bulk density. These profiles have been used to calculate the tensile strength along the charge (last panel on the right).

On one hand, both compaction-induced melt segregation and rigid crystal framework collapse mechanisms are consistent with textures observed in T-gradient experiments. On the other hand, the occurrence of deformed elongated sanidine crystals at the margin of phonolitic belts (Figure 5.9), suggests that the upward melt migration was most likely a rapid process occurring late during the development of the solidification front. Sanidine composition,

indeed, is in chemical equilibrium with phonolitic melt and this constrains its late formation as well as the late formation of glassy belts. Thus the collapse-driven mechanism is the most feasible mechanism to explain the formation of differentiated, glassy belts.

The collapse of the rigid crystal framework and the consequent formation of glassy belts can be summarized in three steps: 1) a solidification front develops due to the thermal gradient; 2) the upper part of the solidification front becomes unstable with ongoing crystallization (60 vol.%, Marsh, 2002; Dufek and Bachmann, 2010; Figure 5.10) and starts to behave like a rigid crystal framework (i.e., solid continuum) floating on a crystal-rich suspension (i.e., liquid continuum); 3) the rigid crystal framework collapses, inducing the rapid upward extraction of the interstitial differentiated melt that accumulates in relatively large volumes (glassy belts) and produces the deformation of sanidine crystals.

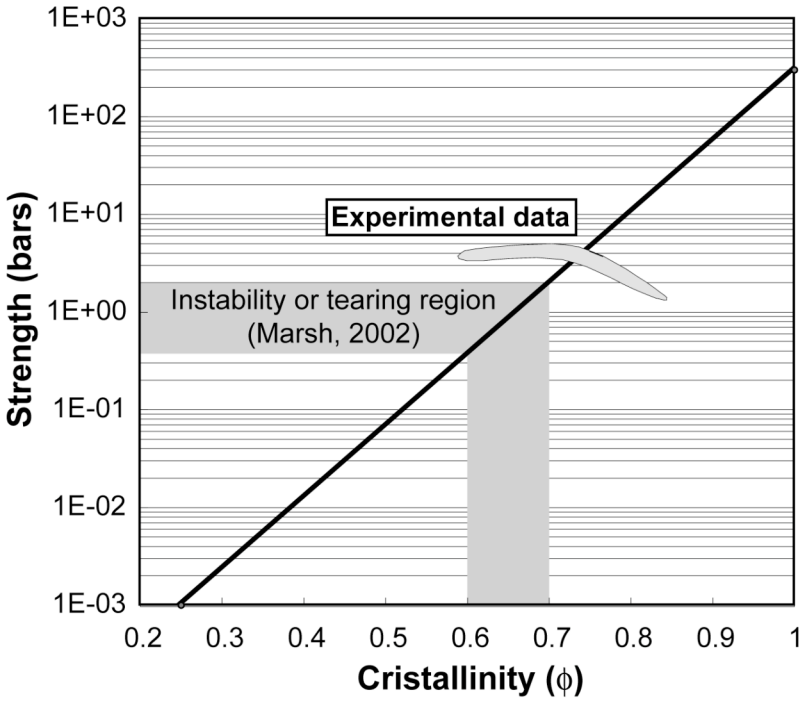

Figure 5.8 - Crystallinity *vs.* tensional strength diagram (after Marsh, 2002). The reported tensional strength acting on the rigid crystal framework of zone 5 has been calculated from experimental data (see text and Figure 5.6 for explanation). The strength calculated from experimental data for a phonolitic system is comparable to the theoretical values inferred by Marsh (2002) for the instability regions of crystal mush in basaltic systems.

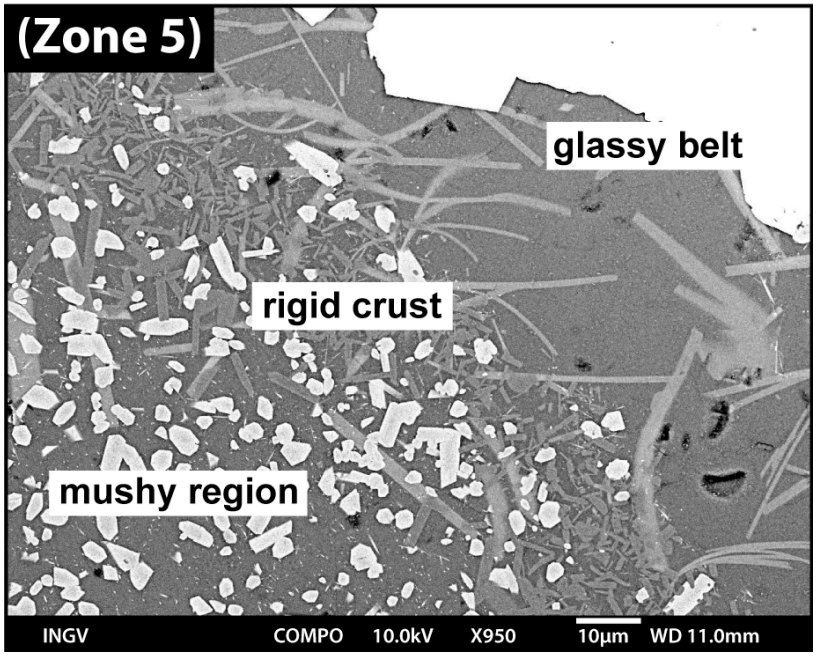

Figure 5.9 - Detail of zone 5 of T-gradient experiments showing the deformed sanidine crystals at the margin of the rigid crust of the collapsing solidification front.

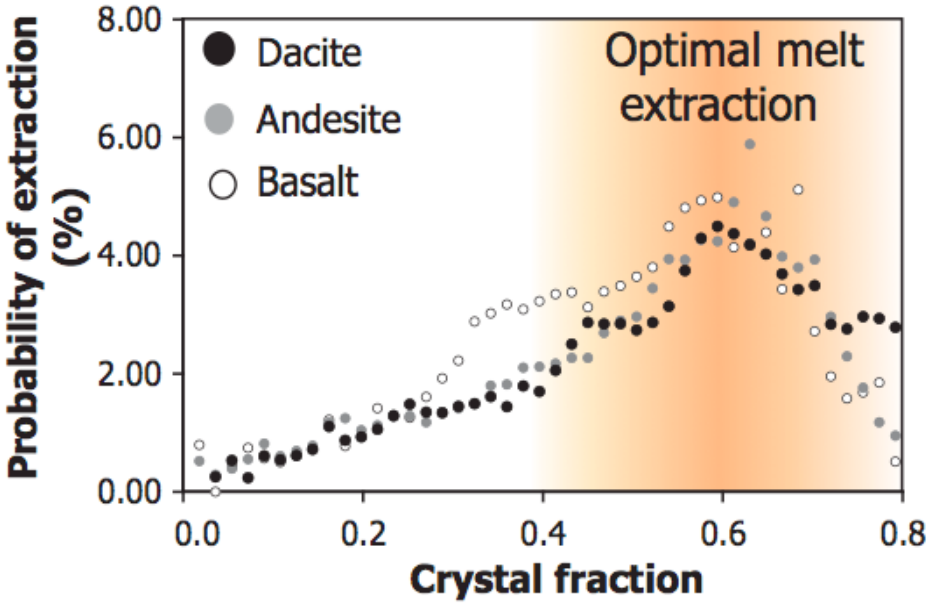

Figure 5.10 - Probability for extracting interstitial melt from crystalline residue resulting from multi-phase numerical modelling (Dufek and Bachmann, 2010). Note how the maximum probability is for crystal fraction of 0.6, in agreement with the averaged crystallinity of the mushy zone in thermal gradient experiments.

5.1.4 Origin of crystal-poor phonolitic magmas: combining natural and experimental evidences

Thermal gradient experiments picture for the first time the formation of the solidification front, conceptually theorized by Marsh (1996). More importantly, they demonstrate the

possibility to extract differentiated melt, forming crystal-poor batches, from a crystal-rich (mushy) region. Such a process of melt extraction may explain the paradox on the origin of crystal-poor differentiated magmas, given the analogy between textures of experimental (T-gradient experiments) and natural products. The alternation of crystal-poor and crystal-rich textures, indeed, is a recurrent feature in many large eruptions of the SVD.

Crystal-melt separation mechanisms occurring in a natural system are discussed in this paragraph in light of the correspondence between textural features of experimental and natural products.

From experiments to nature

Phase equilibria experiments have been performed for decades and judged an important tool to constrain magma differentiation processes and pre-eruptive conditions in magmatic systems. In particular, phase equilibria experiments performed in this study, in agreement with literature data (e.g., Berndt et al., 2001; Freise et al., 2003; Shea et al., 2009), indicate that, starting from a tephri-phonolitic composition, at T ≤900 °C and P ≤300 MPa, a minimum amount of 30 vol.% crystallinity, and water content in the system close to saturation, are the required conditions to form phonolitic magmas (Figure 4.28). These results corroborate the hypothesis that phonolites originate in shallow level magma chambers. However, phase equilibria experiments give no insights into the mechanisms responsible of the formation of differentiated, crystal-poor magmas feeding large explosive eruptions. This is most likely due to the fact that these experiments, being conducted under isothermal conditions, do not strictly reproduce the environment typical of shallow level, thermally zoned magma chambers. Therefore, T-gradient experiments represent a valuable tool and the best complement to phase equilibria experiments, to model processes occurring in such environment. These experiments, indeed, not only reproduce the liquid line of descent of phase equilibria experiments (Figure 4.35) but also picture structures characterized by either highly crystalline or glassy zones (Figure 4.33), as previously inferred for thermally zoned magmatic systems (Marsh, 1996). Moreover and most importantly, T-gradient experiments allow quantifying chemical (composition of phases), textural (crystallinity), and physical (density and viscosity) parameters necessary to model the formation of these glassy regions (Figure 4.33). Since these parameters are size-independent, they can be used to model crystal-melt separation mechanisms producing crystal-poor reservoir in natural magmatic systems as well.

Crystal-melt separation in thermally zoned magma chambers

Since the first studies on crystal fractionation by settling (Bowen, 1928), many alternative mechanisms of crystal-melt separation have been proposed: 1) convective fractionation in a crystallizing boundary layer (Chen and Turner, 1980; Rice, 1981; McBirney et al., 1985; Spera et al., 1995); 2) gas-driven filter press (Anderson et al., 1984; Sisson and Bacon, 1999); 3) thermal gradient responsible for mass transport (thermal migration) resulting in segregation of melt from the mushy, boundary zone of magma chambers (Lesher and Walker, 1988); 4) melt migration induced by crystal compaction (Philpotts et al., 1996; Rabinowicz et al., 2001; Jackson et al., 2003; Bachmann and Bergantz, 2004); 5) instability of the "solidification front" (Marsh, 2002). However, in the frame of a differentiated and thermally zoned pre-eruptive system, the most efficient crystal-melt separation mechanisms are probably those proposed to explain crystal-melt separation in T-gradient experiments.

1) Crystal settling could explain fractionation of denser minerals from the differentiating melt where they form, but is inadequate to explain fractionation of feldspars and leucite due to the high melt viscosity and low density contrast (see below in the text). In analogy, clinopyroxene settling occurred only in the hottest and undifferentiated zone of thermal gradient charges;
2) Crystal compaction, as for settling, may require higher density contrast between liquid and solid phases, as well as lower crystallinity than that resulting at the top of a solidification front. Moreover, the lack of an impermeable boundary layer at the base of the compacting mush would limit the efficacy of compaction or, paradoxally, produce higher compaction rates in the lower (less crystalline) part of the solidification front than at its top (more crystalline);
3) Instability and collapse of the solidification front once again represents the most likely mechanism producing relatively large volumes of silicic segregations. Indeed, gravitational movement of crystal chain structures are typically associated to magma chamber roofs (Marsh, 2002; Annen, 2009) or alternatively at their sloping sidewalls (Humphreys and Holness, 2010), working either in primitive or differentiated magma systems in presence of a thermal gradient.

Collapse of the solidification front and melt extraction in a thermally zoned magma chamber

In order to constrain that the instability and collapse of the solidification front is the most suitable mechanism producing crystal-poor differentiated magmas, experimental textures have been compared with those of juvenile clasts and lithic enclaves occurring in the deposits

of SVD eruptions. It is important to recall that these deposits contain crystal-poor juvenile clasts, phonolitic in composition, and lithic enclaves ranging in composition from phono-tephrite to phonolite. Crystal-poor juvenile clasts are highly vesicular, vitrophyric, with generally less than 10 vol.% crystals, whereas lithic enclaves were classified on the basis of their texture in type A (characterized by PI = 30-60 vol.%), type B (characterized by holocrystalline texture) and type C (characterized by a touching framework of sanidine crystals). Intriguingly, crystal-poor juvenile clasts and lithic enclaves (types A and B) are texturally equivalent to the glassy belts and to the solidification front of the experimental products (Figure 5.11), respectively. In particular, the mushy region of the solidification front (Figure 4.33) shows the same porphyric texture of type A enclaves, whereas the holocrystalline texture of the rigid crystal frame is analogue to texture of type B enclaves. The melt pockets locked up in the mushy region possibly represent batches of phonolitic melt that, crystallizing under hypoabyssal conditions, may form sanidine-rich enclaves. Hence, by analogy with experimental evidences, in the natural system, the collapse of the rigid portions of the solidification front may produce the extraction of the differentiated interstitial melt that in turn accumulates upward, forming the crystal-poor reservoir.

Notably, in deposits associated to large explosive eruptions (e.g., Tufo Giallo della Via Tiberina), the stratigraphic sequence of crystal-poor (white pumice) and crystal-rich (black-grey scoria and lithic enclaves) products is reversed with respect to the position of crystal-poor and crystal-rich textures in the experimental charge. Moreover, the emplacement of primitive magmas during the post-caldera activity associated to these eruptions (feeding effusive activity) may be interpreted as the eruption of the deeper (hotter) and undifferentiated portion of the same magma system. Thus, considering a thermally zoned plumbing system analogue to that pictured by experimental products, the stratigraphic relations among the erupted products could be related to a downward directed withdrawal mechanism (Spera, 1984; Blake and Ivey, 1986; Cioni et al., 1995). In this scenario, crystal-poor products represent the top zone of the phonolitic magma chamber, being emplaced in the early phase of the eruption whilst crystal-rich products (fragments of the collapsed solidification front) are erupted in a later phase from an underlying crystal-rich zone. The final eruption of primitive magmas during the post-caldera activity associated to large explosive eruptions indicates the withdrawal of undifferentiated magma from the deeper portions of the system.

Thermal gradient experiments may also shed light on a long debated topic concerning the complexity of liquid line of descent observed in many volcanic districts, the so-called “Daly Gap” (Daly, 1925). This gap refers to an apparent lack of intermediate compositions among the products emplaced during volcanic activity and also applies to the eruptive history of the

SVD where intermediate tephri-phonolitic compositions are poorly represented (Figure 4.25). In T-gradient experiments, a bimodal distribution of the glassy regions is observed, with a glassy undifferentiated reservoir at the bottom (SiO_2≈51 wt.%) and glassy differentiated belts at the top (SiO_2≈57 wt.%). Glass with intermediate composition occurs only in the moderately and highly crystalline zones (3-4) that in a natural system may represent magma unlike to be erupted because of its high viscosity. This bimodal distribution of crystal-poor melts produced in T-gradient charges may characterize also natural magmatic systems where basalt parental magma differentiates in thermally zoned magma chambers. The non-eruption of the intermediate mushy region may actually explain the abovementioned Daly gap, without necessity to invoke more complex processes of refilling or eruption from multistage magmatic systems.

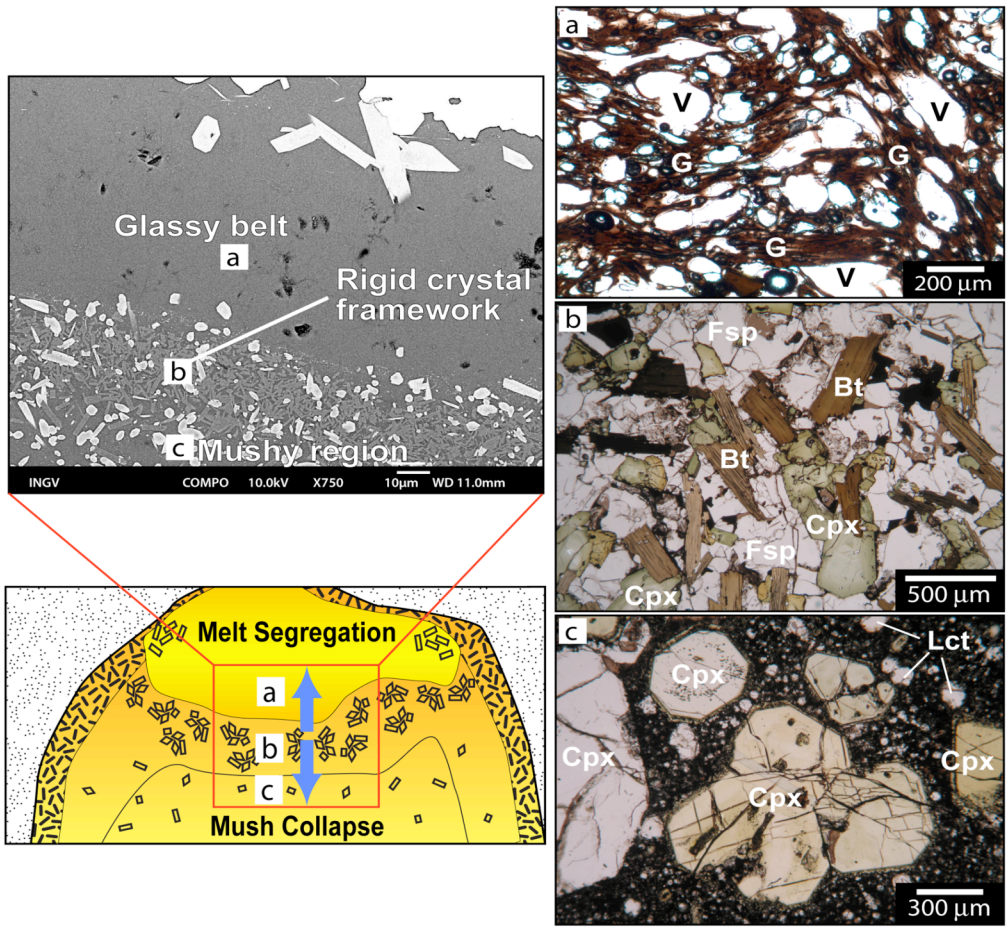

Figure 5.11 - Comparison between textures of experimental and natural products of the SVD. (a) the glassy belt at the top of the charge corresponds to natural crystal-poor juvenile clasts and represents the eruptible crystal-poor magma at the top of the magma chamber; (b) the rigid crystal framework corresponds to equigranular lithic clasts (Type B) and represents the collapsing portion of the solidification front; (c) the mushy region corresponds to porphyritic lithic clasts (Type A) and represents the highly crystalline region underlying the rigid crystal framework. V: vesicles, G: glass, Fsp: feldspar, Cpx: clinopyroxene, Bt: biotite, Lct: leucite.

5.2 Pre-eruptive conditions of SVD magmas

Thermal gradient experiments have shed light on the mechanism leading to the origin of crystal-poor, differentiated magmas. However, they left unanswered the question about the conditions leading to these eruptions. Information on pre-eruptive conditions (temperature, pressure and volatile concentrations) of these magmas should be then obtained merging data from natural products, clinopyroxene-liquid geothermometry (Putirka et al., 2008 and references therein), MELTS simulations (Ghiorso and Sack, 1995), and *ad hoc* phase equilibria experiments. The Tufo Giallo della Via Tiberina eruptions were used as case study for this investigation.

5.2.1 Determination of T, P, X_{H2O}

The Tufo Giallo della Via Tiberina (TGVT) eruptions produced ~10 km^3 DRE of phonolitic deposits cropping out in the eastern sector of the SVD. The TGVT deposits contain white pumice and black-grey scoria clasts sharing similar phonolitic composition but showing different textural features, and lithic enclaves. In particular, white pumice clasts are highly vesicular, vitrophyric, and contain scarce feldspars and clinopyroxene, whereas black-grey scoria clasts are poorly vesicular, highly crystallized, and show diffuse glomerocrysts.

Pre-eruptive temperatures of the feeder magma were determined using the clinopyroxene-liquid geothermometer of Putirka (2008). Temperature estimates obtained using this model are H_2O- and pressure-independent in the low-pressure range (P<500 MPa) hypothesized for the TGVT shallow magma system. Clinopyroxene xenocrysts with mg-*number* higher than 0.70 were assumed not in equilibrium with the phonolitic melt (Kd_{Fe-Mg}>0.40) and thus not used in the calculations. Cpx-glass pairs were used to calculate clinopyroxene crystallization temperature in crystal-poor white pumice. Conversely, to avoid temperature overestimate of crystal-rich black-grey scoria, due to the Mg-enrichment of the glass related to syn-eruptive crystallization of leucite, the Cpx-bulk composition pair was used. Therefore, clinopyroxene crystallization temperatures of 890-920 °C and 925-940 °C were obtained for black-grey scoria and white pumice, respectively.

Pressure conditions were not determined directly by Cpx-Liq equilibria, because of the high uncertainty of clinopyroxene geobarometry at low pressure (Putirka et al., 1996; Nimis and Ulmer, 1998; Putirka, 2008). However, based on the water content in glasses of crystal-poor white pumice (4-5 wt.%), as determined by the "difference from 100" method (i.e., based on the difference to 100% of the total obtained by EMP analyses of glasses, with accuracy of ca. 0.5 wt.% H_2O, Devine et al., 1995; Thomas, 2000), a minimum pressure of 100-150 MPa can be estimated.

MELTS simulations were then performed at the above-determined conditions of pressure and temperature in order to compare them with phase relationships in juvenile clasts and thus to validate these estimates. MELTS simulations also resulted in agreement with phase relationships obtained by equilibria experiments carried out on similar phonolite composition from Vesuvius 79 AD eruption (Shea et al., 2009). These indeed showed clinopyroxene and spinel in equilibrium with liquid at 100 MPa, T = 920-940 °C and 4 wt.% H_2O in the melt, whereas clinopyroxene, spinel, feldspars and leucite were in equilibrium at T = 890-920 °C and 4 wt.% H_2O in the melt. Such conditions represent the pre-eruptive condition of white pumice and black-grey scoria feeder magma, respectively (Figure 5.12).

The H_2O content in the interstitial melt of black-grey scoria indicates a minimum pressure value similar to that deduced for white pumice. Nevertheless, the abundance of leucite in black-grey scoria indicates that their feeder magma remained H_2O-undersaturated (H_2O <4 wt.%) while cooling down to T = 890-920 °C. Conversely, the absence of leucite phenocrysts in white pumice implies that the phonolitic magma remained above the stability field of leucite, until it reached T = 920-940 °C. Pre-eruptive conditions (temperature and H_2O content) of both white pumice and black-grey scoria feeder magmas, as deduced by phase relationships in natural products and petrological modelling, are summarized in Figure 5.12.

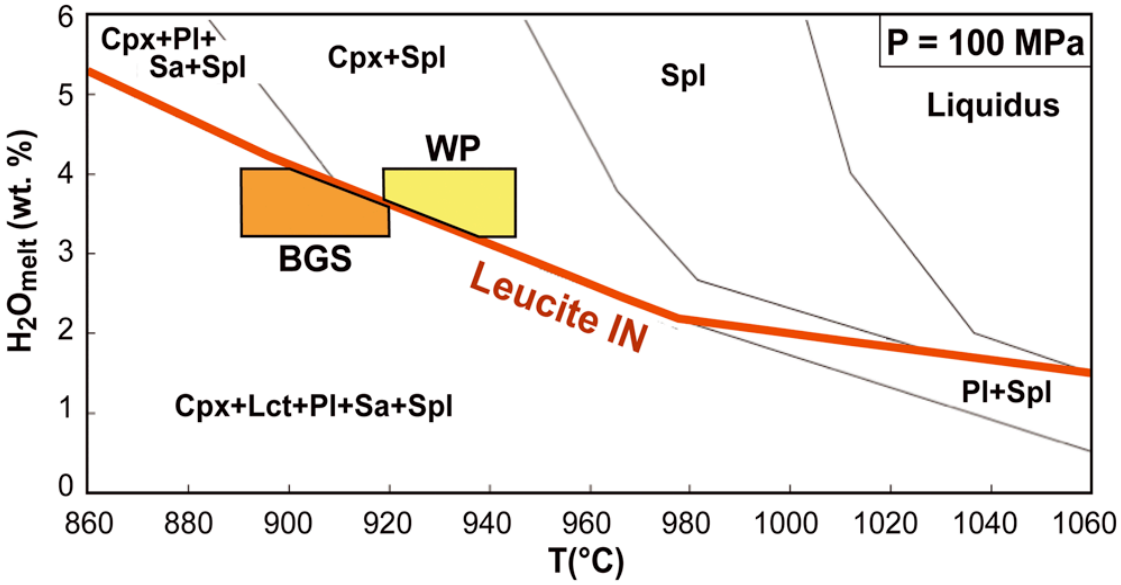

Figure 5.12 - H_2O_{melt} vs. temperature phase stability diagram obtained by MELTS simulations on bulk phonolitic composition (sample MG-21; Table 4.4) at P = 100 MPa. T, X_{H2O} values refer to initial crystallization conditions for black-grey scoria (BGS) feeder magma and to pre-eruptive conditions for white pumice (WP) feeder magma.

Experimental constrain of pre-eruptive conditions of phonolite systems

Phase equilibria experiments performed with tephri-phonolite (SVD-0, Table 4.18) were used to asses the liquid line of descent of SVD magmas and they showed that phonolitic melt is generated at temperatures below 950 °C (in agreement with results from T-gradient experiments). Phase equilibria experiments performed with phonolite (TGVT-0, Table 4.18) were thus performed at 200 MPa, in the temperature range 850-950 °C, in order to constrain the pre-eruptive conditions. Both sets of phase equilibria experiments confirm the role of clinopyroxene in driving melt differentiation and indicate that the best matching between glass composition in experimental and natural products is obtained at 900 °C with about 4 wt.% of H_2O in the melt. In particular, interstitial glass of CO_2-bearing phase equilibria experiments (Table 4.27) better reproduce the compositional variability of TGVT juvenile clasts, which composition ranges between the fields of phonolite and trachyte (Figures 4.2 and 4.6), thus indicating that limited amounts of CO_2 may actually have existed in the TGVT magma (X_{H2O} <1). Moreover, the crystal content of experimental products, run at 900 °C, is in general lower than 15 vol.%, in agreement with crystal content of juvenile clasts. It is worth nothing that leucite is never present in phonolite phase equilibria experiments at 200 MPa (Figure 4.36), suggesting that leucite crystallization may have occurred at a lower pressure or during sin-eruptive decompression.

Chemical composition of clinopyroxene crystallized at 900 °C and H_2O = 3-4 wt.% (in both sets of phase equilibria experiments) matches the average composition of clinopyroxene in TGVT juvenile clasts (Tables 4.6, 4.19 and 4.25; Figure 5.13), thus constraining the above-determined estimates and validating the use of the Cpx-Liq model of Putirka (2008). Conversely, plagioclase and sanidine in natural products are An- and Or-enriched with respect to feldspars crystallized in phase equilibria experiments (Tables 4.7 and 4.26; Figure 5.13). This mismatch may actually be due to a slightly higher concentration of water in the melt (pre-eruptive H_2O over-saturation), rather than to a different crystallization temperature. Indeed, both An_{Pl} and Or_{Sa} increase constantly with the increasing H_2O concentration (Figure 4.40), as well as observed for mg-*number* of clinopyroxene (Figure 4.38).

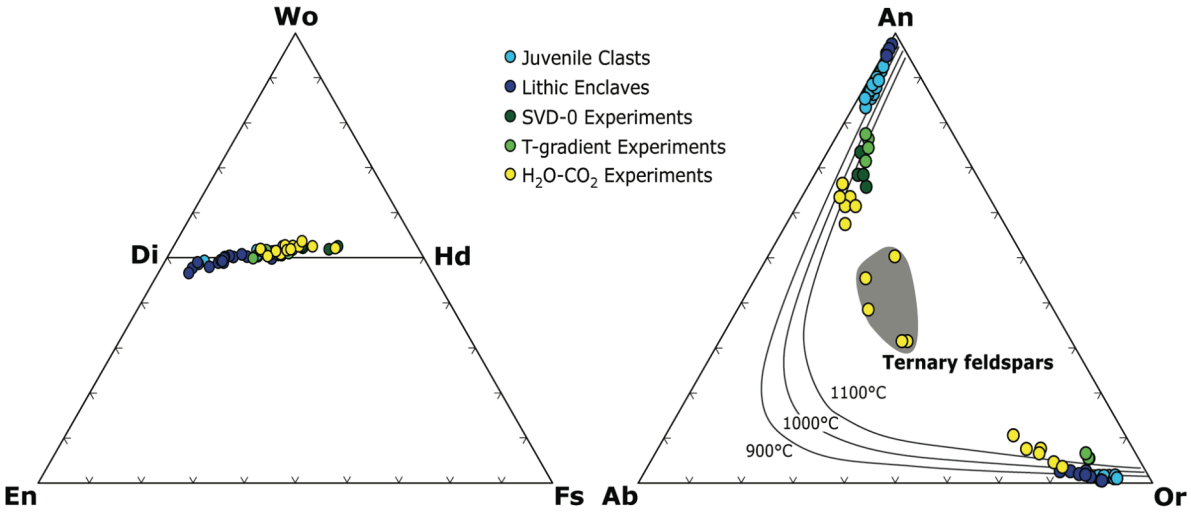

Figure 5.13 - Ternary diagrams showing the comparison between composition of clinopyroxene and feldspars from juvenile clasts and experimental products. Note that the composition of clinopyroxene in experimental products matches that of juvenile clasts, whereas feldspars in natural and experimental products show different composition.

5.2.2 H_2O and temperature zoning in the pre-eruptive system

Both MELTS simulations and phase equilibria experiments were successfully used in estimating the pre-eruptive conditions of the phonolitic system. Because both these approaches are based on the assumption that solid and liquid phases were in equilibrium in the pre-eruptive system, neither MELTS nor phase equilibria experiments answer to the questions on how the magma approached the pre-eruptive conditions and how it was erupted. At this purpose, juvenile clasts erupted during large explosive eruptions provide information on magmatic processes occurring in the shallow magmatic system. On these grounds, using the information gathered on the Tufo Giallo della Via Tiberina eruptive products, a model of H_2O and temperature zoning of the phonolitic magma chamber feeding TGVT eruptions was developed, relating the textural changes of juvenile clasts to physical processes, such as decompression and volatile exsolution, rather than to compositional zoning of the phonolitic system (e.g., Wörner and Schminke 1984; Cioni et al., 1995). These processes may have controlled the pre-eruptive conditions of the phonolite magma during its residence at shallow crustal level.

Achievement of pre-eruptive H_2O-saturation of phonolite magma

A key question arising from the textural features of the TGVT juvenile clasts, in particular for white pumice, is how the crystal-poor magma reached pre-eruptive H_2O-saturation. Although it is well known that volatiles dissolved in silicate melts play a fundamental role in controlling magma evolution (e.g., Huppert and Woods, 2002), the processes controlling the

variation of volatiles concentration in magmas are often poorly constrained. In the TGVT case study, because a low amount of phenocrysts in white pumice clasts (typically even <10 vol.%), the achievement of H_2O-saturation in the magma by mere crystal fractionation seems unlikely. Indeed, given the low density contrast between feldspars (sanidine in particular) and the phonolitic melt, crystal removal by settling is not possible in silicic, differentiated magmas (Figure 5.14).

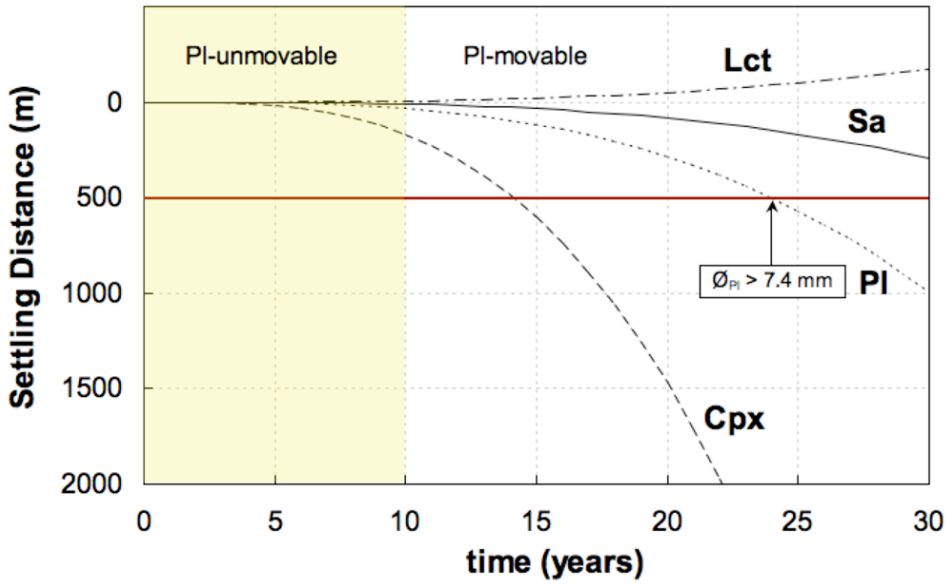

Figure 5.14 - Diagram illustrating crystal settling velocities in a phonolitic melt driven by crystal-melt density contrast, by applying the Stokes law for sinking particles. Phonolite melt viscosity (10^4 Pa s) was calculated at 900 °C and H_2O content of 4 wt.%, following Giordano et al. (2008) and Whittington et al. (2006). Densities (ρ) and maximum growth rates (Y) of different mineral phases have been taken into account in the calculations, as follows: $\rho_{magma} = 2450$ kg/m^3, $\rho_{Cpx} = 3320$ kg/m^3, $\rho_{Pl} = 2620$ kg/m^3, $\rho_{Sa} = 2500$ kg/m^3, $\rho_{Lct} = 2420$ kg/m^3; $Y_{Lct} \approx 10^{-8}$ mm/s (Shea et al., 2009); $Y_{Sa} \approx 10^{-8}$ mm/s (Hammer and Rutherford, 2002); $Y_{Pl} \approx 10^{-8}$ mm/s (Cashman and Marsh, 1988; Cashman, 1993); $Y_{Cpx} \approx 10^{-8}$ mm/s (Crisp et al., 1994). For example, the diagram shows that it takes ~10 years for a plagioclase crystal to attain a size suitable for settling (unmovable-movable boundary), and ~25 years to reach 7.4 mm in size at 500 m settling distance. On these grounds, leucite and sanidine populations are considered as almost unmovable in phonolitic melts (in particular, note that leucite tends to float in these magmas).

Existing models of volatile-zoned magma systems feeding silicic large explosive eruptions indicate higher volatile concentrations in the upper portions of magma chambers, as a result of compositional layering and/or recharge by mafic magmas (e.g., Blake, 1984; Blake and Ivey, 1986; Dunbar and Hervig, 1992; Wallace et al., 1999; Wark et al., 2007). In this regard, the lack of inverse chemical zoning in clinopyroxene, as well as the homogeneity of the

juvenile bulk composition, lead us to rule out the occurrence of pre-eruptive compositional zoning in the TGVT reservoir and/or mixing with less evolved magmas. Alternatively, the emplacement of a near H_2O-saturated, crystal-poor, phonolitic magma at pre-eruptive depth (100-150 MPa) is inconsistent with petrographic evidences from highly porphyritic, leucite-rich, black-grey scoria. Indeed, phase relationships of phonolitic magmas at 100 MPa (Figure 5.12), point out an amount of leucite comparable to that actually occurring in black-grey scoria only at H_2O-undersaturated conditions.

The widening of the leucite stability field, as a result of possible decompression of a H_2O-saturated phonolitic magma can not fully explain the relevant petrographic features of the black-grey scoria. Indeed, the wide range of leucite and plagioclase crystal size in black-grey scoria consistently reflects a range of crystallization conditions (Cashman, 1992). For example, decompression simulations (Figure 5.15) show that a 50 MPa pressure drop acting on a H_2O-saturated, partially crystallized (T = 890-920 °C), phonolitic magma (at the initial estimated P = 100 MPa) would result in up to 20 wt.% increase of solid phase, mostly leucite and plagioclase. Thus, whereas scarce leucite microcrysts (∅<30 μm) in white pumice may record conduit ascent of a H_2O-saturated phonolitic magma, the occurrence in black-grey scoria of leucite + plagioclase-rich groundmass and crown-like poikilitic textures of leucite phenocrysts (Figure 4.5), likely indicates a rapid (i.e., at the eruptive time-scale) decompression-induced crystallization, consequently to the withdrawal of the white pumice feeder magma (cfr. eruption-decompression-crystallization models; Mastrolorenzo and Pappalardo, 2006; Humphreys et al., 2008; Brophy, 2009). Nevertheless, such a decompression event (eruptive time-scale) cannot explain the extensive formation of larger leucite crystals (∅>100 μm) in black-grey scoria magma. Considering an average growth rate of $2x10^{-8}$ mm/s (Shea et al., 2009), the time required to reach >100 μm in size (10^2 days) would be considerably longer than the explosive eruption time-scale (10^{0-1} days). On these grounds, the diffuse occurrence of leucite phenocrysts in black-grey scoria puts constrains on the corresponding pre-eruptive magma domain at initial H_2O-undersaturated conditions (Figure 5.12).

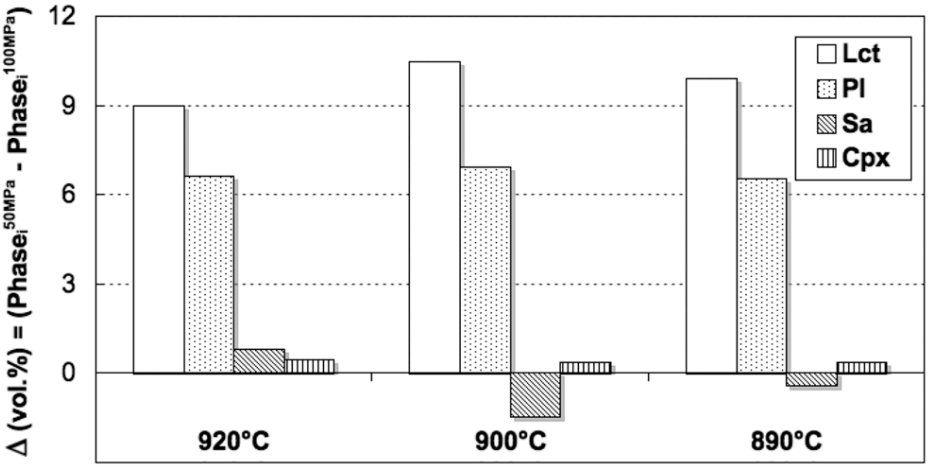

Figure 5.15 - Increasing crystal content (Δ vol.%) in a phonolitic magma as a result of a ΔP = 50 MPa decompression step, at different temperatures (920, 900 and 890 °C), obtained by MELTS simulations. Note that decompression-crystallization mostly involves leucite + plagioclase (Δ up to ~18 vol.%).

H_2O- and Temperature-zoned magma chamber

As discussed above, both crystal fractionation and decompression-induced crystallization do not adequately explain the achievement of H_2O-saturation condition in the crystal-poor magma feeding white pumice eruption and the diffuse occurrence of leucite phenocrysts in black-grey scoria. Therefore, in order to explain the highly variable crystal content in the TGVT juvenile clasts, as well as the diffuse occurrence of crystal-poor juvenile in the products of large explosive eruptions, a model based on a temperature- and volatile-zoned magma system has been proposed. Accordingly, temperature and H_2O-zoning could be the factors controlling the degree of crystallization and phase relationships in different portions of magma chambers. Specifically, the presence of abundant lithic enclaves associated with black-grey scoria (e.g., in subunit (d) of upper TGVT), suggests the tapping of different regions of the phonolitic reservoir during the emission of white pumice and black-grey scoria in the course of individual eruptive event. In particular, assuming a "concentric shells" geometry of the magma chamber (Blake, 1981; Spera, 1984), black-grey scoria would represent late-erupted, cooler, peripheral regions of the system. Phase relationships and crystal growth rates data indicate that crystallization of relatively large leucite (∅>100 μm) should occur under H_2O-undersatured conditions (Hammer and Rutherford, 2002; Freda et al., 2008; Shea et al., 2009). Thus, phonolitic black-grey scoria magmas from the cooler, peripheral regions of the TGVT magma chambers were initially H_2O-undersaturated (H_2O <4 wt.%, at P = 100 MPa and $T_{Cpx\text{-}liquid}$ > 890-925 °C), allowing crystallization of leucite phenocrysts. Conversely, the lack of leucite phenocrysts in white pumice indicates H_2O conditions above the leucite-in curve in the phase diagram (Figure 5.12). Moreover, the

presence of round-shaped, partially resorbed, sanidine phenocrysts, testifies that H_2O-saturation was achieved in the white pumice magma following feldspar crystallization. In particular, due to the relatively small size and low density contrast with the host phonolitic melt that prevented significant crystal sinking (Figure 5.14), sanidine can be considered the record of the changing magma conditions.

Given all these data, it has been deduced that extensive magma crystallization and consequent increase of H_2O at the periphery of the TGVT magma chamber (i.e., the black-grey scoria feeder magma), produced H_2O migration toward the inner portion of the reservoir, where the higher temperature and increasing H_2O content acted to delay crystallization in the white pumice feeder magma (Figure 5.16). Once that the H_2O concentration gradient was established between the crystallizing peripheral regions of the magma chamber and the poorly crystallized inner portion, the H_2O mass flux was actually enhanced by the geometry of the magma system. Hence, considering a roughly concentric geometry of H_2O- and thermal zoning for the TGVT magma chamber (Figure 5.17), at each given point along the radial H_2O-gradient the mass of inward-migrating water would diffuse toward increasingly small volumes, so that the amount of dissolved water in the inner part of magma chamber would increase constantly, eventually leading to pre-eruptive H_2O-saturation. In this regard, re-melting features (i.e., rounded-shape and glass-embayment) in sanidine from white pumice provide evidence of gradually increasing H_2O content that reduced the feldspars + leucite stability field in the inner portion of the magma chamber (Figure 5.12). Such a mechanism of H_2O migration toward the hottest region of the magma chamber is in agreement with experimental evidences of T-gradient experiments. Indeed, H_2O concentration in the hotter, glassy region at the bottom of the charge is constantly increased, due to water diffusion from crystallizing zones. Thus, at the end of the experiments, the water concentration along the charge is actually constant.

This scenario of the phonolitic magma chamber (Figure 5.17) assumes that differentiated (phonolitic), crystal-poor magma is already formed in the shallow magma system from the differentiation of an intermediate magma, as the condition produced in the heterogeneously crystallized region of thermal gradient experiments (Figures 4.31 and 5.11). In fact, the TGVT phonolitic products lack the evidence of mingling/mixing with less differentiated magmas, which are in turn erupted in the post-calderic activity. The association of late-erupted black-grey scoria with lithic enclaves (i.e., representative of portions of the solidification front), as well as the occurrence of Cpx + Pl glomerocrysts and diopsidic clinopyroxene xenocrysts in black-grey scoria, consistently indicates that black-grey scoria represents peripheral, cooler regions of same the magma reservoir. Thus, the late eruption of

black-grey scoria, following the tapping of white pumice from the inner parts of the magma chambers, would be compatible with a concentric shell withdrawal model (Blake, 1981; Spera, 1984). The withdrawal of different portions of the reservoirs in the course of individual eruptive events confirms the remarkable homogeneity of the TGVT phonolitic magma chambers.

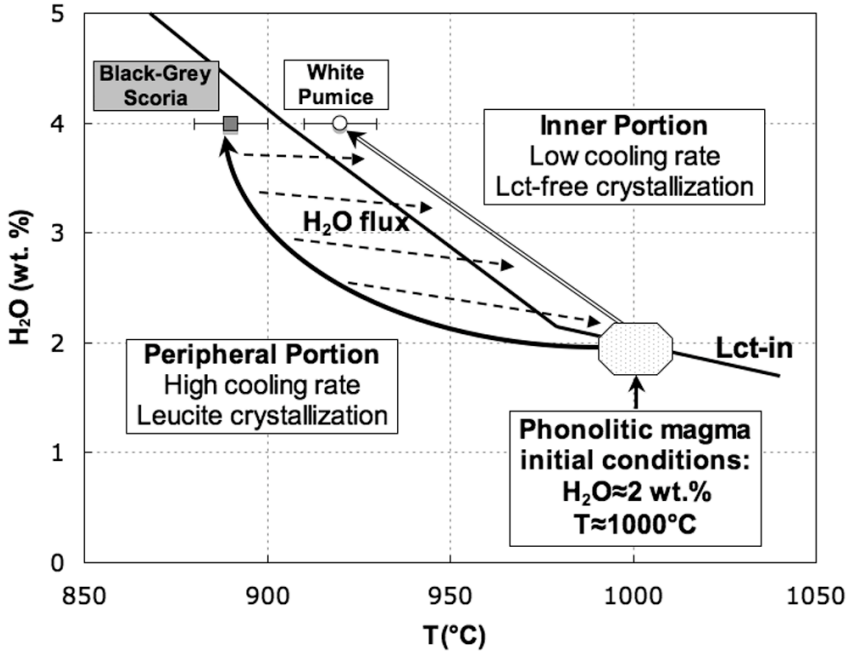

Figure 5.16 - Sketch of H_2O and T paths for the peripheral and inner portions of the phonolite magma reservoirs feeding early SVD eruptive events (FAD, TGVT), represented by black-grey scoria and white pumice, respectively. Starting from H_2O-undersaturated conditions ($H_2O \approx 2$ wt.% at 100 MPa and T ≈ 1000°C), increasing H_2O concentration in the peripheral portions (black arrow) occurred as a result of crystallization within the leucite stability field (leucite-in curve after MELTS simulations) at relatively high cooling rates. On the other hand, H_2O concentration in the inner (hotter) portions (white arrow) increased due to H_2O flux from peripheral regions and leucite-free crystallization. H_2O-saturation conditions ($H_2O \approx 4$ wt.% at 100 MPa) for black-grey scoria and white pumice magmas were eventually achieved at T ≈ 890 and 920 °C, respectively.

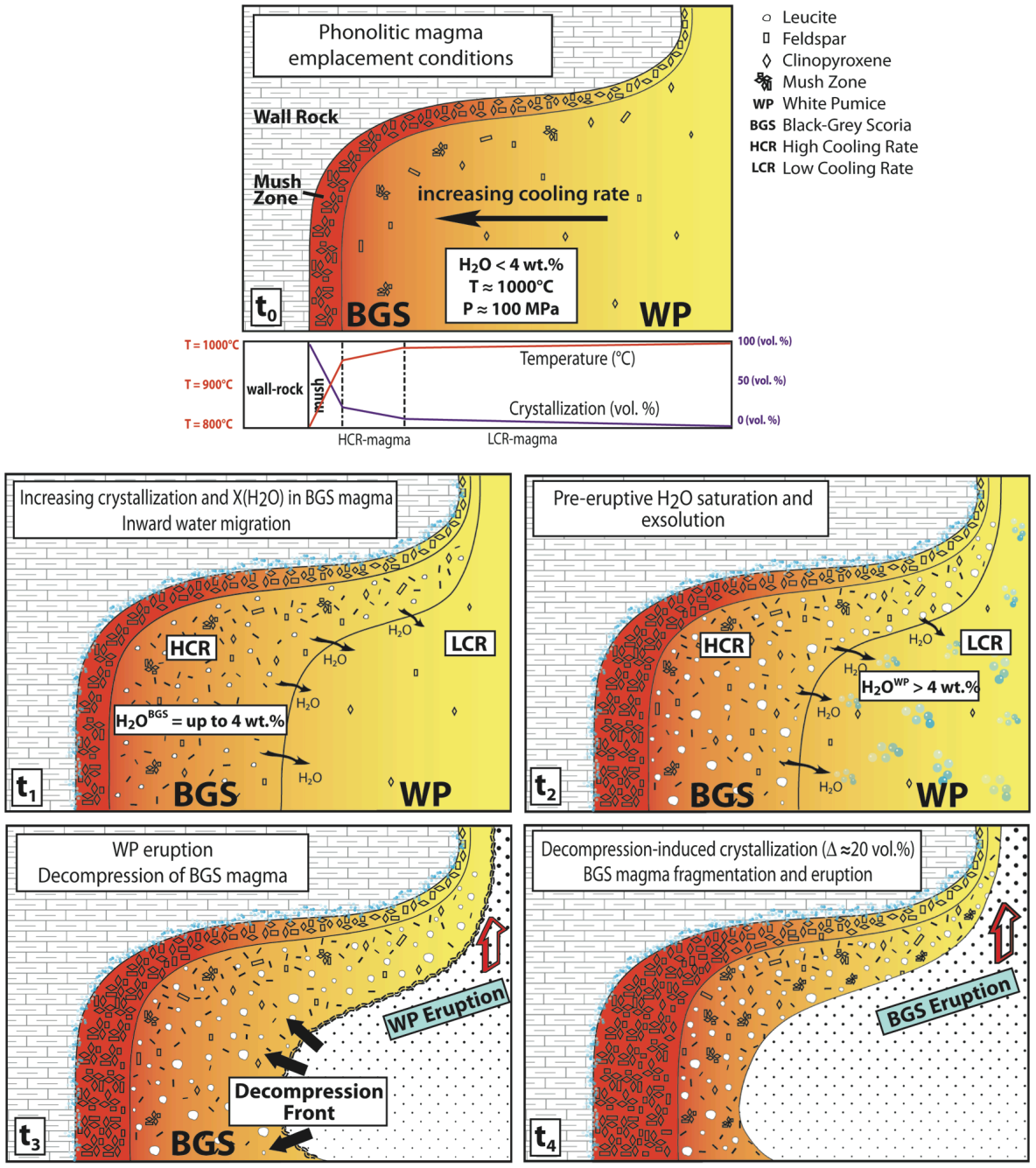

Figure 5.17 - Sketch model of the evolution of T and H_2O-zoned magma chambers feeding FAD and TGVT multiple eruptions. t_0: emplacement of a H_2O-undersaturated phonolite magma body at ca. 100 MPa and onset of crystallization in peripheral portions; t_1: increasing H_2O concentration due to crystallization of black-grey scoria (BGS) feeder magma caused H_2O migration toward inner magma chamber portions (WP); t_2: achievement of pre-eruptive H_2O-saturation conditions; t_3: tapping of inner magma portions feeding the emission of white pumice (WP) at eruption onset, resulting in decompression of BGS magma; t_4: consequent sudden crystallization, magma viscosity increase, H_2O exsolution and bubble expansion leading to BGS magma fragmentation and eruption during late stages of individual eruptive events.

5.2.3 Role of H_2O and CO_2 in the pre-eruptive system

The role of H_2O and CO_2 in the phonolitic system has been investigated through phase equilibria experiments, carried out at 200 MPa, in the temperature range of 850-950 °C. These experiments demonstrate that different conditions of volatiles concentration (X_{H2O}-X_{CO2}) may actually produce variation in the liquid line of descent. Indeed, the variable composition of the TGVT magmas (from phonolite to trachyte) can be explained by means of a slight reduction of X_{H2O} in the melt.

Although H_2O-CO_2-bearing experiments have been carried out taking into account the pre-eruptive conditions determined for the TGVT eruptions, results may be extended to other trachy-phonolitic magma systems typical of other Italian volcanoes. Therefore, H_2O-CO_2-bearing experiments offer an important tool in evaluating the effect of volatile during the late evolution of differentiated magmas.

H_2O and CO_2 effect on mineral chemistry and melt differentiation

The chemical composition of minerals seems not to be significantly affected by the presence of the CO_2, at least up to the 0.5 wt.% used for these experiments. On the contrary, variations of the H_2O content in the melt may explain the chemical variability of feldspars and clinopyroxene within isothermal runs. For example, the An content of plagioclase and the Or content in sanidine crystallized at 900 and 925 °C, relate directly with the H_2O concentration (Figure 4.39). The increase of An concentration with the increase of dissolved water is also in agreement with previous plagioclase-liquid models (Putirka, 2005; Lange et al., 2009). Similarly, mg-*number* of clinopyroxene linearly increases with the increase of H_2O in the melt (Figure 4.38).

Although the phonolitic starting material already represents a highly differentiated composition, the 100 °C temperature range of the experiments allows observing a further differentiation of the interstitial melt towards high-alkali phonolite and trachyte in H_2O-only and H_2O-CO_2-bearing experiments, respectively (Figure 5.18). In particular, in spite of their similar mineral assemblage, CO_2-bearing experiments show higher amounts of feldspars with respect to CO_2-free experiments performed at the same temperature and with similar H_2O concentration (Figure 4.37). Extensive sanidine crystallization may indeed explain the trachytic composition of the interstitial melt of CO_2-bearing experiments, whereas in CO_2-free experiments sanidine crystallizes cotectically with plagioclase and clinopyroxene without producing alkali-depletion in the interstitial melt that in turn remains within the field of phonolite (Figure 5.18). Notably, sanidine is the most abundant mineral phase in natural trachytic products (cfr. natural products description in results section), thus confirming the

role of its fractionation during the differentiation of phonolitic magmas.

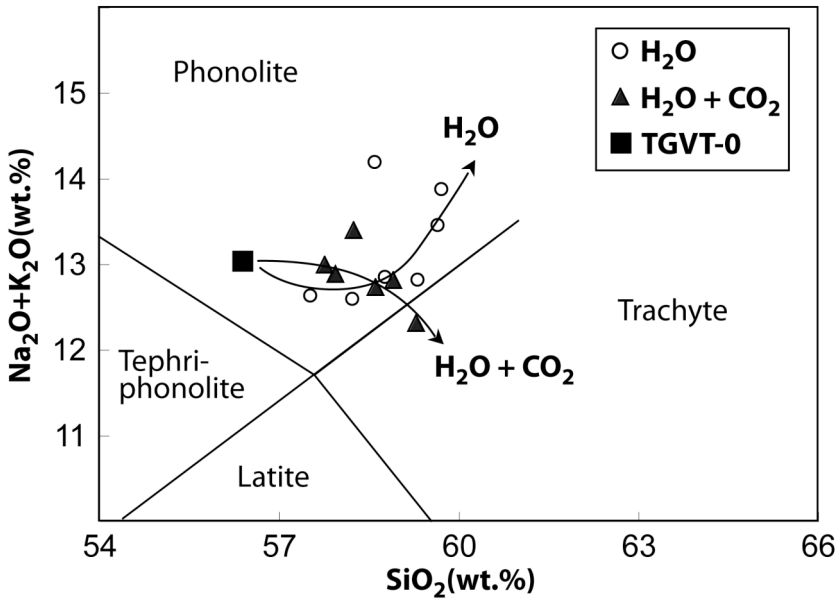

Figure 5.18 - TAS diagram showing the liquid line of descent reproduced by phase equilibria experiments performed with phonolite starting material. Note that in spite of the common SiO_2 enrichment trend, differentiation in CO_2-bearing experiments produces a transition toward the field of trachyte, whereas in CO_2-free experiments the glass composition remains in the phonolite field.

Implications for trachy-phonolitic magmatic systems of central Italy

H_2O- and CO_2-bearing experiments may shed light on a debated question concerning the phonolite-trachyte transition of differentiated magmas feeding explosive eruptions of alkaline volcanism of central Italy (e.g., Vulsini, Campi Flegrei, Vesuvio, Roccamonfina; Figure 5.19). These eruptions are indeed characterized by bimodal phonolitic/trachytic products, whether the magmas is characterized by prevailing leucite or sanidine, respectively (e.g. Vulsini; Palladino and Agosta, 1997). These compositional variations produce in the liquid line of descent of alkaline suites, the transition from tephri-phonolite to latite and from phonolite to trachyte in the TAS diagram (Figure 5.19). Such variations may be interpreted in the light of the different condition of crystallization occurring in the late stages of the differentiation, possibly related to the different depth of the shallow reservoirs and concentration of volatiles (interaction with the substrate). In particular, differentiated phonolitic magmas may further evolve into trachytes if limited amounts of CO_2 are dissolved into the melt from the environment. This may happen in presence of a complex lithological variability (e.g., carbonate and marly rocks), thus constraining the depth where differentiated magmas evolve. In particular, the lithological setting of volcanic district of central Italy constrains the shallow magma systems into a depth range of 0-7 km, roughly corresponding to the pressure range 0-200 MPa.

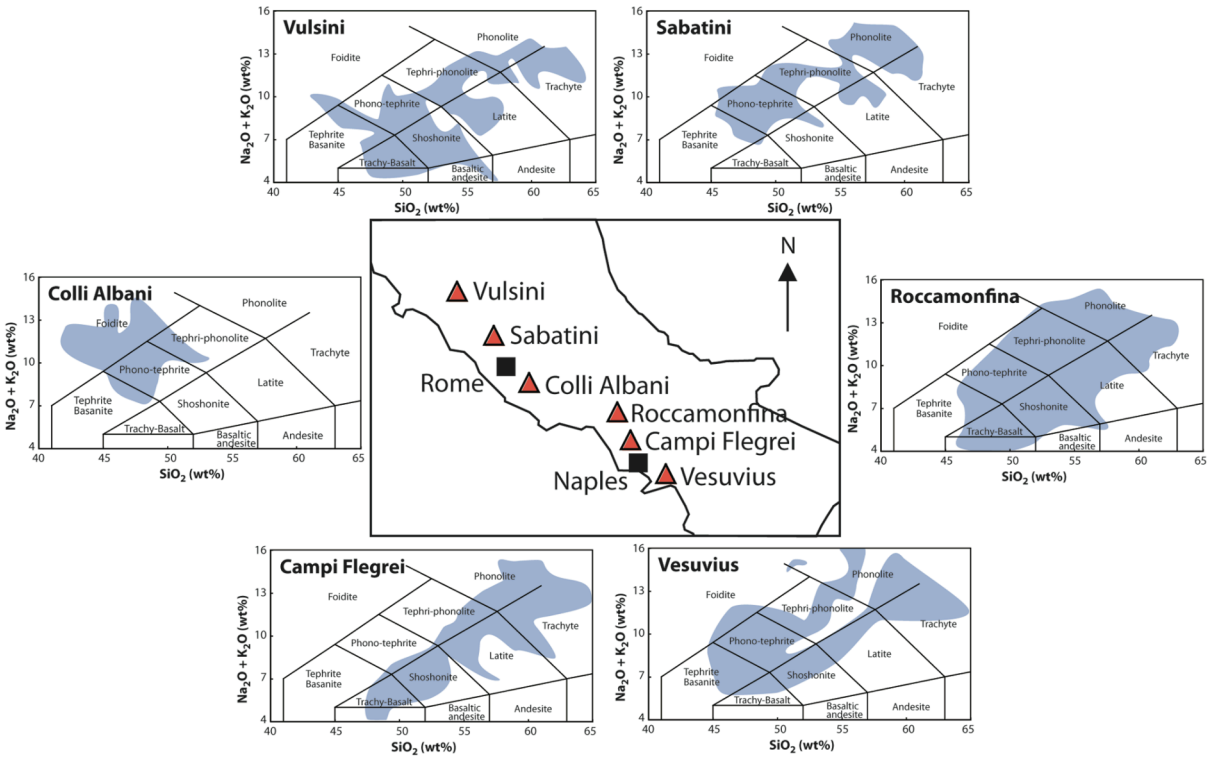

Figure 5.19 - Sketch map of volcanic district of central Italy, showing the bulk composition of erupted products (data from Lustrino et al., 2011). Note how the liquid lines of descent overlap both the fields of phonolite and trachyte (with the exception of Alban Hills), forming branches directed toward SiO_2-richer and alkali-depleted compositions.

The case of Sabatini vs. Colli Albani

Taking a look into a more general context of the magmatism of the Roman Province, it is noteworthy that all the volcanic districts share a K-basaltic parental magma (Conte et al., 2009; Gaeta et al., 2009). Moreover, undifferentiated or poorly differentiated magmas share a common geochemical signature in terms of REE and isotopic ratios (Figure 2.5; Peccerillo, 2005), thus reflecting a homogeneous source region in the mantle for these magmas. The geochemical homogeneity of the primitive/undifferentiated rocks of the Roman Province set against the chemical variability of the differentiated magmas (foidite to trachyte and phonolite). As stated above, the chemical variability of erupted magmas may actually be interpreted in light of the lithological heterogeneity of the crustal rocks and their interaction with the evolving magmas. On these grounds, the liquid lines of descent that characterize the volcanic districts in the Roman Province are explained by means of the different lithological substrate intercepted by primitive magmas during their ascent (and stoping) toward the surface. Taking as example the case of Sabatini and Colli Albani volcanic districts, it is apparent how compositions of erupted products and style of eruptive activity (areal *vs.* central

activity) are very different, although the short horizontal distance between them (less than 50 km; Figure 5.20). The divergence of the liquid lines of the two volcanic districts can be explained by considering the different lithology of the substratum hosting the shallow magma reservoirs and its effects on magma differentiation. Data from geophysical studies (Chiarabba et al., 1997) and geological surveys (Fazzini, 1972; Funiciello and Parotto, 1978; Civitelli and Corda, 1993; de Rita et al., 1993) revealed a very different lithological succession below the volcanic edifices of Sabatini and Colli Albani (Figure 5.21). On one hand, the SVD grew up over a sequence of silicoclastic rocks (Allochthonous Succession of Civitelli and Corda, 1993) laying over a Mesozoic carbonate succession (Basal Carbonate Succession of Mariotti, 1993). On the other hand, a 7-8 km-thick sequence of Mesozoic carbonate extends up to less than 1 km below the Colli Albani area (Chiarabba et al., 1997). Moreover, *horst* structures in the western sector (i.e., Ciampino) raised the Mesozoic carbonate succession at very shallow depth, favouring the late hydromagmatic activity of the Colli Albani (Funiciello and Parotto, 1978).

Accordingly with the variable stratigraphy of Meso-Cenozoic successions in the area and the magma pressure estimates for large explosive eruptions (100 to 200 MPa; Palladino et al., 2001; Masotta et al., 2010; Figure 5.21), it is possible to locate the feeder magma of large explosive eruptions of Sabatini and Colli Albani in silicoclastic and carbonatic rocks, respectively. Further evidences of the different lithology come from the deposits associated to these eruptions, showing abundant thermo-metamorphosed sedimentary clasts providing evidences on the nature of the hosting rocks. In the case of Colli Albani, for example, the occurrence of skarn and carbonate lithics in pyroclastic deposits led several authors to explain the uncommon differentiation toward SiO_2-undersaturated compositions (K-foidite), by means of carbonate assimilation (Mollo et al., 2010 and references therein). Conversely, carbonate assimilation has never been demonstrated in SVD, in which deposits thermo-metamorphosed lithics of silicoclastic nature are more common than carbonatic clasts.

Notably, it has been already pointed out that during their eruptive history, both SVD and CAVD were active during narrow overlapped periods of time, suggesting that the structural evolution of central Italy may have played a central role in controlling the eruptions. This moreover constrains the shallow depth of the magma systems feeding explosive eruptions and, hence, the importance of the interaction between differentiated magmas and crustal rocks.

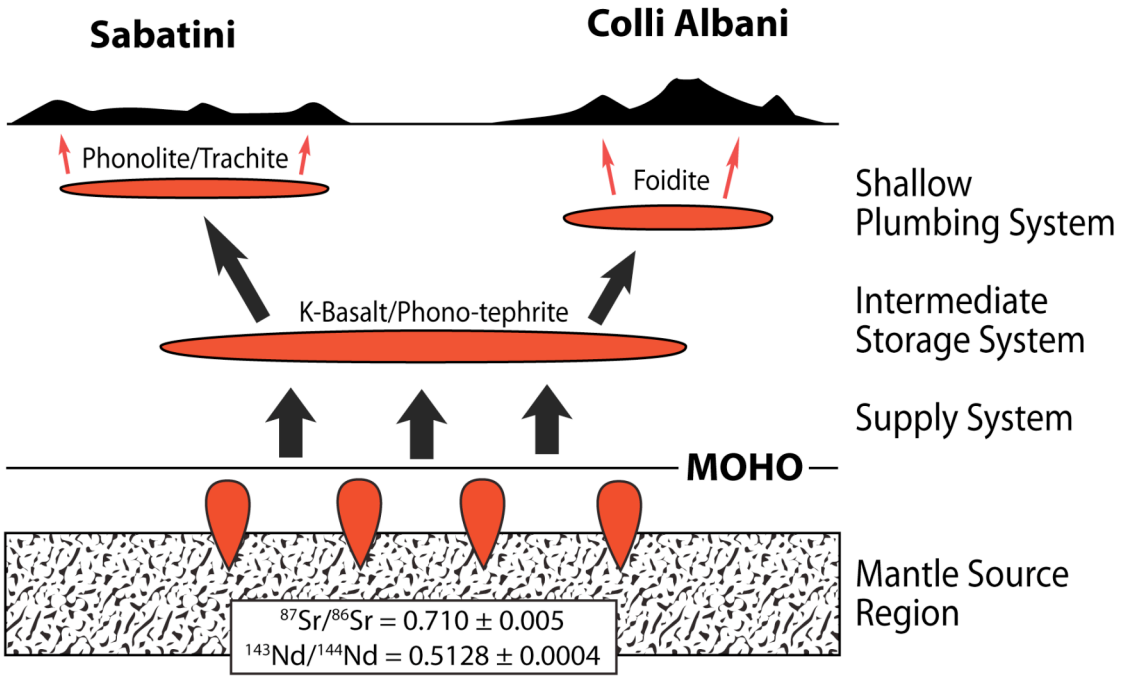

Figure 5.20 - Sketch diagram representative of the hypothesized plumbing system for Sabatini and Colli Albani volcanic districts. The analogue geochemical signature of primitive products (isotopic ratios from Peccerillo, 2005) as well as the theorized K-Basaltic parental composition indicates the existence of a shared Intermediate Storage System (sensu Scandone et al., 2007), feeding two separates Shallow Plumbing Systems. Although there are no available geophysical data demonstrating the existence of a deep sill shaped layer, this has been observed by seismic studies (Auger et al., 2001; De Natale et al., 2001) on the Vesuvio and Campi Flegrei volcanic systems, whose cases are analogue to those of Sabatini and Colli Albani.

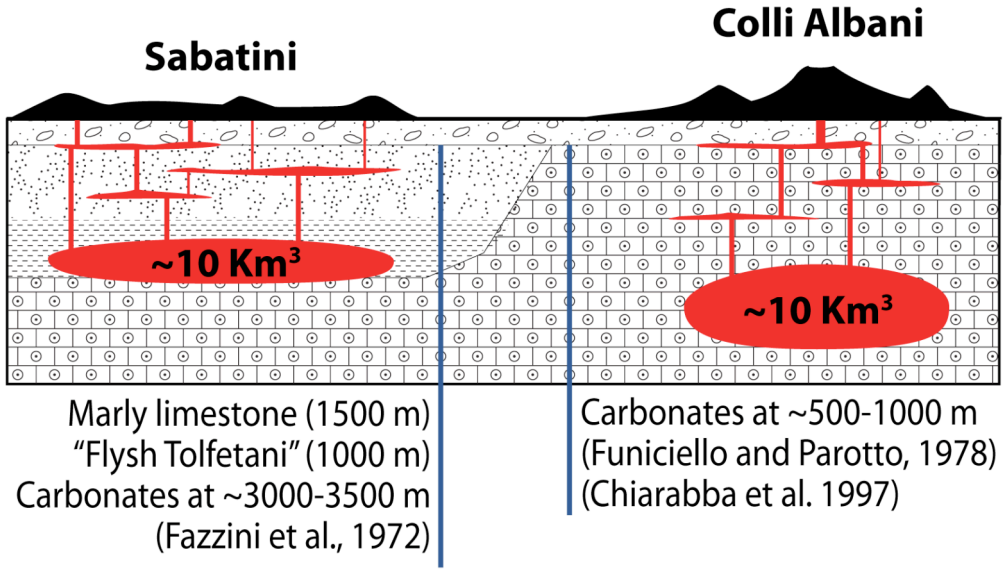

Figure 5.21 - Sketch diagram representative of the substrate rocks of Sabatini and Colli Albani volcanic districts and magma chambers of Tufo Giallo della Via Tiberina (Masotta et al., 2010) and Tufo di Trigoria-Tor de Cenci (Palladino et al., 2001). The location and volume of magma reservoirs have been drawn accordingly with the pressure and volumes estimates of the feeder magma.

6. Conclusions

Large explosive eruptions are typical in the activity of Sabatini Volcanic District. These eruptions produced texturally zoned, but compositionally homogeneous deposits, characterized by abundant crystal-poor juvenile clasts at the bottom of the stratigraphic sequence and by crystal-rich ones at the top. In order to explain such features, juvenile clasts representative of these deposits were collected and analyzed. In particular, the Tufo Giallo della Via Tiberina eruptions were investigated in detail. The combined use of petrology, MELTS simulations and experimental petrology allowed constraining the magmatic differentiation and the pre-eruptive conditions of the SVD magmatic system, as well as the crystal-melt separation processes leading to the origin of crystal-poor differentiated magma. The results obtained from this study can be summarized as follows:

1) Differentiated magmas feeding large explosive eruptions of SVD are essentially phonolites plus rarer trachytes; less differentiated products, mostly phono-tephritic in composition, are commonly erupted during the post-caldera activity; compositions intermediate between phono-tephrites and phonolites are poorly represented. This compositional gap in the liquid line of descent of SVD magmas is interpreted in the light of a two-stages (shallow *vs.* deep) plumbing system. In analogy with other volcanic systems worldwide, the shallow thermally zoned magma chamber feeds the large explosive eruptions of SVD.
2) Lithic enclaves provide insights into thermally zoned system, being representative of the so-called "solidification fronts".
3) Phase equilibria experiments have constrained the SVD liquid line of descent. In particular, in these experiments phonolitic composition, matching that of natural, differentiated products, is obtained below 950 °C after a minimum of 30 vol.% crystallization of an intermediate (tephri-phonolite) starting material.
4) T-gradient experiments have confirmed the liquid line of descent obtained by phase equilibria experiments and, moreover, have demonstrated that phonolitic interstitial melt forms in a solidification front and is then upward extracted during the collapse of the rigid crystal framework.
5) The matching between natural and experimental textures, as well as the stratigraphic relations between crystal-poor and crystal-rich textures in both natural and experimental products, indicate the collapse of the solidification front as a suitable mechanism producing crystal-poor, differentiated magmas.
6) Geothermometry, MELTS simulations, and experimental petrology allowed

estimating the pre-eruptive conditions of SVD phonolitic systems. Pre-eruptive temperature estimates range from 890 to 940 °C; H_2O content in the crystal-poor magma reached values up to 4-5 wt.% (H_2O-saturation conditions), consequently to diffusion from the cooler, crystal-rich magma.

7) Phase equilibria experiments performed with phonolite starting material indicate that limited amounts of CO_2 dissolved in the melt may produce the transition from phonolite to trachyte observed in products of the SVD and other Italian volcanic districts. This evidence constrains the low-pressure differentiation of alkaline magmas of central Italy and the effect of magma-substrate interaction.

References

Ablay GJ, Ernst GGJ, Martí J, Sparks RSJ (1995) The ~2 ka subplinian eruption of Montaña Blanca, Tenerife. Bull Volcanol 57:337-355

Alvarez W (1972) The Treia Valley north of Rome: volcanic stratigraphy, topographic evolution, and geological influences on human settlement. Geol Rom 11:153-176

Anderson AT, Swihart GH, Artioli G, Geiger CA (1984) Segregation vesicles, gas filter-pressing, and igneous differentiation. J Geol 92:55-72

Andujar J, Costa F, Martí J (2010) Magma storage conditions of the last eruption of Teide volcano (Canary Islands, Spain). Bull Volcanol 72:381-395

Andujar J, Costa F, Martí J, Wolff JA, Carroll MR (2008) Experimental constraints on pre-eruptive conditions of phonolitic magma from the caldera-forming El Abrigo eruption, Tenerife (Canary Islands). Chem Geol 257:173-191

Annen C (2009) From plutons to magma chambers: Thermal constraints on the accumulation of eruptible silicic magma in the upper crust. Earth Planet Sci Lett 284:409-416

Auger E, Gasparini P, Virieux J, Zollo A (2001) Seismic evidence of an extended magmatic sill under Mt. Vesuvius. Science 294:1510-1512

Avanzinelli R, Lustrino M, Mattei M, Melluso L, Conticelli L (2009) Potassic and ultrapotassic magmatism in the circum-Tyrrhenian region: Significance of carbonated pelitic vs. pelitic sediment recycling at destructive plate margins. Lithos 113:213-227.

Bachmann O, Bergantz GW (2004) On the origin of crystal-poor rhyolites: extracted from batholithic crystal mushes. J Petrol 45:1565-1582

Baker DR, Freda C (1999) Ising models of undercooled binary system crystallization: comparison with experimental and pegmatite textures. Am Mineral 84:725-732

Baker DR, Freda C (2001) Eutectic crystallization in the undercooled Orthoclase-Quartz-H_2O system: experiments and simulations. Eur J Mineral 13:453-466

Baldi P, Funiciello R, Locardi E, Parotto M (1976) Voicanologic and structural study of the Cesano geothermal area (Rome, Italy). Int. Congr. on Thermal Waters, Geothermal Energy and Volcanism of the Mediterranean Area, Athens Proc Geotherm Energy 1:43-55

Barberi F, Buonasorte G, Cioni R, Fiordelisi A, Foresi L, Iaccarino S, Laurenzi MA, Sbrana A, Vernia L, Villa IM (1994) Plio-Pleistocene geological evolution of the geothermal area of Tuscany and Latium. Mem Descr Carta Geol It 49:77-134

Barnea E, Mizrahi J (1973) A generalized approach to the fluid dynamics of particulate systems. Part I. General correlation for fluidization and sedimentation in solid multiparticulate systems. Chem Eng Journ 5:171-189

Bartolini C, Bernini M., et al. (1982) Carta neotettonica dell'Appennino settentrionale. Note illustrative. Boll Soc Geol It 101:523-549

Battaglia S, Gherardi F, Gianelli G, Leoni L, Origlia F (2007) Clay mineral reactions in an active geothermal area (Mt. Amiata, southern Tuscany, Italy). Clay Minerals 42:353-372

Berndt J, Holtz F, Koepke J (2001) Experimental constraints on storage conditions in the chemically zoned phonolitic magma chamber of the Laacher See volcano. Contrib Mineral Petrol 140:469-486

Bianchi I, Agostinetti NP, De Gori P, Chiarabba C (2008) Deep structure of the Colli Albani volcanic district (central Italy) from receiver function analysis. J Geophys Res 113: B09313

Biasini A, Buonasorte G, Ciccacci S, Fredi P, Lupia Palmieri E (1993) Geomorphological characteristics. In: Di Filippo, M. (Ed.), Sabatini volcanic complex. In: Quad Ric Sci, Vol 114. Progetto Finalizzato Geodinamica C.N.R, Roma, 81-94

Blake S (1981) Eruption from zoned magma chambers. J Geol Soc, London 138:281-287

Blake S (1984) Volatile oversaturation during the evolution of silicic magma chambers as an eruption trigger. J Geophys Res 89:8237-8244

Blake S, Ivey GN (1986) Density and viscosity gradients in zoned magma chambers, and their influence withdrawal dynamics. J Volcanol Geotherm Res 30:201-230

Bowen NL (1928) The Evolution of Igneous Rocks. Dover, New York

Brophy JG (2009) Decompression and H_2O exsolution driven crystallization and fractionation: development of a new model for low pressure fractional crystallization in calc-alkaline magmatic systems. Contrib Mineral Petrol 157:797-811

Baldi P, Decandia FA, Lazzarotto A, Calamai A (1974) Studio geologico del substrato della copertura vulcanica laziale nella zona dei laghi di Bolsena, Vico e Bracciano. Mem Soc Geol It 13:575-606

Buonasorte G, Fiordelisi A, Pandeli E, Rossi U, Sollevanti F (1987) Stratigraphic correlations and structural setting of the pre-neoautochthonous sedimentary sequences of Northen Latium. Per Mineral 56:111-122

Campbell IH (1987) Distribution of orthoeumulate textures in the Jimberlana Intrusion. J Geol 95:35-54

Capitanio F, Mottana A (1998) Sanidine holocrystalline ejecta from central Sabatini Volcanic District, Latium (Italy). II. Intergranular ejecta and minerogenetic deductions. Rend Fis Acc Lincei 9:125:137

Carminati E, Doglioni C (2005) Mediterranean tectonics. In: Encyclopedia of Geology, Elsevier 135-146

Carminati E, Negredo AM, Valera JL, Doglioni C (2005) Subduction-related intermediate-depth and deep seismicity in Italy: insights from thermal and rheological modeling. Phys Earth Planet Int 149:65-79

Carminati E, Lustrino M, Cuffaro M, Doglioni C (2010) Tectonics, magmatism and geodynamics of Italy. What we know and what we imagine. J Virtual Explorer, Electronic Edition, ISSN 1441-8142, volume 36, paper 9 In: (Eds.) Marco Beltrando, Angelo Peccerillo, Massimo Mattei, Sandro Conticelli, and Carlo Doglioni, The Geology of Italy: tectonics and life along plate margins, 2010.

Cashman KV, Marsh BD (1988) Crystal size distribution (CSD) in rocks and the kinetics and dynamics of crystallization II: Makaopuhi lava lake. Contrib Mineral Petrol 99:292-305

Cashman KV (1992) Groundmass crystallization of Mount St Helens dacites, 1980-1986: a tool for interpreting shallow magmatic processes. Contrib Mineral Petrol 109:431-449

Cashman KV (1993) Relationship between plagioclase crystallization and cooling rate in basaltic melts. Contrib Mineral Petrol 113:126-142

Castellarin A, Colacicchi R, Praturlon A, Cantelli C (1982) The Jurassic-Lower Pliocene history of the Ancona-Anzio line (Central Italy). Mem Soc Geol It 24:243-260

Cavazza W, Wezel FC (2003) The Mediterranean region. A geological primer. Episodes 26:160-168

Chen CF, Turner JS (1980) Crystallization in double-diffusive system. J Geophys Res 85:2573-2593

Chiarabba C, Amato A, Delaney PT (1997) Crustal structure, evolution, and volcanic unrest of the Alban Hills, Central Italy. Bull Volcanol 59:161-170

Cioni R, Sbrana A, Bertagnini A, Buonasorte A, Landi P, Rossi U, Salvati L (1987) Tephrostratigraphic correlations in the Vulsini, Vico and Sabati ni volcanic successions. Per Mineral 56:137-155.

Cioni R (1993) Il Complesso di Bolsena e il vulcanismo alcalino-potassico del Lazio settentrionale. Unpubl. PhD Thesis, University of Pisa, Italy, pp. 272

Cioni R, Civetta L, Marianelli P, Metrich N, Santacroce R, Sbrana A (1995) Compositional layering and syn-eruptive mixing of periodically refilled shallow magma chamber: the A.D. 79 Plinian eruption of Vesuvius. J Petrol 36:739-776

Civetta L, Innocenti, F, Manetti P, Peccerillo A, Poli G (1981) Geochemical characteristics of potassic volcanics from Mt. Ernici (Southern, Latium, Italy). Contrib Mineral Petrol 78:37-47

Civitelli G, Corda L (1993) The allochthonous succession. In: Di Filippo, M. (Ed.), Sabatini volcanic complex. In: Quad Ric Sci, Vol 114. Progetto Finalizzato Geodinamica C.N.R, Roma, pp. 19-28

Conte AM, Dolfi D, Gaeta M, Misiti V, Mollo S, Perinelli C (2009) Experimental constraints on evolution of leucite–basanite magma at 1 and 10–4 GPa: implications for parental compositions of Roman high-potassium magmas. Eur J Mineral 214:763-782

Conticelli S, Peccerillo A (1992) Petrology and geochemistry of potassic and ultrapotassic volcanism in Central Italy: petrogenesis and inferences on the evolution of the mantle sources. Lithos 28:221-240

Conticelli S, Francalanci L, Manetti P, Cioni R, Sbrana A (1997) Petrology and geochemistry of the ultrapotassic rocks from the Sabatini Volcanic District, central Italy: the role of evolutionary processes in the genesis of variably enriched alkaline magmas. J Volcanol Geotherm Res 75:107-136

Conticelli S, Laurenzi MA, Giordano G, Mattei M, Avanzinelli R, Melluso L, Tommasini S, Boari E, Cifelli F, Perini G (2010) Leucite-bearing (kamafugitic/leucititic) and -free (lamproitic) ultrapotassic rocks and associated shoshonites from Italy: constraints on petrogenesis and geodynamics. J Virtual Explorer, Electronic Edition, ISSN 1441-8142, volume 36, paper 20 In: (Eds.) Marco Beltrando, Angelo Peccerillo, Massimo Mattei, Sandro Conticelli, and Carlo Doglioni, The Geology of Italy: tectonics and life along plate margins, 2010.

Corda L, de Rita D, Tecce F, Sposato A (1978) Le piroclastiti del sistema vulcanico Sabatino: il complesso dei Tufi Stratificati Varicolori de La Storta. Boll Soc Geol It 97:353-366

Cox HG, Hawkesworth CJ, O'Nions RK, Appleton JD (1976) Isotopic evidence for the derivation of some Roman Region volcanics from anomalously enriched mantle. Contrib Mineral Petrol 56:173-180

Crisp J, Cashman KV, Bonini JA, Hougen SB, Pieri DC (1994) Crystallization history of the 1984 Mauna Loa lava flow. J Geophys Res 99:7177-7198

Cundari A (1979) Petrogenesis of Leucite-bearing lavas in the Roman volcanic region, Italy. The Sabatini Lavas. Contrib Mineral Petrol 70:9-21

De Natale G, Troise C, Pingue F, De Gori P, Chiarabba C (2001) Structure and dynamics of the Somma-Vesuvius volcanic complex. Mineral Petrol 73:5-22

de Rita D, Sposato A (1986) Correlazione tra eventi esplosivi e assetto strutturale del substrato sedimentario nel complesso vulcanico Sabatino. Mem Soc Geol It 35:727-733

de Rita D, Zanetti G (1986) I centri esplosivi di Baccano e Stracciappe (Sabatini orientali, Roma): analogie e differenze della modellistica esplosiva in funzione del grado di interazione acqua/magma. Mem Soc Geol It 35:689-697

de Rita D, Funiciello R, Parotto M (1988) Carta geologica del Complesso vulcanico dei Colli Albani, Progetto Finalizzato Geodinamica. C.N.R., Roma

de Rita D, Funiciello R, Corda L, Sposato A, Rossi U (1993) Volcanic units. In: Di Filippo, M. (Ed.), Sabatini volcanic complex. In: Quad Ric Sci, Vol 114. Progetto Finalizzato Geodinamica C.N.R, Roma, 33-79

de Rita D, Bertagnini A, Carboni G, Ciccacci S, Di Filippo M, Faccenna C, Fredi P, Funiciello R, Landi P, Sciacca P, Vannucci N, Zarlenga F (1994) Geological petrological evolution of the Ceriti Mountains Area (Latium, central Italy). Mem Descr Carta Geol It 49:291-322

de Rita D, Bertagnini A, Faccenna C, Landi P, Rosa C, Zarlenga F, Di Filippo M, Carboni MG (1997) Evoluzione geopetrografica-strutturale dell'area tolfetana. Boll Soc Geol It 116:143-175

Daly RA (1925) The geology of Ascension Island. Am Academy Arts Sci Proceed 60:1-80

Davis RH, Acrivos A (1985) Sedimentation of noncolloidal particles at low Reynolds numbers. Ann Rev Fluid Mechanics 17:91-118

Devine JD, Gardner JE, Brack HP, Layne GD, Rutherford MJ (1995) Comparison of microanalytical methods for estimating H_2O contents of silicic volcanic glasses. Am Mineral 80:319-328

Devoti C, Riguzzi F, Cuffaro M, Doglioni C (2008) New GPS constraints on the kinematics of the Apennines subduction. Earth Planet Sci Lett 273:163-174

Dewey JF, Helman ML, Turco E, Hutton DHW, Knott SD (1989) Kinematics of the western Mediterranean. In Coward MP, Dietrich D, Park RG (Eds.), Alpine tectonics, Geol Soc London Spec Publ, 45:421-443

Di Filippo M, Toro B (1993) Gravimetric study of Sabatini area. In: Di Filippo, M. (Ed.), Sabatini volcanic complex. In: Quad Ric Sci, Vol 114. Progetto Finalizzato Geodinamica C.N.R, Roma, pp. 95-99

Di Filippo M (1993) Sabatini volcanic complex. Quad Ric Sci, Vol 114. Progetto Finalizzato Geodinamica C.N.R., Roma, pp. 109

Doglioni C, Harabaglia P, Merlini S, Mongelli F, Peccerillo A, Piromallo C (1999) Orogens and slabs vs. their direction of subduction. Earth Sci Rev 45:167-208

Dufek J, Bachmann O (2010) Quantum magmatism: Magmatic compositional gaps generated by melt-crystal dynamics. Geology 38:687-690

Dunbar NW, Hervig RL (1992) Petrogenesis and Volatile Stratigraphy of the Bishop Tuff: Evidence From Melt Inclusion Analysis. J Geophys Res 97:15129-15150

Fabbrizio A, Carroll MR (2008) Experimental constraints on the differentiation process and pre-eruptive conditions in the magmatic system of Phlegrean Fields (Naples, Italy). J Volcanol Geotherm Res 171:88-102

Facchinelli V, Gaeta M (1992) Indicazioni petrogenetiche dai granati birifrangenti dei proietti sialici nelle vulcaniti alcalino potassiche dei Monti Sabatini (Lazio). Rendiconti Lincei 34:295-310

Fazzini P, Gelmini R, Mantovani P, Pellegrini M (1972) Geologia dei Monti della Tolfa (Lazio settentrionale; prov. di Viterbo e Roma). Mem Soc Geol It 11:65-144

Fornaseri M, Scherillo A, Ventriglia U (1963) La regione vulcanica dei Colli Albani. CNR, Rome, pp. 561

Fornaseri M (1985) Geochronology of volcanic rocks from Latium (Italy). Rend Soc Ital Mineral Petrol 40:73-106

Franzini M, Leoni M, Saitta M (1972) A simple method to evaluate the matrix effects in X-ray fluorescence analysis. Spectrometry 1:151-154

Freise M, Holtz F, Koepke J, Scoates J, Leyrith H (2003) Experimental constraints on the storage conditions of phonolites from Kerguelen Archipelago. Contrib Mineral Petrol 145:659-672

Funiciello R, Parotto M (1978) Il substrato sedimentario nell'area dei Colli Albani: considerazioni geodinamiche e paleogeografiche sul margine tirrenico dell'Appennino centrale. Geol Rom 17:233-287

Funiciello R, Mariotti G, Parotto M, Preite-Martinez M, Tecce F, Toneatti R, Turi B (1979) Geology, mineralogy and stable isotope geochemistry of the Cesano geothermal field (Sabatini Mts. Volcanic system, Northern Latium, Italy). Geothermics 8:55-73

Freda C, Baker DR, Ottolini L (2001) Reduction of water loss from gold-palladium capsules during piston-cylinder experiments by use of pyrophyllite powder. Am Mineral 86:234-237

Freda C, Gaeta M, Misiti V, Mollo S, Dolfi D, Scarlato P (2008) Magma-carbonate interaction: an experimental study on ultrapotassic rocks from Alban Hills (Central Italy). Lithos 101:397-415

Gaeta M, Di Rocco T, Freda C (2009) Carbonate assimilation in open magmatic systems: the role of melt-bearing skarns and cumulate-forming processes. J Petrol 50:361-385

Ghiorso MS, Sack RO (1995) Chemical mass transfer in magmatic processes IV. A revised and internally consistent thermodynamic model for the interpolation and extrapolation of liquid–solid equilibria in magmatic systems at elevated temperatures and pressures. Contrib Mineral Petrol 119:197-212

Giordano D, Russell JK, Dingwell DB (2008) Viscosity of magmatic liquids: a model. Earth Planet Sci Lett 271:123-134

Gueguen E, Doglioni C, Fernandez M (1998) On the post 25 Ma geodynamic evolution of the western Mediterranean. Tectonophysics 298: 259-269

Hammer JE, Rutherford MJ (2002) An experimental study of the kinetics of decompression-induced crystallization in silicic melt. J Geophys Res 107:1-24

Harms E, Gardner JE, Schminke HU (2004) Phase equilibria of the Lower Laacher See Tephra (East Eifel, Germany): constraints on pre-eruptive storage conditions of a phonolitic magma reservoir. J Volcanol Geotherm Res 134:135-148

Hermes OD, Cornell WC (1981) Quenched crystal mush and associated magma compositions as indicated by intercumulus glasses from Mt. Vesuvius, Italy. J Volcanol Geotherm Res 9:133-149

Holness MB, Bunbury JM (2006) Insights into continental rift-related magma chambers: Cognate nodules from the Kula Volcanic Province, Western Turkey. J Volcanol Geotherm Res 153:241-261

Horvath F, Berckheimer H (1982) Mediterranean backarc-basins. In: Berckheimer H, Hsü K (Eds.), Alpine-Mediterranean-Geodynamics. AGU Geodynamics Series, pp. 141-163

Huang F., Lundstrom CC, Glessner J, Ianno A, Boudreau A, Li J, Ferrè EC, Marshak S, DeFrates J (2009) Chemical and isotopic fractionation of wet andesite in a temperature gradient: Experiments and models suggesting a new mechanism of magma differentiation. Geochim Cosmochim Acta 73:729-749.

Humphreys MCS, Blundy JD, Sparks RSJ (2008) Shallow-level decompression crystallization and deep magma supply at Shiveluch Volcano. Contrib Mineral Petrol 155:45-61

Humphreys MCS, Holness MB (2010) Melt-rich segregations in the Skaergaard Marginal Border Series: Tearing of a vertical silicate mush. Lithos 119:181-192

Huppert HE, Woods AW (2002) The role of volatiles in magma chamber dynamics. Nature 420:493-495

Jackson MD, Cheadle MJ, Atherton MP (2003) Quantitative modelling of granitic melt generation and segregation in the continental crust. J Geophys Res 108:2332

Karner DB, Renne PR (1998) $^{40}Ar/^{39}Ar$ geochronology of Roman Province tephra in the Tiber River Valley: age calibration of Middle Pleistocene sea-level changes. Geol Soc Am Bull 110:740-747

Karner DB, Marra F, Renne PR (2001) The history of the Monti Sabatini and Alban Hills volcanoes: groundwork for assessing volcanic-tectonic hazards for Rome. J Volcanol Geotherm Res 107:185-21

Kirkpatrick RJ (1981) Kinetics of crystallization of igneous rocks. Rev Mineral Geochem 8:321-395

Lange RA, Frey HM, Hector J (2009) A thermodynamic model for the plagioclase-liquid hygrometer/thermometer. Am Mineral 94:494-506

Lesher CE, Walker D (1988) Cumulate maturation and melt migration in a temperature gradient. J Geophys Res 93:10295-10311

Locardi E, Nicholich R (1988) Geodinamica del Tirreno e dell'Appennino centro-meridionale: la nuova carta della Moho. Mem Soc Geol It 41:121-140

Lombardi G, Nicoletti M, Petrucciani C (1974) Età delle vulcaniti dei complessi Tolfetano, Cerite e Manziate (Lazio Nord-occidentale). Per Mineral 43:351-376

Lombardi G, Meucci C (2006) Il Tufo Giallo della Via Tiberina (Roma) utilizzato nei monumenti romani. Rend Fis Acc Lincei 17:263-287

Lustrino M, Morra V, Fedele L, Serracino M (2007) The transition between 'orogenic' and 'anorogenic' magmatism in the western Mediterranean area: The Middle Miocene volcanic rocks of Isola del Toro (SW Sardinia, Italy). Terra Nova, 19:148-159

Lustrino M, Duggen S, Rosenberg CL (2011) The Central-Western Mediterranean: Anomalous igneous activity in an anomalous collisional tectonic setting. Earth Sci Rev 104:1-40

Mariotti G (1993) Basal carbonate succession. In: Di Filippo, M. (Ed.), Sabatini volcanic complex. In: Quad Ric Sci, Vol 114. Progetto Finalizzato Geodinamica C.N.R, Roma, pp. 11-18

Marra F, Freda C, Scarlato P, Taddeucci J, Karner DB, Renne PR, Gaeta M, Palladino DM, Trigila R, Cavarretta G (2003) The post-caldera phase of activity in the Alban Hills Volcanic District (Italy): $^{40}Ar/^{39}Ar$ geochronology and insights into magma evolution. Bull Volcanol 65:227-247

Marsh BD (1996) Solidification fronts and magmatic evolution. Mineral Mag 60:5-40

Marsh BD (2002) On bimodal differentiation by solidification front instability in basaltic magmas, part 1: basic mechanics. Geochim Cosmochim Acta 66:2211-2229

Masotta M, Gaeta M, Gozzi F, Marra F, Palladino DM, Sottili G (2010) H_2O- and temperature-zoning in magma chambers: the example of the Tufo Giallo della Via Tiberina eruptions (Sabatini Volcanic District, central Italy). Lithos 118:119-130

Masotta M, Freda C, Gaeta M (2011) Origin of crystal-poor, differentiated magmas: insights from thermal gradient experiments. Contrib Mineral Petrol in press, DOI 10.1007/s00410-011-0658-8.

Mastrolorenzo G, Pappalardo L (2006) Magma degassing and crystallization processes during eruptions of high-risk Neapolitan-volcanoes: Evidence of common equilibrium rising processes in alkaline magmas. J Volcanol Geotherm Res 83:219-239

Mattias PP, Ventriglia U (1970) La regione vulcanica dei Monti Sabatini. Mem Soc Geol It 9:331-384

McBirney AR, Baker BH, Nilson RH (1985) Liquid fractionation. Part 1: Basic principles and experimental simulations. J Volcanol Geotherm Res 24:1-24

McBirney AR, Noyes RM (1979) Crystallization and layering of the Skaergaard Intrusion. J Petrol 20:487-554

McKenzie D (1984). The generation and compaction of partially molten rock. J Petrol 25:713–765

Mollo S, Gaeta M, Freda C, Di Rocco T, Misiti V, Scarlato P (2010) Carbonate assimilation in magmas: a reappraisal based on experimental petrology. Lithos 114:503-514

Mollo S, Lanzafame G, Masotta M, Iezzi G, Ferlito C, Scarlato P (2011) Cooling history of a dike as revealed by mineral chemistry: A case study from Mt. Etna volcano. Chem Geol 288:39-52

Naimo D, Balassone G, Beran A, Amalfitano C, Imperato M, Stanzione D (2003) Garnets in volcanic breccias of the Phlegraean Fields (southern Italy): mineralogical, geochemical and genetic features. Mineral Petrol 77:259-270

Nimis P, Ulmer P (1998) Clinopyroxene geobarometry of magmatic rocks Part 1: An expanded structural geobarometer for anhydrous and hydrous, basic and ultrabasic systems. Contrib Mineral Petrol 133:122-135

Palladino DM, Agosta E (1997) Pumice fall deposits of the western Vulsini Volcanoes (central Italy). J Volcanol Geotherm Res 78:77-102

Palladino DM, Gaeta M, Marra F (2001) A large K-foiditic hydromagmatic eruption from the early activity of the Alban Hills Volcanic District, Italy. Bull Volcanol 63:345-359

Peccerillo A (1999) Multiple mantle metasomatism in central-southern Italy: geochemical effects, timing and geodynamic implications. Geology 27:315-318

Peccerillo, A (2003) Plio-Quaternary magmatism in Italy. Episodes 26:222-226

Peccerillo A (2005) Plio-Quaternary Volcanism in Italy. Springer-Verlag, Berlin Heidelberg, pp. 365

Peccerillo A, Lustrino M (2005) Compositional variations of Plio-Quaternary magmatism in the circum-Tyrrhenian area: Deep versus shallow mantle processes. Spec Paper Geol Soc of America 388:421-434

Philpotts AR, Carrol MR, Hill JM (1996) Crystal-mush compaction and the origin of pegmatitic segregation sheets in a thick flood-basalt flow in the Mesozoic Hartford Basin, Connecticut. J Petrol 37:811-836

Piochi M, Bruno PP, De Astis G (2005) Relative roles of rifting tectonics and magma ascent processes: Inferences from geophysical, structural, volcanological, and geochemical data for the Neapolitan volcanic region (southern Italy). Geochem Geophys Geosyst 6:Q07005, doi:10.1029/2004GC000885

Putirka KD, Johnson M, Kinzler R, Longhi J, Walker D (1996) Thermobarometry of mafic igneous rocks based on clinopyroxene-liquid equilibria, 0-30 kbar. Contrib Mineral Petrol 123:92-108

Putirka KD (2005). Igneous thermometers and barometers based on plagioclase + liquid equilibria: test of some existing models and new calibrations. Am Mineral 90:336-346

Putirka KD (2008) Thermometers and barometers for volcanic systems. In: Putirka, K.D., Tepley, F. (Eds.), Minerals, Inclusions, and Volcanic Processes: Reviews in Mineralogy and Geochemistry, 69, pp. 61-120

Rabinowicz M, Genthon P, Ceuleneer G, Hillairet M (2001) Compaction in a mantle mush with high melt concentrations and the generation of magma chambers. Earth Planet Sci Lett 188:313-328

Rice A (1981) Convective fractionation: a mechanism to provide cryptic zoning (macrosegregation), layering crescumulates, banded tuffs and explosive volcanism in igneous processes. J Geophys Res 86:405-417

Rosenbaum G, Lister GS, Duboz C (2002) Relative motions of Africa, Iberia and Europe during Alpine orogeny. Tectonophysics 359, 117-129

Scandone R, Cashman KV, Malone SD (2007) Magma supply, magma ascent and the style of volcanic eruptions. Earth Planet Sci Lett 253:513-529

Scherillo A (1941) Studi su alcuni tufi gialli della regione sabazia orientale. Per Mineral 12:381-417

Schmitt AK, Wetzel F, Cooper KM, Zou H, Wörner G (2010) Magmatic longevity of Laacher See Volcano (Eifel, Germany) indicated by U-Th dating of intrusive carbonatites. J Petrol 51:1053-1085

Selvaggi G, Amato A (1992) Subcrustal earthquakes in the northern Apennines (Italy): evidence for a still active subduction? Geophys Res Lett 19:2127-2130

Shea T, Larsen JF, Gurioli L, Hammer JE, Houghton BF, Cioni R (2009) Leucite crystal: surviving witnesses of magmatic processes preceding the 79 AD eruption at Vesuvius, Italy. Earth Planet Sci Lett 281:88-98

Sisson TW, Bacon CR (1999) Gas-driven filter pressing in magmas. Geology 27:613-616

Soret C (1879) Concentrations differentes d'une dissolution dont deux parties sont a' des temperatures differentes, Arch Sci Phys Nat 2:48-61

Sottili G, Palladino DM, Zanon V (2004) Plinian activity during the early eruptive history of the Sabatini Volcanic District, Central Italy. J Volcanol Geotherm Res 135:361-379

Sottili G, Palladino DM, Marra F, Jicha B, Karner DB, Renne P (2010) Geochronology of the most recent activity in the Sabatini Volcanic District, Roman Province, central Italy. J Volcanol Geotherm Res 196:20-30

Sottili G, Palladino DM, Gaeta M, Masotta M (2011) Origins and energetics of maar volcanoes: examples from the ultrapotassic Sabatini Volcanic District (Roman Province, Central Italy). Bull Volcanol, *DOI: 10.1007/s00445-011-0506-8*

Spera FJ (1984) Some numerical experiments on the withdrawal of magma from crustal reservoirs. J Geophys Res 89:8222-8236

Spera FJ, Oldenburg CM, Christiensen C, Todesco M (1995) Simulations of convection with crystallization in the system $KAlSi_2O_6$–$CaMgSi_2O_6$: implications for compositionally zoned magma bodies. Am Mineral 40:1188-1207

Sun, S. S. & McDonough, W. F. (1989). Chemical and isotopic systematic of oceanic basalts: implication for mantle composition and processes. In: Saunders, A. D. & Norry, M. G. (eds) Magmatism in the Ocean Basins. Geol Soc London, Spec Publ 42:313-345

Tait SR (1988) Samples form the crystallising boundary layer of a zoned magma chamber. Contrib Mineral Petrol 100:470-483

Tait SR, Wörner G, Van Den Bogaard P, Schminke HU (1989) Cumulate nodules as evidence for convective fractionation in a phonolite magma chamber. J Volcanol Geotherm Res 37:21-37

Tegner C, Thy P, Holness MB, Jakobsen JK, Lesher CE (2009) Differentiation and compaction in the Skaergaard intrusion. J Petrol 5:813-840

Thomas R (2000) Estimation of water contents of granite melt inclusions by confocal laser Raman microprobe spectroscopy. Am Mineral 85:868-872

Thompson RN (1977) Primary basalts and magma genesis. III. Alban Hills, Roman Comagmatic Province, Central Italy. Contrib Mineral Petrol 50:91-108

Tiepolo M, Bottazzi P, Palenzona M, Vannucci R (2003) A laser probe coupled with ICP-double-focusing sector-field mass spectrometer for in situ analysis of geological samples and U-Pb dating of zircon. Canadian Mineral 41:259-272

Turbeville BN (1993) Sidewall differentiation in an alkalic magma chamber: evidence from syenite xenoliths in tuffs of the Latera caldera, Italy. Geol Mag 130:453-470

van Achterbergh E, Ryan CG, Jackson SE, Griffin WL (2001) Data reducing software for LA-ICP-MS. Mineral Assoc Canada, Short Course Series 29, 239-243

Vance JA, Gilreath JP (1967) The effect of synneusis on phenocryst distribution patterns in some porphyritic igneous rocks. Am Mineral 52:529-536

Vernon RH (2004) A practical guide to rock microstructures. Cambridge, Cambridge University Press pp. 594

Vogt JHL (1921) The physical chemistry of the crystallization and magmatic differentiation of the igneous rocks. J Geol 29:318-350

Walker GPL (1985) Origin of coarse lithic breccias near ignimbrite source vents. J Volcanol Geotherm Res 25:157-171

Wallace PJ, Anderson Jr AT, Davis AM (1999) Gradients in H_2O, CO_2, and exsolved gas in large-volume silicic magma system: interpreting the record preserved in melt inclusions from the Bishop Tuff. J Geophys Res, 104:20097-20122

Wark DA, Hildreth W, Spear FS, Cherniak DJ, Watson EB (2007) Pre-eruption recharge of the Bishop magma system. Geology 35:235-238

Washington HS (1906) The Roman Comagmatic Region. Carnegie Inst Washington Publ 57, pp. 199

Watson EB, Wark DA, Price JD, Van Orman JA (2002) Mapping the thermal structure of solid-media pressure assembly. Contrib Mineral Petrol 142:640-652

Whittington A, Richet P, Linard Y, Holtz F (2006) The viscosity of hydrous phonolites and trachytes. Chem Geol 174:209-223

Wörner G, Schminke HU (1984) Petrogenesis of the zoned Laacher See tephra. J Petrol 25:836-851

Acknowledgements

If you have read all this manuscript and arrived at this point, you are acknowledged. If you jumped to here directly from the title, you are also acknowledged because you are supposed to know what is in between the appendix and the conclusion. If you are only curious to read something that is not science and that probably you expect to find at the end of this manuscript, you are also acknowledged because you are paying attention to my thoughts, even if you have no idea of what I've discussed so far. In any case, I appreciate your interest and you are acknowledged.

At this point, you may ask why also acknowledgements are in English. Not for those who don't speak Italian, anyway they would be able to understand that they are acknowledged just reading their name on this page…one reason is that long time ago I made a promise (someone will understand), and I hope, this thesis means that I didn't fail. Well, this doesn't mean that I never failed during these years…I failed many times and anytime I had something to learn, so, in the end, failure is not so bad as it may sound. Sometimes, before an experiment, I like to say: "failure is not an option". I like this sentence because it tells me the hundred reasons for which I failed and then, how I can avoid to fail again doing twice the same mistake…in other words, it is just to say that you never stop learning and that often a failed experiment can tell you more than a good one.

Ok, seriously, I wish to thank so many people that I cannot effort now to write a new manuscript! Then, starting from the beginning of this journey, I would like to thank my supervisors Mario and Lilli that gave me the possibility to walk on my own legs. Then all people I met along the road, because from anyone I had something to learn…Gordon, thanks for making me feel in Italy even at 40°C in the shadow. Amanda and Ramon, thanks for your hospitality and the fantastic De Longhi oven. Craig, thanks for discovering every Tuesday the secret words at the MoJo. Kurt, thanks for the beer and chicken wings (I'm sorry for the burnt plug). Amber and Erika, thanks for your presence in and out the lab. Kayla, I arrived to late to meet you at ASU but thanks for the sticker you put on Daisy. Very special thanks go to you Tracy, for teaching me to fish…and also for making me discover the dog agility.

Special thanks go to my friend Fabio, we walked together during this long journey and now I'm happy that we both reached our goal. Thanks to the friends that made everyday spent at the university a special day, so thanks to Francesco, Fernando, Carmine (split-apple), Georgia, Ameha, Veronica, Daniela, Valentina, Luca (Panda) and the two Simone (Colucci and Cocomello). Thanks to Valeria, Betta, Silvio, Andrea, Jacopo and Piergiorgio for every coffee-time I had at INGV, Andrea is also acknowledged for help during micro-analysis.

Thanks to Prof. Val Troll (Uppsala) for useful discussion on my projects and all the revisions of abstract and proposals, thanks also to his team of women (Frances, Fiona and Lara). Thanks to Dr. Anat Shahar (Carnegie Institution) for nice days I spent in DC. Thanks to Prof. Lee (Yonsei University) for nice days spent in Seoul. Thanks to Prof. Michele Lustrino and Prof. Mike Carroll for their constructive reviews of this thesis.

Finally, I wish to conclude this chapter of my life expressing my infinite gratitude to my parents, even if they decided to paint my room purple after I came back from Arizona, Tori for taking my place when I left home and Alessandra, for her patience in learning the art of cooking and for her attitude to break the silence in (too) peaceful moments.

Appendix

"Low pressure", P≥150 MPa, experiments in the piston cylinder apparatus

Abstract

We present new calibration data demonstrating that the piston cylinder apparatus is suitable for experiments at pressure as low as 150 MPa. Two new designs for the 25 mm furnace assembly have been developed and calibrated using two different calibration methods: the NaCl melting curve and the solubility of H_2O in albite and rhyolite melts. The NaCl calibration data show that positive pressure corrections of 45, 55, and 60 MPa are necessary to establish sample pressures of 300, 200, and 150 MPa, respectively. The H_2O solubility experiments in albite and rhyolite confirm the corrections determined using the NaCl calibration method and indicate that the pressure correction is the same even when operating at temperatures higher than 800°C and for 24-hours duration. The accuracy of the pressure estimate associated with the calibration methods is ±25 MPa.

The major advantage of using the new assemblies is that low pressure experiments that require rapid heating and quenching rates (e.g. volcanic and hydrothermal systems), can be performed with the same ease and precision as standard experiments for which piston cylinder is routinely used.

1. Introduction

The piston cylinder apparatus (Boyd and England, 1960) is one of the most versatile instruments operating in experimental petrology laboratories because it provides a safe, inexpensive, and easy-to-use technique for accessing high-pressure and high-temperature conditions. The operating pressure of the piston cylinder usually ranges between 0.5 and 5 GPa (Johannes et al., 1971; Holloway and Wood, 1988; Nelson and Montana, 1992), which allows Earth scientists to investigate materials and processes under deep crustal to upper mantle conditions. Incomplete compaction of the furnace assembly and thermocouple failure are typical problems in experiments performed at pressures lower than 0.5 GPa (Moore et al., 2008). Due to this operative limit, internally heated pressure vessels and cold seal pressure vessels are commonly preferred for low-pressure experiments (i.e. ≤0.5 GPa). However, unlike gas media pressure vessels, the piston cylinder apparatus offers faster heating and cooling rates, lower operating effort and maintenance, and increased safety, thereby making the device attracting for geochemical studies, including phase equilibria, volatile solubility, and chemical diffusion in volcanic systems. For these reasons, experimentalists have invested

considerable time and efforts to calibrate the piston cylinder for pressures lower than 0.5 GPa. Pressure calibration implies corrections of the nominal pressure (i.e. force applied to the piston) that generally differs from the real pressure inside the sample, due to the internal friction in the assembly. Pressure corrections vary according with operative conditions (temperature and pressure) and assembly components. Baker (2004) has demonstrated that the piston cylinder can be calibrated and operated reliably down to 400 MPa. More recently, experiments were successfully performed at a yet lower limit of 300 MPa (Moore et al., 2008; Masotta et al., 2011). In this work, two new designs of crushable MgO-Glass-NaCl furnace assemblies are used to calibrate a non-endloaded piston cylinder apparatus down to 150 MPa. Calibration methods used are the NaCl melting curve and the solubility of H_2O in albite and rhyolite melts.

2. Experimental assembly

Experiments were carried out using non-endloaded piston cylinder apparatus (QUICKpress design by Depths of the Earth Co.) at the Department of Chemistry and Biochemistry (Arizona State University, Tempe, AZ, US) and at the High Pressure High Temperature Laboratory of Experimental Volcanology and Geophysics of Istituto Nazionale di Geofisica e Vulcanologia (Rome, Italy). The calibration experiments presented in this study (Table 1) were performed using two newly designed furnace assemblies, hereafter called 19-25 mm and 25 mm assemblies, both of which are comprised of crushable MgO-borosilicate glass-NaCl components (Figure 1). The differences between the two assemblies are the diameter of the graphite furnace and the thickness of the borosilicate insulator and the NaCl cell. The 19-25 mm assembly design comprises a 11.0 mm outer diameter (OD) graphite furnace, as in the standard 19 mm assembly (see Masotta et al., 2011), but with a thicker borosilicate glass insulator and NaCl cell. The 25 mm furnace assembly design comprises a 18.2 mm OD graphite furnace and thinner borosilicate glass insulator and NaCl cell.

The larger diameter of the graphite furnace in the 25 mm assembly requires substantial current (ca. 30 ampere), when operating at high temperature (i.e. T≥1100 °C). Therefore, the assembly is best suited for experiments below 1100 °C. The 25 mm assembly also presents a slightly lower quench rate (ca. 100°C/s) as compared to that of the 19-25 mm assembly (>100°C/s). The primary advantage of using the 25 mm assembly is the large volume that can accommodate either up to four noble metal capsules of 3 mm OD or one single capsule up to 10 mm OD. Only a single capsule (up to 5 mm OD) can be accommodated in the 19-25 mm assembly.

Despite these differences, the assemblies are similar and can be prepared following a similar protocol. In both designs, the sample holder is made of crushable MgO. The space for thermocouple and capsule/s is drilled into the MgO, according to the required geometry. In the 19-25 mm assembly the thermocouple is positioned below the sample, whereas in the 25 mm, the thermocouple connection is positioned at the half-length of the furnace (Figure 1). The latter configuration offers a more accurate determination of the temperature near the capsules, since the vertical temperature gradient is roughly symmetric with respect to the furnace centre (Masotta et al., 2011).

To ensure easy extraction and cleaning of capsules after the experiment, the capsules are surrounded by either borosilicate glass powder or pyrophyllite powder. The use of pyrophyllite powder as soft supporting medium has the further advantage of inhibiting water loss from noble metal capsules (Freda et al., 2001). The furnace assembly materials give an oxygen fugacity equal to NNO+2 (Kushiro, 1990; Kawamoto and Hirose, 1994; Freda et al., 2008; Masotta et al., 2011). The sample holder is inserted in the graphite furnace, a 5 mm thick layer of powdered borosilicate glass is used to fill the space up to the top of the furnace, and the graphite lid is positioned on top. Then, thermocouple is inserted from the bottom of the assembly through the metal base plug, over which the sample holder and graphite furnace are seated. The insulating borosilicate glass sleeve and the NaCl salt cell are placed around the furnace and the complete assembly is seated on the metal base plug. The final height of the assembly is 44.7 mm (Figure 1).

Following the procedure of Moore et al. (2008), the four-bore alumina thermocouple housing is impregnated under vacuum using alumina cement (i.e., water and fine crushed alumina). This procedure is crucial because the impregnation inhibits the flow of soft material from the assembly into the thermocouple bore, thus preventing the failure of thermocouple when operating at low pressure.

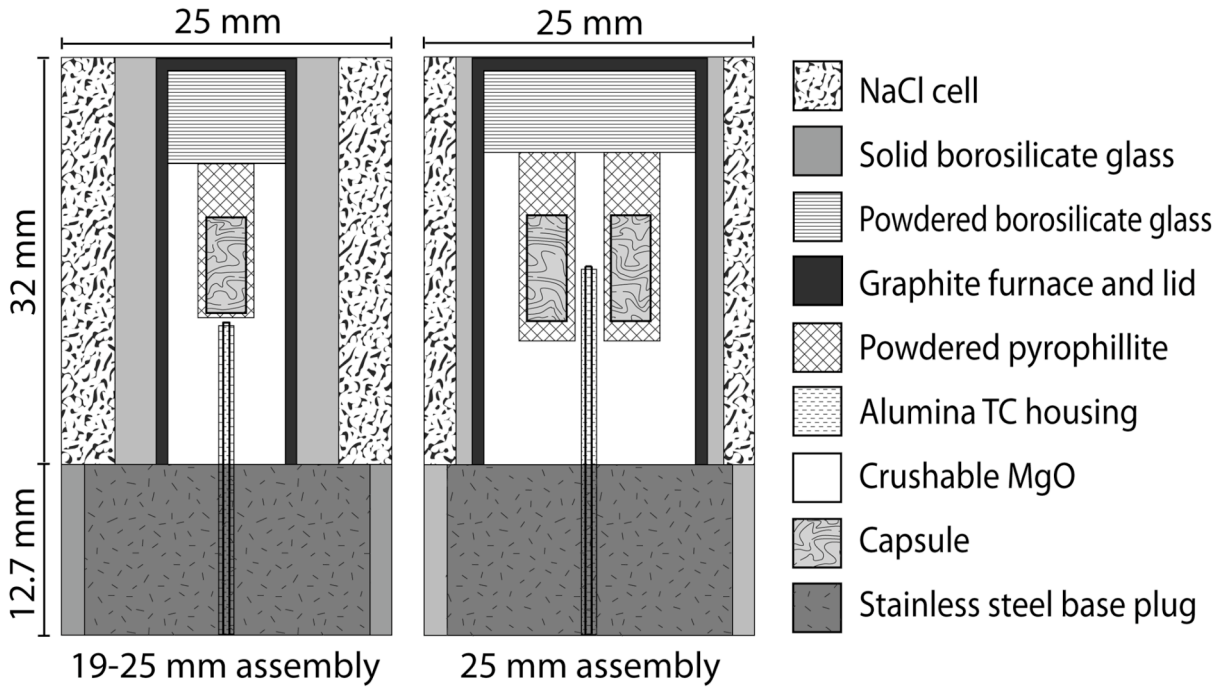

Figure 1 - Schematic cross sections of 19-25 mm and 25 mm furnace assemblies.

3. Calibration methods and analytical techniques

The NaCl melting method (Bohlen, 1984) has been used to calibrate pressure at 500, 300, 200, and 150 MPa and the solubility of H_2O in albite and rhyolite melts has been used to confirm the results at 200 and 150 MPa.

For the NaCl melting method, noble metal capsules (AuPd or Pt, 3 mm diameter) were filled with reagent-grade NaCl and a Pt-sphere (ca. 0.5 mm diameter) was positioned at the top. The capsules were then dried at 110°C for 1 hour before being welded closed. Calibration charges were run at the NaCl melting temperatures in the pressure range 150-500 MPa and held in these conditions for 20 minutes (melting relations for NaCl from Siewert et al., 1998). After each run the capsule was sanded longitudinally and the position of the Pt sphere was checked by binocular. The falling of the sphere at the bottom of the capsule indicates the melting of the salt. Salt melting occurred already at temperature lower than the predicted NaCl melting temperature for the given pressure (Siewert et al., 1998), thus indicating a mismatch between real and nominal pressures. Keeping the temperature constant, runs were repeated at increasing pressure until the NaCl remained solid (i.e. Pt sphere on top). The difference between real and nominal pressures corresponds to the correction that needs to be applied (Figures 2 and 3).

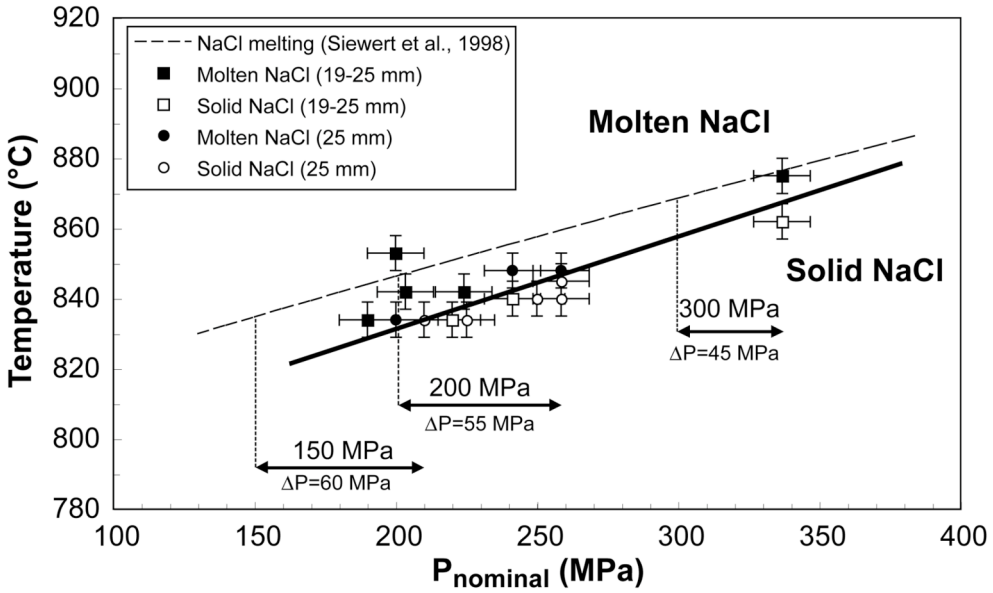

Figure 2 – Results of the NaCl calibration experiments. Note that the nominal pressure is calculated using a 25 multiplier based on the ratio of the surface area of the ram to the surface area of the piston. Variation with the real pressure obtained from the calibration is given in Figure 3.

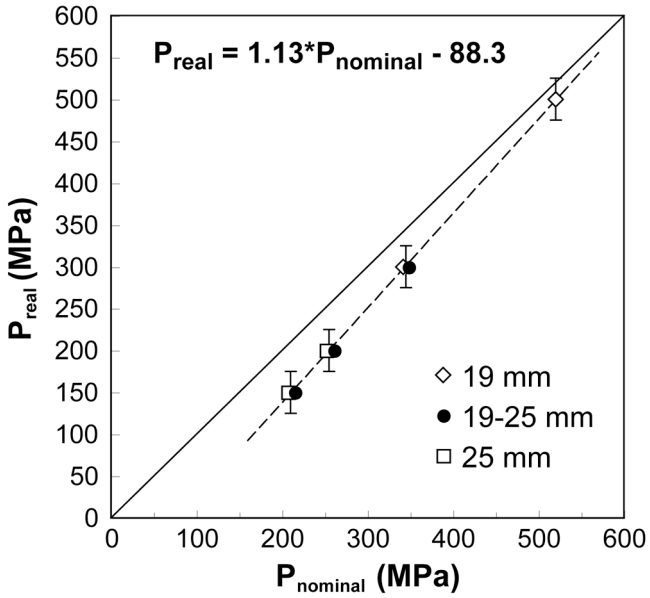

Figure 3 - Pressure correction chart for standard 19 mm assembly and the new 19-25 and 25 mm assemblies. Note that the same equation can be used for all assemblies to calculate the correction.

For the H_2O solubility experiments, the albite glass of Baker (2004) and a glassy obsidian from Pietre Cotte lava flow (Vulcano Island, Southern Italy) have been used as starting materials. Experimental data of Behrens et al. (2001) and the H_2O solubility model of Moore et al. (1998) provide reference models for H_2O solubility in albite and rhyolite, respectively.

Dissolved H_2O in melts was estimated using the 'by difference' technique (Devine et al., 1995), assuming that the discrepancy between the analytical sum of the microprobe analysis and 100 wt.% represents the H_2O concentration. Two capsules bearing either H_2O-undersaturated (4 wt.% H_2O added by microsyringe) or H_2O-oversaturated albite powder (10 wt.% H_2O added by microsyringe) were run together at 900°C and 200 MPa for two hours. Chemical compositions of both H_2O-undersaturated and H_2O-oversaturated glasses were then compared with the composition of the anhydrous albite glass obtained by melting the starting material at 1200°C and ambient pressure (Table 2) in a AuPd crucible. The H_2O determined 'by difference' in the H_2O-oversaturated run was then used to assess the pressure. Following the same procedure as for albite, three additional experiments using the rhyolite composition were performed at 975°C and 150 MPa. Chemical compositions of anhydrous and hydrous glasses are reported in Table 2.

Field Emission Scanning Electron Microscope (FE-SEM) images and electron microprobe analyses (EMPA) of experimental products were obtained at Istituto Nazionale di Geofisica e Vulcanologia (Rome, Italy) with a Jeol FE-SEM 6500F equipped with an energy dispersive microanalysis system and a Jeol-JXA8200 EDS-WDS combined electron microprobe, respectively. The electron microprobe is equipped with five wavelength-dispersive spectrometers. Chemical spot analyses were performed by using 15 kV accelerating voltage and 10 nA beam current and a defocused electron beam of 7 μm and a counting time of 5 s on background and 15 s on peak. The following standards have been adopted for the various chemical elements in albitic melt: albite (Si, Al, Na), forsterite (Mg), andradite (Fe), rutile (Ti), orthoclase (K), barite (Ba), apatite (P) and spessartine (Mn). For analyses of the rhyolitic glasses, the additional standards orthoclase (Si, Al) and jadeite (Na) were used. Sodium and potassium were analyzed before any other element to reduce possible volatilization effects.

4. Results and discussion

The calibration performed following the NaCl melting curve method demonstrates that using the newly designed 19-25 and 25 mm furnace assemblies it is possible to successfully perform experiments at pressure as low as 150 MPa without encountering incomplete compaction and/or thermocouple failure due to the low load applied to the piston. Positive pressure corrections of 45, 55, and 60 MPa to the force applied to the piston (nominal pressure) are necessary to ensure real pressures of 300, 200, and 150 MPa, respectively (Figures 2 and 3). The accuracy of the pressure estimate associated with the calibration methods is ±25 MPa.

In order to directly assess the real pressure on the sample and test the pressure corrections determined by the NaCl melting technique, the above determined pressure corrections were applied and H_2O solubility experiments were performed in the 25 mm assembly at pressures of 200 and 150 MPa (cfr. Baker, 2004),

4.1 H_2O solubility calibration

Images obtained by FE-SEM reveal the presence of bubbles in both the albite and rhyolite glasses synthesized under H_2O-oversaturated conditions, whereas glasses synthesized in anhydrous and H_2O-undersaturated experiments are bubble-free (Figure 4). Bubbles in the H_2O-oversaturated glasses are homogeneous in size and distribution throughout the charges. The lack of bubbles in the H_2O-undersaturated runs suggests a pressure greater than the H_2O-saturation pressure. Notably, all glasses (anhydrous, H_2O-undersaturated and H_2O-oversaturated) are chemically homogeneous and comparable when normalized to 100 wt.% (Table 2).

In the albite H_2O-oversaturated experiment performed at 900°C and 200 MPa, a H_2O content of 7.11 wt.% by difference has been calculated. At the same conditions, Behrens et al. (2001), found 6.5 wt.% H_2O as the saturation limit. Considering that analyses of both anhydrous and undersaturated glasses have given ca. 0.6 wt.% of excess H_2O (Table 2), the calculated value of 7.11 wt.% is in agreement with the value for albite saturation at 200 MPa reported in Behrens et al. (2001). Even without considering the water excess, a water content of 7.11 wt.% in the glass would produce an overestimate of the real pressure in the order of 30 MPa. This is very close to the 25 MPa error for both, the NaCl calibration method and the ±0.5 wt.% accuracy of the H_2O determination 'by difference' (Devine et al., 1995).

Using the same strategy as for the albite experiments, but longer run duration (24 hours), charges loaded with water amounts adequate to obtain glass compositions either below or above the H_2O saturation of the rhyolite melt were conducted at 150 MPa and 975°C. Water concentrations of the H_2O-oversaturated runs (4.8 and 5.5 wt.%) are in agreement with the H_2O-saturation (ca. 5 wt.%) in rhyolite at 150 MPa and 975°C obtained by Moore et al. (1998). The H_2O concentration in the H_2O-undersaturated run is comparable with the initial weight of water in the charge. Notably, glass compositions of both, anhydrous and hydrous charges are nearly identical (Table 2). The uncertainty in the determination of H_2O in the H_2O-oversaturated rhyolitic glass produces only small variations on the pressure estimate (within the 25 MPa accuracy of NaCl method), thus validating the NaCl calibrations also at high temperature.

The simultaneous synthesis of H_2O-undersaturated and H_2O-oversaturated charges can be used to constrain the pressure calibration and to determine the minimum pressure correction required. Even if the analytical error on H_2O introduces an uncertainty on the pressure, the comparison of chemical composition of anhydrous and hydrous glasses allows assessment of the accuracy of the results (i.e. the 0.6 wt.% defect is present in all EPM analyses of albite glasses).

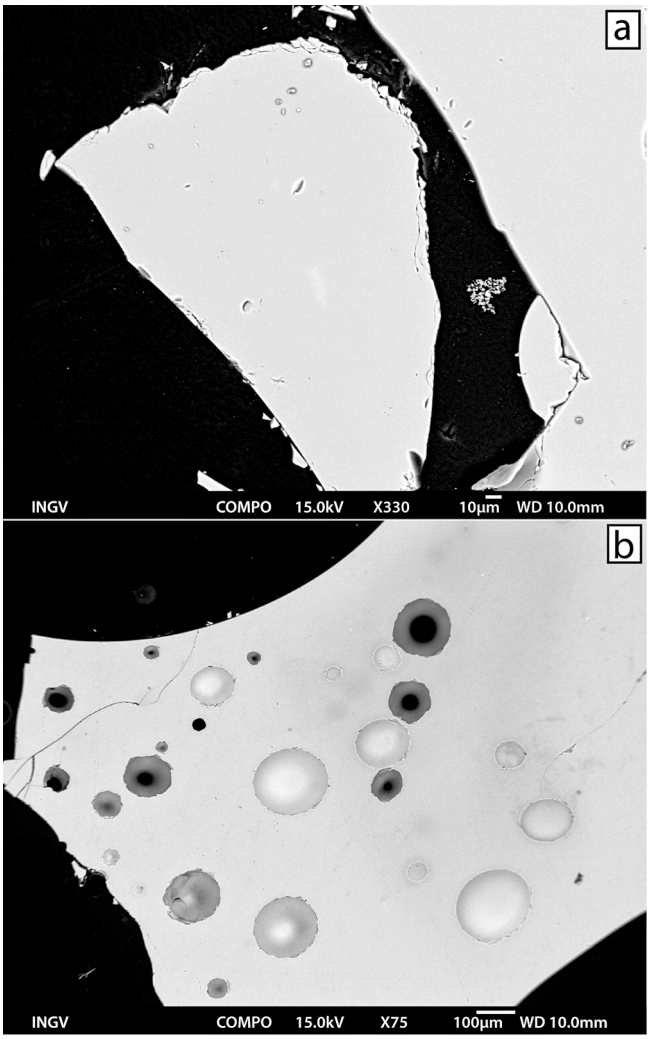

Figure 4 – FE-SEM images of H_2O-solubility experiments: (a) H_2O-undersaturated run showing the albite bubble-free glass and (b) H_2O-oversaturated run showing albite bubble-bearing glass.

4.2 Comparison of calibration methods

An accurate calibration correction is fundamental to experimental results. Our calibration throughout NaCl melting curves demonstrates that the pressure correction decreases at a rate of approximately 1 MPa for every 10 MPa of increase in nominal pressure, over the investigated pressure range (Figure 2). Both, 19-25 mm and 25 mm assemblies require the

same pressure correction in the range 150-300 MPa. Notably, at 300 MPa the pressure correction for the new assemblies is the same as that found for the standard 19 mm assembly (Figure 3), indicating that the different sizes of the assembly components do not significantly affect the pressure correction.

The uncertainty of the NaCl calibration method is associated with thermocouple accuracy (±5°C), yielding an error of ±25 MPa for pressure determinations. This is comparable to the calibration based on the H_2O solubility in albite (Baker, 2004), if the H_2O concentration is determined using the 'by difference' method. This error could be reduced by more accurate determination of dissolved water, through e.g, Fourier Transform Infra-Red spectroscopy or Karl-Fischer titration (cfr. Behrens et al., 1996). However, the comparison of the two used calibration methods presented here is a rapid and inexpensive way to calibrate the piston cylinder. Our experiments demonstrate that the H_2O solubility calibration agrees with the NaCl calibration within the limits of the methods (i.e. in the range of 30 MPa). Moreover, the high degree of consistency between the albite and rhyolite experiments confirms that no significant pressure variation occurs within the assembly in 24-hour experimental run durations.

The main limitation of the NaCl calibration, if compared to the H_2O solubility method, depends on the temperature at which the calibration is conducted. The NaCl calibration experiments are performed at temperatures close to the NaCl melting curve (i.e. 830-870°C in the pressure range 150-300 MPa), thus constraining the pressure calibration to a narrow range of temperatures near the NaCl melting temperature. On the other hand, H_2O solubility experiments can be performed over a wide range of temperatures, being useful for low pressure-high temperature calibrations (e.g. $P<300$ MPa, $T>900$°C). In this study, no differences of pressure correction were found to be necessary between the low temperature (830-870°C) NaCl calibration experiments and the high temperature (900-975°C) H_2O solubility experiments. This result indicates that the NaCl method alone can be effectively used in low pressure calibrations for a wide range of temperatures (800-1000°C). This method is the easier way to calibrate pressure in the piston cylinder, although it may require several experiments than the H_2O solubility method. Solubility experiments can be employed to either verify the NaCl calibration over a range of different temperatures or as a monitor of pressure in multiple charge experiments.

5. Conclusions

This work demonstrates that using the proper assembly, here introduced as the 19-25 and 25 mm furnace assemblies, the piston cylinder apparatus can successfully perform experiments at

pressure as low as 150 MPa. The large surface area of the assemblies implies a nominal pressure on the piston that is higher than that used for the standard 19 mm assembly. This makes the 19-25 and 25 mm assemblies more suitable for operating at pressure below 400 MPa, a value that represents the critical threshold for experiments performed with the standard 19 mm assembly. However, under low pressure conditions (i.e. 150 to 300 MPa), a progressively higher friction occurs and the nominal pressure needs to be increased at a rate of 1 MPa every 10 MPa.

References

Baker, D.R., 2004. Piston-cylinder calibration at 400–500 MPa: A comparison of using water solubility in albite melt and NaCl melting. Am. Mineral. 89, 1553-1556.

Behrens, H., Romano, C., Nowak, M., Holtz, F., Dingwell, D.B., 1996. Near-infrared spectroscopic determination of water species in glasses of the system $MAlSi_3O_8$ (M=Li, Na, K): an interlaboratory study. Chem. Geol. 128, 41-63.

Behrens, H., Meyer, M., Holtz, F., Benne, D., Nowak, M., 2001. The effect of alkali ionic radius, temperature, and pressure on the solubility of water in MAlSiO melts (M = Li, Na, K, Rb). Chem. Geol. 174, 275-289.

Bohlen, S.R., 1984. Equilibria for precise pressure calibration and a frictionless furnace assembly for the piston-cylinder apparatus. N. Jb. Miner. Monatsh. 9, 404-412.

Boyd, J.R., England, J.L., 1960. Apparatus for phase-equilibrium measurements at pressures up to 50 kilobars and temperatures up to 1750 °C. J. Geophys. Res. 65, 741-748.

Devine, J.D., Gardner, J.E., Brack, H.P., Layne, G.D., Rutherford, M.J., 1995. Comparison of microanalytical methods for estimating H_2O contents of silicic volcanic glasses. Am. Mineral. 80, 319-328.

Holloway, J.R., Wood, B.J., 1988. Simulating the Earth, 196 p. Unwin Hyman, Winchester, Massachusetts.

Freda, C., Baker, D.R., Ottolini, L., 2001. reduction of water loss from gold-palladium capsules during piston-cylinder experiments by use of pyrophyllite powder. Am. Mineral. 86, 234-237.

Freda, C., Gaeta, M., Misiti, V., Mollo, S., Dolfi, D., Scarlato, P., 2008. Magma–carbonate interaction: an experimental study on ultrapotassic rocks from Alban Hills (Central Italy). Lithos 101, 397-415.

Kawamoto, T., Hirose, K., 1994. Au-Pd sample containers for melting experiments on iron and water bearing systems. Eur. J. Mineral. 6, 381-385.

Kushiro, I., 1990. Partial melting of mantle wedge and evolution of island arc crust. J.

Geophys. Res. 95, 15929-15939.

Johannes, W., Bell, P.M., Mao, H.K., Boettcher, A.l., Chipman, D.W., Hays, J.F., Newton, R.C., Seifert, F., 1971. An interlaboratory comparison of piston-cylinder pressure calibration using the albite-breakdown reaction. Contrib. Mineral. Petrol. 32, 24-38.

Masotta, M., Freda, C., Gaeta, M., 2011. Origin of crystal-poor, differentiated magmas: insights from thermal gradient experiments. Contrib. Min. Petrol. DOI 10.1007/s00410-011-0658-8.

Moore, G., Vennemann, T., Carmichael, I.S.E., 1998. An empirical model for the solubility of H_2O in magmas to 3 kbar. Am. Mineral. 83, 36-42.

Moore, G., Roggensack, K., Klonowski, S., 2008. A low-pressure-high-temperature technique for the piston-cylinder. Am. Mineral. 93, 48-52.

Nelson, S.T., Montana, A., 1992. Sieve-textured plagioclase in volcanic rocks produced by rapid decompression. Am. Mineral. 77, 1242-1249.

Siewert, R., Büttner, H., Rosenhauer, M., 1998. Experimental investigation of thermodynamic melting properties in the system NaCl-KCl at pressures of up to 7000 bar. N. Jb. Miner. Abh., 172, 259-278.

Table 1 - List of calibration experiments

Sample	Assembly	Calibration method	Temperature (°C)	Pressure[a] (MPa)	Duration (h)	note
QP34-4	19 mm	NaCl	911	482	0.3	molten NaCl
QP34-6	19 mm	NaCl	906	499	0.3	solid NaCl
QP34-12	19 mm	NaCl	862	292	0.3	solid NaCl
QP34-13	19 mm	NaCl	875	292	0.3	molten NaCl
QP1-12	19-25 mm	NaCl	862	291	0.3	solid NaCl
QP1-13	19-25 mm	NaCl	875	291	0.3	molten NaCl
MIA-2	19-25 mm	NaCl	853	137	0.3	molten NaCl
MIA-3	19-25 mm	NaCl	842	141	0.3	molten NaCl
MIA-4	19-25 mm	NaCl	842	165	0.3	molten NaCl
MIA-5	19-25 mm	NaCl	840	184	0.3	solid NaCl
QP1-17	19-25 mm	NaCl	834	161	0.3	solid NaCl
QP1-18	19-25 mm	NaCl	834	126	0.3	molten NaCl
QP1-1	25 mm	NaCl	840	204	0.3	solid NaCl
QP1-2	25 mm	NaCl	845	204	0.3	solid NaCl
QP1-3	25 mm	NaCl	848	204	0.3	molten NaCl
QP1-4	25 mm	NaCl	840	194	0.3	solid NaCl
QP1-5	25 mm	NaCl	848	184	0.3	molten NaCl
QP1-19	25 mm	NaCl	834	165	0.3	solid NaCl
QP1-20	25 mm	NaCl	834	149	0.3	solid NaCl
QP1-21	25 mm	NaCl	834	136	0.3	molten NaCl
AB-1	25 mm	H_2O+Ab	900	204	2	Hydrous
AB-3	25 mm	H_2O+Ab	900	204	2	H_2O-sat
RIO-C6	25 mm	H_2O+Rhy	975	145	24	H_2O-sat
RIO-C7	25 mm	H_2O+Rhy	975	145	24	H_2O-sat
RIO-2	25 mm	H_2O+Rhy	975	145	24	Hydrous

[a] Real pressure calculated from equation shown in figure 3.

Table 2 - Average composition of experimental glasses determined by EMPA, normalized to 100 wt.% on a H_2O-free basis.

Sample	AB-0		AB-1		AB-3		RIO-0		RIO-C6		RIO-C7		RIO-2	
T (°C)	1200		900		900		1200		975		975		975	
P (MPa)	0.1		200		200		0.1		150		150		150	
		sd(8)		sd(5)		sd(5)		sd(6)		sd(10)		sd(10)		sd(10)
SiO_2	69.90	0.32	69.74	0.27	69.47	0.20	75.03	0.17	74.57	0.66	74.97	0.61	74.49	0.47
TiO_2	0.01	0.01	0.00	0.00	0.00	0.00	0.11	0.04	0.07	0.06	0.15	0.04	0.12	0.06
Al_2O_3	18.49	0.19	18.65	0.24	18.88	0.05	12.68	0.19	12.86	0.37	12.74	0.23	12.46	0.21
FeO	0.03	0.03	0.01	0.01	0.02	0.01	1.55	0.17	1.70	0.09	1.48	0.17	1.76	0.13
MnO	0.01	0.02	0.01	0.02	0.01	0.02	0.10	0.02	0.05	0.03	0.08	0.05	0.08	0.04
MgO	0.00	0.00	0.02	0.02	0.02	0.01	0.11	0.04	0.16	0.03	0.11	0.04	0.18	0.04
CaO	0.02	0.02	0.07	0.01	0.02	0.02	0.81	0.06	0.97	0.08	0.90	0.05	0.91	0.07
Na_2O	11.48	0.18	11.46	0.25	11.50	0.13	4.10	0.16	4.10	0.05	4.16	0.13	4.35	0.21
K_2O	0.03	0.02	0.04	0.03	0.07	0.01	5.35	0.05	5.24	0.11	5.18	0.09	5.32	0.09
P_2O_5	0.02	0.01	0.00	0.00	0.01	0.02	0.03	0.03	0.03	0.03	0.05	0.02	0.05	0.05
Cl	0.00		0.00		0.00		0.12	0.04	0.24	0.04	0.18	0.03	0.27	0.04
EPM total	99.38		95.27		92.89		99.27		94.47		95.23		96.11	
H_2O_{in} (wt.%)[a]	0.0		4.0 (-)		10.0 (+)		0.0		7.5 (+)		11.8 (+)		3.5 (-)	
H_2O_{sat} (wt.%)[b]	-		6.50		6.50		-		5.02		5.02		5.02	
H_2O_{diff} (wt.%)[c]	0.62		4.73		7.11		0.73		5.53		4.77		3.89	

[a] Initial H_2O in the charges, (+) and (-) refer respectively to H_2O concentrations above and below theoretical H_2O saturation
[b] H_2O saturation in albite and rhyolite at the experimental conditions (see text for details)
[c] H_2O determined by difference (100 - EMPA total)